UNIVERSIDADE DE LISBOA
INSTITUTO SUPERIOR TÉCNICO

Measurements of Higgs boson properties in associated production with top quarks with the ATLAS detector

Ana Luísa Moreira de Carvalho

Supervisors : Doctor José Ricardo Morais Silva Gonçalo
Doctor Patrícia Conde Muíño

Thesis approved in public session to obtain the PhD Degree in
Physics

Jury final classification: **Pass with Distinction**

2023

UNIVERSIDADE DE LISBOA
INSTITUTO SUPERIOR TÉCNICO

Measurements of Higgs boson properties in associated production with top quarks with the ATLAS detector

Ana Luísa Moreira de Carvalho

Supervisors : Doctor José Ricardo Morais Silva Gonçalo
Doctor Patrícia Conde Muíño

Thesis approved in public session to obtain the PhD Degree in
Physics

Jury final classification: **Pass with Distinction**

Jury

Chairperson : Doctor Mário João Martins Pimenta, Instituto Superior Técnico, Universidade de Lisboa

Members of the Committee :

Doctor Yvonne Peters, The University of Manchester, UK

Doctor João Paulo Ferreira da Silva, Instituto Superior Técnico, Universidade de Lisboa

Doctor José Ricardo Morais Silva Gonçalo, Faculdade de Ciências e Tecnologia, Universidade de Coimbra

Doctor Michele Gallinaro, Instituto Superior Técnico, Universidade de Lisboa

Doctor Tamara Vázquez Schröder, CERN - European Organization for Nuclear Research, Suíça

Funding Institution - Fundação para a Ciência e a Tecnologia

2023

Abstract

Measurements of Higgs boson production in association with top quarks were performed using 139 fb^{-1} of data collected with the ATLAS detector at the Large Hadron Collider. The analyses target events with one or two electrons or muons in the final state and the $H \to b\bar{b}$ decay mode. The $t\bar{t}H(H \to b\bar{b})$ cross-section was measured differentially in bins of Higgs boson transverse momentum. An excess of events over the predicted background hypothesis was observed with a significance of 1.0σ (2.7σ expected). The signal strength was measured to be 0.35 ± 0.20(stat.)$^{+0.30}_{-0.28}$(syst.). The charge-parity (CP) structure of the top-Higgs Yukawa coupling was measured for the first time in the $H \to b\bar{b}$ channel and targeting the $t\bar{t}H$ and tH production processes. Novel angular variables based on the reconstructed top quarks transverse momenta were used to discriminate between different CP scenarios. The mixing angle between CP-even and CP-odd couplings is measured to be $11^{\circ}{}^{+52^{\circ}}_{-73^{\circ}}$. The analyses sensitivity is limited by systematic uncertainties associated with the modelling of the dominant $t\bar{t}+\geq 1b$ background.

Measurements of top quark pair production in association with c-jets were performed using 140 fb^{-1} of data. The cross-section of $t\bar{t}+\geq 2c$ is found to be $\sim 30\%$ larger than predicted.

Studies related to the development of the ATLAS trigger system were also performed. For Run 3, triggers targeting the central exclusive production of jets were implemented, combining the central and AFP detectors. For the High-Luminosity LHC, the performance of a hardware tracking trigger in signatures with two muons was evaluated using a software emulation.

Keywords: Standard Model, Higgs boson, Top-Yukawa coupling, charge-parity, CP-admixture

Resumo

Medições da produção associada de bosões de Higgs com quarks top foram realizadas utilizando 139 fb^{-1} de dados recolhidos pela experiência ATLAS no LHC, em eventos com $H \to b\bar{b}$. A secção eficaz de $t\bar{t}H(H \to b\bar{b})$ foi medida de forma diferencial em bins do momento transverso do bosão de Higgs. Foi observado um excesso de eventos relativamente à previsão do fundo com uma significância estatística de 1.0σ (2.7σ esperada). A força do sinal foi medida: $0.35 \pm 0.20(\text{stat.})^{+0.30}_{-0.28}(\text{syst.})$. As propriedades de carga-paridade da interação de Yukawa entre o quark top e o bosão de Higgs foram medidas pela primeira vez no canal $H \to b\bar{b}$ em eventos de $t\bar{t}H$ e tH. O valor medido do ângulo de mistura de CP é $11^{\circ}{}^{+52^{\circ}}_{-73^{\circ}}$.

Medições da produção associada de pares de quarks top com jatos c foram realizadas utilizando 140 fb^{-1} de dados. O valor da secção eficaz de $t\bar{t}+\geq 2c$ é $\sim 30\%$ superior ao esperado.

Estudos relacionados com o desenvolvimento do sistema de *trigger* da experiência ATLAS foram também realizados. Para a Run 3, *triggers* dedicados a medidas da produção exclusiva de pares de jatos, combinando informação do detetor central e do AFP, foram implementados. Para a fase de alta luminosidade do *LHC*, o desempenho de um sistema de *trigger* que reconstrói traços em *hardware* em eventos com um par de muões foi estudado, utilizando uma simulação em *software*.

Palavras-chave: Modelo Padrão, bosão de Higgs, acoplamento de Yukawa do quark top, carga-paridade, mistura de CP

Acknowledgments

I would like to begin by acknowledging my privilege that ultimately allowed me to produce this thesis. I had the amazing opportunity to learn, focus on my studies and pursue my deep scientific interests, always supported and cheered on by my family. For that I am immensely grateful.

To my mother who is the greatest example of resilience, strength and perseverance. To my father for his dedication and hard-working mindset. To my sister for being a source of light and for inspiring me with her creative mindset and focused demeanor. You inspire and motivate me everyday, thank you. To my grandmother who worries about this not being a real job. To my aunts and uncle who continuously show me alternative ways of thinking and being in the world.

To my friends from Aveiro, who are now also scattered around the world, it is a pleasure having you as part of the home I always go back to.

To my friends and colleagues at CERN, LIP, Saint-Genis-Pouilly and Geneva, this journey would not have been nearly as easy without you. I am very grateful for you presence and continued support.

To my flatmates in Allée des Ormes, thank you for the companionship; you made my life brighter and smoother in the years we have lived together.

To my supervisors from LIP, Ricardo and Patricia, it has been a pleasure learning from you and developing this work under your guidance. Your dedication to science and scientific proficiency are true sources of inspiration. And yet I am mostly grateful for your human competences: your understanding, support and kind words in every situation. Thank you for welcoming me into the world of particle physics and for guiding me throughout my masters and PhD.

To Francesca, thank you for the opportunity to explore the performance of a hardware tracking trigger that might become a reality one day.

To Tamara, thank you for creating a warm and very welcoming environment when I first arrived at CERN. Your passion for scientific research is truly inspiring. A close second to your kindness and love for life. Thank you for pushing me to explore new projects.

To the people in the LIP and ATLAS secretariats, the world would not work without you, thank you.

To the Portuguese National Science Foundation (FCT) for giving me the opportunity to work on this thesis full time through the grant SFRH/BD/143435/2019 and for allowing me to spend some time at CERN, which has been crucial for my scientific development.

To Instituto Superior Técnico for providing the institutional support required to produce this work.

Contents

List of Figures

List of Tables

1

Introduction

With the discovery of the Higgs boson in 2012, all particles predicted by the Standard Model (SM) have been found; and yet there are multiple experimental observations that this model cannot explain. In this current landscape of particle physics, the Higgs boson can be used as tool to test the predictions of the SM until reaching its breaking point and to continue the search for physics beyond the SM.

The Yukawa interaction of the Higgs boson with the heaviest SM particle, the top quark, might be particularly sensitive to new physics effects. Due to the large mass of the top quark, the decay of the Higgs boson to a pair of top quarks is kinematically suppressed and it is extremely rare at the LHC. Therefore, the top Yukawa coupling can only be directly studied in associated production of a Higgs boson with top quarks ($t\bar{t}H$ and tH). These production modes are particularly appealing because they occur at tree-level, thus eliminating the need to account for potential BSM particles in quantum loops. This thesis targets the Higgs boson decay to a pair of b-quarks ($H \to b\bar{b}$). It benefits from the largest branching ratio, gives access to the boosted regime and allows for a full final state reconstruction.

The work described in this thesis was developed within the ATLAS Collaboration. It encompasses the first cross-section measurement of $t\bar{t}H(H \to b\bar{b})$ in the Simplified Template Cross-Section framework (STXS) and the first ever measurement of the charge-parity properties (CP) of the top-Higgs Yukawa coupling using $t\bar{t}H$ and tH events in the same decay channel. Both measurements use the full Run 2 dataset corresponding to 139 fb^{-1} and their strategies evolved in parallel. They are described in chapter 7. Some highlights of the author's contributions are detailed below. In both analysis, the author was the main analyser in the single-lepton channel during the internal review process of the collaboration, performing additional investigations of the largest observed pulls and constraints and being responsible for producing the final results for the publications.

STXS analysis:

- Evaluated theoretical uncertainties in W+jets modelling related to the variation of the factorization and renormalisation scales of the matrix element calculation;
- Evaluated the flexibility of the systematics model by performing fits to pseudodata created from alternative background samples;
- Assessed the impact of the main modelling systematics on the post-fit yields of the MC samples;
- Evaluated the impact in the fit of including a systematic uncertainty comparing the $t\bar{t}+\geq 1b$ five- and four-flavor scheme predictions (this uncertainty was included in the final result in the CP analysis);

CP analysis:

- Validated the linear interpolation between $t\bar{t}H$ CP-even and CP-odd samples at truth level in single-lepton and dilepton channels (through the supervision of a LIP Summer student);

- Optimized the sensitivity and systematics modelling by replacing the CP-discriminant BDT by a single CP-sensitive angular variable (this was the final strategy adopted);
- Developed the fit using the $\Delta R(bb)^{\text{avg}}$ variable in the control regions with exactly five-jets instead of the CP-BDT, following the strategy of the STXS analysis (adopted in the final result);
- Evaluated the possibility of further subdividing the boosted region to improve sensitivity (not adopted in the final result).

The precision of these measurements is strongly limited by systematic uncertainties associated with the modelling of the dominant background of $t\bar{t}$ production with additional heavy-flavor jets. While the theoretical and experimental knowledge of $t\bar{t}$ with additional b-jets has been greatly improved over the last few years, the same is not true for $t\bar{t}$ production with additional c-jets. The first ATLAS measurement of the $t\bar{t}+\geq 2c$ and $t\bar{t}+1c$ cross-sections in the final state with exactly two leptons has been developed by the author. It is described in chapter 8. The combination with the single-lepton channel is ongoing and a paper is in preparation. The author's contributions are listed below.

- Defined and optimized the analysis regions and implemented the baseline fit strategy;
- Tested an alternative reconstruction method for the $t\bar{t}$ system based on kinematic constraints on pairs of (b-)jets (not adopted);

The trigger system is a crucial part of the ATLAS experiment. It ensures that high-quality data is collected for physics analyses. An important part of this work has been the participation in the operation and development of the ATLAS trigger system during Run 3 and beyond. Operational tasks involved the participation in control room and on-call trigger shifts as well as the development of the trigger menu for Run 3. Given their inherently technical nature, they are not described further in this thesis.

An essential part of the ATLAS Forward Proton detectors (AFP) physics program for Run 3 includes taking data in standard pileup conditions to study, among other processes, the central exclusive production of jets. In this way, the AFP detector enlarges the physics program of the ATLAS experiment and allows to study central exclusive production processes that would otherwise be inaccessible. These processes provide valuable insight into the theory of QCD and, in a high-luminosity environment, could become discovery channels for BSM particles that couple to gluons. As part of this effort, a dedicated trigger algorithm that combines information from the jets reconstructed in the central detector with the tracks reconstructed in the AFP silicon detectors was developed and implemented by the author, and is described in chapter 6, section 6.1. It constitutes a proof of principle of the usage of the AFP detector triggering capabilities at the Level-1 and High Level triggers in high-luminosity runs and opens the door to the development of similar triggers targeting other central exclusive production processes.

The upgrade of the ATLAS trigger system for the High-Luminosity phase of the LHC (HL-LHC) is essential to guarantee that the physics acceptance of the ATLAS experiment does not deteriorate in the more challenging pileup conditions that are foreseen. One way of tackling this is by using tracking information early on in the trigger. This would provide crude primary vertex identification and thus allow for early rejection of events with objects originating from pileup vertices. Within the ATLAS Collaboration, the possibility of performing track reconstruction in hardware in the Level-1 trigger was studied. The author contributed to these studies by assessing the performance of the hardware tracking trigger in signatures with two muons, using a software emulation of the hardware system. The muons reconstructed in the previous trigger level are matched to the tracks reconstructed in the Level-1. To further enhance background rejection, the tracks are required to originate from the same position along the z-axis. The development of the fast emulation procedure is not part of this work but it is used in the di-muon performance study. Therefore, it is documented together with the results in chapter 6, section 6.2. These studies contributed to the decision making process of the ATLAS Collaboration regarding the optimal trigger architecture for the HL-LHC.

The work described in this thesis has been presented at multiple international conferences in the form of posters and ATLAS talks. The author also participated in workshops and schools, and presented the analyses in various collaboration meetings.

2

Theoretical framework

Contents

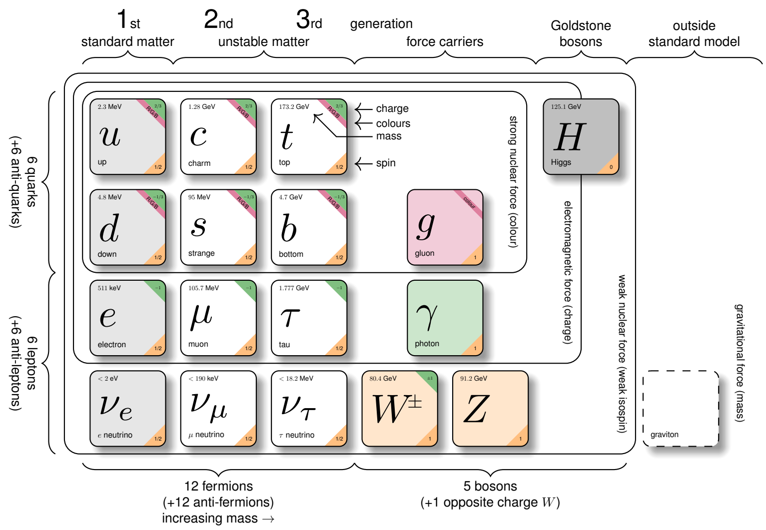

Figure 2.1: Summary table of the particle content of the SM

The Standard Model (SM) of particle physics summarizes our present knowledge of fundamental particles and their interactions. It is formulated in the framework of Quantum Field Theory (QFT) and describes the subatomic world in terms of quantized fields whose excitations correspond to the fundamental particles that can be observed. The particle content of the SM is summarized in figure 2.1. Each particle is represented inside a square. The electric and colour charges are shown in the right upper corner and the spin in the right lower corner. The masses of the particles are also shown. Fundamental particles can be divided into fermions and bosons. Fermions are matter particles, and can be thought of as the building blocks that make up all the matter in our world. A special class of bosons, referred to as gauge bosons, are responsible for mediating the electromagnetic, weak and strong fundamental interactions.

Fermions carry half integer odd spin and obey the Fermi-Dirac statistics. They can be further divided into quarks and leptons. There are six flavors of quarks: three of the 'up type' (up, charm and top represented by u, c and t) with electric charge of $+2/3$ and three of 'down type' (down, strange and bottom represented by d, s and b) with electric charge of $-1/3$. The electric charge is measured in units of the electron electric charge. Similarly, there are three leptons with charge -1 (electron, muon and tau represented by e, μ and τ) and three neutral leptons (electron, muon and tau neutrinos represented by ν with the symbol of the corresponding charged lepton as subscript) that are, within the SM, massless. However, from neutrino oscillation measurements, neutrinos are known to have a small mass. We can classify quarks and leptons in three generations, each composed of an up type and a down type quark and of a charged lepton and the corresponding neutrino.

Bosons carry integer spin and follow the Bose-Einstein statistics. Gauge bosons are associated with the fundamental interactions: strong, electromagnetic and weak. Each interaction can be interpreted as the result of the exchange of the corresponding gauge boson. Gluons (g) and photons (γ) are the mediators of the strong and electromagnetic interactions, respectively. They are massless, electrically neutral and have spin 1. The $W^{\pm}$ and Z bosons are the mediators of the weak interaction and have a mass of 80.385 ± 0.015 GeV [16] and 91.1876 ± 0.0021 GeV [16], respectively. The W^{+} and

W^- bosons have electric charges of $+1$ and -1, respectively, and spin 1. The Z boson is electrically neutral and also has spin 1.

In addition to matter particles and gauge bosons, the theoretical formulation of the SM rests on the existence of the Higgs boson that is an electrically neutral spin 0 particle. It has a mass of 125.09 ± 0.21(stat.) $\pm$ (syst.) GeV [17] and it interacts with every particle that has mass.

Historically, an empirically successful quantum theory of electromagnetism, Quantum Electrodynamics (QED), was developed in the late 1940's. In the early 1950's there were high hopes that quantum theories could also be formulated for the weak and strong interactions. This is the context in which Yang-Mills theories emerged [18]. They extend the concept of gauge theory from abelian groups, that led to the development of QED, to non-abelian gauge groups. However, the quanta of the fields predicted by these theories must be massless in order to maintain gauge invariance and Yang-Mills theories were set aside until the 1960's. Nevertheless, these theories succeeded in developing a recipe to apply local gauge invariance to non-abelian groups and were recovered when the idea of particles acquiring mass through symmetry breaking in massless theories was put forward by Goldstone [19] and Nambu and Jona-Lasinio [20].

All the fundamental interactions of the SM can be described in the formalism of Lagrangian field theory, of which general aspects are presented in section 2.1. From the Lagrangian, the interactions and propagation of the free fields can be derived. Quantum electrodynamics is introduced in section 2.2. The Higgs mechanism is discussed in section 2.3. It solves the problem of generating mass for the weak gauge bosons and allows for the unification of the electromagnetic and weak interactions in a single gauge theory that is presented in section 2.4. The strong interaction of quarks and gluons are described by quantum chromodynamics, which is presented in section 2.5.

Despite the striking success of the SM, there are some experimental observations that it cannot explain. Among them are the nature of dark matter [21–23], the existence of non-zero neutrino masses [24–26] and the current asymmetry between matter and anti-matter [27, 28]. For the latter to be realized, more CP-violating effects are needed. This is discussed in section 2.6.

A central aspect of this thesis is to set constraints on CP-violation in the top Yukawa coupling, based on an effective model that allows for the existence of a pseudoscalar component in the interaction between the Higgs boson and the top quark. This is detailed in section 2.7.

The theoretical descriptions in this chapter follow mainly references [29],[30] and [31].

2.1 Lagrangian formulation and symmetries

Quantum field theories, in which particles are described as excitations of fields, generically represented by $\phi(x)$, where x is the position four-vector, can be studied using the Lagrangian field theory formalism. In this formalism, the Lagrangian density is defined as a function of the fields, ϕ, and their derivatives and it encodes the information about their properties and interactions:

$$\mathcal{L}(x) = \mathcal{L}(\phi, \partial_\mu \phi). \tag{2.1}$$

Imposing that the action, $S = \int d^4x\, \mathcal{L}$, is stationary yields the equations of motion of the field:

$$\delta S = \int d^4x \left[\frac{\partial \mathcal{L}}{\partial \phi} \delta\phi + \frac{\partial \mathcal{L}}{\partial(\partial_\mu \phi)} \delta(\partial_\mu \phi) \right] \tag{2.2}$$

$$= \int d^4x \left[\frac{\partial \mathcal{L}}{\partial \phi} - \partial_\mu \frac{\partial \mathcal{L}}{\partial(\partial_\mu \phi)} \right] \delta\phi = 0. \tag{2.3}$$

By equating the term in square brackets in equation 2.3 to zero, one obtains the Euler-Lagrange equations of motion. Integration by parts is applied to go from equation 2.2 to 2.3.

Symmetries played a crucial role in the development of the SM. A symmetry can be defined as a group of transformations of the fields that leave the Lagrangian invariant. The Lagrangian formulation is particularly well suited to study symmetries and to understand their importance, in particular through Noether's theorem [32], which states that the invariance of the Lagrangian density under a continuous transformation implies a conserved quantity. Conversely, this means that every conserved quantity is associated with an underlying symmetry.

If one considers the transformation:

$$\phi(x) \to \phi'(x) = \phi(x) + \delta\phi(x), \tag{2.4}$$

the corresponding change induced in the Lagrangian is given by:

$$\begin{aligned} \delta\mathcal{L} &= \frac{\partial \mathcal{L}}{\partial \phi} \delta\phi + \frac{\partial \mathcal{L}}{\partial(\partial_\mu \phi)} \delta(\partial_\mu \phi) \\ &= \left[\frac{\partial \mathcal{L}}{\partial \phi} - \partial_\mu \left(\frac{\partial \mathcal{L}}{\partial(\partial_\mu \phi)} \right) \right] \delta\phi + \partial_\mu \left(\frac{\partial \mathcal{L}}{\partial(\partial_\mu \phi)} \delta\phi \right), \end{aligned} \tag{2.5}$$

where the term in square brackets is zero, according to the Euler-Lagrange equation (equation 2.3). By imposing that the Lagrangian is invariant under this transformation ($\delta\mathcal{L} = 0$), one obtains, according to Noether's theorem, the conserved current, J^μ, and charge, Q:

$$\partial_\mu J^\mu = 0, \qquad J^\mu \equiv \frac{\partial \mathcal{L}}{\partial(\partial_\mu \phi)} \delta\phi, \qquad Q = \int d^3x J^0. \tag{2.6}$$

2.2 Quantum electrodynamics

Quantum electrodynamics is the theory that describes the propagation and interaction of fermions. For a free (non-interacting) fermion of mass m, the Dirac Lagrangian takes the form [33]:

$$\mathcal{L}_{\text{free}} = \bar{\psi}(x)(i\gamma^\mu \partial_\mu - m)\psi(x), \tag{2.7}$$

where $\psi(x)$ is a Dirac spinor, with its complex conjugate $\bar{\psi}(x)$ given by $\psi(x)^\dagger \gamma^0$, and γ^μ are the Dirac matrices, that can be written in terms of the Pauli matrices in the Weyl or chiral representation:

$$\gamma^0 = \begin{pmatrix} 0 & 1 \\ 1 & 0 \end{pmatrix} \qquad \gamma^i = \begin{pmatrix} 0 & \sigma^i \\ -\sigma^i & 0 \end{pmatrix}. \tag{2.8}$$

This Lagrangian is invariant under a global gauge transformation of the $U(1)$ symmetry group given by $\psi(x) \to \psi'(x) = e^{i\theta}\psi(x)$, where θ is an arbitrary constant. However, when one tries to extend global gauge invariance to local gauge invariance by making θ a function of x^{μ}, the Lagrangian does not remain invariant because the derivative of the field, $\partial_{\mu}\psi(x)$ picks up an extra term:

$$\partial_{\mu}\psi(x) \to e^{i\theta(x)}\partial_{\mu}\psi(x) + ie^{i\theta(x)}\psi(x)\partial_{\mu}\theta(x). \tag{2.9}$$

The invariance of the Lagrangian can be retained if the derivative of the field is promoted to a covariant derivative that transforms under a local gauge transformation such that it cancels out the second term in equation 2.9. One can define the covariant derivative as:

$$\mathcal{D}_{\mu} = \partial_{\mu} + iqA_{\mu}(x), \tag{2.10}$$

where q is an arbitrary real constant and $A_{\mu}(x)$ is a gauge vector field that transforms as

$$A_{\mu}(x) \to A_{\mu}(x) - \frac{1}{q}\partial_{\mu}\theta(x). \tag{2.11}$$

Using the covariant derivative, the Lagrangian takes the form:

$$\mathcal{L} = \bar{\psi}(x)(i\gamma^{\mu}\mathcal{D}_{\mu} - m)\psi(x) = \mathcal{L}_{\text{free}} - q\bar{\psi}(x)\gamma^{\mu}A_{\mu}(x)\psi(x), \tag{2.12}$$

where the last term describes the interaction between a fermion with charge q and an external electromagnetic potential $A_{\mu}(x)$. A kinetic term, describing the propagation of the field associated to the electromagnetic potential, can also be added:

$$\mathcal{L}_{\text{kinetic}} = -\frac{1}{4}F_{\mu\nu}F^{\mu\nu}, \tag{2.13}$$

where $F_{\mu\nu} = \partial_{\mu}A_{\nu} - \partial_{\nu}A_{\mu}$ is the electromagnetic field tensor. This term does not break local gauge invariance. The full Lagrangian can thus be written as:

$$\mathcal{L} = \bar{\psi}(x)(i\gamma^{\mu}\partial_{\mu} - m)\psi(x) - q\bar{\psi}(x)\gamma^{\mu}A_{\mu}\psi(x) - \frac{1}{4}F_{\mu\nu}F^{\mu\nu}, \tag{2.14}$$

where the second term describes the electromagnetic interaction between fermions and photons. Note that in this case a mass term for $A_{\mu}(x)$ of the form $m^2A_{\mu}A^{\mu}$ cannot be added because it would break local gauge invariance. In the case of QED this is not a problem since the photon is known to be massless.

The example of QED has been used to demonstrate how the requirement of local gauge invariance requires the addition of a gauge vector field that, in this case, represents the photon. Additionally, by requiring that the theory is invariant under the $U(1)$ group one obtains a conserved quantity that can be identified with the electric charge.

The $U(1)$ symmetry group is abelian, i.e., the operations that generate the group are commutative. It is natural to wonder if the same steps that led to the development of QED can be applied when the symmetry group is non-abelian, for example $SU(2)$ or $SU(3)$. They can, and when the symmetry group is $SU(3)$ this produces the theory of strong interaction, quantum chromodynamics, described in section 2.5.

However, in this framework it is not possible to include mass terms for the gauge bosons. Both the gluon and photon are massless so this is not a problem for QED and QCD. Conversely, for the weak interactions, it was known that the associated W- and Z-bosons should be massive. Therefore, the theory of weak interactions can not be directly obtained from the application of local gauge invariance to the $SU(2)$ group.

The breakthrough happens by introducing the concept of spontaneous symmetry breaking (SSB). This is a phenomenon in which the lowest energy state (vacuum state) of one of the fields in the theory does not share the symmetry of the Lagrangian. When combined with local gauge invariance, SSB requires that gauge bosons acquire mass, leading to the current model of weak interactions. This is the Higgs mechanism, detailed in section 2.3. Remarkably, this model also unifies the weak and electromagnetic interactions in a single larger gauge theory that is presented in section 2.4.

2.2.1 Weyl representation

So far we have not specified the form of the Dirac spinors. Multiple notations can be used; in the context of the SM, a particularly suitable one is the Weyl representation:

$$\psi = \begin{pmatrix} \psi_L \\ \psi_R \end{pmatrix}, \tag{2.15}$$

where ψ_L and ψ_R are the left- and right-handed spinors that relate to the Dirac spinors via the helicity projectors, P_L and P_R:

$$\psi_L = P_L\psi = \frac{1-\gamma_5}{2}\psi, \qquad \psi_R = P_R\psi = \frac{1+\gamma_5}{2}\psi, \tag{2.16}$$

defined in terms of the fifth Dirac's matrix $\gamma_5 = i\gamma_0\gamma_1\gamma_2\gamma_3$.

This representation is particularly useful to study the weak interactions because it has been shown experimentally that these violate charge-parity symmetry and thus differentiate between left- and right-handed chiral particles. The left- and right-handed spinors, ψ_L and ψ_R, belong to different $SU(2)$ representations and have different $U(1)$ charges. ψ_L is an $SU(2)$ doublet while ψ_R is a singlet. In this representation, the fermion content of the first SM family can be written as:

$$E_L = \begin{pmatrix} \nu_e \\ e \end{pmatrix}_L, \qquad E_R = e_R, \qquad Q_L = \begin{pmatrix} u \\ d \end{pmatrix}_L, \qquad Q_R = u_R, d_R, \tag{2.17}$$

where $E_L(E_R)$ and $Q_L(Q_R)$ are the left-(right-)handed components of the first family lepton and quark fields. Since neutrinos are purely left-handed particles within the SM, there is no right-handed component for the neutrino.

By making use of the identity $\psi = \psi_L + \psi_R$ [29] one can expand the free Dirac Lagrangian (equation 2.7) in terms of the Weyl spinors:

$$\mathcal{L}_{\text{free}} = \bar{\psi_L} i\gamma^\mu \partial_\mu \psi_L + \bar{\psi_R} i\gamma^\mu \partial_\mu \psi_R - m\bar{\psi_L}\psi_R - m\bar{\psi_R}\psi_L. \tag{2.18}$$

It can be shown, using equation 2.16, that the mixed kinetic terms and mass terms proportional to $\bar{\psi_L}\psi_L$ ($\bar{\psi_R}\psi_R$) are zero. It would in principle be possible to construct the mass terms shown in grey. These, however, do not preserve local gauge invariance because the Weyl spinors transform differently under the $SU(2) \times U(1)$ gauge group.

For a while, the construction of mass terms for the fermions was a serious problem. It was solved by the introduction of the Higgs mechanism, described in what follows.

2.3 Higgs mechanism

In the SM formulation of the electroweak interactions, the symmetry group is $SU(2) \times U(1)$. It is not possible to include explicit mass terms in the Lagrangian for the weak gauge bosons because they would violate gauge invariance. The Higgs mechanism provides a solution to this problem by combining local gauge invariance with spontaneous symmetry breaking.

The Lagrangian corresponding to the Higgs sector is given by:

$$\mathcal{L} = (D_\mu \phi)^\dagger (D^\mu \phi) - V(\phi^\dagger \phi), \tag{2.19}$$

where ϕ is a scalar field that transforms as a $SU(2)$ spinor and the Higgs potential, $V(\phi^\dagger \phi)$, is given by:

$$V(\phi^\dagger \phi) = \mu^2 \phi^\dagger \phi + \lambda (\phi^\dagger \phi)^2. \tag{2.20}$$

The covariant derivative, D_μ, is given by:

$$D_\mu = \partial_\mu - igW_\mu^a T^a - ig' Y B_\mu, \tag{2.21}$$

where W_μ^a and B_μ are the gauge fields of $SU(2)_L$ and $U(1)_Y$, respectively, Y is the $U(1)$ charge, also referred to as hypercharge, and T^a is defined in terms of the Pauli matrices: $T^a = \frac{\sigma^a}{2}$. For the Higgs boson the value of the hypercharge is $\frac{1}{2}$. Note that in the definition of the covariant derivative both $SU(2)$ and $U(1)$ symmetries are present. It can be shown that by combining spontaneous symmetry breaking with only an $SU(2)$ symmetry leads to a theory with no massless gauge bosons. For any field that is an $SU(2)$ singlet, and therefore has zero $SU(2)$ charge, the covariant derivative takes the form $D_\mu = \partial_\mu - ig' Y B_\mu$.

Due to the requirement of Lorentz invariance, only the scalar field can have a vacuum expectation value (VEV), v, different from zero. The values of v are determined by the stationary points of the potential:

$$v = 0 \qquad \text{or} \qquad v = \sqrt{\frac{-\mu^2}{2\lambda}}. \tag{2.22}$$

The equation on the right only gives a real value for v if $\mu^2 < 0$. Therefore it corresponds to $\mu^2 \leq 0$ while the equation on the left corresponds to $\mu^2 \geq 0$. In both cases λ has to be larger than zero to guarantee that the energy of the field is bounded from below.

The shapes of the Higgs potential for $\mu^2 > 0$ and $\mu^2 < 0$ are shown in Figure 2.2 on the left and right, respectively. For $\mu^2 > 0$ there is a single minimum located at $\langle \phi \rangle = 0$. For $\mu^2 < 0$ the potential has an infinite number of minima located in a circumference centered at zero. In this case the minima occur for $\langle \phi \rangle, \langle \phi^\dagger \rangle \neq 0$. Therefore the field acquires a VEV different than zero and this is what leads to the SSB.

The scalar field can be written in terms of its minimum value, v, and of perturbations around that minimum, h (which corresponds to the Higgs field):

$$\phi = \begin{bmatrix} 0 \\ v + \frac{h}{\sqrt{2}} \end{bmatrix} \qquad (\textit{unitary gauge}). \tag{2.23}$$

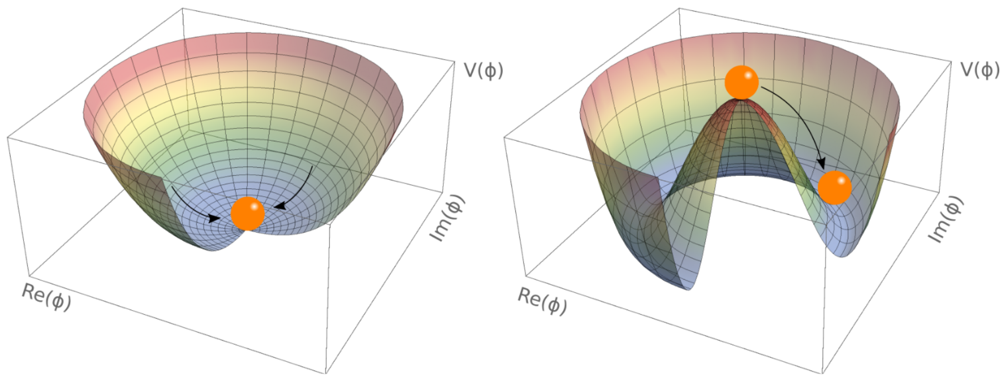

Figure 2.2: Higgs potential for $\mu^2 > 0$ (left) and $\mu^2 < 0$ (right).

Expanding the first term in equation 2.19 one obtains:

$$\mathcal{L} = \frac{1}{2}\partial_\mu h \partial^\mu h \tag{2.24}$$

$$+ \frac{g^2}{4}\left(v^2 + \frac{h^2}{2} + \sqrt{2}vh\right)\left(W^1_\mu W^{1\mu} + W^2_\mu W^{2\mu}\right) \tag{2.25}$$

$$+ \frac{1}{4}\left(v^2 + \frac{h^2}{2} + \sqrt{2}vh\right)\left(gW^3_\mu - g'B_\mu\right)\left(gW^{3\mu} - g'B^\mu\right), \tag{2.26}$$

where in the last line there are terms that mix the W^3_μ and B_μ fields, indicating that these are not the physical (mass) states of the theory. These can be found by diagonalizing the mass matrix:

$$\begin{bmatrix} g^2 & -gg' \\ -gg' & g'^2 \end{bmatrix}\begin{bmatrix} W^3_\mu \\ B_\mu \end{bmatrix} \xrightarrow{\text{Diagonalization}} \begin{bmatrix} 0 & 0 \\ 0 & g^2+g'^2 \end{bmatrix}\begin{bmatrix} A_\mu \\ Z_\mu \end{bmatrix}. \tag{2.27}$$

A_μ and Z_μ are the physical fields that are related with W^3_μ and B_μ by means of a rotation matrix:

$$\begin{bmatrix} A_\mu \\ Z_\mu \end{bmatrix} = \begin{bmatrix} \cos\theta_W & -\sin\theta_W \\ \sin\theta_W & \cos\theta_W \end{bmatrix}\begin{bmatrix} W^3_\mu \\ B_\mu \end{bmatrix}, \tag{2.28}$$

where θ_W is the Weinberg angle. By inverting this relation, W^3_μ and B_μ can be written as a function of A_μ and Z_μ. Additionally, W^1_μ and W^2_μ are related to the physical $W^\pm$ bosons by: $W^\mp = \frac{1}{\sqrt{2}}\left(W^1_\mu \pm iW^2_\mu\right)$. Imposing that the A_μ is the eigenvector with null mass, one can determine θ_W: $\tan\theta_W = \frac{g'}{g}$. The Lagrangian of equation 2.26 takes then the form:

$$\mathcal{L} = \frac{1}{2}\partial_\mu h \partial^\mu h \tag{2.29}$$

$$+ \frac{1}{2}\frac{g^2v^2}{2}W^+_\mu W^{\mu-} + \frac{1}{2}\frac{(g^2+g'^2)v^2}{2}Z_\mu Z^\mu \tag{2.30}$$

$$+ \frac{g^2h^2}{4}W^+_\mu W^{\mu-} + \frac{(g^2+g'^2)h^2}{4}Z_\mu Z^\mu \tag{2.31}$$

$$+ \frac{g^2vh}{2\sqrt{2}}W^+_\mu W^{\mu-} + \frac{(g^2+g'^2)vh}{2\sqrt{2}}Z_\mu Z^\mu, \tag{2.32}$$

where 2.30 gives the mass terms for the gauge bosons and 2.31 and 2.32 represent the four- and three-point interactions of the Higgs boson with the gauge bosons, respectively. Note that, by construction, there is no mass term for the photon, nor an interaction term with the Higgs boson. The masses of the Z and W bosons are given by $M_Z = \sqrt{\frac{1}{2}v^2(g^2+g'^2)}$ and $M_W = \sqrt{\frac{1}{2}v^2g^2}$, respectively.

Expanding now the Higgs potential, one obtains the Lagrangian for the Higgs boson mass (first row) and self interactions (second row):

$$V(\phi^\dagger\phi) = \frac{1}{2}(-2\mu^2)h^2 \tag{2.33}$$

$$+ h^3\sqrt{-\mu^2\lambda} + \frac{1}{4}h^4\lambda. \tag{2.34}$$

2.3.1 Fermion masses

As mentioned at the end of section 2.2.1, fermion mass terms of the form $-m\bar{\psi_L}\psi_R$ are not invariant under $SU(2) \times U(1)$ transformations and thus cannot be added to the Lagrangian. By requiring that fermions acquire mass through the electroweak symmetry breaking mechanism one can write the following Lorentz- and gauge-invariant Lagrangian:

$$\mathcal{L}^e_{\text{Yukawa}} = -f_e\bar{E}_L\phi e_R - f_e\bar{e}_R\phi^\dagger E_L, \tag{2.35}$$

where f_e is a dimensionless coupling constant, and e_R and E_L are the right- and left-handed chiral components of the electron spinor field. Here, we consider first, for simplicity, a single fermionic field corresponding to the electron. Expanding the Higgs field as a perturbation around the VEV and making use of the helicity projectors, the Lagrangian can be rewritten as:

$$\mathcal{L}^e_{\text{Yukawa}} = -f_e v\bar{e}e - \frac{1}{\sqrt{2}}f_e h\bar{e}e, \tag{2.36}$$

where the first term corresponds to the electron mass term and thus $f_e = \frac{m_e}{v}$. The second term corresponds to the interaction between the Higgs boson and the electron.

2.4 Weak interactions and electroweak unification

The Lagrangian for the unified electroweak interactions can be written as:

$$\sum_f \bar{\psi_f}(i\gamma^\mu D_\mu - m)\psi_f - \frac{1}{4}W^a_{\mu\nu}W^{\mu\nu}_a - \frac{1}{4}B_{\mu\nu}B^{\mu\nu}, \tag{2.37}$$

where the sum runs over all fermionic fields ψ_f of the theory. $W^a_{\mu\nu}$ $(a = 1,2,3)$ and $B_{\mu\nu}$ are field strength tensors associated with the gauge fields W^a_μ and B_μ, respectively. The field tensors are defined as:

$$W^a_{\mu\nu} = \partial_\mu W^a_\nu - \partial_\nu W^a_\mu - g\epsilon^{abc}W^b_\mu W^c_\nu \tag{2.38}$$

$$B_{\mu\nu} = \partial_\mu B_\nu - \partial_\nu B_\mu. \tag{2.39}$$

It is convenient to write the covariant derivative in equation 2.21 in terms of the mass eigenstates of the theory:

$$D_\mu = \partial_\mu - i\frac{g}{\sqrt{2}}(W^+_\mu T^+ + W^-_\mu T^-) - i\frac{g}{\cos\theta_W}Z_\mu(T^3 - \sin^2\theta_W Q) - ieA_\mu Q, \tag{2.40}$$

where $T^\pm = \frac{1}{2}(\sigma^1 \pm i\sigma^2)$ and σ^i are the Pauli matrices, $e = g\sin\theta_W$ is the electron charge, and $Q = T^3 + Y$ is the electric charge quantum number operator.

Using the notation of Weyl spinors introduced in section 2.2.1 and considering, for simplicity, only the first fermionic family, the first term of the electroweak Lagrangian can be written as:

$$\mathcal{L} = \bar{E}_L i\gamma^\mu D_\mu E_L + \bar{e}_R i\gamma^\mu D_\mu e_R \quad \text{(leptons)} \tag{2.41}$$

$$+ \bar{Q}_L i\gamma^\mu D_\mu Q_L + \bar{u}_R i\gamma^\mu D_\mu u_R + \bar{d}_R i\gamma^\mu D_\mu d_R \quad \text{(quarks)}. \tag{2.42}$$

Using equation 2.40 and the definition of the helicity projectors, one can obtain the Lagrangian for the charged, neutral and electromagnetic lepton interactions:

$$\mathcal{L}^{\text{leptons}}_{\text{interaction}} = -\frac{g}{2\sqrt{2}}\left[\bar{\nu_e}\gamma^\mu(1-\gamma_5)W^+_\mu e + \bar{e}\gamma^\mu(1-\gamma_5)W^-_\mu \nu_e\right] \tag{2.43}$$

$$-\frac{g}{\cos\theta_W}\left[\bar{\nu_e}\gamma^\mu(g^\nu_V - g^\nu_A\gamma_5)Z_\mu\nu_e + \bar{e}\gamma^\mu(g^e_V - g^e_A\gamma_5)Z_\mu e\right] \tag{2.44}$$

$$-(-e)\bar{e}\gamma^\mu e A_\mu. \tag{2.45}$$

For quarks, the picture is slightly more complicated because the down quark states that enter the weak interactions (d', s' and b') are not the mass eigenstates (d, s and b). They are related through the Cabibbo-Kobayashi-Maskawa (CKM) matrix [34, 35]:

$$\begin{pmatrix} d' \\ s' \\ b' \end{pmatrix} = \begin{pmatrix} V_{ud} & V_{us} & V_{ub} \\ V_{cd} & V_{cs} & V_{cb} \\ V_{td} & V_{ts} & V_{tb} \end{pmatrix} \begin{pmatrix} d \\ s \\ b \end{pmatrix}, \tag{2.46}$$

where $|V_{ij}|^2$ can be complex numbers that represent the probability for a quark of type j to decay to a quark of type i and need to be determined experimentally. The electroweak interaction Lagrangian for quarks can thus be written as:

$$\mathcal{L}^{\text{quarks}}_{\text{interaction}} = -\frac{g}{2\sqrt{2}}\left[\bar{u}\gamma^\mu(1-\gamma_5)W^+_\mu d' + \bar{d'}\gamma^\mu(1-\gamma_5)W^-_\mu u\right] \tag{2.47}$$

$$-\frac{g}{\cos\theta_W}\left[\bar{u}\gamma^\mu(g^u_V - g^u_A\gamma_5)Z_\mu u + \bar{d'}\gamma^\mu(g^d_V - g^d_A\gamma_5)Z_\mu d'\right] \tag{2.48}$$

$$+ eQ_u\bar{u}\gamma^\mu u A_\mu + eQ_d\bar{d'}\gamma^\mu d' A_\mu \tag{2.49}$$

$$+\begin{pmatrix} u \to c \\ d' \to s' \end{pmatrix} + \begin{pmatrix} u \to t \\ d' \to b' \end{pmatrix}. \tag{2.50}$$

The term 2.50 indicates that the complete Langrangian describing the electroweak interactions of quarks also contains terms similar to 2.47, 2.48 and 2.49 but for the quarks of the second and third generations.

Using the CKM matrix, one can write this Lagrangian as a function of the quark mass eigenstates. Here, we rewrite only the terms representing the interactions of quarks with the W-boson (equation 2.47), since it will be useful later on:

$$\mathcal{L}^{\text{quarks-W}}_{\text{interaction}} = -\frac{g}{2\sqrt{2}}\left[\bar{u}\gamma^\mu(1-\gamma_5)W^+_\mu V_{ud}d + \bar{d}V^*_{ud}\gamma^\mu(1-\gamma_5)W^-_\mu u\right] \tag{2.51}$$

2.5 Quantum Chromodynamics

Quantum Chromodynamics (QCD) is the quantum field theory that describes the propagation and interaction of quarks and gluons. Similarly to what was done for QED, one can start from the free Dirac

Lagrangian and impose local gauge invariance to obtain the full interaction Lagrangian. However, in the case of QCD, the underlying symmetry group is $SU(3)$ in the colour space (denoted $SU(3)_C$). Under this symmetry group, quarks are triplets of colour and can be represented as vectors with three components.

For free quarks, the Lagrangian takes the form:

$$\mathcal{L} = \sum_f \bar{\psi}_f (i\gamma^\mu \partial_\mu - m_f)\psi_f, \tag{2.52}$$

where f runs over all possible quark flavors ($f = 1, ..., 6$) and ψ_f are Dirac spinors. The summation over the quark flavor f will be omitted henceforth, but it is implied. Under $SU(3)_C$ the fields transform as

$$\psi(x) \to \psi'(x) = e^{ig_s\theta_a(x)T_a}\psi(x), \tag{2.53}$$

where $T_a, (a = 1, ..., 8)$ are the generators of the $SU(3)_C$ symmetry group, which in the fundamental representation are related to the Gell-Mann matrices, λ_a, by $T_a = \lambda_a/2$. The θ_a are a set of eight functions of the space-time coordinate, x. Under this local gauge transformation, the Dirac Lagrangian becomes

$$\mathcal{L} = \bar{\psi}_f \left[i\gamma^\mu(\partial_\mu + ig_s\partial_\mu\theta_a(x)T_a) - m\right]\psi_f. \tag{2.54}$$

Local gauge invariance is asserted by introducing eight new gauge fields, the gluons, $G^a_\mu(x)$, that transform as

$$G^a_\mu \to G^a_\mu - \partial_\mu\theta_a - g_s f_{abc}\theta_b G^c_\mu, \tag{2.55}$$

and that allow the definition of the covariant derivative as

$$\mathcal{D}_\mu = \partial_\mu - ig_s\frac{\lambda_a}{2}G^a_\mu(x). \tag{2.56}$$

The f_{abc} in equation 2.55 are the structure constants of the $SU(3)$ group, defined by the commutation relations $[\lambda_a, \lambda_b] = 2if_{abc}\lambda_c$. The presence of this term, that does not exist in QED, gives rise to the self-interaction of gluons.

Replacing the partial derivative by the covariant derivative in equation 2.52 and adding a gauge-invariant propagation term for gluons leads to the final QCD Lagrangian:

$$\begin{aligned}
\mathcal{L}_{QCD} &= \sum_f \bar{\psi}_f(i\gamma^\mu\partial_\mu - g_s\gamma^\mu G^a_\mu\frac{\lambda_a}{2} - m_f)\psi_f - \frac{1}{4}G^a_{\mu\nu}G^{\mu\nu}_a && (2.57)\\
&= \sum_f \bar{\psi}_f(i\gamma^\mu\partial_\mu - m_f)\psi_f - \frac{1}{4}(\partial_\mu G^a_\nu - \partial_\nu G^a_\mu)(\partial^\mu G^\nu_a - \partial^\nu G^\mu_a) && (2.58)\\
&- g_s\sum_f \bar{\psi}_f\gamma^\mu G^a_\mu\frac{\lambda_a}{2}\psi_f && (2.59)\\
&- \frac{g_s}{2}(\partial^\mu G^\nu_a - \partial^\nu G^\mu_a)G^b_\mu G^c_\nu - \frac{g_s^2}{4}f^{abc}f_{ade}G^\mu_b G^\nu_c G^d_\mu G^e_\nu. && (2.60)
\end{aligned}$$

To expand equation 2.57 the definition of the gluon field tensor, $G^a_{\mu\nu}$, was used:

$$G^a_{\mu\nu} = \partial_\mu G^a_\nu - \partial_\nu G^a_\mu - g_s f_{abc}G^b_\mu G^c_\nu. \tag{2.61}$$

Equation 2.59 represents the colour interaction between the quarks and gluons and the terms in equation 2.60 represent the the gluon's three- and four-point interactions.

The self-interaction of the gluons entails a series of consequences. It is thought to be at the origin of *colour confinement*. Under this hypothesis, objects with non-zero colour charge cannot propagate freely and are always confined inside colour-singlet states, such as baryons and mesons. It was proposed to explain the lack of experimental observation of free quarks. There is currently no analytical description of colour confinement but a qualitative understanding can be attained by considering what happens when a pair of free quarks is pulled apart [31]. They interact via the exchange of virtual gluons, among which an attractive force is established. This attractive interaction between the gluons squeezes the colour field between the quarks to a tube. In this configuration, the energy stored in this field is linearly proportional to the distance between the quarks, with the proportionality constant determined experimentally to be ~ 1 GeV/fm. It would thus require an infinite amount of energy to separate two quarks to an infinite distancec. Therefore, as quarks separate, it becomes more energetically favorable to create pairs of quarks and anti-quarks.

This behavior explains the experimental observation of jets of colourless particles. Starting from two quarks separating at high-energy, pairs of quarks and anti-quarks are created iteratively until the energy of the colour field is small enough to allow for the creation of colourless hadrons, in a process referred to as hadronization. This process is poorly understood but there are a few phenomenological models with tunable parameters that are used in the simulation of physics processes and provide a reasonable description of experimental data. These are briefly described in section 3.2. In high-energy physics experiments, quarks are always observed as jets of hadrons, which can be visualized as colimated sprays of particles with an approximately conical shape. More details on the definition of jets are given in section 3.1.

Another interesting characteristic of QCD is *asymptotic freedom*. As opposed to QED, the value of the strong coupling constant, α_S, decreases as the momentum transfer Q increases. This is a direct consequence of additional corrections to the gluon propagator originating from gluon-gluon interactions. For most higher-order QFT calculations, a procedure referred to as *renormalisation* needs to be employed to handle ultraviolet (i.e. high-energy) divergences that appear in loop diagrams. In this process, an arbitrary renormalisation scale, μ, is introduced. The value of this scale is a choice. It is common to set it to a value close to the momentum transfer, Q, involved in the process under study: $\mu \sim Q$. For QCD in particular, it can be shown, by solving the renormalisation group equations, that the value of the strong coupling constant depends on this scale [30]:

$$\alpha_S(\mu^2) \sim \frac{1}{b_0 \ln \frac{\mu^2}{\Lambda^2}}, \tag{2.62}$$

where Λ is a non-perturbative constant and represents the scale at which the coupling diverges. Equation 2.62 shows that the value of α_S decreases as μ^2 increases. The summary of the measurements of α_S is shown in Figure 2.3.

At low-energy, the value of α_S is large ($\alpha_S \sim O(1)$) and therefore perturbation theory cannot be used to calculate QCD processes. At high-energies, however, it becomes small enough that

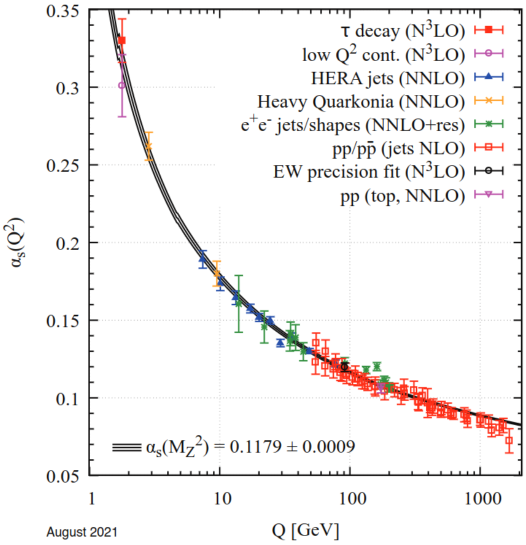

Figure 2.3: Summary of the measurements of α_S as a function of the energy scale Q [1]. The order of QCD perturbation theory used in the extraction of α_S is indicated in parentheses.

perturbation theory can again be used. At an energy corresponding to the Z-boson mass ($m_Z \sim 91$ GeV), it is $\alpha_S \sim 0.11$.

2.6 CP violation in the SM and beyond

The charge-parity transformation (CP) combines charge conjugation (C) with parity transformation (P). Charge conjugation interchanges particles with anti-particles by conjugating all internal quantum numbers (for example, the electromagnetic charge changes sign). Parity reverses the sign of the spacial components: $\vec{x} \to -\vec{x}$. Therefore, CP transforms a left-handed electron (e_L^-) into a right-handed positron (e_R^+) [1].

Within the SM, CP is conserved in electromagnetic and strong interactions but violated in the weak interactions of quarks, because the CKM matrix has an irreducible complex phase. By applying a CP transformation to the Lagrangian in equation 2.51 one obtains the following Lagrangian:

$$\mathcal{L}^{\text{quarks-W}}_{\text{interaction}} \to -\frac{g}{2\sqrt{2}} \left[\bar{u}\gamma^{\mu}(1-\gamma_5)W^{+}_{\mu}V^{*}_{ud}d + \bar{d}V_{ud}\gamma^{\mu}(1-\gamma_5)W^{-}_{\mu}u \right] , \tag{2.63}$$

which would be CP-invariant if $V_{ud} = V^{*}_{ud}$ (and similarly for the other flavors). This is not the case in the SM and thus CP is violated in the weak interactions of quarks.

This was first established in neutral K meson decays [36]. It was discovered that the longer-lived neutral Kaon, K^0_L, which often decays to three pions and would thus have odd parity, also decays to a pair of pions (CP-even state). This effect can be explain by considering that the short- and long-lived neutral Kaons are not CP eigenstates but an admixture of CP-even and CP-odd states. It was later discovered that CP was also violated in the decay amplitude itself [37, 38], although this is a subdominant effect with respect to the state mixing. Similar effects have been observed in neutral and charged B mesons [39–43] and in the charm sector, through the decay of neutral D mesons [44].

With the observation of neutrino oscillations, and thus the inference that they are massive particles, the possibility of mixing between the flavor and mass states in the lepton sector arises. It could be governed by a complex mixing matrix similar to the CKM matrix, which would introduce the possibility for CP-violation in the lepton sector. It is clear that this requires a new mechanism beyond the SM. This discussion will not be pursued here. In principle, it is also possible to introduce a CP-violating term in the QCD lagrangian but this term is phenomenologically known to be very small. Therefore, in the current formulation of the SM, CP-violation is limited to the weak interaction of quarks.

However, the CP-violating effects observed to date in this interaction are not enough to explain the matter-antimatter asymmetry of the Universe. In the early Universe, the thermal energy was large compared to the mass of hadrons [31]. Equal amounts of baryons and anti-baryons existed and were initially in thermal equilibrium with the highly energetic photons that permeated the entire Universe. As the Universe expanded, the temperature decreased, and so did the energy of the photons. At some point, the combination of photons to produce baryon-anti-baryon pairs was no longer possible. With the expansion, the density of baryons and anti-baryons also decreased, such that the annihalation of a baryon and anti-baryon into a pair of photons also became very unlikely. At this point in time, without the possibility to interact with photons, the number of baryons and anti-baryons became fixed. This hypothesis is referred to as Big Bang baryogenesis.

Based on the baryogenesis hypothesis, the predicted baryon asymmetry of the Universe today can be calculated. The same quantity can be calculated from independent experimental observations:

from the abundance of light elements in the intergalactic medium and from the power spectrum of the thermal fluctuations in the cosmic microwave background. The measured numbers are in good agreement but are widely different from the predicted one. The baryon asymmetry today is measured to be $\sim 10^{-10}$ [45] which is orders of magnitude larger than the asymmetry predicted by the Big Bang baryogenesis model ($\sim 10^{-18}$) [31].

To explain the measured value of the baryon asymmetry in the present Universe, more CP violating effects are needed. It is fairly simple to introduce additional CP violation in the scalar sector. One of the simplest extensions of the SM consists of adding an extra Higgs doublet with the same quantum numbers as the SM one. This is realized in the Two-Higgs-Doublet-Model (2HDM) [46]. The mass spectrum of this theory contains one charged Higgs field and three neutral ones (two scalars and one pseudoscalar). The coupling of the pseudoscalar field to the fermions is CP-odd. Measuring a value of this coupling different from zero would be a clear indication of CP-violation in the Higgs sector and thus of physics beyond the SM.

In this work, instead of relying on a specific model, the possible CP-odd component of the top Yukawa coupling is parameterized using an effective model that is described in the following section.

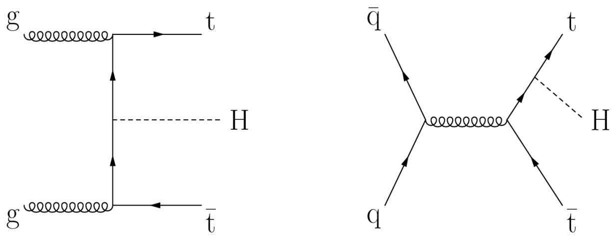

(a) **(b)**

Figure 2.4: Tree-level Feynman diagrams for $t\bar{t}H$ production through gluon-gluon fusion (3.4a) and quark-anti-quark annihilation (3.4b) [2].

2.7 Higgs-Top Yukawa coupling

Following the spontaneous breaking of the electroweak symmetry, charged fermions couple to the Higgs field with a strength proportional to the fermion mass (section 2.3). For the top quark, the heaviest SM particle ($m_t = 171.11 \pm 0.38$ GeV [47]), the value of the Yukawa coupling is expeccted to be close to unity. This coupling is thus more sensitive to potential BSM effects, making its measurement a crucial test of the SM. Additionally, the top quark has a lifetime of $\sim 0.5 \times 10^{-24}$ seconds which is smaller than the typical strong interaction time scale of $\sim 10^{-23}$ seconds [48]. Therefore, it decays before hadronizing and offers a unique probe into the properties of bare quarks.

Due to the large on-shell mass of the top quark, the top Yukawa coupling cannot be studied by measuring the Higgs boson decay rate to top quarks, as it is done for other fermions. However, it is directly accessible through the associated production of a Higgs boson with a pair of top quarks ($t\bar{t}H$). This process is realized at lowest order in perturbation theory, allowing to directly extract information about the top quark Yukawa coupling, without the need for assumptions on potential BSM physics that could contribute to loop-induced processes. It can proceed through gluon-gluon fusion or quark-anti-quark annihilation. Figure 2.4 shows the Feynamn diagrams representing these processes. For a center-of-mass energy $\sqrt{s} = 13$ TeV and considering the measured value of the Higgs mass of 125.09 GeV, the $t\bar{t}H$ production cross section calculated at NLO in QCD and including electroweak corrections is $506.5^{+5.8\%}_{-9.2\%}$(scale) $\pm\, 3.6\%$(PDF+α_S) fb [49].

Another Higgs boson production mode to which the top Yukawa coupling contributes is the associated production with a single top quark (tH and $\bar{t}H$). It can proceed through the t-channel (Figure 2.5a), s-channel (Figure 2.5b) and W-boson associated production (Figure 2.5c). It is clear from the Feynman diagrams in Figure 2.5 that the coupling between the Higgs boson and the top quarks is the same as for $t\bar{t}H$ production. At the LHC, the NLO QCD production cross-section of $tH + \bar{t}H$ is $74.26^{+6.5\%}_{-14.7\%}$(scale+FS) $\pm\, 3.7\%$(PDF+α_S) fb [49].

In the SM, the Higgs boson is predicted to be a scalar CP-even particle ($J^{CP} = 0^{++}$). In the search for potential BSM effects, placing stringent constraints on a possible CP-odd component of the Higgs boson is an important and active research field. Given the current lack of experimental evidence for BSM physics, an approach based on effective field theory (EFT) is particularly suitable. To this end, the Higgs Characterisation (HC) framework [50] was developed. It features only one additional

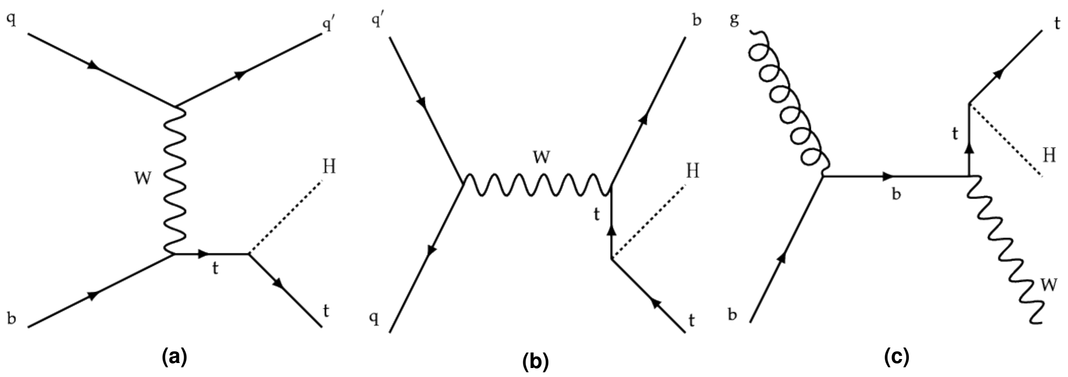

Figure 2.5: Tree-level Feynman diagrams for tH production in the t-channel (2.5a), s-channel (2.5b) and in association with a W-boson (2.5c) [2].

bosonic state, $X(J^P)$ with $J^P = 0^{\pm}$, $1^{\pm}$ or 2^{+} and a mass around 125 GeV, and it is particularly suited to perform studies addressing the spin and parity of the Higgs boson. CP conservation is not imposed, such that the new boson might be a scalar with mixed CP properties.

In the case of the spin-0 boson, which is the relevant one for the work described in this thesis, all $SU(2)_L \times U(1)_Y$ invariant dimension-six operators that modify the Higgs boson three-point interactions are considered. For the fermions, there is only one operator that modifies the Yukawa interaction. For the top quark it takes the form $\mathcal{L}^{\text{dim=6}} = \left(\phi^{\dagger}\phi\right) Q_L \tilde{\phi} t_R$. By adding this term to the SM Lagrangian, one can obtain the Lagrangian that describes the interaction between the Higgs boson and the top quark in the framework of the HC model:

$$\mathcal{L}_{t\bar{t}H} = -k_t^{'} y_t \phi \bar{\psi}_t (\cos\alpha + i\gamma_5 \sin\alpha)\psi_t, \tag{2.64}$$

where y_t is the SM top Yukawa coupling strength, modified by the coupling modifier $k_t^{'}$ and α is the CP-mixing angle. The SM can be recovered by setting $k_t' = 1$ and $\alpha = 0$. The term proportional to γ_5 corresponds to the (possible) pseudoscalar component of the coupling, which is CP-odd. Any measurement of α different from zero would establish the existence of a CP-odd component in the top Yukawa coupling and would constitute clear evidence of physics beyond the SM.

3

LHC phenomenology

Contents

A large part of the LHC program is focused on proton-proton collisions. Protons, and more generally hadrons, are composite particles, composed of quarks and gluons. Valence quarks can be described as the ones that give rise to the hadron quantum numbers. For the proton these are two up- and one down-quark. Inside hadrons, quarks are in constant interaction through the exchange of gluons. In turn, gluons can radiate quark-anti-quark pairs that quickly annihilate. This gives rise to a more complex model of hadrons, qualitatively described as a sea of quarks and gluons. In high-energy proton collisions, any of these constituent partons can interact.

The probability to find a parton inside a hadron with a fraction x of the hadron's momentum is given by the parton distribution functions (pdfs). These are empirical distributions that are used because the interactions of quarks and gluons inside hadrons take place in an energy regime that is not accessible to perturbative calculations. The interaction between hadrons can be described in terms of the parton-level cross-section for a given subprocess weighted by the pdfs. The hadron collider cross-section to produce a given particle X from protons with four momenta p_1 and p_2 is given by [51]:

$$\sigma = \int dx_1 f_{a/p}(x_1, \mu_F) \int dx_2 f_{b/p}(x_2, \mu_F) \hat{\sigma}_{ab\to X}(x_1, x_2, s), \tag{3.1}$$

where $s = (p_1 + p_2)^2$ is the squared center-of-mass energy, a, b are any two partons, depending on the process under study, and $f_{a/p}$, $f_{b/p}$ are the corresponding pdfs. The cross-section of the hard-scattering, $\hat{\sigma}_{ab\to X}(x_1, x_2, s)$, is a function of the squared partonic center-of-mass energy $\hat{s} = x_1 x_2 s$. It is calculated in perturbative QCD, up to a fixed order in perturbation theory:

$$\hat{\sigma}_{ab\to X} = \hat{\sigma}_{0,ab\to X} + \alpha_S(\mu_R)\hat{\sigma}_{1,ab\to X} + \alpha_S^2(\mu_R)\hat{\sigma}_{2,ab\to X} + ..., \tag{3.2}$$

where μ_R is the renormalisation scale and α_S is the strong coupling constant. The first term is the leading order calculation and the terms proportional to α_S and α_S^2 are the next-to-leading-order (NLO) and next-to-next-to-leading-order (NNLO) contributions.

The pdfs in equation 3.1 are also defined as a function of μ_F, referred to as the *factorization* scale, that is introduced to handle divergences related to initial state partons. The idea is that any emission from an initial state parton with an energy below this scale is absorbed into the pdf. The pdfs thus become functions of μ_F. As for the renormalisation scale, introduced in section 2.5, the choice of the factorization scale is somewhat arbitrary.

Most of the current knowledge about pdfs comes from deep inelastic scattering (DIS), i.e., lepton-proton scattering in which the exchanged photon has a large transverse momentum. The cross section depends on the structure function of the proton, that parameterizes the deviation of its structure from a point-like particle. The structure functions can be written as the sum of parton densities inside the proton. Thus by measuring the cross-section of DIS as a function of momentum fraction of the quark inside the proton one can obtain information about the pdfs. The recommended NNLO pdfs for Run 2 are shown in Figure 3.1 for unpolarized partons at two different factorization scales ($\mu^2 = 10$ GeV^2 on the left and $\mu^2 = 10^4$ GeV^2 on the right) [3].

At the LHC the picture is more complex. Initial and final state quarks radiate gluons as they propagate, which in turn produce short-lived quark-anti-quark pairs, giving rise to inital- and final-state

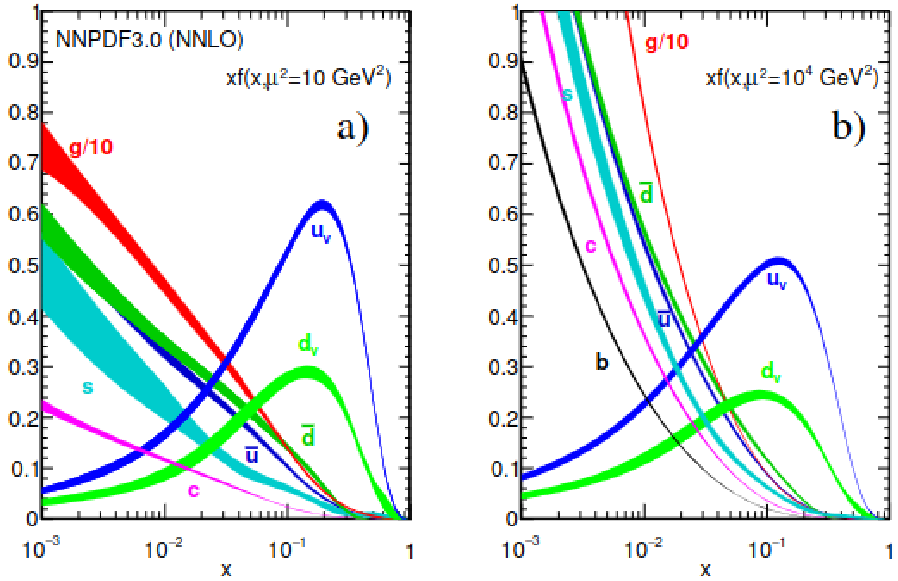

Figure 3.1: Unpolarized parton distribution functions obtained from the global NNLO NNPDF3.0 analysis [3] at scales $\mu^2 = 10$ GeV^2 (left) and $\mu^2 = 10^4$ GeV^2 (right), with $\alpha_S(M_Z^2) = 0.118$ [4].

radiation (ISR and FSR). The remnants of the proton not participating in the hard-scattering continue to interact, usually through low-energy QCD processes, producing what is referred to as underlying event. Partons additionally undergo the hadronization process, through which they become confined inside colourless states and produce colimated sprays of hadrons, referred to as jets (section 3.1). It is currently not possible to describe these processes analytically starting from QCD principles. Some progress has been made in numerical calculations, mainly in the framework of lattice QCD but generally they are simulated using phenomenological models implemented in Monte Carlo (MC) event generator programs, discussed in section 3.2.

The study of the Higgs boson, in particular its interaction with top quarks, is the central topic of this thesis. Phenomenological aspects of Higgs boson production and decays at the LHC are discussed in section 3.3.

3.1 Jets

Almost immediately after being produced, quarks and gluons fragment and hadronize, leading to a collimated spray of hadrons referred to as a jet. This is a direct consequence of the colour confinement property of QCD. Jets are structures that can be identified when visually analyzing an event display. In practice, they need to be defined via a set of rules, a jet definition, that indicates how a list of objects can be grouped together to return a list of jets. These objects can be, for example, calorimeter cells or truth particles from a MC event record.

A good jet definition should be robust to the emission of soft and collinear radiation. For theory calculations, this means that the order of perturbation theory used should not greatly affect the jet properties. When using such a definition, the properties of the jets are good approximations to the properties of the original partons and can be used to calculate and measure physics quantities such as cross-sections. They thus provide a way of directly comparing theoretical predictions with measured quantities.

Jet clustering algorithms are based on distances between objects, d_{ij}, and between a given object and the beam, d_{iB}. They proceed by finding the particles i and j with the smallest relative distance which are then combined into a single object by summing their four-momenta. If instead the smallest difference is between particle i and the beam, the particle is considered to be a jet and removed from the list of input objects. The distances are then recalculated and the procedure repeated until no objects are left.

The more widely used algorithm in ATLAS is the anti-k_t algorithm [52]. The distances are defined as:

$$d_{ij} = \min\left(k_{ti}^{2p}, k_{tj}^{2p}\right) \frac{\Delta_{ij}^2}{R^2}, \tag{3.3}$$

$$d_{iB} = k_{ti}^{2p}, \tag{3.4}$$

where $\Delta_{ij}^2 = (y_i - y_j)^2 + (\phi_i - \phi_j)^2$ and k_{ti}, y_i and ϕ_i are the transverse momentum, rapidity and azimuth of entity i, measured with respect to the beam direction. The parameter R governs the size of the jet and, assuming a perfectly conical jet, it can be interpreted as the radius. The parameter p is set to -1.

Other examples of widely used jet clustering algorithms are the k_t [53] and Cambridge-Aachen [54]. They follow the same clustering procedure as described for anti-k_t but use slightly different distance measurements. For the k_t (Cambridge-Aachen) algorithm the parameter p in equation 3.3 is set to one (zero). These algorithms are often used to study the internal structure of jets because they preserve the angular ordering of the jet constituents. For example, if a jet has two hard cores they will be clustered last in the k_t and Cambridge-Aachen algorithms while the anti-k_t algorithm will often merge the two hard cores first.

In the anti-k_t algorithm, the distance between two entities depends on the inverse of the squared momentum of the hardest particle. This feature implies that the distance between a hard and a soft particle is largely determined by the transverse momentum of the former and their geometric distance, while the distance between two soft particles is instead much larger. Therefore, soft particles tend to cluster first with the hard ones, long before clustering among themselves. If a single hard particle exists within a distance $2R$, it will simply accumulate around it all the soft particles, resulting in a perfectly conical jets with radius R.

If two hard particles exists within $R < \Delta_{12} < 2R$ there will be two hard jets, both without perfectly conical shapes. If $k_{t1} >> k_{t2}$, jet 1 will be conical and jet 2 will be partially conical with the missing part corresponding to the overlap with jet 1. If $k_{t1} = k_{t2}$ neither jet will be conical and the overlaping part will be equally divided by a straight line between the two jets. If instead $\Delta_{12} < R$, then the two hard particles will be clustered into a single jet, with a more complex shape.

The key feature of the anti-k_t algorithm is that soft particles do not modify the shape of the jet. The shape is determined by the hard particles and it is not sensitive to the emission of soft or colinear radiation.

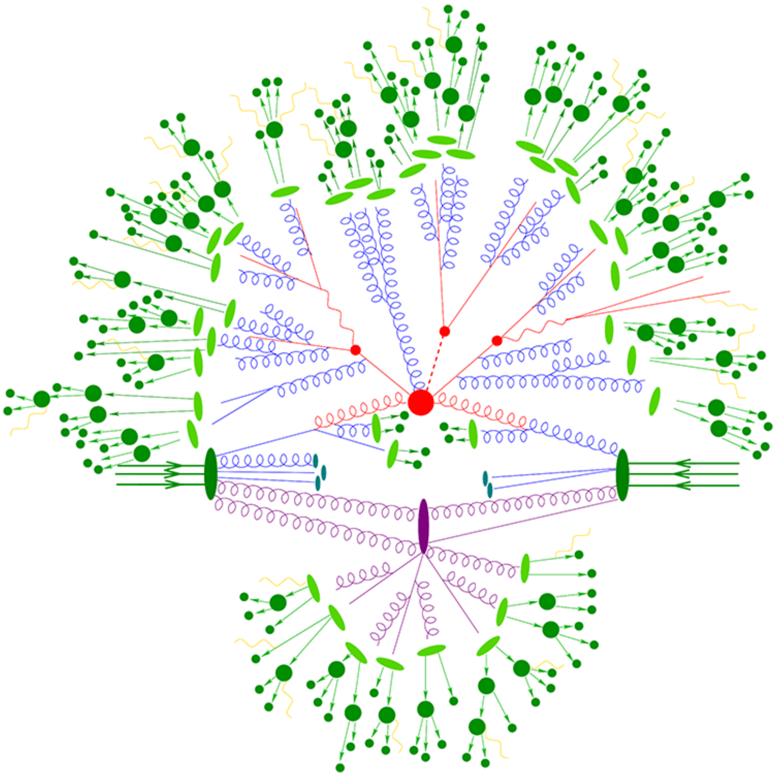

Figure 3.2: Illustration of a proton-proton collision event [5].

3.2 MC simulation of collider processes

For simulation purposes, a typical proton-proton collision event can be divided into multiple steps based on the energy scales involved. A pictorial representation is shown in Figure 3.2. The hard-scatter event, involving high-energy particles, is represented in red. The partons and gluons shown in blue are created by the parton shower process. Once the energy is low enough, quarks are grouped together to form hadrons, highlighted in green. The underlying event is represented in purple.

The simulation of collider processes starts with the computation of the matrix element of the partonic cross-section at some order in perturbation theory. Since most processes of interest involve large momentum transfers this can be done even for QCD processes. Examples of widely used matrix element generator programs are Alpgen [55], MadGraph [56], Powheg [57] and Sherpa [58]. Currently, for a large number of processes, NLO calculations are available and for a handful of them even NNLO or higher-order calculations exist. However, the complexity of the calculation increases with the order of perturbation theory and with the number of partons in the final state.

For all processes that include b-quarks, as it is the case for the processes studied in this work, there are two ways of performing the matrix element calculation, referred to as four- and five-flavor schemes. In the four-flavor scheme, the b-quark is considered as massive object but is not assigned a parton distribution function. Therefore it never appears in the initial state. In the five-flavor scheme, the b-quark is considered massless and treated in equal footing with the lighter quarks. The four-flavor scheme has the advantage of taking into account mass effects which are important in energy regimes near the production threshold. For higher energies, mass effects become negligible and the five-flavor scheme is more accurate. Ideally, one would like to combine the four- and five-flavor scheme calculations. At the moment, this is not available for the processes of interest studied here. For $t\bar{t}b\bar{b}$ production, in the phase space targeted by the $t\bar{t}H$ analyses, the four-flavor scheme calculation is more precise and reliable, since it more accurately predicts the emissions of high-energy b-quarks at large angles.

Parton shower programs approximate higher-order real emission corrections to the hard scattering by simulating the branching of an external parton into two partons. They follow an iterative approach in the sense that multi-parton final states can be obtained from successive branchings into pairs of partons. The probability to emit a gluon from a quark or to produce a quark-anti-quark pair from a gluon can be calculated as a function of the emitted parton momentum using a Monte Carlo method. This procedure is repeated until it is found that the next parton to be emitted would have a momentum below a pre-defined cutoff scale. Variations of this approach are followed for initial and final state partons, thus simulating initial and final state radiation. Some of the most widely used parton shower programs are Pythia [59], Herwig [60, 61] and Sherpa [58]. Most programs have the capability of both calculating the matrix element and simulating the parton shower.

A draw-back of MC parton shower programs is that they do not properly simulate hard emissions at large angles. These are often the most interesting configurations, especially when simulating backgrounds for new physics processes, since they might more closely resemble the signal. Fixed-order programs describe these configurations correctly. Therefore, it is highly desirable to combine matrix element calculations with parton showers.

The main idea for this combination is to simulate, for example, the LO matrix element and then shower each configuration composed of the final state particles predicted by the fixed order calculation. In this context, the word "shower" is used as a verb and it refers to the simulation of the emission of additional partons from the ones produced by the matrix element calculation. Suppose one wants to simulate the production of particle X with two additional partons (or jets). One can calculate the matrix element of $X + j$ and rely on the parton shower to simulate the additional jet or directly calculate $X + 2j$ and then shower it. When showering the $X + j$ process it can happen that one emission leads to the production of an extra hard jet, leading to the same final state as already calculated for $X + 2j$. Therefore, possible double-counting of effects is introduced. Two main methods exist to handle double-counting: CKKW [62] and MLM matching [63]. The basic idea of matching algorithms is to reject events in which a high-energy jet produced by the parton shower is not matched to a parton generated by the matrix element calculation.

The last step to obtain the final state particles that can be detected is hadronization [64, 65]; a process through which quarks produced in the hard scatter become confined inside hadrons. There are some general ideas about this process but no description from first principles. Therefore, its simulation currently relies on phenomenological models. The two main ones are the cluster and string models, used in Herwig [61] and Pythia [59], respectively.

In the cluster model [66, 67], gluons left at the end of the parton shower are forced to decay into quark-anti-quark pairs. Following this decay, the event contains only colour-connected pairs of (anti-) quarks. These colour singlets are grouped into clusters, which undergo an isotropic decay to pairs of hadrons chosen from all possible states with appropriate quantum numbers.

In the string model [68–71], motivated by the observation that the QCD potential is linear at large distance values, the colour flux between a quark and anti-quark is modelled as a relativistic attractive string. The potential energy of the string increases with the separation between the original quark and anti-quark. Once it is energetically favorable, a quark-anti-quark pair is created from the string, thus breaking it into smaller strings. The most modern implementation of this model is the Lund string model.

The interaction of the final state particles with the detector is simulated with the Geant4 software [72]. It contains a broad collection of models describing the interaction of particles with matter across a wide energy range. Each particle is moved throughout the detector step-by-step with a given tolerance. Each physics process associated with the particle proposes a step. In each step, the smallest distance is chosen, between a maximum stipulated by the user and the step length propose by each physical process acting on the particle. Moving each particle step-by-step is known to be the most CPU-intensive task in detector simulation.

In Geant4, detectors are implemented as geometric solids with associated materials. In a complex detector like ATLAS, the number of volumes easily reaches thousands. Due to this complexity, it becomes impossible to obtain the required simulated statistics for the plethora of physics studies of the collaboration without a much faster simulation [73]. To this end, "fast simulation" programs have been developed by ATLAS to complement the standard Geant4 simulation (referred to as "full simulation").

Close to 80% of the full simulation time is spent on particle interactions with the calorimeters, and about 75% of the time is spent simulating electromagnetic particles [73]. The fast simulation aims at speeding up the slowest parts and thus it removes low energy electromagnetic particles from the calorimeters and replaces them with pre-simulated showers stored in memory.

ATLASFAST-II [73], or AFII in short, is used in multiple Run 2 analyses, including the ones presented in this thesis. Its main component is the fast calorimeter simulation (FastCaloSim) [74]. Instead of simulating the particle interactions with the detector material, the energy deposited by single particle showers is replaced by parameterizations of the longitudinal and lateral energy profiles. The simulation speed is increased by a factor ~ 20 through the use of FastCaloSim alone. Additional performance improvements can be achieved by introducing a fast simulation of the tracking in the inner detector and muon systems. These are not included in he default version of ATLASFAST-II used in ATLAS analyses.

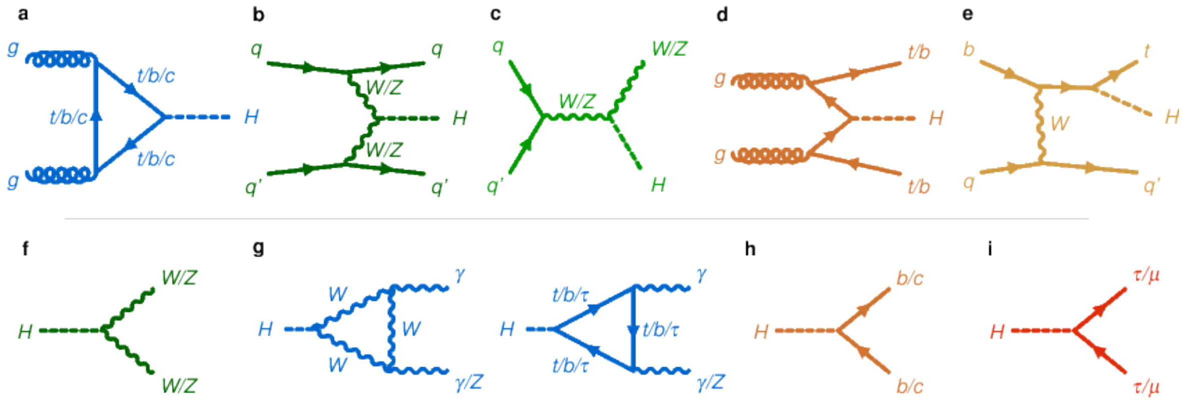

Figure 3.3: Examples of Feynman diagrams for Higgs boson production (top row) and decay (bottom row) [6].

3.3 Phenomenology of Higgs boson processes

Following the observation of the Higgs boson by the ATLAS [75] and CMS Collaborations [76] in 2012, and given the sizable dataset delivered by the LHC during Run 2, detailed measurements of the Higgs boson properties and couplings have been performed with increasingly higher precision, as a way of testing the predictions of the SM. The main LO Feynman diagrams of the Higgs boson production and decay modes currently accessible at the LHC are shown in Figure 3.3.

The Higgs boson production through gluon-gluon fusion (ggF), in a process mediated by a loop of heavy-flavor quarks, accounts for 87% of the total Higgs boson production cross-section at the LHC. The production through vector boson fusion (VBF) and in association with a vector boson (VH) account for 7% and 4% of the total rate, respectively. The associated production with a pair of top quarks ($t\bar{t}H$) accounts for 1% of the total production cross-section. Only about 0.05% of Higgs bosons are produced in association with a single top quark (tH) [6].

With a lifetime of 1.6×10^{-22} seconds, the Higgs boson decays almost immediately after being produced. The main decay mode is to a pair of b-quarks, with a probability (branching ratio) of 58%. The branching ratios of the remaining decays to second and third generation quarks and leptons are 6% for τ-leptons, 3% for c-quarks and 0.02% for muons. The branching ratio to first generation quarks and charged lepton is currently not experimentally accessible. The Higgs boson can also decay to a pair of gauge bosons with branching ratios of 22% for W-bosons, 3% for Z-bosons, 0.2% for photons and 0.2% for Z-boson and photon. The decay modes listed here account for more than 90% of the total Higgs boson branching ratio.

Independent measurements of Higgs boson production and decays targeting all the channels described above are combined in a single measurement, taking into account the correlation between their uncertainties. Different couplings generally contribute to the production and decay, such that a combined measurement is necessary to individually constrain each coupling. The production cross-section σ_i of a given process i and the branching fraction B_f of decay mode f cannot be measured without further assumptions. For example, when measuring a given production cross-section, the value of the branching ratio is assumed to be the SM one. Therefore, the observed signal yield for a given process is expressed in terms of a single signal strength modifier $\mu_{if} = (\sigma_i/\sigma_i^{SM})(B_f/B_f^{SM})$, where the superscript SM denotes the corresponding SM prediction. Assuming that all processes scale with the same signal strength $\mu = \mu_{if}$, the Higgs boson inclusive signal strength is currently measured to be $\mu = 1.05 \pm 0.06$, with twice the precision achieved in Run 1 [6].

The increasing LHC dataset opens the door to more detailed measurements of the Higgs boson production rates and properties. Moving away from the simple signal strength measurements performed during Run 1, the LHC experiments adopted the Simplified Template Cross Sections framework (STXS) [77] that provides more fine-grained measurements of individual Higgs boson production modes in various kinematic regimes and reduces the theoretical uncertainties. Simultaneously, it provides a common framework for the combination of measurements in different decay channels and production modes and even between experiments. Measurements of the charge-conjugation and parity (CP) properties of the Higgs boson couplings have also become possible.

The analyses presented in this thesis focus on the $t\bar{t}H$ and tH production modes. Being the top quark the heaviest elementary particle of the SM, its coupling to the Higgs boson could be particularly sensitive to BSM effects and thus its precise measurement and a detailed understanding of its properties constitute an important test of the SM. This production mode was observed by ATLAS [78] and CMS [79] in 2018, using a combination of channels. The top Yukawa coupling has also been indirectly constrained from measurements of ggF Higgs production. Targeting the properties of the top quark Yukawa coupling, measurements have been performed using $t\bar{t}H$ and tH events in the $H \to \gamma\gamma$ decay channel by the ATLAS [80] and CMS [81] Collaborations.

Pure CP-odd couplings of the Higgs boson to the vector bosons have been ruled out [82–88]. Analyses of $t\bar{t}H$ and tH events in the $H \to \gamma\gamma$ decay channel [80, 81] have excluded a pure CP-odd top-Higgs coupling with a significance above 3σ. However, a mixture of CP-even and CP-odd couplings is still allowed, and its observation would be a clear sign of physics beyond the SM, opening up the possibility for CP-violation in the Higgs sector.

When considering $t\bar{t}H$ production, the $H \to b\bar{b}$ decay mode brings some experimental challenges: it leads to a final state with multiple jets, which is more susceptible to reconstruction, identification and flavor-tagging inefficiencies and it is hard to separate from backgrounds arising from QCD production of top quark pairs with additional heavy-flavor jets. Despite the challenges, this decay mode has a distinctive experimental signature and some clear advantages: being the most probable decay mode it maximizes the available statistics and provides access to the high-p_{T} regime; it also allows for a full reconstruction of the final state and thus of the intermediate Higgs boson and top quarks, which is crucial to calculate CP-sensitive observables. The analyses presented here target this decay mode.

The top quark decays to a b-quark and a W-boson with a branching ratio of 99.8% [4]. The W-boson subsequently decays to a charged lepton and a neutrino with a probability of $\sim 10\%$ per lepton flavor or to a pair of quarks with probability around 67% [4]. The decay of the W-bosons thus defines the final state. The probability for both W-bosons to decay leptonically is around 10%, leading to a final state with two high-energy leptons, referred to as *dileptonic* channel. In about 44% of the $t\bar{t}$ decays, one W-boson decays leptonically and the other hadronically, leading to a final state with a

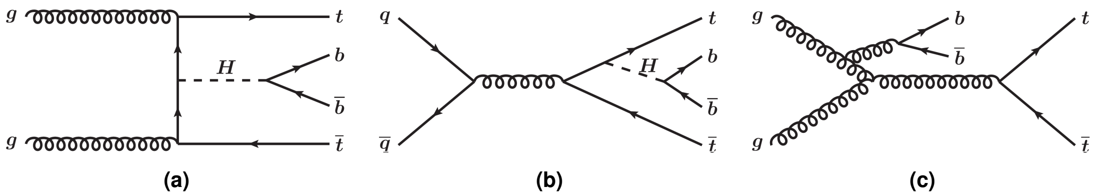

Figure 3.4: Examples of tree-level Feynman diagrams representing the production of a Higgs boson in association with a pair of top quarks in the t-channel (3.4a) and s-channel (3.4b) and subsequent decay of a pair of b-quarks, and the main $t\bar{t} + b\bar{b}$ background (3.4c).

single high-energy lepton, referred to as *semileptonic* or *single-lepton* channel. These are the final states considered in the analyses presented here. The fully hadronic channel, defined by the hadronic decays of both W-bosons, is not considered here. It poses additional experimental complications, not only due to the increased number of jets, but also because the absence of isolated, high-energy leptons in the final state requires the use of multijet triggers.

In $t\bar{t}H(H \to b\bar{b})$, the final state has at least four b-jets: two from the top quark decays and two from the Higgs boson decay. In the single-lepton channel, two additional jets are produced in the decay of the W-boson, leading to a final state with six jets. In the dileptonic (semileptonic) channel, events with three (five) jets are also considered to account for the possibility of a jet produced outside the detector acceptance or misreconstructed. Examples of Feynman diagrams representing $t\bar{t}H$ production in t- and s-channels are shown in Figures 3.4a and 3.4b, respectively.

Higgs boson production in association with a single top quark is always mediated by a tWb vertex and therefore it entails the presence of a b-quark in either the initial (t-channel and associated production with a W-boson) or final state (s-channel) [7]. At the LHC, tH production proceeds mainly through t-channel diagrams, with the Higgs boson radiated from a top quark or a W-boson, as shown in Figures 3.5a and 3.5b, respectively. As these couplings have opposite signs, the diagrams interfere destructively, leading to a predicted NLO cross-section of 18 fb. It can be shown that, due to this interference, the t-channel cross-section has a component that depends linearly on the top Yukawa coupling. Therefore, the cross-section of tH production is sensitive to the sign of the top Yukawa coupling, unlike that of $t\bar{t}H$ production [7]. Figure 3.6 shows the NLO cross sections for $t\bar{t}X_0$ and t-channel tX_0 production at $\sqrt{s} = 13$ TeV as a function of the CP-mixing angle α, obtained with the Higgs characterization model [7]. Here, X_0 indicates a boson with $J^P = 0^+$ and thus corresponds to the SM Higgs boson. It illustrates the sensitivity of tH production to the sign of the top Yukawa coupling.

The main experimental challenge in measurements of Higgs boson production in association with top quarks is the presence of a very large background of $t\bar{t}$+jets processes, in particular those with additional b- or c-jets (commonly referred to as $t\bar{t}$ + heavy flavor (HF)), which have a production cross-section many orders of magnitude larger than that of the signal. The dominant background is $t\bar{t} + b\bar{b}$ whose final state signature mimics the signal (irreducible background) while $t\bar{t}+ \geq 1c$ events infiltrate the analysis regions due to non-negligible rate of c-jets misidentified as b-jets. A representative Feynman diagram of $t\bar{t} + b\bar{b}$ production is shown in Figure 3.4c.

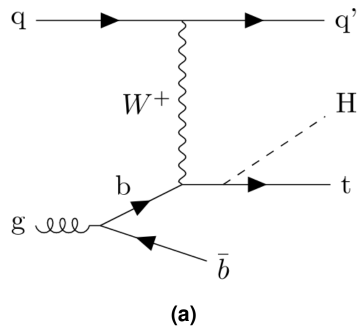

Figure 3.5: Tree-level Feynman diagrams for $tHjb$ t-channel production with a Higgs boson radiated from a top quark (3.5a) or from a W-boson (3.5b)

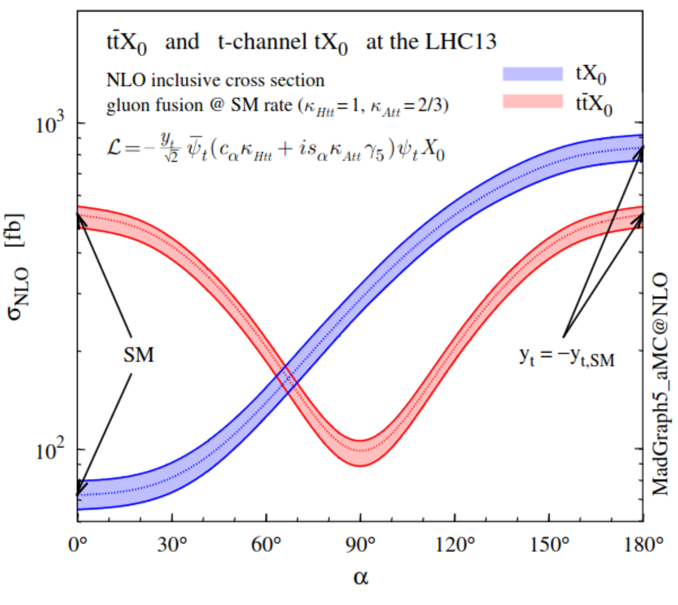

Figure 3.6: NLO cross-sections for $t\bar{t}X_0$ and t-channel tX_0 production at $\sqrt{s} = 13$ TeV as a function of the CP-mixing angle α [7]. The results are obtained using the Higgs characterization model. For every value of α the overall coupling modifiers for the CP-even and CP-odd components are set to reproduce the SM ggF production cross-section. The coloured bands correspond to the scale uncertainties.

4

Experimental setup

Contents

The experimental apparatus used to collect the data analysed in this thesis is the ATLAS detector. It is one of the main general-purpose experiments located in one of the four interaction points of the Large Hadron Collider (LHC). The construction and operation of the LHC and of the ATLAS experiment are huge collective efforts, undertaken by thousands of people. Any description is bound to be incomplete. Nonetheless, the LHC and the corresponding accelerator chain are presented in section 4.1, while the ATLAS experiment and its subdetectors are described in section 4.2.

4.1 Large Hadron Collider

The LHC is a 26.7 km ring capable of accelerating protons and heavy ions to unprecedentedly high energies [89]. It is housed by CERN and located beneath the French-Swiss boarder, a few hundred meters underground. It is installed in the tunnel that previously held the Large Electron-Positron Collider (LEP), which operated for 11 years, between 1989 and 2000. The LHC Project was approved by the CERN Council in 1994 and, after 14 years of construction, it was commissioned in 2008.

Protons are supplied to the LHC by an injector chain composed by a linear accelerator (Linac), Proton Synchrotron Booster (PSB), Proton Synchrotoron (PS) and Super Proton Synchrotron (SPS). They are sourced from gaseous hydrogen that is ionized in a duoplasmatron. The energy of the protons is increased successively until they are injected in the LHC where they are accelerated to their ultimate energy. The CERN accelerator complex, that includes the LHC injector chain, is represented in Figure 4.1.

Linac2 served as the first accelerator in the chain until 2018. It accelerated protons up to an energy of 50 MeV using radiofrequency (RF) cavities. It was replaced by Linac4 which was inaugurated in 2017 and connected to the PSB in 2020, during LHC's Long Shutdown 2. Linac4 accelerates negative hydrogen ions (H^-) up to an energy of 160 MeV using the same technique as Linac2. The ions are stripped off their two electrons during injection from Linac4 to PSB, leaving only the protons. Accelerating ions allows more particles to be accumulated in the synchrotron, simplifies injections, reduces beam loss and gives a more brilliant beam, making the Linac4 a key element in the project to increase the luminosity of the LHC.

The PSB is made up of four superimposed synchrotron rings. From 1978 until 2018, it received protons from Linac2 and accelerated them to 1.4 GeV. From 2020, it receives a beam of negative hydrogen ions from which the electrons are stripped during injection from Linac4 and it then accelerates the protons to 2 GeV. Protons are then injected into the PS and the SPS, successively, where they are accelerated to 25 and 450 GeV, respectively. They are finally transferred to the LHC, both in a clockwise and anticlockwise direction, where they are accelerated for 20 minutes until they reach an energy of 6.5 TeV (in Run 2).

There are seven experiments installed at the LHC: A Large Ion Collider Experiment (ALICE) [90], A Toroidal LHC ApparatuS (ATLAS) [91], the Compact Muon Solenoid (CMS) [92], the Large Hadron Collider beauty (LHCb) experiment [93], the Large Hadron Collider forward (LHCf) experiment [94], the TOTal Elastic and diffractive cross section Measurement (TOTEM) experiment [95] and Monopole and Exotics Detector at the LHC (MoEDAL) [96]. The four biggest experiments, ALICE, ATLAS, CMS and LHCb, are located around the four collision points. The TOTEM experiment is installed close to the CMS interaction point, LHCf is installed near ATLAS and MoEDAL is close to the LHCb detector.

ALICE is dedicated to heavy-ion physics and optimized to study lead-ion collisions at a center of mass energy up to 5.02 TeV per nucleon pair. It is designed to study strongly-interacting matter at extremely high energy densities, where a phase of matter called quark-gluon plasma (QGP) forms.

LHCb specializes in investigating differences between matter and antimatter by studying charm and beauty quarks. It differs from the other three big experiments in that it does not enclose the entire interaction point. Instead, the experiment focuses on a smaller rapidity range, detecting particles that are thrown forward by the collision in one direction.

ATLAS and CMS are multi-layered general-purpose detectors, designed and optimized to study proton-proton collisions. They provide a coverage close to 4π around the interaction point. The ATLAS detector is the experimental apparatus used to collect the data analysed in this thesis. It is described in detail in section 4.2.

The three smaller experiments, TOTEM, LHCf and MoEDAL are located further away from the closest interaction points. TOTEM is designed to measure protons that emerge at very small angles with respect to the beam pipe, a regime that is inaccessible to the other LHC experiments. LHCf is made up of two detectors, located on each side of the ATLAS experiment, 140 meters away from the collision point. It uses particles emitted in the forward direction to simulate cosmic rays in laboratory conditions. MoEDAL is deployed around the same interaction point as LHCb. Its prime motivation is to directly search for magnetic monopoles, a hypothetical particle with a magnetic charge.

The LHC is a two-ring, superconducting accelerator and collider, composed of eight arcs and straight sections. Each straight section is approximately 528 m long and can be used as an experimental insertion. ATLAS and CMS are located in diametrically opposite straight sections, at Points 1 and 5, respectively. The proton beams travel in opposite directions in separate beam pipes, with separate magnetic fields and vacuum chambers in the main arcs and with common sections at the insertion regions where the detectors are located.

The proton beams are accelerated using RF cavities, installed in the long straight sections. There are eight cavities per beam, grouped in two cryomodules, that operate at a temperature of 4.5 K. In each cavity, a voltage generator klystron induces a longitudinal oscillating electric field with a radio frequency of 400 MHz. This frequency is chosen to be an integer multiple of the proton's revolution frequency ($f_{\mathrm{RF}}/f_{\mathrm{rev}} = h$, where h is the harmonic number), such that a proton always sees an accelerating voltage. In the case of the LHC, and considering protons traveling at the speed of light, $h \sim 35640$. The segments of the LHC circumference centered around these 35640 points are referred to as *buckets* [97].

A particle with an energy such that its revolution frequency is exactly the same as the RF frequency will pass through the RF cavities when the voltage is zero and thus feel no force. These are referred to as synchronous particles. All other protons oscillate longitudinally around the synchronous ones and become grouped around them in *bunches*. In nominal proton-proton operation mode, the LHC is filled with 2808 proton bunches, each contained in a RF bucket. The beam emittance can be defined as the elipse that contains a certain percentage of the particles that constitute the beam. It is closely related to the size of the beam.

A large variety of superconducting magnets is present at the LHC, including dipoles, quadrupoles, sextupoles and octopoles, all contributing to the optimization of the particle trajectories [98]. There are 1232 dipole magnets responsible for bending and separating the beams. They are made of niobium titanium (NbTi) Rutherford cables and provide a nominal magnetic field of 8.3 T. The core of each dipole magnet is cooled to 1.9 K and consists of an iron yoke through which both beam pipes are inserted (referred to as cold mass). The quadrupole magnets are based on the same technology and have a similar structure. A special class of quadrupoles, referred to as insertion magnets, are responsible for focusing the beam at the interaction points. Most of the remaining correction magnets are embedded in the cold masses of the dipoles and quadrupoles.

The number of events generated at the LHC, N, is given by [98]:

$$N = \int L \, \mathrm{d}t \times \sigma = \mathcal{L} \times \sigma, \tag{4.1}$$

where L is the instantaneous luminosity of the machine, σ is the cross-section of the process under study and $\mathcal{L}$ is the (time) integrated luminosity, usually expressed in units of inverse cross-section (barn^{-1}). The instantaneous luminosity depends only on the beam parameters. Assuming beams with Gaussian profiles, it can be expressed as:

$$L = \frac{N_b^2 n_b f_{\text{rev}} \gamma_r}{4\pi \epsilon_n \beta^*} F, \tag{4.2}$$

where N_b is the number of protons per bunch, n_b the number of bunches per beam, f_{rev} the revolution frequency, γ_r the relativistic gamma factor, ϵ_n the normalised transverse beam emittance, β^* the beta function at the interaction point, and F a geometric luminosity reduction factor due to the crossing angle at the interaction point. The beta function determines the envelope containing the trajectories of all particles at a given position along the storage ring and it reflect the magnet structure. The instantaneous luminosity can also be expressed as:

$$L = n_b \frac{\langle \mu \rangle f_{\text{rev}}}{\sigma_{\text{inelastic}}}, \tag{4.3}$$

where $\sigma_{\text{inelastic}}$ is the reference inelastic cross-section, taken to be ~ 80 mb for pp collisions at a center of mass energy of $\sqrt{s} = 13$ TeV [99]. The mean pileup parameter, $\langle \mu \rangle$, represents the average number of inelastic interactions per bunch crossing, averaged over all colliding bunch pairs.

The peak luminosity delivered to ATLAS and CMS is $L \sim 10^{34}$ cm^{-2}s^{-1}. The peak beam energy depends on the maximum achievable dipole magnetic field. The nominal value of 8.3 T corresponds to an energy per beam of 7 TeV. However, the actual field that can be attained depends on the heat load and temperature margins inside the cryo-magnets and therefore on the beam losses during operation.

The LHC operates in fills: a fill begins whenever the desired number of bunches is injected into the machine and it ends when the beam is dumped. When the beam conditions are safe, stable and good for physics data-taking, *stable beams* are declared. In these conditions, the experiments start collecting data for physics analyses. During a fill, the instantaneous luminosity decreases as the protons are consumed in collisions or lost outside the interaction regions. After around 10-20 hours, the collision rate becomes low enough that it is more advantageous to dump the beam and spend a few hours re-injecting a new beam.

Between 2009 and 2013, a period referred to as Run 1 [100], the LHC was operated with protons at beam energies of 3.5 and 4 TeV. Lead ion (Pb^{82}_{208}) runs were also performed in 2010 and 2011 and a mixed proton-ion run was achieved at the beginning of 2013.

During Run 2, which spanned from 2015 to 2018, the LHC was operated with protons at energies of 6.5 TeV with a total integrated luminosity of 160 fb^{-1} being delivered to ATLAS and CMS. The peak proton luminosity exceeded the design value by a factor of two due to very small transverse beam emittances and β^* of 30 cm (nominal design value being 55 cm). The nominal bunch spacing of 25 ns was used for high intensity operation. Heavy ion runs were also performed every year, including lead-proton and lead-lead runs and a short xenon-xenon (Xe^{54}_{129}) pilot run.

Run 3 started in 2022 and will extend for four production years. The restart of the machine coincides with the completion of the LHC Injectors Upgrade project [101], which is a key milestone to guarantee that the High-Luminosity LHC (HL-LHC) [102] can be successfully operated during Run 4, after the Long Shutdown 3. For Run 3, the nominal center-of-mass energy for proton-proton collisions is 13.6 TeV and a total integrated luminosity of 300 fb^{-1} is expected to be accumulated, depending on the exact data-taking conditions.

4.2 ATLAS experiment

ATLAS is a multipurpose cylindrical-shaped detector with 44 m in length and 25 m in diameter built around the LHC interaction region 1 in a concentric structure of different subdetectors, each dedicated to measuring the properties of a different type of particle or object resulting from the collisions. The nominal interaction point defines the origin of a right-handed Cartesian coordinate system. The $z-$axis is defined by the beam direction and the $x-y$ plane is transverse to it. The $x-$axis points towards the center of the LHC ring and the $y-$axis points upwards. Two sides of the detector are defined, side-A and side-C, corresponding to positive and negative values of z, respectively. The azimuthal angle ϕ is measured around the beam direction in the $x-y$ plane, with its origin coinciding with the positive $x-$axis. The polar angle θ is measured in the longitudinal plane from the positive $z-$axis. A more commonly used quantity, due to its similarity to a particle's rapidity, is the pseudorapidity, $\eta = -\ln\tan(\theta/2)$. The origin $\eta = 0$ corresponds to the positive $y-$axis and positive (negative) values correspond to $\theta < \pi/2$ ($\theta > \pi/2$). The distance in the $\eta-\phi$ plane is defined as $\Delta R = \sqrt{\Delta\eta^2 + \Delta\phi^2}$.

The ATLAS experiment was designed to allow for the detailed study of a broad spectrum of physics processes. The design criteria include the need for very good electromagnetic calorimetry for electron and photon identification, complemented by wide-coverage hadronic calorimetry for precise measurements of jets and missing transverse energy. A high-resolution muon spectrometer guarantees pre-

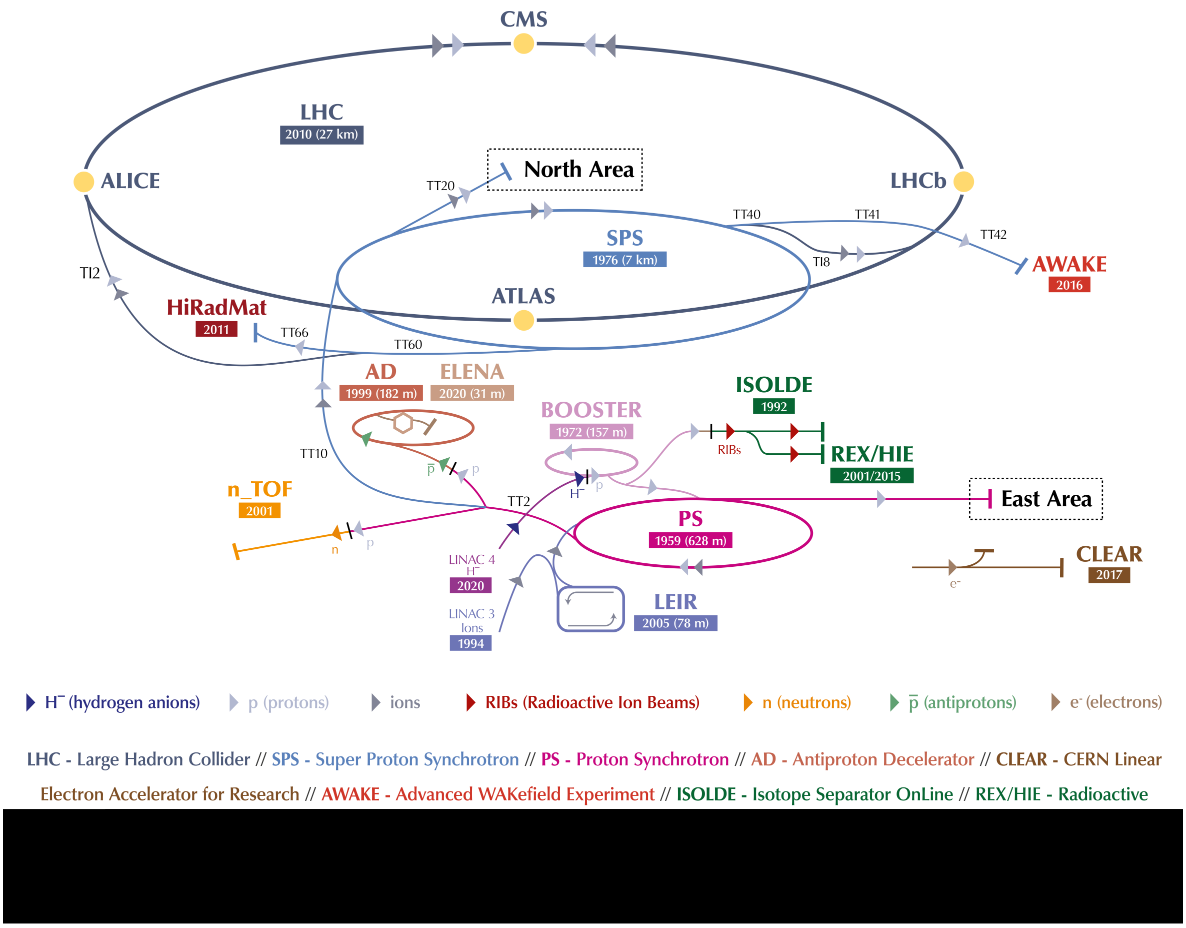

Figure 4.1: The CERN accelerator complex [8].

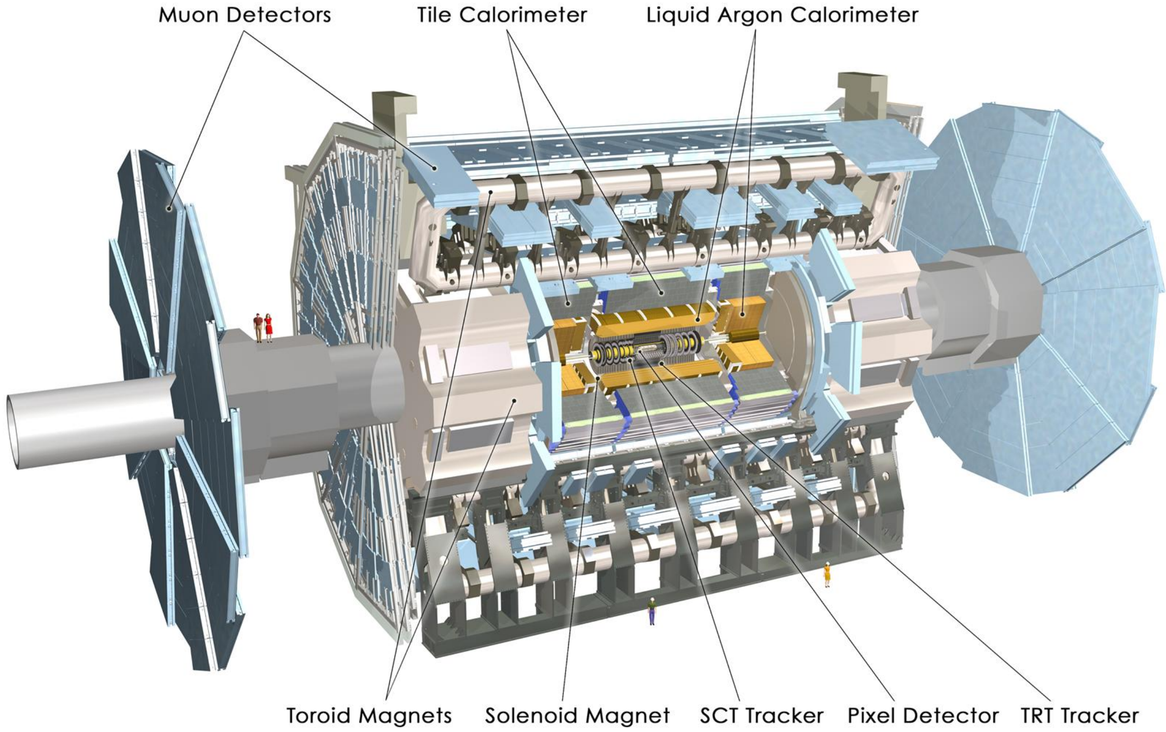

Figure 4.2: Schematic representation of the ATLAS experiment [9].

cise measurements of muon energy and trajectory, and high-efficiency tracking is required to allow for particle identification at high luminosity and full event reconstruction at low luminosity. A highly efficient trigger system provides high acceptance for most physics processes of interest, including those where particles with low transverse momentum are created. Figure 4.2 shows a representation of the ATLAS experiment, including the main subdetectors.

ATLAS subdetectors can be divided into three main categories [103]: inner tracker, calorimeters and muon spectrometer. The inner detector (section 4.2.2), located closest to the beam pipe, inside the solenoid magnet, is composed of three types of tracking detectors (silicon pixels, silicon microstrips and straw tubes) that allow for high-precision reconstruction of particle trajectories and momentum measurements. Electromagnetic and hadronic calorimeters (section 4.2.3) are placed outside the solenoid magnet and are designed to absorb the energy of photons, electrons and hadrons. The barrel toroidal magnet is placed outside the calorimeters and followed by a set of gaseous tracking detectors dedicated to measuring muon trajectories and momenta (section 4.2.4). The magnetic system is described in section 4.2.1 and section 4.2.5 is dedicated to a special class of subdetectors, referred to as forward detectors, that are located along the beam pipe, further away from the central ATLAS detector and the interaction point. The operation of the ATLAS experiment relies on the existence of a trigger system (section 4.2.6), comprising a hardware-based Level-1 (L1), followed by a software-based High Level Trigger (HLT).

4.2.1 Magnet system

The ATLAS experiment relies on powerful magnets to bend the trajectories of particles as they travel through the detector, allowing for particle identification and momentum measurements. The ATLAS magnet system [104] consists of four superconducting magnets: a Central Solenoid (CS), a Barrel Toroid (BT) and two End-Cap Toroids (ECT).

The CS provides an axial magnetic field of 2 T in the inner detector. The solenoid is mounted in the vacuum vessel of the Liquid Argon calorimeter. The toroidal magnets provide a magnetic field to the muon chambers. The BT consists of eight flat coils, in a racetrack configuration, assembled radially and symmetrically around the beam axis. Each coil is contained in its own individual cryostat. Each ECT consists of 8 superconducting coils mounted as a single cold mass unit in a large cryostat and it is designed to be retracted from the operating position to allow access to the central part of the ATLAS detector.

The type of conductor used in all coils is a composite of a flat NbTi/Cu Rutherford cable positioned in the center of an aluminum stabilizer with a rectangular cross-section. In normal operational conditions the magnets are cooled to 4.5 K using super-fluid Helium.

4.2.2 Inner detector

The inner detector occupies the innermost part of the ATLAS detector. It is located inside in the solenoidal magnet and immersed in a 2 T magnetic field parallel to the beam axis. It is designed to measure the direction, momentum and charge of electrically-charged particles by combining high-resolution detectors at small radii with continuous tracking elements at larger radii. Closest to the interaction point, the pixel detector provides at least three very high-granularity, high-precision space point measurements. Due to material and cost considerations, the number of pixel layers needs to be limited. In the intermediate radial region, the semiconductor tracker (SCT) provides four precision measurements per track. At large radii, the Transition Radiation Tracker (TRT) allows for continuous track-following by providing a large number of measurements (typically 36) with less material per point and at a lower cost. Both pixel and SCT are cooled to around or below $0°$ Celsius using an evaporative cooling system of a fluorocarbon fluid to prevent reverse annealing of the silicon sensors.

The transverse momentum resolution of the inner detector can be parameterized as:

$$\frac{\sigma(p_{\mathrm{T}})}{p_{\mathrm{T}}} = a \bigoplus b \times p_{\mathrm{T}}, \tag{4.4}$$

where the factor a is related to multiple scattering and b to the intrinsic resolution of the detector [105]. The values of a and b are measured from data and for the ATLAS inner detector are of the order of $a \sim 2\%$ and $b \sim 10^{-5}$ GeV^{-1}.

The pixel detector is composed of four barrel layers and six disk layers, three on each side of the interaction point, to provide full coverage in the range $|\eta| < 2.5$ [106, 107]. The basic building blocks of the active parts of the pixel detector are silicon pixel sensors composed of an array of bipolar diodes. The innermost layer, the B-layer, is located 3.3 cm from the beam pipe to provide optimal impact parameter resolution. It is composed of pixels with area 50×250 μm^2 and with thickness

$200-230$ µm. The barrel layers are organized in a concentric structure around the beam axis, starting at 5.5 cm from the beam pipe. The disk layers are placed perpendicular to the beam axis. The pixel sensors in these layers have an area of 50×400 µm^2 and are 250 µm thick.

The SCT extends the tracking capabilities of the ATLAS detector to radial distances of $299 < r < 560$ mm [108, 109]. It consists of four layers of silicon microstrip sensors in the barrel and nine disks in each of the end-caps. Each barrel layer consists of 12 rings of modules along the z direction. Each module consists of four rectangular 285 µm-thick silicon sensors with strips of pitch 80 µm.

The TRT covers the region $|\eta| < 2.0$. The barrel section is composed of three concentric layers that cover the radial region $560 < r < 1080$ mm and the longitudinal region $|z| < 712$ mm [110, 111]. In each end-cap section, two independent wheels are placed perpendicular to the beam pipe and cover the regions $644 < r < 1004$ mm and $827 < |z| < 2744$ mm. The building blocks of the TRT detector are carbon-fiber-reinforced kapton straws with 4 mm diameter, held at a potential of -1530 V with respect to a gold-platted tungsten wire at the center. The straws are filled with a gas mixture. A particle traversing a straw ionizes the gas and the electrons drift to the central wire. In addition to being used in track reconstruction, the TRT also contributes to electron identification based on transition radiation produced due to foils interleaved between the straws. Charged particles traversing the boundary between materials with different dielectric constants emit X-ray photons that then ionize the gas inside the straws. The transition radiation deposits a lot more energy in a single straw than an ionizing particle usually does.

4.2.3 Calorimeters

The ATLAS calorimetry system consists of electromagnetic and hadronic sampling calorimeters, composed of active material interleaved with layers of dense absorber material. Particles traversing the calorimeters interact with the absorber plates originating an electromagnetic or hadronic shower, whose particles ionize the active material or produce scintillation photons, depending on the type of calorimeter. For electromagnetic showers, the optimal absorbers are materials with a high atomic number, Z, while for hadronic showers the absorption length is determined by the nuclear interaction length, λ. The calorimeter system ensures an hermetic coverage of $|\eta| < 4.9$, which is an essential condition for the measurement of the missing transverse energy. The energy resolution of a calorimeter can be parameterized as:

$$\frac{\sigma(E)}{E} = \frac{a}{\sqrt{E}} \bigoplus \frac{b}{E} \bigoplus c, \tag{4.5}$$

where a, b and c correspond to stochastic, noise and constant terms, respectively.

Electromagnetic (EM) calorimetry is provided by lead-liquid Argon (LAr) sampling calorimeters with an accordion structure, which provide continuous coverage in azimuth and a faster readout [112]. The particles produced in electromagnetic showers ionize the liquid argon and the resulting ions and electrons drift towards the electrodes due to a high-voltage applied in the gap filled with active material. The barrel calorimeter is placed right outside the solenoid magnet and covers pseudorapidity $|\eta| < 1.475$, with a minimal thickness of 22 radiation lengths (X_0). Two end-cap calorimeters cover

$1.375 < |\eta| < 3.2$, with minimal depth $24\ X_0$. The energy resolution of the EM calorimeter is given by $\sigma(E)/E = 10\%/\sqrt{E[\text{GeV}]} \bigoplus 0.7\%$.

In the region dedicated to precision physics ($|\eta| < 2.5$, the region also covered by the inner detector) the EM calorimeter is segmented into three sampling layers. The first layer has a very high granularity in η, providing a very precise position measurement and assisting with particle identification. The second layer is segmented into square towers of size $\Delta\eta \times \Delta\phi = 0.025 \times 0.025$, while the third one has a granularity that is twice as coarse in η. For $|\eta| > 2.5$, the calorimeter has only two sampling layers and coarser granularity in $\Delta\eta \times \Delta\phi$ than for the rest of the acceptance.

Hadronic calorimetry comprises three main devices. In the end-caps ($1.5 < |\eta| < 3.2$) and forward regions ($3.1 < |\eta| < 4.9$), LAr sampling calorimeters employ copper and tungsten as absorber material, respectively [112]. The first layer of the forward calorimeter, closest to the interaction point, is also used for electromagnetic measurements. The tile calorimeter covers the barrel region ($|\eta| < 1.7$), and can be subdivided into barrel ($|\eta| < 1.0$) and two extended-barrels ($0.8 < |\eta| < 1.7$) [113]. It uses scintilator tiles based on polystyrene as active material, interleaved with steel plates as absorber material. The light produced by scintillation as particles traverse the tiles is collected on both edges of each tile by wavelength-shifting optical fibres. These fibers convert the wavelength of the scintillation photons from ultraviolet to visible, while guiding them to photomultiplier tubes which convert photons to electrons and amplify the signal.

4.2.4 Muon systems

The muon spectrometer occupies the outermost part of the ATLAS detector [103, 114]. It is designed to measure the trajectory and momentum of muons in the pseudorapity range $|\eta| < 2.7$ and it also provides triggering capabilities for $|\eta| < 2.4$. It consists of four subsystems: Monitored Drift Tubes (MDT), Cathode Strip Chambers (CSC), Resistive Plate Chambers (RPC) and Thin Gap Chambers (TGC). MDT and CSC provide precision measurements while RPC and TGC are mainly used for triggering.

The ATLAS toroidal magnets create a field mostly perpendicular to the muon trajectories with values between 0.5 and 2 T, which allows for the momentum measurements. In the barrel region ($|\eta| < 1.0$) the field is provided by the barrel toroid while in the end-caps ($1.4 < |\eta| < 2.7$) it is generated by the end-cap toroids. In the transition region ($1.0 < |\eta| < 1.4$), the field is a superposition of the barrel and end-cap fields.

In the barrel, the muon chambers are arranged in three concentric cylinders located at radii 5 m, 7.5 m and 10 m around the beam axis. The end-cap chambers form four disks on each side of the interaction point, placed perpendicular to the beam pipe and at z distances between 7.4 m and 21.5 m from the interaction point.

The MDTs perform the precision coordinate measurements in the bending direction of the toroidal magnetic field, providing the momentum measurements in the full pseudorapidity range $|\eta| < 2.7$. In the innermost layer of the end-caps ($2.0 < |\eta| < 2.7$), where particle fluxes are highest, they are replaced with CSCs. The MDT chambers consist of three to eight layers of drift tubes with a diameter of ~ 30 mm, operating with an Ar/CO_2 gas mixture at a pressure of 3 bar. A central tungsten-rhenium wire at a potential of 3080 V collects the electrons produced by the ionization of the gaseous medium. A resolution of 80 µm can be achieved per tube. The CSCs are multiwire proportional chambers with the wires oriented in the radial direction. There are two cathodes, operating at a potential of 1900 V, which are segmented into strips that are perpendicular or parallel to the wires. The perpendicular strips provide the precision measurements while the parallel ones provide the transverse coordinate. In the bending direction, a resolution of 60 µm can be achieved per plane. In the non-bending direction the cathode segmentation is coarser, leading to a resolution of 5 mm.

The RPCs provide trigger signals in the barrel region. They consist of three stations each with two detector layers. Two stations are located near the center of the magnetic fied region and provide low-p_T triggers ($p_T > 6$ GeV) while the third station is located outside the magnet. Together with the inner stations it has enough lever arm to provide high-p_T triggers ($p_T > 20$ GeV). The trigger logic requires hits in three out of four of the inner layers and one out of two additional hits in the outer layers for the high-p_T triggers. The RPCs are gaseous parallel electrode-plate detectors. The two resistive plates are kept at a distance of 2 mm with an electric field between them of 4.9 kV/mm.

The TGCs provide trigger capabilities in the end-caps. They also provide the azimuthal coordinate used to complement the bending coordinates measured by the MDTs. The operating principle is the same as the CSC.

In the $|\eta| > 1$ region of the muon spectrometer, a significant part of the L1 trigger rate is due to fake muons. Low energy particles, mainly protons, are generated in the material located between the small wheel and the end-cap middle layer station and hit the end-cap trigger chambers in an angle similar to high-p_T muons. To mitigate this issue in the forward region ($|\eta| > 1.3$), a New Small Wheel (NSW) was installed for Run 3. It additionally recovers the tracking efficiency and resolution in the inner end-cap station. The NSW layout consists of 16 detector planes in two multilayers, each consisting of four small-strip TGCs (sTGC) and four Migromegas (MM) detector planes. In the region $1.0 < |\eta| < 1.3$, 16 new muon stations made of one smaller MDT (sMDT) chamber and two RPC triplets will be installed to further reduce the fake rate.

4.2.5 Forward detectors

ATLAS features several smaller, highly-specialized subdetectors located in very forward regions. LUCID (LUminosity measurement with Cherenkov Integration Detector) [115] and ALFA (Absolute Luminosity for ATLAS) [116] provide dedicated luminosity measurements. The ZDC (Zero-Degree calorimeter) [117] is crucial for the heavy-ion physics program: it measures the number of participants in the collisions by detecting the spectator neutrons. The AFP (ATLAS Forward Proton) [118] detector tags and measures the properties of protons emerging intact from the collision, enabling the study of elastic or diffractive processes which are otherwise inaccessible.

LUCID is a dedicated luminosity detector for the ATLAS experiment. The current LUCID has been commissioned in 2016 and used throughout Run 2, following an upgrade of the previous detector due to radiation damage and to cope with the additional radiation coming from a new ATLAS beam pipe made of aluminum instead of stainless steel. This is the detector described here and referred to as LUCID henceforward. It consists of two modules placed 17 m away from the interaction point, on each side of the central detector. Each module consists of 16 photomultipliers (PMTs) whose quartz windows act as a Cherenkov medium for particle counting. It provides the primary and most precise luminosity measurement, being crucial to the determination of the total integrated luminosity.

ALFA is a subdetector dedicated to measuring the total proton-proton cross-section by detecting elastically-scattered protons [116]. It consists of two stations placed 240 m away from the interaction point on both sides. The stations are equipped with tracking detectors based on scintillating fibers.

The ZDC [117] consists of two modules located at approximately zero degrees on each side of the interaction point, 140 m downstream, at the region where the beam pipes merge into a single one. Its primary role is event characterization in heavy-ion collisions. It detects "spectator" neutrons providing an important handle on heavy-ion collision centrality and allowing to trigger on ultra-peripheral collisions. When used in combination with the central detector, ZDC can also provide important information for beam tuning and luminosity monitoring. Coincidences between both ZDC arms are only due to beam-beam collisions while coincidences between ZDC and the central detector can be due to beam-gas or beam halo-wall events. Therefore, ZDC-ZDC coincidences provide a very clean handle for the total inelastic rate.

AFP is dedicated to tagging and measuring the momentum and emission angle of protons that emerge intact from the collision traveling at very small angles with respect to the beam pipe [118]. This opens up the possibility to study processes in which one or both protons remain intact, therefore extending the physics reach of the ATLAS experiment. AFP, shown in Figure 4.3, consists of four Roman pot stations, two on each side of the interaction point, equipped with silicon tracker and time-of-flight (ToF) detectors. On each side, the near station is located at $z = \pm 206$ m and the far station at $z = \pm 217$ m. Planes of three-dimensional silicon pixel tracking detectors are located in both the near and far stations, four in each one, at a small angle with respect to the $z-$axis. The ToF detectors are placed in the far stations. They consist of quartz bars placed at the Cherenkov angle with respect to the proton's flight direction, which act as Cherenkov radiators and as light guides that transport the light to PMT tubes. A high timing resolution, of up to 10 ps, is crucial for reducing the pileup backgrounds at high-μ operation. Using data collected during 2017, the time resolution of the ToF detectors was measured to be 20 ± 4 ps for side A and 26 ± 5 ps for side C.

The Minimum Bias Trigger Scintillators (MBTS) provide the least biased trigger signals during low-luminosity runs, allowing the measurement of fundamental quantities such as track multiplicity and underlying event characteristics. They consist of polystyrene scintillator disks located along the beam pipe on each side of the central detector, 3.6 m away from the interaction point. Each side has an inner ($2.08 < |\eta| < 2.78$) and outer ($2.78 < |\eta| < 3.75$) ring with eight counters in the azimuthal angle, read out by wavelength-shifting optical fibers.

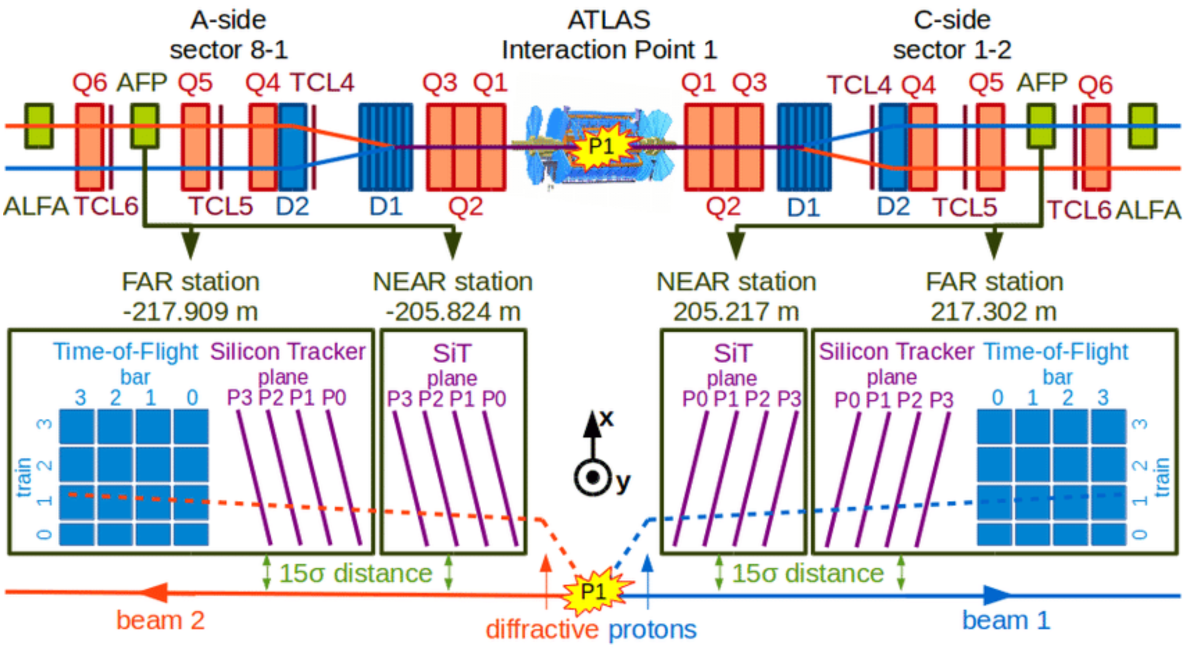

Figure 4.3: Diagram of the AFP detectors, showing the near and far stations with the corresponding silicon tracking and time-of-flight detectors. The distances with respect to the interaction point are also shown.

4.2.6 Trigger and Data Acquisition

With bunch crossing rates reaching up to 40 MHz, the amount of data produced largely exceeds the storage capabilities of the ATLAS data disks, making it completely unfeasible to store information about every single event. The Trigger and Data Acquisition system (TDAQ) is designed to select in real time which events should be stored for further analysis, based on two selection steps, referred to as the Level-1 (L1) trigger [119] and the High Level Trigger (HLT) [10, 120]. The architecture of the trigger system during Run 2 is described in section 4.2.6.A. A schematic overview is shown in Figure 4.4. In section 4.2.6.B, the upgrades introduced for Run 3 are described. Finally, in section 4.2.6.C, an overview of the current proposal of the trigger system for HL-LHC is presented.

4.2.6.A Run 2

The L1 trigger is a hardware system based on custom electronics that uses low-granularity information from the calorimeter (L1Calo) [121] and muon (L1Muon) detectors as input. In the L1Calo trigger, a preprocessor digitises the analogue detector signals that are then sent in parallel to the Cluster Processor (CP) and to the Jet/Energy-sum processor (JEP). The CP identifies electron, photon and $\tau-$lepton candidates above a configurable threshold and the JEP identifies jet candidates and produces global sums of total and missing transverse energy. The L1Muon trigger uses hits from the RPCs in the barrel ($|\eta| < 1.05$) and from the TGC in the end-caps ($1.05 < |\eta| < 2.4$). The hits from different layers are required to be geometrically matched within a programmable window, referred to as "road", whose width depends on the p_{T} threshold of the trigger. Information from L1Calo and L1Muon can be combined through the L1Topo system that has the capability to compute event-level quantities and apply topological selections.

The L1 trigger decision is formed by the Central Trigger Processor (CTP) which receives inputs from L1Calo, L1Muon (through the L1Muon Central Trigger Processor Interface, MUCTPi) and L1Topo systems, as well as trigger signals from other subdetectors such as MBTS, LUCID and ZDC. The L1 trigger reduces the event rate from the bunch crossing rate of 40 MHz up to a the maximum detector read-out rate of 100 Hz, within a latency of 2.5 µs. Whenever the L1 system accepts an event, the event data is read out from all detectors by the front-end detector electronics. The data is first sent to the ReadOut Drivers (RODs) where an initial processing and formatting is performed and then to the ReadOut System (ROS) to buffer the data.

The second stage of triggering, the HLT, is software-based. The HLT requests data from the ROS and uses it as input to offline-like reconstruction algorithms which form a decision within a few hundred milliseconds and run in a large computer farm with approximately 40000 Processing Units (PUs) . A typical reconstruction sequence makes use of dedicated, quasi-offline, fast algorithms that are run on L1 Regions of Interest (RoIs) in order to provide early rejection. More precise and more CPU-intensive algorithms are then used to make the final decision. In the HLT, at a lower rate, it is also possible to perform full-event reconstruction in which information from the entire detector is used. A reconstruction sequence usually starts with a feature extraction algorithm that uses the event-data fragments to reconstruct physics objects, followed by a hypothesis algorithm which uses the reconstructed features to decide whether or not a set of trigger conditions are satisfied. Events accepted by the HLT are written into different data streams.

4.2.6.B Run 3

For Run 3, the L1Calo electronics are augmented by new subsystems: the electromagnetic and jet feature extractors (eFEX and jFEX, respectively) as well as a global feature extractor (gFEX) [122]. During commissioning, these new systems worked in parallel with the CP and JEP systems and were removed once the outputs from eFEX and jFEX were fully validated. The eFEX subsystem identifies isolated electron, photon and hadronically-decaying tau candidates. The electromagnetic information is provided in the form of SuperCells consisting of four or eight calorimeter cells. The jFEX subsystem identifies energetic jets with radius $R = 0.4$ or $R = 0.8$, hadronically-decaying tau leptons within $|\eta| < 2.5$ and electromagnetic objects in the forward region ($2.3 \leq |\eta| \leq 4.9$). The granularity used by the jFEX is 0.1×0.1 for $|\eta| < 2.5$ and becomes coarser in the end-caps and forward regions. The gFEX identifies large- and small-R jets with radius $R = 0.9$ and $R = 0.3$, local pileup density and substructure information. The gFEX granularity varies from 0.2×0.2 for $|\eta| < 2.2$ to 0.4×0.4 for $|\eta| > 3.5$. The resulting trigger objects from eFEX and jFEX are transmitted to L1Topo via optical fibers.

During Run 2, LAr and Tile calorimeter electronics provided analogue data to L1Calo. For Run 3, a new on-detector Digital Processing System (DPS) allows LAr to provide digitised data to L1Calo, which receives 10 samples per each tower of $\Delta\eta \times \Delta\phi = 0.1 \times 0.1$, derived from longitudinal segments and transverse sums of groups of calorimeter cells, each sum forming a SuperCell. Tile calorimeter data is still digitised by L1Calo, in an upgraded Pre-Processor Module (PPM).

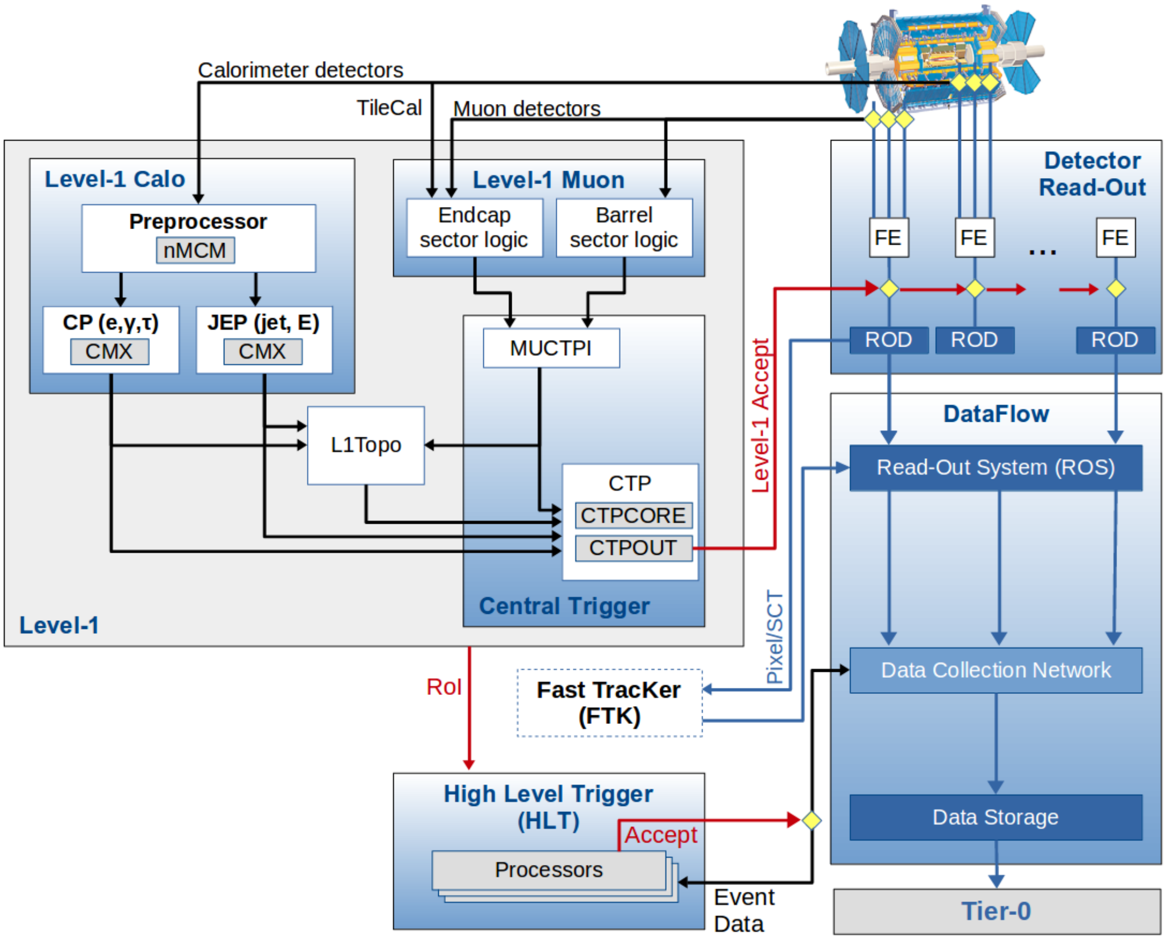

Figure 4.4: Functional diagram of the ATLAS Trigger and Data Acquisition system in Run 2 with specific focus given to the components of the L1 trigger system [10].

For Run 3, the muon detectors underwent extensive upgrades, which are described in detail in section 4.2.4. The NSW, based on small-strip TGC and MM technologies, and additional RPCs (RPC-BIS78) are installed in the inner region of the muon spectrometer and integrated in the end-cap muon trigger. Taking the coincidence between the TGC in the Big Wheel (BW-TGC) and the new inner systems (NSW, RPC-BIS78) reduces the two main sources of background for the end-cap muon trigger, arising from fake muons emanating from the end-cap toroid or shielding due to slow protons and contamination from low-p_{T} muons below the threshold. The upgrade of the trigger processor boards, referred to as Sector Logic, allows to increase the number of TGC low-p_{T} thresholds from 6 (in Run 2) to 15, which in turn increases the resolution of dimuon invariant mass, crucial for B-physics and light meson triggers. Additionally, four new flags are defined for each muon candidate, indicating the electric charge and the stations with registered hits.

The MUCTPi is upgraded to provide full-granularity RoI information and to interface with the new Sector Logic. It can send up to 32 combinations of p_{T} thresholds and flags to the CTP, to be compared to 6 during Run 2.

The L1Topo system is upgraded with three new modules (Topo1, Topo2 and Topo3). The Topo1 module applies basic selections based on object multiplicity. The other two modules apply topological selections.

4.2.6.C High Luminosity LHC

For the HL-LHC, a baseline two-level trigger system was originally foreseen [123]. It consisted of the Level-0 (L0) hardware trigger (similar to the current Level-1), followed by the Event Filter system that consisted of a CPU farm and a hardware co-processor with the capability of performing regional and global track reconstruction (HTT - Hardware Track Trigger). Hardware-based fast tracking, performed by the HTT in RoIs identified by L0 (regional HTT), was intended to achieve early rejection of hadronic signatures at the trigger. After this step, HTT would be used to perform track reconstruction using full-detector information (global HTT) and thus offload part of this task from the CPU-farm.

In the baseline proposal, HTT used custom Associative Memory ASICs for pattern recognition and FPGAs for track finding and fitting. Regional HTT reconstructs tracks with $p_{\mathrm{T}} > 2$ GeV in L0 RoIs. It performs single-stage track reconstruction using eight inner detector layers and reduces the rate from 1 MHz (L0 accept rate) to 400 kHz. Global HTT is capable of reconstructing tracks with $p_{\mathrm{T}} > 1$ GeV at a rate of 100 kHz. In addition to the first-stage track reconstruction (common with regional HTT) it performs a second-stage track processing, using all inner detector layers and thus providing high-quality tracks that can be used in the Event Filter to calculate isolation variables, reconstruct primary vertices and missing transverse momentum or as input to b-tagging algorithms.

Two main risks can impact the expected performance of the baseline system described above. On the one hand, the trigger rates from hadronic signatures at the ultimate pileup of $<\mu>$=200 are hard to predict from simulation. They are extremely sensitive to the contribution from stochastic jets and their values may largely exceed expectations. On the other hand, the number of hits per chip (occupancy) in the layers of the pixel detector may also exceed expectations. The occupancy drives the readout rate for the pixel detector. If the occupancy is larger than estimated, the increase in the event size would lead to an intolerable increase of the bandwidth for the pixel detector readout electronics.

The addition of a second hardware-level trigger (Level-1) mitigates both of these risks. In this scenario, referred to as *evolved*, HTT would be used in the regional mode to build low-resolution tracks from the strip and outer pixel layers of the upgraded inner detector (ITk), where the occupancy is expected to be lower.

In view of recent advances in tracking software and heterogeneous computing systems as well as design choices for the ITk detector, the proposals for baseline and evolved trigger architectures proposed in the TDAQ Technical Design Report (TDR) were reevaluated with the goal of deciding on the optimal trigger system for Run 4. During this process, it was decided against the evolved scenario with a low-latency L1 hardware track trigger. In the baseline scenario, the HTT was discarded in favor of a non-custom system based mainly on software, described in the TDAQ TDR amendment [124].

Extensive performance studies were done to evaluate the impact of the evolved trigger system on the selection of hadronic and multilepton signatures. These studies update and extend the ones documented in the TDAQ TDR [123] and were a crucial input to the decision making process within the ATLAS Collaboration. Despite the decision against HTT and the evolved scenario, these studies highlight the expected performance of a future Level-1 tracking system.

5 Object reconstruction and identification

Contents

The reconstruction of physics objects from the raw detector measurements is a key step in any physics analysis. In this chapter, the offline reconstruction and calibration algorithms are described. The (mostly small) differences with respect to the algorithms executed at the HLT are highlighted in dedicated subsections.

Tracks are fundamental components in the reconstruction of other physics objects such as electrons, muons and (b-)jets. The spatial intersection of multiple tracks also allows to identify collision vertices, or decay vertices of unstable particles, which can then be used, for example, as input to b-tagging algorithms. The reconstruction of tracks and vertices is described in section 5.1.

Another key component to the reconstruction of physics objects is to cluster the active, highly-energetic calorimeter cells together. These clusters, referred to as topo-clusters, are key aspects of the reconstruction of electrons, taus and jets. The topo-clustering algorithm is described in section 5.2.

The reconstruction of electrons and muons is described in sections 5.3 and 5.4, respectively. Section 5.5 covers the reconstruction of hadronically-decaying τ-leptons. The reconstruction of jets and missing transverse momentum is described in section 5.6.

Another crucial aspect of a plethora of physics analyses is to identify the flavor of the parton from which a jet originated. This encompasses a broad class of algorithms, jointly referred to as flavor tagging algorithms. It is particularly important in analyses targeting final states with multiple jets, as it is the case of $t\bar{t}H(H \to b\bar{b})$. These algorithms are described in section 5.7.

5.1 Tracks and vertices

Tracks are a representation of the trajectories of charged particles that traverse the inner detector, with associated kinematic properties. A track is described by a set of five parameters: the charged curvature, q/p_{T}, where q denotes the electric charge and p_{T} the transverse momentum; the azimuthal and polar angles, ϕ and θ, respectively; the distance of closest approach of the track to a reference point (usually the primary vertex or beamspot position) in the $x-y$ plane, d_0, referred to as transverse impact parameter; and the distance in the z-axis between the track position at the point of closest approach and the reference point, z_0, referred to as longitudinal impact parameter.

Primary track reconstruction is performed using mainly information from the pixel and SCT detectors, in a reconstruction scheme designated "inside-out" [125]. As a first step, raw hits in these two subdetectors are clustered to form three-dimensional measurements referred to as space-points. They represent a point where a charged particle traversed the active material of the pixel or SCT detectors. Track seeds are then formed from sets of three space-points, which already allows for a crude estimation of the momentum, based on which the track parameters can be estimated assuming a perfectly helical trajectory in a uniform magnetic field. A combinatorial Kalman filter [126] is then used to build track candidates from the seeds by incorporating additional space-points in the pixel and SCT detectors compatible with the trajectory estimated from the seed.

Track candidates are assigned a score based on the number of clusters and holes (layers of the inner detector where a measurement would be expected given the track trajectory but is missing) associated to them, the χ^2 of the track fit and the track momentum in order to give preference to energetic tracks. The ambiguity solver algorithm then processes every track individually in descending order of their score and deals with the clusters assigned to multiple tracks. Once ambiguities in the assignment of clusters to tracks are resolved, tracks are scored again and must fulfill basic quality criteria: $p_{\mathrm{T}} > 400$ MeV, $|\eta| < 2.5$, a minimum of 7 pixel and SCT clusters, a maximum of one shared pixel cluster or two shared SCT clusters in the same layer, no more than two holes with no more than one in the pixel detector, and $d_0^{\mathrm{BL}} < 2.0$ mm and $z_0^{\mathrm{BL}} < 3.0$ mm, where the track parameters are measured with respect to the beam-line (BL). For track candidates fulfilling these requirements, a high-resolution fit is performed.

The track reconstruction procedure described up to now is optimized to reconstruct particles produced in the hard-scatter interaction of proton-proton collisions. To increase acceptance of particles produced at a larger distance from the beam-line, such as electrons originating from photon conversions in the detector material or secondary particles produced by decays inside the detector, outside-in track reconstruction is performed using hits not used in the previous step.

It starts with segments of hits in the TRT subdetector, compatible with a RoI determined by an energy deposit in the EM calorimeter. Short track seeds are created from two space-points in the pixel and SCT layers compatible with the TRT seed. The track finding and fitting procedure progress as in the primary track reconstruction. TRT segments not used in outside-in track reconstruction are fitted and used as TRT standalone tracks, which typically have low quality and are very susceptible to a high rate of fake tracks.

The reconstruction of vertices follows an iterative procedure that uses as input the beamspot location and size, and the subset of reconstructed tracks that pass a quality selection designed to remove poorly-measured and fake tracks [127]. In the first step, tracks not yet associated with any vertex are analysed to find the most likely position of a primary vertex based on the maximum track density along the beam axis. Once a seed is found, the set of nearby tracks to fit is chosen, such that each track is generally associated with more than one vertex. A weighted adaptative Kalman filter is then used to fit the position of the vertex using the linearized helical parameters of the assigned tracks as input. Each track is assigned a weight based on the compatibility with the fitted vertex. Tracks incompatible with the current candidate by more than 7σ are used to seed another vertex. The vertex candidate is accepted if it has more than two tracks associated to it. The procedure is repeated until no more than two tracks are left. The primary (or hard-scatter) vertex is defined as the vertex with the largest $\sum p_T^2$ of associated tracks. The remaining tracks are considered to originate from pileup interactions.

5.1.1 HLT reconstruction and identification

At the HLT, track reconstruction is divided into a fast and a precision step. As in offline track reconstruction, three-dimensional space-points are created by clustering the raw measurements in the pixel and SCT detectors and are used as input for track finding and fitting. The cluster positions in the ATLAS coordinate system are determined using the module geometry obtained from the offline alignment procedure. To reduce processing time, TRT hits are not used in the fast tracking step. The tracks reconstructed in the fast step are used to seed the precision tracking algorithms.

The Fast Track Finder (FTF) starts by constructing track seeds from triplets of space-points in bins of radius and approximately 50 sectors in ϕ. Triplet formation starts from a middle space point and adds outer and inner space points at larger and smaller radii, respectively, provided that they are compatible with the trajectory of a particle originating from the interaction region. The triplet track parameters are estimated using a conformal transformation. Initial track candidates are formed using a track finding algorithm similar to offline, but with a modified configuration optimized for faster execution. Duplicate tracks are removed and fitted using a fast Kalman filter. Fake tracks are rejected by requiring $d_0 \leq 4$ mm. For the muon trigger signature this requirement is relaxed ($d_0 \leq 10$ mm) to include tracks associated with the decay of B-hadrons, that create a displaced secondary vertex.

In the precision step, the offline track reconstruction algorithms are executed using as input the FTF tracks identified in the previous step. The configuration of the algorithms is adjusted to run in the trigger. Full detector information regarding inactive sensors and calibration corrections is also taken into account at this stage.

To reconstruct the primary vertex, most trigger signatures use the offline algorithm configured for online running. For b-jet triggers, a histogram-based algorithm is used together with the offline one to maximize vertex finding efficiency. It proceeds by filling an histogram with the point of closest approach to the beam line of each track. The 1 mm sliding window with the largest number of tracks is chosen. The z-position of the vertex is calculated in this window as the mean of the bin centers weighted by the number of tracks in each bin.

For tau and b-jet signatures, a multistage tracking strategy is used. Tracking algorithms are run more than once: firstly over a reduced RoI and secondly over a different RoI that overlaps, extends or updates the previous one. These signatures benefit from tracking in large RoIs to allow for the reconstruction of tracks originating from three-prong tau decays or secondary B-hadron decays. The two-stage tracking approach allows for this while keeping the CPU time to a manageable level. The details of the algorithms are briefly discussed in the corresponding sections.

5.2 Topo-clustering

Topo-clusters are built from topologically-connected calorimeter cells that contain a significant signal above the noise threshold. They are designed to follow the shower development of single or neighbouring incident particles, taking advantage of the fine granularity of the ATLAS calorimeters.

The topo-clustering algorithm [128] starts from a seed cell whose signal-to-noise ratio, $E_{\text{cell}}^{\text{EM}}/\sigma_{\text{noise}}$, is above 4. Both the cell signal, $E_{\text{cell}}^{\text{EM}}$, and noise, σ_{noise}, are measured at the EM scale, which provides a precise measurement of the energy of electrons and photons but does not account for the lower signal produced by hadrons. Cells neighbouring the seed cell with $E_{\text{cell}}^{\text{EM}}/\sigma_{\text{noise}} \geq 2$ are included in the cluster iteratively. Finally, all cells neighbouring the formed topo-cluster are included.

A splitting step follows in order to optimize the separation of showers originating from close-by particles. In each topo-cluster, cells corresponding to local energy maxima (with $E_{\text{cell}}^{\text{EM}} > 500$ MeV) are identified and used as seeds for a new iteration of the topo-clustering algorithm. The original topo-clusters are thus split and cells can be shared by, at most, two clusters. A topo-cluster has an energy corresponding to the sum of the energy of all constituent cells, it is defined to have zero mass and its reconstructed direction is calculated from the weighted average of the pseudo-rapidity and azimuthal angles of the constituent cells.

5.3 Electrons and photons

Electrons and photons are reconstructed within $|\eta| < 2.47$ from EM topo-clusters and tracks identified in the inner detector.

Electron and photon reconstruction [129], [130] starts from topo-clusters from which only the energy deposited in the EM calorimeter is used. This energy must be above 400 MeV and the ratio to the total cluster energy is required to be larger than 0.5 to reject pileup clusters.

Standard track-pattern reconstruction is performed in the inner detector. If pattern recognition fails for a silicon track in a region of interest around an EM cluster, a modified pattern recognition algorithm based on a Kalman filter is used, allowing for up to 30% energy loss due to breamstrahlung at each material intersection. Track candidates are then refitted allowing for additional energy loss if the standard fit fails. Tracks with at least four silicon hits and loosely matched in η and ϕ to EM clusters are refitted using a Gaussian sum filter, a non-linear generalization of the Kalman filter, designed to better account for charged particle's energy loss in the material. If multiple tracks are matched to a cluster, the one with more pixel hits and closest in ΔR is preferred.

Selection requirements are imposed to ensure that electron tracks are consistent with the primary vertex of the event. The d_0 significance is required to satisfy $d_0/\sigma(d_0) < 5$ and the longitudinal impact parameter is required to satisfy $|z_0 \sin\theta| < 5$ mm.

Photon conversion vertices are reconstructed from pairs of tracks with opposite charge and forming a vertex consistent with the decay of a massless particle. Both tracks with hits in the silicon detectors and with hits only in the TRT detector are considered. Conversion vertices are then matched to EM topo-clusters through $\Delta\eta$ and $\Delta\phi$ requirements.

Superclusters are then formed by associating seed clusters ($E_T > 1$ GeV and matched to a track with at least four silicon hits) with nearby EM clusters, referred to as satellite clusters. These may be created from breamsstrahlung or from topo-cluster splitting. By collecting more of the energy deposited by a particle, superclusters lead to an improved energy resolution. A cluster is considered satellite if it lies within $\Delta\eta \times \Delta\phi = 0.075 \times 0.125$ of a seed cluster or within $\Delta\eta \times \Delta\phi = 0.125 \times 0.300$ if its best-matched track is also the best-matched track of the seed cluster. The last step in the formation of superclusters is the association of the calorimeter cells. Only cells from the presampler and the first three layers of the LAr calorimeter are considered, except in the transition region ($1.4 < |\eta| < 1.6$), where the energy from the scintillator between the calorimeter cryostats is also added. The size of each constituent topo-cluster is limited to 0.075 (0.125) in the barrel (end-cap) region, to reduce the superclusters' sensitivity to pileup. An initial energy calibration and position correction are applied to the superclusters. Finally, tracks and conversion vertices are matched to superclusters creating the analysis-level electron and photon objects, respectively.

Several energy corrections are then applied to data. They include the intercalibration of the first and second calorimeter layers and of the energy of the presampler, corrections for pileup-induced energy shifts and corrections to improve the uniformity of the energy response.

Muons are mostly insensitive to the amount of passive material in front of the EM calorimeter.

As such, muons from $Z \rightarrow \mu\mu$ decays with $p_{\mathrm{T}} > 27$ GeV are used to study the intercalibration of the first and second calorimeter layers. The relative calibration of the two layers is derived as function of $|\eta|$ by calculating the ratio between the muon energy measured in data and in simulation: $\alpha_{1/2} = \left(\langle E_1\rangle^{\text{data}}/\langle E_1\rangle^{\text{MC}}\right) / \left(\langle E_2\rangle^{\text{data}}/\langle E_2\rangle^{\text{MC}}\right)$.

The energy of the presampler is also calibrated using electrons from W and Z decays to correct for the effects of passive material mismodelling in the shower development. Several simulations with additional passive material upstream of the presampler (inner detector, services and cryostat) are used to study the correlation between the energy deposited in the presampler and the ratio of energies deposited in the first two layers, $E_{1/2}$. A linear correlation is observed: additional passive material upstream of the presampler leads to earlier shower development and thus more energy deposited in the presampler and larger $E_{1/2}$. The linear parameterization that describes this relation is then applied to correct the presampler energy in MC. The ratio between the presampler energy in data and the corrected MC energy corresponds to the final presampler energy scale correction.

Variations in bunch-to-bunch luminosity and the finite bunch length can create energy shifts that depend on the position inside the bunch train and on the luminosity. To mitigate this effect, the average expected pileup energy shift is subtracted cell-by-cell.

After all corrections described above, the energy of electrons and photons is calibrated to account for energy loss in the material upstream of the calorimeter and beyond the LAr calorimeter, and for the energy deposited in the neighbouring cells of the supercluster. A single correction factor is derived for all these effects using a regression algorithm based on a BDT and is applied to the uncalibrated supercluster energy, E_{raw}. The BDT is trained on single-particle samples without pileup, independently for electrons, converted photons and unconverted photons. The target value for the regression algorithm is $E_{\text{true}}/E_{\text{raw}}$, where E_{true} is the truth energy of the particle as given by the MC generator prior to any detector simulation. The input variables for the BDT training include the energy deposited in different calorimeter layers and ratios between them, the pseudorapidity of the shower impact point in the calorimeter, and the distance in η and ϕ between the impact point and the center of the closest cell in the second calorimeter layer.

To further improve the uniformity of the energy response, corrections are derived as a function of the impact point of the shower in the calorimeter and applied to the energy of the electron or photon. Two effects are corrected for: reduced energy response at the boundaries of the modules due to a larger gap and differences in energy response due to inhomogeneities in the high-voltage of the sectors.

Finally, an energy correction is applied to data to account for differences with respect to MC simulation: $E^{\text{data, corr}} = E^{\text{data}}/(1+\alpha_i)$, where i denotes the η region. Similarly, the differences in energy resolution between data and MC are parameterized by an η-dependent additional constant term and the corrections are applied to simulation: $(\sigma_E/E)^{\text{MC,corr}} = (\sigma_E/E)^{\text{MC}} \oplus c_i$, where $\oplus$ denotes the sum in quadrature. The values of α_i and c_i are measured from data in a fit to the dilepton invariant mass in $Z \rightarrow ee$ events.

Prompt electrons are distinguished from energy deposits from hadronic jets, from converted photons and from genuine electrons produced in heavy-flavor decays using a likelihood discriminant that combines information from the primary electron track, the lateral and longitudinal development of the electromagnetic shower, and the spatial compatibility between the tracks and the cluster. The likelihood of a reconstructed electron to originate from signal or background is calculated from the product of probability density functions (pdfs) of the discriminant variables, in $|\eta|$ and E_{T} bins. The pdfs for signal are derived from $Z \to ee$ (for $E_{\mathrm{T}} > 15$ GeV) and $J/\psi \to ee$ (for $E_{\mathrm{T}} < 15$ GeV) data events selected using the tag-and-probe method. Events with at least one reconstructed electron are selected to derive the background pdfs, leading to a sample enriched in dijet events.

Three working points (WPs) are defined based on the efficiency to identify a prompt electron with $E_{\mathrm{T}} > 40$ GeV: *Loose* (93%), *Medium* (88%) and *Tight* (80%). Additional requirements are imposed for electron identification. If a two-track conversion vertex is reconstructed with a momentum closer to the cluster energy than the primary track, the electron is rejected. To satisfy the *Tight* WP, electrons must have $E/p < 10$ and their primary electron track must have $p_{\mathrm{T}} > 2$ GeV.

A characteristic signature of prompt electrons is the low activity in the calorimeter and inner detector in an area surrounding the electron candidate. Isolation variables, based on the amount of energy or momentum of the tracks in a cone around the electron candidate, can be defined to quantify the activity near electrons. The fully corrected calorimeter isolation variable is calculated as:

$$E_{\mathrm{T}}^{\mathrm{coneXX}} = E_{\mathrm{T,\,raw}}^{\mathrm{isolXX}} - E_{\mathrm{T,core}} - E_{\mathrm{T,leakage}}(E_{\mathrm{T}}, \eta, \Delta R) - E_{\mathrm{T,pileup}}(\eta, \Delta R), \tag{5.1}$$

where XX denotes the size of the used cone, $\Delta R = XX/100$. A cone size $\Delta R = 0.2$ is used to defined the electron working points ($E_{\mathrm{T}}^{\mathrm{cone20}}$). The raw calorimeter isolation variable, $E_{\mathrm{T,raw}}^{\mathrm{isol}}$, is computed as the transverse energy sum of the positive-energy EM scale topoclusters whose barycentre lies within the cone centered around the electron or photon cluster barycentre. $E_{\mathrm{T,core}}$ is the energy of the EM particle that is subtracted by removing the EM cells within a cone around the barycenter of the particle cluster. This method does not remove the totality of the EM particle energy and therefore a leakage correction is applied as a function of E_{T} and η: $E_{\mathrm{T,leakage}}(E_{\mathrm{T}}, \eta, \Delta R)$. An additional pileup and underlying event correction, $E_{\mathrm{T,pileup}}(\eta, \Delta R)$, is also included.

The track isolation variable, $p_{\mathrm{T}}^{\mathrm{varconeXX}}$ is computed by summing the transverse momentum of the tracks in a variable-size cone around the electron track or the photon cluster direction. The maximum cone size is $\Delta R_{\mathrm{max}} = 0.2$ and it varies with the momentum of the electron as:

$$\Delta R = \min\left(\frac{10}{p_{\mathrm{T}}[\mathrm{GeV}]}, \Delta R_{\mathrm{max}}\right). \tag{5.2}$$

Three WPs are defined with fixed requirements on the calorimeter and track isolation variables: *HighPtCaloOnly*, *Loose* and *Tight*. An additional WP, referred to as *Gradient*, is defined with varying cuts in the isolation variables to give an efficiency with respect to electrons passing the *Tight* identification requirement of 90% at $p_{\mathrm{T}} = 25$ GeV and 99% at $p_{\mathrm{T}} = 60$ GeV, uniform in η. The *Gradient* isolation WP is used in the $t\bar{t}H$ analyses. The *Tight* WP is used in the $t\bar{t}c\bar{c}$ analysis and it requires $E_{\mathrm{T}}^{\mathrm{cone20}}/p_{\mathrm{T}} < 0.06$ and $p_{\mathrm{T}}^{\mathrm{varcone20}}/p_{\mathrm{T}} < 0.06$. It gives an efficiency of $\sim 70\%$ at $p_{\mathrm{T}} = 25$ GeV and reaches 98% for $p_{\mathrm{T}} = 60$ GeV.

The reconstruction of the electric charge of an electron relies only on the measurement of the curvature of the associated inner detector track. Its determination is crucial, for example, in the event selection of the $t\bar{t}H$ dileptonic topology, since two electrons with opposite charge are required. Incorrect charge reconstruction can be caused by an incorrect determination of the track curvature, or by the choice of the wrong track. The first effect becomes dominant for electrons with a high transverse momentum. The output discriminant of a BDT is used to suppress electrons with wrongly reconstructed electric charge. It is trained on data from $Z \to ee$ decays, selected by requiring an electron within $|\eta| < 0.6$ passing the *Tight* identification. Any additionally reconstructed electron in the event is used for the training as signal (background) if the electrical charge is different (equal) from the first electron. The input variables include the electron E_{T} and η, the transverse impact parameter multiplied by the electron charge and the average charge of all tracks matched to the electron. The efficiency of the requirement on the BDT discriminant output is 98% in $Z \to ee$ events for electrons satisfying *Medium* or *Tight* identification with the *Tight* isolation requirement, and that have the correct electric charge.

The probability of charge misidentification is measured in seven η bins and six E_{T} bins in the range $20 < E_{\mathrm{T}} < 95$ GeV in $Z \to ee$ events. With the BDT selection described above, the probability of charge misidentification in data ranges from close to zero for $E_{\mathrm{T}} > 20$ GeV to 0.8% at $E_{\mathrm{T}} \sim 200$ GeV and it is fairly flat in η.

5.3.1 HLT reconstruction and identification

The reconstruction of electrons at the HLT is performed in each EM RoI provided by the L1 electron trigger. Fast algorithms perform the reconstruction of energy deposits in the calorimeters and of tracks in the inner detector using only information inside each RoI. Electron candidates are required to have tracks from the fast tracking step matched to the corresponding clusters. Electrons with $E_{\mathrm{T}} < 15$ GeV are selected by a cut-based algorithm using information about the cluster energy and shower shape. For electrons with $E_{\mathrm{T}} \geq 15$ GeV, the *Ringer* multivariate algorithm is used. The energy deposited in concentric rings centered around the most energetic cell in each calorimeter layer is used as input to an ensemble of neural networks for each $E_{\mathrm{T}} \times \eta$ region.

For electron candidates passing the fast reconstruction and identification, precision algorithms are executed. They have access to the full detector information and are very similar to the ones used offline with the following exceptions: calorimeter cluster reconstruction is based on a sliding-window algorithm instead of topo-clusters, and pileup is assessed using $<\mu>$ instead of the number of primary vertices. Additionally, some cell-level energy corrections are either not available online or differ in implementation. In 2017, following the developments in the offline electron reconstruction, the sliding-window algorithm was replaced by the use of superclusters.

5.4 Muons

Muons can be reconstructed using information from the muon spectrometer alone (standalone reconstruction) or including also information from the inner detector and calorimeters [131].

Standalone muon track reconstruction starts by identifying short straight-line local track segments reconstructed from hits in each individual MS layer. Segments in the three MS stations are combined into preliminary track candidates, assuming a parabolic trajectory of muons in the magnetic field, and applying a loose constraint based on the position of the interaction point. Three dimensional track candidates are created by combining information in the bending plane from the precision chambers with the azimuthal coordinate measured in the trigger chambers. A global χ^2 fit is performed to the muon trajectory, taking into account interactions with the detector material and possible misalignment between chambers. Outliers are removed and hits consistent with the estimated trajectory not already included in the original track candidate are added. The track fit is performed again using updated information from all the hits.

Global muon reconstruction combines information from the muon spectrometer, inner detector and calorimeters. It can proceed through different strategies, producing muon collections with the corresponding designations: combined, inside-out combined, muon-spectrometer extrapolated, segment-tagged, and calorimeter-tagged. Combined muons are the default objects used in most analyses, and particularly in the analyses presented in this thesis, and thus the combined reconstruction strategy is described below. For the other strategies, please refer to Reference [131].

Combined muons are reconstructed by matching MS tracks to ID tracks and performing a track fit with information from the hits in the muon spectrometer and inner detector, taking into account energy loss in the calorimeters. For $|\eta| > 2.5$, MS tracks can be combined with short track segments in the pixel and SCT detectors.

After reconstruction, high-quality muon candidates to be used in physics analyses are selected through a set of requirements, including the number of hits and holes in the inner detector and muon spectrometer, the track fit quality and the compatibility between the momentum measurements obtained from the two subdetectors. The q/p compatibility is defined as:

$$q/p \text{ compatibility} = \frac{|q/p_{\text{ID}} - q/p_{\text{MS}}|}{\sqrt{\sigma^2(q/p_{\text{ID}}) + \sigma^2(q/p_{\text{MS}})}}, \tag{5.3}$$

where q/p_{ID} and q/p_{MS} are the ratios of the charge and momentum measured in the inner detector and muon spectrometer, respectively; $\sigma^2(q/p_{\text{ID}})$ and $\sigma^2(q/p_{\text{MS}})$ are the corresponding uncertainties. An additional variable, ρ', is also defined as the absolute difference between the transverse momentum measurements from the ID and the MS divided by the p_{T} of the combined muon track.

Selection WPs mainly target the rejection of non-prompt muons produced in the decay of light hadrons which usually lead to low-quality muon tracks. Non-prompt muons originating from the decays of heavy flavor hadrons produce good-quality tracks. They can be distinguished from prompt muons through vertex association and isolation requirements.

Three main WPs, *Loose*, *Medium* and *Tight*, are defined with increasing purity in prompt muons and decreasing efficiency. Efficiency is defined as the probability that a prompt muon traversing the detector is reconstructed as a muon and satisfies the WP. Purity is defined as one minus the light hadron rejection rate, which is the fraction of light hadrons reconstructed as muons and passing the WP. Within $|\eta| < 2.5$, the *Medium* WP accepts muon candidates with hits in an least two precision stations, and the q/p compatibility is required to be less than 7. For muons passing the *Medium* WP, additional requirements are imposed to define the *Tight* WP. The χ^2 of the combined track fit is required to be less than 8 and p_{T} and η dependent q/p compatibility and ρ' requirements are imposed and optimized to provide better background rejection of lower-p_{T} muons. The *Medium* WP, used in the analyses described here, reaches a maximum efficiency of 97% for $p_{\mathrm{T}} > 20$ GeV, with a light hadron misidentification efficiency between 0.17% and 0.07%.

Further selection requirements are imposed to ensure that the muon tracks are consistent with the beamspot position or primary vertex and thus reject muons from in-flight decays of hadrons or muons originating from pileup interactions. The d_0 significance measured with respect to the beamspot is required to satisfy $d_0/\sigma(d_0) < 3$. The requirement $|z_0 \sin\theta| < 5$ mm ensures compatibility with the primary vertex.

The amount of hadronic activity in the vicinity of reconstructed muons allows to distinguish muons produced in heavy hadron decays. Isolation variables are defined as the ratio between the transverse energy in a cone around a reconstructed muon and the muon p_{T}. They take values between zero and one and have a steeply decreasing shape for prompt muons while they are relatively flat for non-prompt muons. Isolation WPs are defined using information from the inner detector, calorimeters or both, through the particle flow algorithm (described in detail in section 5.6.2). Calorimeter- and track-based isolation variables are defined in a very similar manner to those used for electrons, described in section 5.3. The particle-flow-based isolation variable is defined as the sum of track-based isolation and the transverse energy of neutral particle-flow objects in a cone of size $\Delta R = 0.2$ around the muon.

The track-only isolation WPs are more robust with respect to pileup and less susceptible to inefficiency due to nearby objects. The *TightTrackOnly* WP is the one used in the $t\bar{t}H(H \to b\bar{b})$ and $t\bar{t}c\bar{c}$ analyses described in this thesis. It requires $p_{\mathrm{T}}^{\text{varcone30}} < 0.06 \cdot p_{\mathrm{T}}^{\mu}$ and its efficiency ranges from 94% in the range $20 < p_{\mathrm{T}} < 100$ GeV to 99% for $p_{\mathrm{T}} > 100$ GeV. The corresponding efficiencies for muons from semileptonic decays of B- and C-hadrons are $3.2\% - 3.3\%$.

5.4.1 HLT reconstruction and identification

Fast reconstruction algorithms run in RoIs identified by the L1 muon trigger [132]. Standalone muons are reconstructed using MDT hits within the RoIs, removing hits originating from noise. The muon candidate momentum is crudely estimated using a look up table. Additional hit information from the Extended Endcap (located between the endcap and the barrel) and CSC chambers is included in the regions $1.05 < |\eta| < 1.35$ and $2.0 < |\eta| < 2.4$, respectively. The standalone muon track is then back-extrapolated to the inner detector using the offline algorithm and combined with the inner detector tracks to form a combined muon candidate with refined track parameter resolution.

The final step is the precision stage. It can be executed in L1 muon trigger RoIs or using information from the full detector (full-scan mode). Precision standalone muons are reconstructed using offline-like algorithms and are combined with inner detector tracks to create precision combined muons. If no combined muons are found at this stage, muon candidates are searched for by extrapolating ID tracks to the MS. Isolation criteria can be applied based on the ratio between the sum of track momenta within $\Delta z < 6(2)$ mm of the muon candidate and the muon momentum. The tighter cut $\Delta z < 2$ mm was introduced to handle the challenging pileup conditions during 2017 data-taking.

5.5 Taus

The decay of τ-leptons to hadrons (mostly pions) and neutrinos represents approximately 65% of all the possible decay modes. The neutral and charged hadrons that originate from the decay make up the visible part of the τ decay, referred to as $\tau_{\text{had-vis}}$, and allow for their reconstruction.

The reconstruction of $\tau_{\text{had-vis}}$ leptons is seeded by jets reconstructed from topo-clusters with local hadronic calibration (LC) using the anti-k_t algorithm with $R = 0.4$ [133]. Jets are required to be within $|\eta| < 2.5$ and have $p_T > 5$ GeV before any energy scale corrections. Tracks within $\Delta R < 0.2$ of the jet are used to perform vertex reconstruction. The vertex with the highest p_{T} fraction is chosen as the $\tau_{\text{had-vis}}$ production vertex. The $\tau_{\text{had-vis}}$ four-momentum is calculated as the vector sum of the topo-clusters four-momenta within $\Delta R < 0.2$ of the barycenter of the seed jet, using the tau vertex as origin.

The energy of $\tau_{\text{had-vis}}$ candidates is calibrated to match that of the generator-level visible decay products. Firstly, a pileup correction is applied to the LC-calibrated energy sum of all topo-clusters, E_{LC}, within $\Delta R < 0.2$ of the $\tau_{\text{had-vis}}$ candidate, by subtracting the energy associated with pileup deposits, E_{pileup}. The corrected energy is then divided by the detector response function, $\mathcal{R}$:

$$E_{\text{calib}} = \frac{E_{\text{LC}} - E_{\text{pileup}}}{\mathcal{R}(E_{\text{LC}} - E_{\text{pileup}}, |\eta|, n_p)}. \tag{5.4}$$

The pileup correction is known to depend linearly on the number of primary vertices. The linear coefficient is derived from a fit to E_{LC} from simulated samples in bins of $|\eta|$. The detector response function is calculated as the Gaussian mean of $(E_{\text{LC}} - E_{\text{pileup}})/E^{\text{vis}}_{\text{true}}$ in $|\eta|$ bins and independently for 1-prong and 3-prong decays, denoted n_p. $E^{\text{vis}}_{\text{true}}$ is the energy of the generator-level visible tau decay products.

To correctly determine the charge and number of charged decay products of the τ lepton, tracks associated with the τ decay need to be distinguished from the rest. Tracks within $\Delta R < 0.25$ of the $\tau_{\text{had-vis}}$ are associated with the tau candidate if they have $p_{\text{T}} > 1$ GeV and pass track reconstruction criteria related to the number of hits in the different inner detectors. Requirements on the distance of closest approach to the tau vertex are also imposed. Tracks in the region $0.25 < \Delta R < 0.4$ are also associated to $\tau_{\text{had-vis}}$ if they are either ghost-matched to the seeding jet or if their closest jet is the $\tau_{\text{had-vis}}$ seeding jet. Ghost-matching or ghost-association [134–136] is a technique in which tracks are given a very soft momentum ($p_{\text{T}} = 1$ eV) and added to the list of inputs for jet finding algorithms. In this way, the tracks do not affect the kinematic properties of the reconstructed jets but it is possible to identify which tracks are clustered into which jet or subjet.

To discriminate between truth $\tau_{\text{had-vis}}$ and misidentified $\tau_{\text{had-vis}}$ originating from quark- or gluon-initiated jets a multivariate approach is employed. An ensemble of BDTs was initially used. It was replaced by a Recurrent Neural Network (RNN) during Run 2. The MVA methods are trained separately for 1-prong and 3-prong τ decays, using low-level variables related to the tracks and clusters, as well as high-level variables calculated from track and calorimeter quantities. The signal sample is obtained from $Z/\gamma^* \to \tau\tau$ simulated events, in which the reconstructed $\tau_{\text{had-vis}}$ is required to be matched to a truth $\tau_{\text{had-vis}}$ and be correctly reconstructed as 1- or 3-prong decays. Dijet events are used to obtain a background sample. Four working points are defined with the following efficiencies for 1-prong (3-prong) truth $\tau_{\text{had-vis}}$: *Tight*, $60\%(45\%)$; *Medium*, $75\%(60\%)$; *Loose*, $85\%(75\%)$; and *Very Loose*, $95\%(95\%)$. For the *Medium* WP the background rejection of 1-prong (3-prong) decays increases from 20 (150) with the BDT to 35 (240) with the RNN.

In order to reduce electron background, a BDT is trained using simulated $Z \to \tau\tau$ events as signal and $Z \to ee$ events as background, in multiple pseudorapidity regions. Three WPs, *Loose*, *Medium* and *Tight*, are defined to yield efficiencies of 95%, 85% and 75%, respectively.

5.5.1 HLT reconstruction and identification

Tau reconstruction at the HLT [137] proceeds in three steps: calorimeter-only pre-selection, track pre-selection and offline-like selection. The first step starts with the reconstruction of topo-clusters following a procedure close to the offline one. The pileup corrections applied to the $\tau_{\text{had-vis}}$ seed jets are based on the online-measured $< \mu >$ that is slightly larger than the actual one since it's based on preliminary calibrations available at the time of data-taking. Additionally, due to the lack of track information at this stage, the tau energy calibration is performed inclusively and not as a function of the track multiplicity of the tau candidate.

A two-stage fast tracking step follows. In the first stage, a wedge-shaped RoI is defined directed towards the tau candidate calorimeter cluster with a width of 0.2 in η and ϕ but fully extended along the beamline ($|z| < 225$ mm). The second stage RoI is centered on the z-position of the leading track identified in the previous stage. It utilizes the full width of 0.8 in η and ϕ and it is restricted to $|\Delta z| < 10$ mm relative to the leading track. After the two-stage fast tracking, tracks with $p_{\text{T}} > 1$ GeV are associated to the tau candidates as in offline reconstruction. The number of tracks associated with the tau candidate, as well as the number of tracks around it, are used to determine if the candidate is accepted.

In the final step, precision, offline-like tracking is run over the tracks identified in the second-stage of the fast tracking. $\tau_{\text{had-vis}}$ candidates are identified using the BDT used offline. Towards the end of Run 2 and during Run 3, $\tau_{\text{had-vis}}$ identification is performed using the RNN.

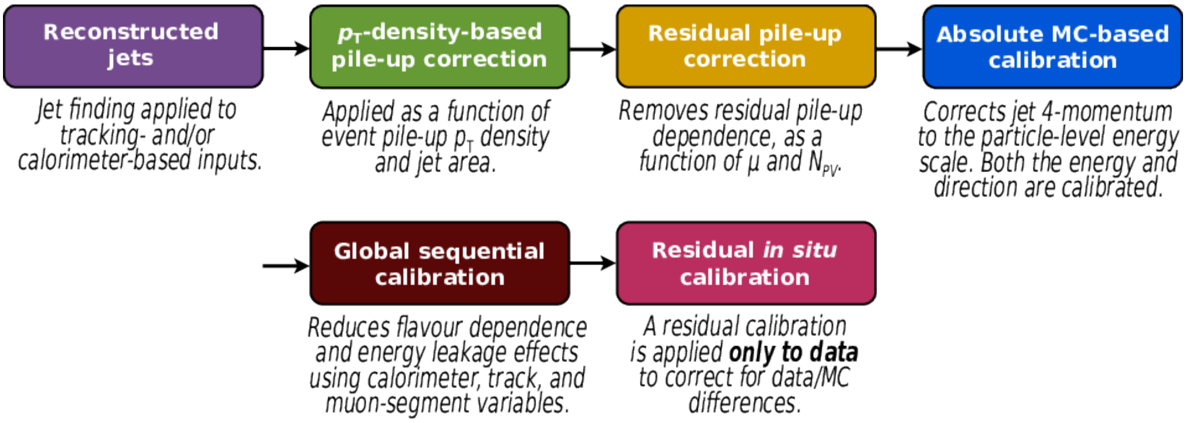

Figure 5.1: Stages of jet energy scale calibrations [11].

5.6 Jets and Missing Transverse Momentum

Jets are reconstructed using the anti-k_t clustering algorithm with radius parameters $R = 0.4$ (default small-radius jets) or $R = 1.0$ (large-radius jets), implemented in the FASTJET software [138]. The total jet four-momentum is defined as the sum of the four-momenta of all its constituents. The inputs to the jet clustering algorithm can be stable simulated particles (*truth* jets), energy deposits in the calorimeter (*calorimeter* jets) or a combination of calorimeter and track information (*particle flow* jets). The reconstruction of calorimeter and particle flow jets is described in sections 5.6.1 and 5.6.2, respectively.

Additionally, the constituents of small-radius jets can be used as input to a new execution of the jet clustering algorithm with a larger radius parameter. These are referred to as *reclustered* jets. These are used extensively in $t\bar{t}H(H \to b\bar{b})$ analyses. They have the advantage of not requiring additional calibrations.

5.6.1 Calorimeter jets

Calorimeter jets are reconstructed from topo-clusters with energy measured at the EM scale. Jets are required to have $p_{\mathrm{T}} > 7$ GeV and be within $|\eta| < 2.5$.

The jet energy is calibrated to match those of truth jets [11, 139]. Different types of correction factors are applied sequentially, as indicated in Figure 5.1: origin correction, pileup corrections, jet energy and pseudorapidity corrections based on MC simulation, global sequential calibration, and *in-situ* corrections.

The origin correction recalculates the jet four-momentum per event to ensure that the direction of each topo-cluster points to the primary vertex instead of the geometrical center of the ATLAS detector. This procedure improves the angular resolution and results in a small improvement in the jet p_{T} response ($< 1\%$).

Pileup corrections are derived from MC simulation in two components: an area-based p_{T} density subtraction applied per event and a residual correction based on the number of reconstructed vertices per event, N_{PV}, and on the average number of interactions per bunch-crossing, μ, sensitive to out-of-time pileup, in bins of pseudorapidity and jet p_{T}. The pileup-corrected p_{T} is defined as:

$$p_{\mathrm{T}}^{\mathrm{corr}} = p_{\mathrm{T}}^{\mathrm{reco}} - \rho \times A - \alpha \times (N_{\mathrm{PV}} - 1) - \beta \times \mu, \tag{5.5}$$

where $p_{\mathrm{T}}^{\mathrm{reco}}$ is the jet p_{T} measured at the EM scale before any pileup corrections are applied, A is the jet area calculated using ghost association [134–136] and ρ is the median of the p_{T} density, calculated using positive-energy topo-clusters with $|\eta| < 2$, clustered with the k_t algorithm with $R = 0.4$, chosen due to its sensitivity to soft radiation. The residual p_{T} correction is assumed to have a linear dependence on N_{PV} and μ and it is calculated with respect to a chosen pileup condition. The values of the α and β coefficients are extracted from linear fits in bins of pseudorapidity and $p_{\mathrm{T}}^{\mathrm{truth}}$.

The absolute jet energy scale and η calibration corrects the reconstructed jet four-momentum to particle-level energy scale. Scale factors are derived based on the ratio between the energy of the reconstructed jet and the corresponding geometrically-matched truth jet, in bins of pseudorapidity and truth energy. A second correction is derived as the difference between the reconstructed and truth jet pseudorapidity to account for a bias due to poorly-instrumented calorimeter transition regions and differences in granularity.

The global sequential calibration is designed to reduce the dependence of the jet energy response on the flavor of the parton initiating the jet (quark or gluon). The correction is based on global properties of the jet. In particular, five observables are identified that improve the resolution of the jet energy scale through this procedure: the fractions of the jet energy measured in the first layer of the tile calorimeter and in the third layer of the EM LAr calorimeter; the number of tracks ghost-associated to the jet; the p_{T}-weighted average of the distance in the $\eta - \phi$ plane between the jet axis and all tracks ghost-associated to the jet; and the number of muon track segments ghost-associated to the jet. An independent correction factor is derived for each variable in bins of jet truth p_{T} and pseudorapidity based on the ratio between the reconstructed quantity and the corresponding truth quantity. The corrections are applied to the four-momentum of the jet in a sequential manner. The correlations between the variables are neglected.

As a final step in the jet energy scale calibration, *in-situ* corrections are derived based on data to correct for remaining data-to-MC differences. In the central region, these *in-situ* techniques exploit the momentum balance between a jet and a well measured reference object, a photon or a Z-boson. Jets in the forward region of the detector are calibrated using the central region as reference using dijet events, in a procedure referred to as η-intercalibration.

Jet quality criteria are applied to reject jets originating from beam-gas and beam-halo events, cosmic-ray muons or calorimeter noise backgrounds while keeping a high efficiency for jets produced in proton-proton collisions [140]. Two sets of criteria are defined with increasing background rejection (and decreasing efficiency): *Loose* and *Tight*. The *Loose* (*Tight*) selection provides an efficiency of selecting jets from proton-proton collisions above 99.5% (95%) for $p_{\mathrm{T}} > 20$ GeV. The discrimination between jets originating from background sources and proton-proton collisions is based on variables from three categories: signal pulse shape in the LAr calorimeters, energy ratios, and track-based variables.

5.6.2 Particle flow jets

The *particle flow* reconstruction algorithm [141] combines measurements from the inner detector and calorimeters to create particle flow objects that are then used as input to jet reconstruction. The main advantage of combining tracking and calorimeter information is to benefit from the superior momentum resolution of the tracking system for low-energy particles. The tracking system also has a better angular resolution and is able to reconstruct tracks with a minimum p_{T} of 400 MeV, whose corresponding energy deposits in the calorimeter are likely to not pass the noise thresholds required to seed topo-clusters. In turn, the calorimeters are able to reconstruct both charged and neutral particles, provide coverage in the forward region and, at high-energies, have a better energy resolution.

The basic working principle of particle flow reconstruction is to geometrically match tracks in the inner detector to topo-clusters in the calorimeters and remove overlaps between the momentum and energy measurements performed in these two subsystems. The average energy deposited by a particle with measured momentum in the tracker p^{trk} can be calculated as $\langle E_{\mathrm{dep}}\rangle = p^{\mathrm{trk}} \left\langle E^{\mathrm{clus}}_{\mathrm{ref}}/p^{\mathrm{trk}}_{\mathrm{ref}}\right\rangle$, where $E^{\mathrm{clus}}_{\mathrm{ref}}$ and $p^{\mathrm{trk}}_{\mathrm{ref}}$ are the energy and momentum associated with a reference particle. The expectation value $\left\langle E^{\mathrm{clus}}_{\mathrm{ref}}/p^{\mathrm{trk}}_{\mathrm{ref}}\right\rangle$ is determined using single-pion samples without pileup by summing the energies of topo-clusters within $\Delta R < 0.4$ of the track position as a function of the p_{T} and η of the track as well as of the calorimeter layer with the highest energy density (LHED). If $\langle E_{\mathrm{dep}}\rangle$ exceeds the total energy of the topo-clusters matched to a track, then all topo-clusters are removed. Otherwise, subtraction is performed cell-by-cell until the expected energy deposit is reached.

The inputs to jet reconstruction are the ensemble of positive energy topo-clusters surviving the energy subtraction with η and ϕ recalculated with respect to the primary vertex and the selected tracks that are matched to the primary vertex ($|z_0 \sin\theta| < 2$ mm). The calibration of particle flow jets follows closely the procedure used for standard calorimeter jets (described in section 5.6.1) and it is performed in the range $20 < p_{\mathrm{T}} < 1500$ GeV.

The relative jet energy resolution ranges from 0.25 (0.35) to 0.04 for particle flow (calorimeter) jets as a function of jet p_{T} [11]. Systematic uncertainties in the jet energy scale for central jets ($|\eta| < 1.2$) vary from 1% for a large range of high-p_{T} jets ($250 < p_{\mathrm{T}} < 2000$ GeV), to 5% at very low p_{T} (20 GeV)

Particle flow jet reconstruction is the default during Run 3. Analyses of Run 2 data can be rerun using jets reconstructed with the particle flow algorithm to benefit from the increased momentum resolution.

5.6.3 Missing transverse momentum

The missing transverse momentum, referred to as $E_{\mathrm{T}}^{\mathrm{miss}}$ or MET, is reconstructed as the negative vector sum of the energy of calibrated hard objects with an additional soft term reconstructed from detector signals not associated with any physics object, in particular tracks [142].

Electrons and muons are identified with the *Medium* WP and are required to have $p_{\mathrm{T}} > 10$ GeV. Photons are required to pass the *Tight* WP and must have $p_{\mathrm{T}} > 25$ GeV. Hadronically-decaying tau leptons are selected using the *Medium* WP with $p_{\mathrm{T}} > 20$ GeV. Standard calorimeter jets with $R = 0.4$ and $p_{\mathrm{T}} > 20$ GeV are used. They are fully calibrated and a pileup correction is also applied.

The soft term is constructed from tracks with $p_{\mathrm{T}} > 0.4$ GeV and passing basic quality requirements. Only tracks associated with the primary vertex through requirements on the longitudinal and transverse impact parameters are considered. The overlap between tracks and clusters associated with the previously reconstructed objects is removed. Tracks within $\Delta R < 0.05$ ($\Delta R < 0.2$) of an electron/photon (tau) cluster are removed. Tracks ghost-associated to jets are removed.

5.6.4 HLT reconstruction and identification

Jet reconstruction at the HLT [143] follows a very similar procedure to that used offline. Jets are reconstructed using the anti-k_t algorithm with a radius parameters of $R = 0.4$ or $R = 1.0$. The inputs are calorimeter topo-clusters reconstructed using information from all cells and calibrated by default at the EM scale, following a similar procedure to that adopted offline and described in section 5.6.1. By default, in jet calibration at the trigger, both pileup subtraction and jet response corrections are applied.

The reconstruction of jets at the HLT is fully configurable and highly flexible. Non-standard inputs or alternative calibration procedures can be used. For example, jets can be reconstructed using only cells from RoIs identified by the L1 jet trigger or local calibration weights can be applied to the clusters. Additionally, jet reconstruction can be run in two steps to produce reclustered jets.

Even with the good calorimeter resolution available for jet reconstruction at the HLT, the large rate of hadronic jet production and pileup contributions can lead to very large $E_{\mathrm{T}}^{\mathrm{miss}}$ trigger rates. Several $E_{\mathrm{T}}^{\mathrm{miss}}$ algorithms were thus deployed at HLT, using information from calorimeter cells, jets or topoclusters, to fulfill the requirements of multiple analyses and mitigate the pileup contribution.

The simplest $E_{\mathrm{T}}^{\mathrm{miss}}$ reconstruction algorithm uses the sum of the energy of all cells from the LAr and Tile calorimeters. The position and energy of the cells are used to calculate their momentum, in the massless particle approximation. Only cells above the electronic noise threshold are included ($|E_{\mathrm{cell}}| > 2\sigma_{\mathrm{cell}}$, where σ_{cell} is the expected energy-equivalent noise in that cell). Cells with $E_{\mathrm{cell}} < -5\sigma_{\mathrm{cell}}$ are removed. $E_{\mathrm{T}}^{\mathrm{miss}}$ can also be calculated from all the reconstructed small-R jets with $p_{\mathrm{T}} > 7$ GeV before calibration or from topo-clusters. For the latter method, a pileup suppression algorithm can be included. It combines topo-clusters into $\eta - \phi$ towers that approximately correspond to the area of a $R = 0.4$ jet. All towers with energy below 45 GeV are assumed to be pileup contributions and used to calculate the average pileup density. The pileup contribution to highly energetic towers is estimated through a least squares fit that constrains the pileup contributions to E_x and E_y to zero in the entire event; and then subtracted.

5.7 Flavour tagging

Identifying the flavor of the parton that created a jet, flavor tagging, is a crucial aspect of most ATLAS physics analyses. In particular, jets initiated by b-quarks can be tagged using b-tagging algorithms that exploit the long lifetime, high mass and high decay multiplicity of b-hadrons as well as the properties of the b-quark fragmentation [12]. The strategy adopted by ATLAS is two-staged: low-level algorithms reconstruct characteristic features of heavy-flavor jets and their outputs are then combined in multivariate classifiers to maximize performance.

5.7.1 Low-level taggers

The low-level algorithms can be grouped into three broad categories: exploiting the large impact parameters of tracks belonging to heavy-flavor jets, explicitly reconstructing displaced vertices or using information about the muons produced in heavy-flavor decays.

The simplest impact-parameter based (IP-based) algorithm, `IP2D`, uses the signed transverse impact parameter significance to construct a discriminant variable [144]. The `IP3D` algorithm extends this concept by using both the transverse and longitudinal impact parameters in a two-dimensional template to exploit correlations between them [144]. Both algorithms are based on a log-likelihood ratio discriminant that is computed as the sum of per-track contributions: $\sum_{i=1}^{N} \log\left(\frac{p_b}{p_u}\right)$, where N is the number of tracks in a given jet and p_b, p_u are the template probability density functions for the b- and light-jet hypothesis, respectively, obtained from reference MC histograms of the impact parameters.

The `IP3D` algorithm treats every track within a jet, thus ignoring correlations between their properties. These correlations can be particularly useful because in b-jets multiple particles usually emerge from the same secondary vertex. RNNs can be used to learn sequential dependencies between variables, as it is the case for tracks in a jet. This is the approach used by the `RNNIP` algorithm [145]. For each track, the transverse and longitudinal impact parameters, the fraction of transverse momentum carried by the track relative to the jet p_{T}, the angular distance between the track and the jet axis, and the log-likelihood ratios defined for the `IP2D` and `IP3D` algorithms are fed to a RNN that outputs the b-, c-, light- and τ-jet probabilities.

Two algorithms are employed for secondary vertex reconstruction: one reconstructs a single displaced vertex (`SV1`) [146], while the other performs a topological reconstruction of the vertex structure of heavy decays inside a jet (`JetFitter`) [147]. The former starts from all possible two-track vertices and removes tracks that are compatible with the decay of long-lived particles, photon conversion or hadronic interaction with the detector material. A secondary vertex is then reconstructed from the remaining tracks, with outliers iteratively removed from the fit. In the latter algorithm, a Kalman filter is used to find the approximate b-hadron flight path, in which the primary and secondary vertices lie. This allows to reconstruct secondary b- or c-hadron vertices even if only one track is associated to them.

The presence of muons in b-jets is enhanced with respect to c- or light-jets due to the sizable semileptonic decay branching ratio of b-hadrons, $BR(b \to \mu\nu X) \sim 11\%$, and c-hadrons produced in sequential b-hadron decays, $BR(b \to c \to \mu\nu X) \sim 10\%$. These muons have a sizable p_{T} and a large transverse momentum with respect to the jet axis ($p_{\mathrm{T}}^{\mathrm{rel}}$). They are labeled "soft" since their p_{T} is smaller than the typical p_{T} of leptons produced in electroweak boson decays. The `Soft Muon Tagger` algorithm exploits the properties of these muons [144]. The angular distance between the muon and the jet axis, the $p_{\mathrm{T}}^{\mathrm{rel}}$ and the muon tranverse impact parameter are combined with variables that quantify the quality of the muon track in a dedicated multivariate algorithm.

5.7.2 High-level taggers

Two high-level taggers are used to combine the outputs of the low-level taggers in order to maximize b-tagging performance: `MV2` based on a boosted decision tree (BDT) and `DL1r` based on a deep neural network (DNN) [144]. Both algorithms are trained to distinguish between b-, c- and light-jets. In order to cover the full p_{T} spectra, a hybrid training sample is used, using $t\bar{t}$ events to characterize the low p_{T} region and Z' events to cover the high p_{T} regime. The mixing of the samples works as follows: b-jets are taken from the $t\bar{t}$ sample if the corresponding b-hadron has $p_{\mathrm{T}} < 250$ GeV and from the Z' sample if the b-hadron has $p_{\mathrm{T}} > 250$ GeV. The same mixing strategy is used for c- and light-jets.

The standard version of the `MV2` algorithm is trained using as inputs the variables computed by the `IP2D`, `IP3D`, `SV1` and `JetFitter` and including the kinematic properties of the jets (p_{T} and η). The variant referred to as `MV2c10` is used in this thesis. The name originally indicated that a mixture of 90% light-flavor jets and 10% c-jets had been used in the training. The light versus c-jet rejection can be tuned by changing the fraction of c-jets used in the training. Given that most physics analyses are limited by c-jet rejection, the composition of the training sample has evolved to increase c-jet rejection while keeping similar light-jet rejection. Therefore, the c-jet fraction in the current training of `MV2c10` is set to 7%.

The `DL1` designation refers to a family of high-level taggers that consist of artificial neural networks with a multidimensional output corresponding to the probabilities for a jet to be b-, c- or light-flavored. Different variants are defined based on the input variables used in the training. The `DL1r` variant, used in this thesis, is trained using the input variables used for `MV2` and additionally includes c-tagging variables from `JetFitter` and the flavor probabilities provided by the `RNNIP` algorithm.

The performance of the low- and high-level b-tagging algorithms is shown in Figure 5.2 in terms of the light-jet rejection (5.2a) and c-jet rejection (5.2b) versus b-tagging efficiency.

5.7.3 Working points and calibration

The heavy-flavor tagging algorithms are trained and optimized using MC simulation. Their performance in data usually deviates from that obtained in MC due to imperfect modelling of detector effects and of physics processes. Thus, the probability of tagging a true b-, c- or light-jet as such needs to be measured in collision data. The differences in performance are accounted for in the form of scale factors measured independently for all three jet flavors and calculated as the ratio between

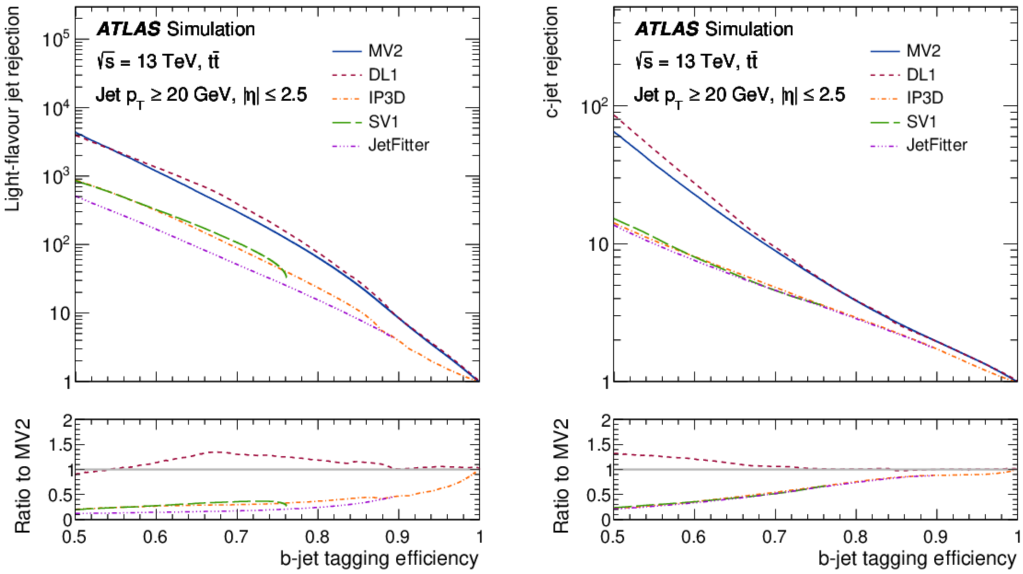

(a) **(b)**

Figure 5.2: Light (5.2a) and c-jet (5.2b) rejections versus the b-jet tagging efficiency for the `IP3D`, `SV1`, `JetFitter`, `MV2` and `DL1` algorithms, evaluated on $t\bar{t}$ events [12].

ϵ_b	MV2				DL1			
	Selection	Rejection			Selection	Rejection		
		c-jet	τ-jet	Light-flavour jet		c-jet	τ-jet	Light-flavour jet
60%	> 0.94	23	140	1200	> 2.74	27	220	1300
70%	> 0.83	8.9	36	300	> 2.02	9.4	43	390
77%	> 0.64	4.9	15	110	> 1.45	4.9	14	130
85%	> 0.11	2.7	6.1	25	> 0.46	2.6	3.9	29

Figure 5.3: Rejection factors of c-, τ- and light-jets corresponding to the different b-tagging single-cut WPs for the MV2 and DL1 b-tagging algorithms, evaluated on $t\bar{t}$ events [12].

the efficiencies in data and in MC. These scale factors are then combined into an event-level b-tagging weight that is applied to MC in the physics analyses.

The calibration is performed in four b-tagging WPs defined by the b-jet efficiency: 60%, 70%, 77% and 85%. Each WP is also characterized by the c- and light-jet rejection, defined as the inverse of the c- and light-jet efficiencies. These are shown in Table 5.3. WPs with a lower b-tagging efficiency are referred to as tighter due to the associated higher c- and light-jet rejection that leads to a higher signal purity. Five pseudo-continuous WPs are also defined in bins of the b-tagging discriminant delimited by the selections used to define the single-cut WPs described previously and the trivial 100% and 0%. Each jet is assigned a b-tagging score based on the tightest WP that it satisfies. The pseudo-continuous calibration has the advantage of including additional information: identifying a b-jet is no longer a binary decision; instead the jets are attributed a probability of being tagged as such.

The b-tagging efficiency is calibrated using dileptonic $t\bar{t}$ events, selected by requiring exactly two lepton candidates and two jets [148]. Events are labeled based on the generator-level flavor of the two jets: two b- or light-jets (bb and ll, respectively) or one b-jet and one non-b-jet (bl or lb, where the first jet corresponds to the one with the highest p_{T}). Events are categorized based on the p_{T} of the leading and subleading jets. In each p_{T} bin, signal and control regions are defined to be enriched in bb and bl or ll, respectively. The region definition is based on the invariant mass between the pairs of leptons and jets that minimise $(m^2_{j_1,l_i} + m^2_{j_2,l_j})$, where $j_1(j_2)$ is the leading (subleading) jet and $l_{i,j}$ are the two leptons. This metric penalizes asymmetric decays which are unlikely for the $t\bar{t}$ system. The events in the signal region are then classified according to the b-tagging discriminant of the two jets. A binned maximum log-likelihood fit is performed in all regions simultaneously to extract the b-jet tagging probabilities and the flavor compositions.

The efficiency to identify true c-jets as b-jets, referred to as c-mistag rate, is calibrated using semileptonic $t\bar{t}$ events, selected by requiring exactly one trigger-matched lepton, exactly four jets, two of which are b-tagged at 77% WP using the MV2c10 or DL1r algorithm [149]. Events are additionally required to have $E_{\mathrm{T}}^{\mathrm{miss}} > 20$ GeV, assumed to originate from the neutrino produced by the leptonically-decaying W-boson. A kinematic likelihood fit is performed to assign jets to the partons originating from the $t\bar{t}$ and W-boson decays. Only events with a large value of the likelihood discriminant and for which there is zero or one b-tag in the pair of jets originating from the W-boson decay are considered. The c-jet efficiency is extracted from a maximum likelihood fit in three p_{T} bins of the leading and subleading jets: $[25, 40]$ GeV, $[40, 65]$ GeV and $[65, 140]$ GeV.

For flavor taggers reaching a very high rejection of light-jets, as it is the case for the taggers currently used in ATLAS, the fraction of light-jets passing the WPs is too low to allow for an estimation of the light-jet mistag rate in data. Therefore, this is calibrated using the flipped tagger method [150]. The impact parameters of tracks associated with light-flavor jets have values consistent with zero within the IP resolution, leading to an approximately symmetric distribution. The flipped tagger method assumes that the probability for a light-jet to be mistagged remains almost the same when inverting the sign of the track impact parameters and displaced vertices. The low-level algorithms are retrained after flipping the sign of the track impact parameters and used as input to retrain the high-level taggers. The tag rate of light-jets measured in data from the flipped taggers is considered to be a good approximation for the light-jet mistag rate of the standard algorithms. Correction factors derived from MC simulation are additionally applied to account for the presence of true b- and c-jets in the sample and true displaced vertices inside light-jets.

The light-jet mistag rate is measured following the procedure described above in data events selected by requiring at least one reconstructed vertex with at least two tracks associated to it and at least two jets. A good angular separation between the jets ($\Delta\phi > 2$ rad) is also required to reject events with two jets originating from a gluon splitting. Events are split based on the pseudorapidity and p_{T} of the leading jet. Two η bins, corresponding to the central and forward regions ($|\eta| < 1.2$ and $1.2 < |\eta| < 2.5$), and eight p_{T} bins (ranging from 20 GeV to 3000 GeV) are considered. The calibration is performed in each bin.

5.7.4 HLT reconstruction and identification

For the b-jet HLT algorithms, $R = 0.4$ jets are reconstructed following the offline procedure. Two sets of jets are used in the b-jet trigger: as a first step, all jets with $E_{\mathrm{T}} > 30$ GeV are used to find the primary vertex of the event; in the second step, RoIs are defined around the jets identified in the previous step.

In events with a lot of hadronic activity, multiple overlapping RoIs may be identified by the L1 jet trigger. Individually processing these RoIs leads to the same regions of the detector being processed multiple times, which is not CPU-efficient. Additionally, it can lead to a double counting of the tracks in the overlapping regions and thus to a bias in primary-vertex finding. The alternative approach followed from 2016 onwards is to group overlapping RoIs into a 'super-RoI' that covers the full z range of the detector and is used to perform primary-vertex finding. All jets with $E_{\mathrm{T}} > 30$ GeV and $|\eta| < 2.5$ are used to create the 'super-RoI'. Vertex-finding proceeds through the histogramming algorithm, described in section 5.1.

For every jet within the super-RoI, a smaller RoI is constructed around it, with half-width in η and ϕ of 0.4, such that the whole jet with $R = 0.4$ is contained by it. The width in the z-direction is constrained to $20(10)$ mm around the primary vertex during 2016 (2017/2018). The apex of the RoI is centered on the primary-vertex. Fast and precision tracking algorithms are executed in these RoIs, using all tracks with $p_{\mathrm{T}} > 1$ GeV. The tracks in the RoI, together with information about the jet direction and primary vertex, are used as input to b-tagging algorithms. During Run 2, the MV2 offline algorithm was used online.

6

Trigger studies for Run 3 and HL-LHC

Contents

The trigger system is a crucial piece of the ATLAS data-taking machinery. It needs to work reliably to ensure that high-quality data is collected for physics analyses. As the trigger system evolves throughout Run 3 and for HL-LHC, innovative trigger algorithms, capable of providing early background rejection are key to allow for the exploration of very low cross-section processes in a very high-pileup environment.

This chapter covers the trigger-related work developed throughout this thesis. HLT algorithms targeting the central exclusive production of pairs of jets have been developed and will be deployed during Run 3. These studies are detailed in section 6.1, that includes a brief introduction to the phenomenology of central exclusive production processes. The design and implementation of the triggers are discussed in sections 6.1.2 and 6.1.3, respectively. A preliminary estimation of the trigger rates and signal efficiency is presented in section 6.1.4.

As input to the development of the HL-LHC ATLAS trigger system architecture, the performance of a first level hardware trigger was studied in final states with two muons, using an emulation of the hardware system. This study is detailed in section 6.2 and follows reference [14].

6.1 Design and implementation of dijet central exclusive production trigger for Run 3

6.1.1 Motivation

Central Exclusive Production (CEP) is a special class among diffractive processes in which both protons remain intact after the collision. All the energy that is available due to the colourless exchange between the protons is used to produce the central system. These processes provide access to generalized PDFs and important information on QCD aspects of vacuum quantum number exchange. At the highest luminosities delivered by the LHC, it may become a discovery channel for BSM particles that couple to gluons and allow for the study of CEP of Higgs bosons. On the one hand, if the protons are scattered at very small angles with respect to the beam pipe then the central system is produced with $J_z = 0$, i.e. to a good approximation, it is a CP-even state. On the other hand, the mass of the central system can be very precisely determined from the protons' energy loss (ξ_1 and ξ_2) using the missing mass method, $M^2 = s\xi_1\xi_2$, which is independent of the decay mode.

In diffractive processes, the centrally produced system can be reconstructed in the central ATLAS detector. The intact protons continue to travel along the beam pipe and can be identified by dedicated forward detectors, the AFP, placed a few hundred meters away from the interaction point. A proton tag in the AFP stations on both sides of the central ATLAS detector is the key feature of a CEP process. In the CEP of a pair of jets, the central system is composed only of two jets, without any additional radiation produced in the same proton interaction. The leading order Feynman diagram for the CEP of a dijet pair is depicted in Figure 6.1.

Measuring these processes, especially those containing jets, is challenging. At a center-of-mass energy of $\sqrt{s} = 14$ TeV, the dijet CEP cross-section with a leading jet with $p_{\mathrm{T}} > 150$ GeV is 0.5 nb [151]. This cross-section is small enough that it cannot be measured in dedicated runs with low

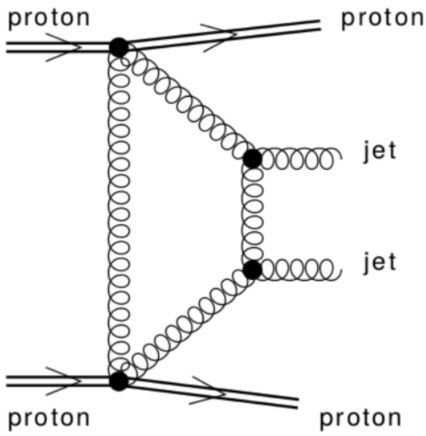

Figure 6.1: Feynman diagram of central exclusive production of a pair of jets.

pileup because the accumulated luminosity would not suffice. Therefore, its measurement needs to be performed in a high-pileup environment. The main background originates from pileup interactions in which at least one of the protons remains intact and can reach one of the AFP stations. Considering the geometric acceptance of AFP and the probability of having an accidental coincidence in both AFP stations, the cross-section for this background is of the order of 0.5 mb [151], three orders of magnitude larger than the targeted signal.

To have any chance of measuring this process, early background rejection in the trigger is essential. Given the large dijet production cross section of ~ 100 nb at $\sqrt{s} = 13$ TeV [152], single- or dijet triggers do not provide enough background rejection. One must explore the triggering capabilities of the AFP detectors, both at L1 and HLT. This is crucial to fully exploit the rich diffractive physics program that is accessible during Run 3 of the LHC.

The design and implementation of a dedicated trigger for CEP of a pair of jets is the first step towards this goal and opens the door for future triggers targeting other CEP signatures.

6.1.2 Design of the trigger

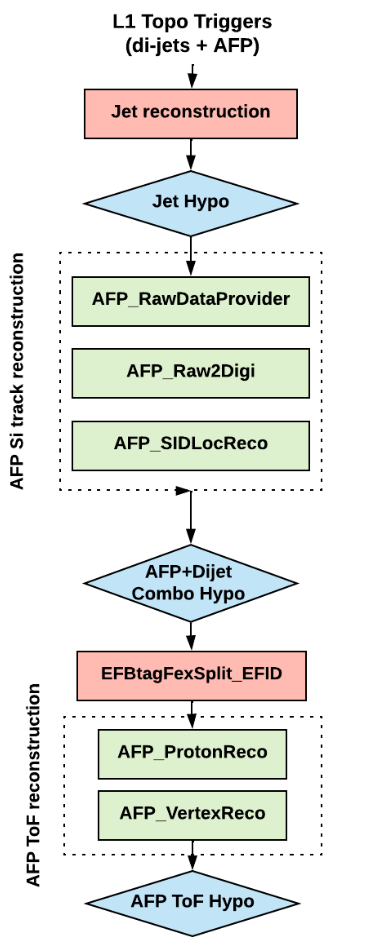

Figure 6.2: AFP dijet trigger chain.

The key features of CEP processes that drive the trigger strategy are the proton tags in both AFP stations and correlations between the kinematic properties of the central system and of the diffracted protons. The implementation of the trigger targeting dijet CEP is represented schematically in Figure 6.2 and described in what follows.

Each AFP station contains a silicon tracking detector and a ToF detector, as described in section 4.2. In an event with two forward protons, it is expected that there is at least one reconstructed track in each AFP station. Additionally, in signal events, the protons are expected to originate from the same interaction vertex and therefore to reach the AFP stations within a pre-defined time-window. Both of these characteristics can be exploited at the L1 trigger, using the trigger capabilities of the AFP silicon and ToF detectors. The correlation between the central system and the forward protons can also be exploited at the L1 trigger using the L1Topo board to compute the expected protons' energy loss based on the kinematic properties of a dijet pair. Another option is to require a pair of jets with a given momentum. This is also possible at the L1 trigger and it is necessary to implement the topological algorithm described previously. However, due to momentum balance considerations, the rate reduction achieved with dijet and a single-jet trigger requirements is very similar. Therefore, requiring only a single jet is also a valid possibility.

At HLT, more complex algorithms can be used. For Run 3, it is recommended to use the offline reconstruction and selection algorithms in the trigger. This is the procedure followed here. It allows to reuse existing code and facilitates its validation and maintenance. More importantly, it reduces the difference in efficiency between the online and offline selections. The jets are reconstructed with the default radius parameter of $R = 0.4$ and using the particle flow algorithm. Each event is required to have at least two jets with a p_{T} above a configurable threshold. The reconstruction of tracks in the AFP silicon detectors follows. It proceeds by clustering the hits in the individual pixel modules and using them to reconstruct tracks based on a Kalman filter. Once the AFP tracks have been reconstructed they are used together with the jets to exploit the correlations between the central and forward detectors.

The kinematic properties of the dijet pair, namely the invariant mass, M_{jj}, and pseudorapidity, η_{jj}, are used to calculate the relative energy loss of each proton, ξ_{j_1,j_2}, defined on the left of equation 6.1. Based on the values of the relative energy loss, it is possible to estimate the energy of the outgoing protons at the interaction point, as shown on the right of equation 6.1. An analytical transport function is then used to estimate the protons' position in the AFP stations. This position is compared with the x and y coordinates of the tracks reconstructed in the same station. The closest track to each proton is found through an iterative procedure. Events are accepted if the geometric distance between the extrapolated proton position and the closest track is within a configurable value.

$$\xi_{j_1,j_2} = \frac{M_{jj}}{\sqrt{s}} \cdot \exp(\pm\eta_{jj}) \qquad \rightarrow \qquad E_{p_1,p_2} = \frac{\sqrt{s}}{2} \cdot (1 - \xi_{j_1,j_2}). \tag{6.1}$$

The following step in the trigger chain exploits the timing capabilities of the AFP ToF detectors. Based on the relative difference between the time of arrival of the protons to each AFP ToF detector, Δt, the position of the vertex from where the protons originate can be calculated as $z_{\text{AFP}} = (1/2) \times \Delta t \times c$. The proton position along the z-axis is then compared with the position of the primary vertex of the event (reconstructed using inner detector tracks). For reference, a time resolution of 10 ps corresponds to a z resolution of 2.1 mm. The difference between the z-coordinates of these two vertices is required to be smaller than a configurable value (of the order of 10 mm) to ensure that the diffracted protons originate from the hard scattering. The development and implementation of the algorithms related to the ToF is not a part of this work and therefore it is not described further.

With the trigger design complete, it is necessary to define the values for the jet p_{T} thresholds and of the allowed geometric distance between the extrapolated protons and the closest tracks. These depend on the beam properties at the interaction point, the detector geometry and the distance between the detector edge and the beam center, which limit the acceptance of the AFP detector. The minimal reachable value of the protons' energy loss during Run 3 is $\xi^{\text{min}} = \xi_1^{\text{min}} = \xi_2^{\text{min}} \sim 0.015 - 0.02$. Considering $\xi^{\text{min}} = 0.02$, the mass of the central system, $M_X = \sqrt{s \cdot \xi_1 \cdot \xi_2}$, is therefore limited to approximately $M_X > 260$ GeV. When the central system is composed of only two objects, each one of them is expected to carry approximately half of this energy, which corresponds to $p_{\text{T}} \gtrsim 130$ GeV. This is the value to be taken into account by any offline analysis and determines the p_{T} thresholds that should be used in the trigger.

In the baseline trigger design, the maximum allowed difference between the x and y coordinates of the extrapolated protons and the closest tracks is set to 2.5 mm. The absolute distance in the $x - y$ plane is required to be below 2 mm. The matching requirements are loose to avoid compromising the trigger efficiency while the algorithm is under validation.

6.1.3 Implementation

Although the trigger follows the strategy presented in the previous section, its specific implementation depends on additional factors. At L1, the number of allowed algorithms is limited by the number of inputs to the CTP. Therefore, at the beginning of Run 3, the topological algorithm that would estimate the protons' energy loss based on the momentum of a pair of jets could not be included. The algorithm that requires one hit in each of the AFP stations exists and can be readily used. It is referred to as `L1_AFP_A_AND_C`, indicating that there is one electronic signal in the silicon stations on side A and another on side C. At the time of writing of this thesis, the ToF detectors are installed and have been validated in standalone operation. Their efficiency was found to be lower than expected in 2023 data. Additionally, their ability to provide L1 accept trigger signals within the ATLAS TDAQ system is still being validated. For these reasons, they are not used in the trigger implementation proposed here.

In addition to requiring hits in the AFP stations, requirements on the p_{T} of the leading jet can further reduce the L1 rate. However, in the context of this work, L1 items based on jets are mostly useful to seed triggers that can be used as reference when calculating the efficiency of the triggers dedicated to the measurement of CEP of jets. Figure 6.3a shows the efficiency of a set of L1 triggers in 2015 and 2016 data as a function of the offline p_{T} of the most energetic jet. The equivalent plots from Run 3 are not yet public but they show similar features. Therefore, the plots from Run 2 will be used to guide the discussion that follows. The efficiencies are calculated with respect to reference triggers which are indicated in brackets in the legend. The jet p_{T} threshold indicated in the trigger name corresponds to the mid-point of the curve. Based on this figure, the L1 item with the highest p_{T} threshold that is fully efficient for an offline p_{T} of 130 GeV is `L1_J50`. Therefore, this L1 threshold is considered as the baseline.

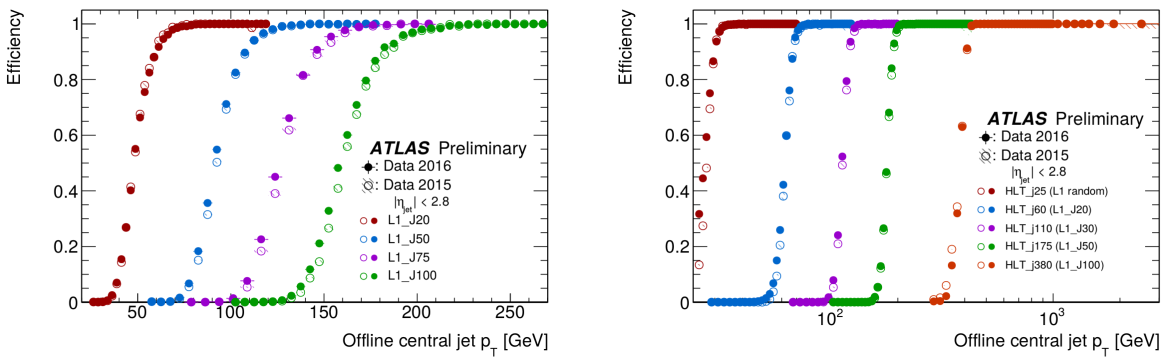

(a) (b)

Figure 6.3: Efficiency of single jet L1 legacy (6.3a) and HLT (6.3b) trigger selections in the central region. The efficiency is computed using the bootstrap method with respect to events taken by an independent trigger, shown in brackets, that is 100% efficient in the relevant region [13].

Given the available options described above, the most suitable L1 item is `L1_AFP_A_AND_C_J50`. As mentioned before, the nomenclature indicates that this trigger requires signals in both AFP silicon tracking detectors as well as a reconstructed jet with $p_{\mathrm{T}} > 50$ GeV at L1. Unfortunately, the simulation of the AFP L1 algorithms does not exist and therefore the trigger rates, discussed in the following section, are estimated for triggers seeded only by L1 jet items. It is clear that this is a conservative estimate because once the coincidence between AFP stations is required at L1, the rate will be lower. The exact rate reduction factor will depend on the pileup conditions and detector performance.

At the HLT, there are less constraints because the trigger implementation is done purely in software. For Run 3, the ATLAS central software framework, ATHENAMT, works in multi-threaded mode and it schedules trigger algorithms following a pre-specified order once their required inputs become available. Reconstruction algorithms process detector data to extract features and hypothesis algorithms test selection criteria. These are represented by rectangles and diamond shapes in Figure 6.2, respectively. Subsequent combinatorial hypothesis algorithms allow for topological selections to be performed using multiple sets of candidate physics objects. This is the case of the algorithm combining jets and AFP tracks. The order in which the algorithms should be executed, as well as the input and output objects, are defined via configuration files.

Following a similar reasoning as for L1, the adequate HLT jet p_{T} threshold can be determined based on the trigger efficiency curves shown in Figure 6.3b. Most triggers become fully efficient approximately 20 GeV after the point where the efficiency departs from zero. For example, the efficiency of `HLT_j110` becomes non-zero for $p_{\mathrm{T}} \sim 100$ GeV and reaches 100% for p_{T} between 110 and 120 GeV. Assuming that a similar behavior is verified for `HLT_j120`, this trigger is suitable to select events to be used in an offline analysis for which the minimum jet p_{T} threshold is $\gtrsim 130$ GeV.

Based on the available options for L1 and HLT algorithms discussed thus far, the baseline proposal for a trigger combining AFP tracks with jets measured in the central ATLAS detector is `HLT_2j120_mb_afprec_afpdijet_L1AFP_A_AND_C_J50`. As mentioned previously, this nomenclature encodes information about which trigger algorithms are run and in which order. Everything after the `L1` word indicates the L1 trigger algorithms. The first part of the trigger chain name, i.e., the words following `HLT`, refer to the HLT trigger algorithms. In general, each word, separated by an underscore, configures an algorithm. Their order also corresponds to the order in which the algorithms are run. The trigger starts by requiring at least two HLT jets with $p_{\mathrm{T}} > 120$ GeV (`2j120`), followed by the AFP track reconstruction (`afprec`). The jets and AFP tracks are then combined (`afpdijet`). Simply changing the values of the thresholds in the trigger naming changes the values of the selection cuts of the corresponding algorithms. Triggers with higher L1 and HLT thresholds have also been studied to understand how much the rate can be reduced.

6.1.4 Validation and performance

One of the first steps in the validation of the trigger implementation is to guarantee that the AFP silicon tracks reconstructed at the HLT match those reconstructed offline. Since in both cases the tracks are reconstructed using the same algorithm and the same input data, any possible differences should be due to different configurations of the algorithm online and offline. For example, the relative alignment of the multiple silicon planes within a given station might differ between online and offline since the most up-to-date constants are not always available during data-taking.

In principle this study is straightforward to perform. However, a difficulty arises due to particularities of the ATLAS data acquisition and reconstruction workflow. In order to obtain data files with information about the AFP tracks reconstructed at the HLT, it is necessary that there are triggers enabled that require the readout of the AFP detector. Moreover, the triggers must configure the track reconstruction in the AFP silicon detectors. These triggers are usually enabled in low-pileup runs. However, the triggers under development target a high-pileup environment and therefore using low-pileup data for validation is not ideal. In the high-pileup runs performed up to now, AFP triggers are used only for calibration of the detector and do not configure the track reconstruction in the silicon tracks. This means that data files with AFP tracks are not readily available for high-pileup runs.

Despite the limitations discussed in the previous paragraph, data from a low-pileup run is used to validate the AFP track reconstruction at the HLT. Data from run 427929 is used. For each event, every offline track is matched to the closest trigger track. The difference between the x- and y-coordinates of the online and offline tracks is shown in Figures 6.4a and 6.4b, respectively. Tracks from stations A and C are plotted together. For most tracks, the difference between the online and offline coordinates is well below 0.1 mm.

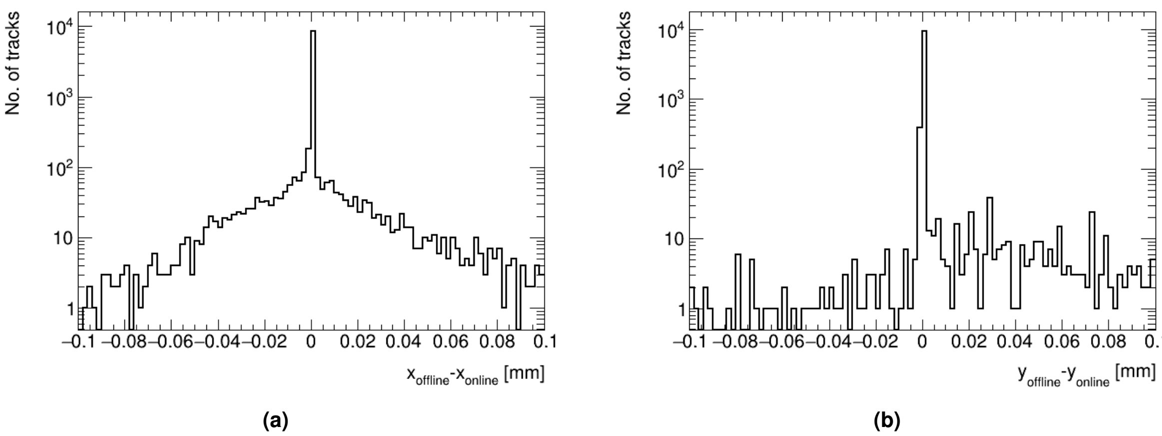

Figure 6.4: Difference in the x- (6.4a) and y-coordinates (6.4b) between the AFP offline-reconstructed tracks and the closest HLT track. Data a specific luminosity block from run 427929 is used.

In CEP, the diffracted protons continue to travel in opposite directions along the beam pipe. Due to the existence of magnets between the ATLAS interaction point and the AFP stations, they are deflected in the $x-y$ plane. The deflection in the x-direction (towards the outside of the LHC ring) and $(-y)$-direction (towards the LHC floor) increases with decreasing proton energy, i.e., with increasing proton relative energy loss [151]. If the beam properties are well known, this deflection can be parameterized as a function of the proton's energy and initial position and momentum.

It is clear that a reliable parameterization of the proton's trajectories between the interaction point and the AFP stations is a crucial component of the trigger algorithm. The coordinates of the tracks reconstructed in the AFP stations are compared with the proton's coordinates predicted by the parameterized transport function. A dedicated parameterization for Run 3, updated with the center-of-mass energy of 13.6 TeV and the most recent beamspot and beam crossing parameters, does not exist. Therefore, the Run 2 parameterization is currently used in the combinatorial algorithm.

The default method to validate the implementation of new trigger algorithms is to re-run the HLT software over raw detector data collected during dedicated runs and with a specially tailored trigger menu, referred to as an enhanced bias dataset. Ideally, the number of events passing a given trigger chain (trigger rate) could be obtained by running the corresponding algorithms over a sample of data collected with zero trigger bias (for example, by randomly triggering on events). However, most processes of interest have cross-sections much smaller than the total inelastic cross-section, meaning that a prohibitively large data sample would be required. Therefore, the enhanced bias dataset is designed to be richer in high-p_{T} events and collected using a variety of L1 triggers covering all signatures and p_{T} ranges. For each event, a weight is then calculated to correct for the prescales applied during data-taking and recover the energy spectrum of a zero bias sample [153]. A prescale defines which fraction of the events is kept, out of all the events that would have passed a given trigger.

The procedure of rerunning the HLT software over raw detector data is referred to as HLT reprocessing. It allows to estimate the rate and thus define prescales based on the available bandwidth and rate limitations of the system. The HLT reprocessing procedure is implemented within the `TrigCost` framework [154]. The HLT reprocessing of data is also useful to understand the distribution of the backgrounds in key variables for the various triggers.

The combinatorial algorithm using information from the jets and from the AFP tracks is validated using a data HLT reprocessing of run 440499, consisting of proton-proton collision data collected during 2022 at a center-of-mass energy of 13.6 TeV. The plots and rate estimates discussed in what follows are based on this reprocessing.

Figures 6.7a and 6.7b show the predicted x and y protons' positions on the AFP near station on side C. In the algorithm, these coordinates are compared with the AFP track x- and y- coordinates shown in Figure 6.6a and 6.6b, respectively. For x, both the predicted proton coordinate and the reconstructed track coordinate have values below zero and shapes that are comparable. This is not the case for the y-coordinate. The values of y of the reconstructed tracks are always above zero while the predicted proton's y positions are below zero. In this scenario, the difference between these two coordinates leads to a distribution that is not centered around zero, as shown in Figure 6.7b. The equivalent distribution for the difference between the x-coordinates is shown in Figure 6.7a and it is centered around zero, as expected.

From these plots, and from private discussions with the experts involved in deriving the proton transport functions, it is concluded that the prediction of the proton's y coordinate is not behaving as expected and therefore cannot be used in the trigger. Conversely, the parameterization in the x-direction seems to be robust enough and comparable with data. While a new parameterization does not become available, it is decided to configure the algorithm to require only the matching in the x-coordinate. In practice, this is done by setting the threshold for the y-coordinate matching to a very large value.

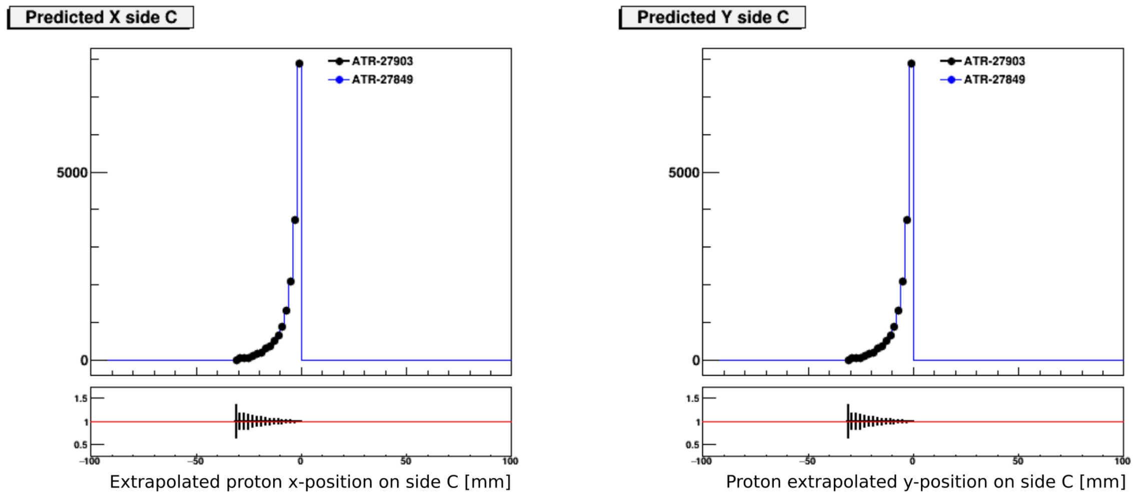

(a) (b)

Figure 6.5: Predicted x- (6.5a) and y-coordinates (6.5b) of the protons on the AFP station on side C. These plots are based on the parameterization used during Run 2.

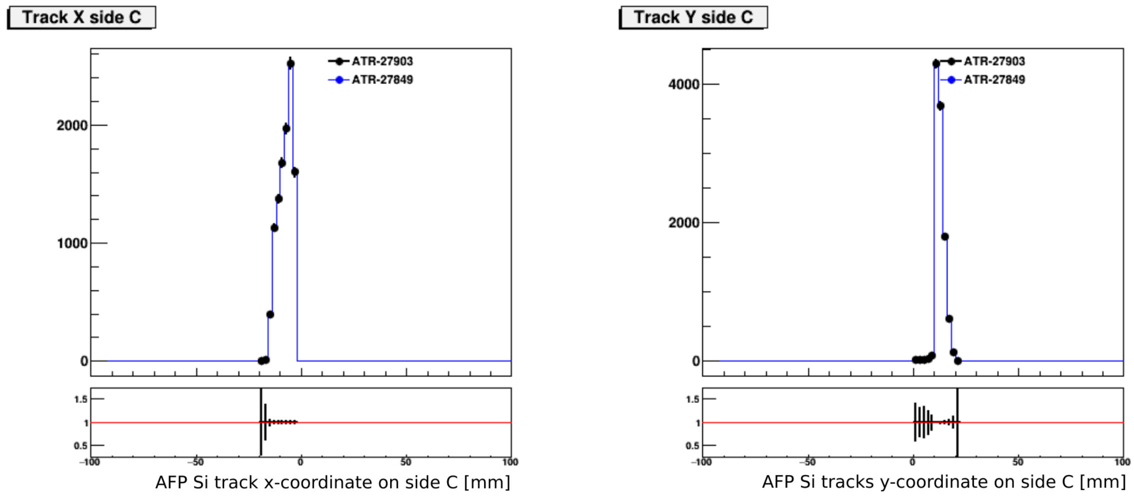

(a) (b)

Figure 6.6: x- (6.6a) and y-coordinates (6.6b) of the tracks reconstructed in the AFP silicon detectors on side C at the HLT.

This solution is not ideal because it almost certainly leads to a decrease in background rejection with respect to the baseline trigger implementation. However, it leads to a functional algorithm that allows to estimate the background rejection and signal efficiency of the trigger. This is a necessary step before enabling these triggers during online data-taking.

Another thing that could contribute to a mismatch between the coordinates of the reconstructed tracks and of the extrapolated protons is the lack of alignment between the central ATLAS detector

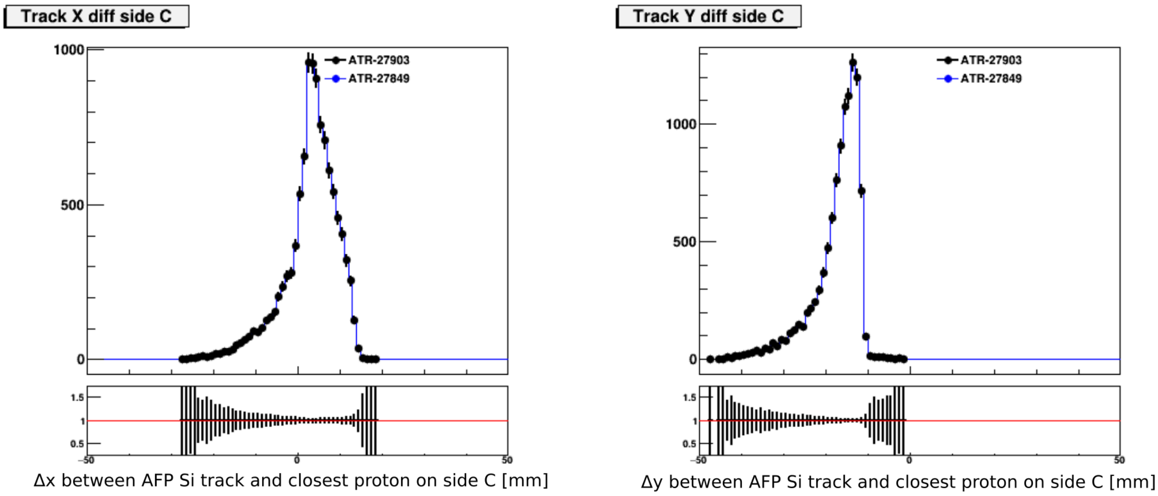

(a) **(b)**

Figure 6.7: Difference in x- (6.7a) and y-coordinates (6.7b) between the predicted proton coordinates and the reconstructed track coordinates on the AFP station on side C.

Trigger chain	Estimated rate and error [Hz]
`HLT_2j175_mb_afprec_afpdijet_L1J100`	9 ± 1
`HLT_2j140_mb_afprec_afpdijet_L1J50`	23 ± 2
`HLT_2j120_mb_afprec_afpdijet_L1J100`	24 ± 2
`HLT_2j130_mb_afprec_afpdijet_L1J50`	28 ± 3
`HLT_2j120_mb_afprec_afpdijet_L1J75`	33 ± 3
`HLT_2j120_mb_afprec_afpdijet_L1J50`	48 ± 15

Table 6.1: Estimated rates for the trigger chains combining AFP tracks and a pair of jets for an instantaneous luminosity of $\mathcal{L} = 2.0 \times 10^{34}$ cm^{-2}s^{-1}.

and the AFP stations. A possible solution that could be implemented on a longer time scale would be to use the first few luminosity blocks of each run to calculate the average values of the x- and y-coordinates of the AFP tracks, and use them as an offset in the combinatorial algorithm such that they could be directly compared with the position predicted by the parameterization.

Trigger chains with different L1 and HLT jet p_{T} thresholds were tested. They all use the baseline threshold for the matching in x between the predicted proton position and the closest AFP track: $\Delta x < 2.5$ mm. The total rate of each chain and corresponding errors are displayed in Table 6.1.

Considering a minimum offline jet p_{T} of 130 GeV, as discussed in section 6.1, the last trigger chain in Table 6.1 (`HLT_2j120_mb_afprec_afpdijet_L1J50`) would be the preferred one. However, the rate is too high to be able to run it without a prescale at the maximum instantaneous luminosity of $\mathcal{L} = 2.0 \times 10^{34}$ cm^{-2}s^{-1}. Additionally, the rate varies linearly with the instantaneous luminosity, as expressed by Equation 4.1 and, for a typical LHC run, the luminosity usually does not drop below $\mathcal{L} = 1.0 \times 10^{34}$ cm^{-2}s^{-1}, for which the rate would remain too high. Therefore, even at the end of a fill, enabling these chains unprescaled does not seem feasible. This is far from the ideal scenario because it does not maximize the collected integrated luminosity, but with the current system these limitations are hard to circumvent.

Trigger chain	Estimated efficiency [%]
HLT_2j140_mb_afprec_afpdijet_L1J50	63 ± 25
HLT_2j130_mb_afprec_afpdijet_L1J50	75 ± 29
HLT_2j120_mb_afprec_afpdijet_L1J50	81 ± 30

Table 6.2: Efficiency of triggers with HLT jet p_{T} thresholds 120, 130 and 140 GeV, calculated with respect to $gg \to jj$ events with at least two offline jets with $p_{\mathrm{T}} > 130$ GeV and at least one reconstructed proton in each AFP stations. The uncertainties are statistical only.

To estimate the signal efficiency, a MC sample of central exclusive production of jets produced through gluon-gluon fusion ($gg \to jj$) is used. The minimum p_{T} of the jets at generator level is 70 GeV, which is not the most suitable value given the large jet p_{T} that is of interest. The sample includes full detector simulation. The total number of events available in the reconstructed sample is 44×10^3. The efficiency is usually calculated with respect to the events that would be selected by an offline analysis. Therefore, simple cuts similar to those applied in a reference offline analysis are used. Events are required to have at least two offline-reconstructed jets with $p_{\mathrm{T}} > 130$ GeV and at least one offline-reconstructed proton in each AFP station. After applying these cuts, only 16 events from this sample survive. Nonetheless, given the unavailability of additional samples in a suitable format, this sample is used to provide a rough estimate of the signal efficiency. The signal efficiencies for trigger chains with HLT jet p_{T} thresholds of 120, 130 and 140 GeV are presented in Table 6.2.

It is clear from Table 6.1 that increasing the jet p_{T} threshold both at L1 and HLT is an effective way of reducing the rate. Reducing the HLT jet p_{T} threshold from 120 to 140 GeV, while keeping the remaining algorithms unchanged, allows to reduce the rate from 48 to 23 Hz, which corresponds to a reduction around 50%. The corresponding signal efficiency decreases from 81% to 63% (Table 6.2), corresponding to a decrease of 23%.

Another alternative that could be explored to reduce the rate is to tighten the geometric matching requirements between the protons and tracks. Preliminary estimates indicate that this strategy, although effective in reducing the rate, leads to a much larger reduction in the signal efficiency with respect to increasing the jet p_{T} threshold. However, it should be noted that this study strongly relies on the alignment between the central ATLAS detector and the AFP stations. As mentioned before, this is not included by default and therefore it could impact the results. This option should thus be further explored in the future.

Therefore, the baseline strategy for the deployment of the triggers targeting the CEP of jet pairs is to add multiple trigger chains to the menu, with different jet p_{T} thresholds. As the luminosity decreases, the prescales can be decreased and chains with lower jet p_{T} thresholds can be activated. As a first stage, having these chains enabled during data-taking will also allow to perform more detailed performance studies and possibly further tune the HLT combinatorial algorithm.

6.2 Performance studies of a hardware tracking trigger system for HL-LHC

An evolution to the baseline TDAQ architecture planned for the Phase-II upgrades of the ATLAS experiment (described in section 4.2.6.C) was proposed in the TDAQ Technical Design Report (TDAQ TDR) [123]. It includes a Level-0 (L0) system that reduces the event rate from 40 MHz to 4 MHz and a second hardware-trigger level (Level-1, L1) that further reduces the rate to less than 1 MHz using tracking information. The main component of the L1 system is the Hardware Tracking Trigger (HTT), a pure hardware system capable of performing track reconstruction with low latency, referred to as `L1Track`. This system would provide rudimentary primary vertex identification and allow for selections based on the impact parameters of tracks.

The `L1Track` reconstruction strategy is performed in two steps. A first track-finding step identifies low resolution patterns, which can potentially contain tracks, using a fast pattern-matching procedure implemented in Associative Memory (AM) ASICs. A total of 13824 AM ASICs were included in the design [123]. The low resolution patterns are compared to template patterns produced from a large number of simulated single-muon tracks. In the second step, track-fitting is performed in large FPGAs using all combinations of hits selected in the previous step and a linearised algorithm based on Principal Component Analysis.

Multiple studies have been conducted to assess the feasibility of this evolved architecture, using both hardware demonstrators and software simulations. The studies described in this section are included in that effort. They assessed the performance of a future `L1Track` system to signatures with multiple objects in the final state using a software emulation of the hardware system. In 2021, the TDAQ architecture was re-evaluated in view of the fast evolution of tools and technology used for track reconstruction and of design choices for the ITk detector. The two-level hardware trigger scenario was discarded in favor of a non-custom system based on software.

Nonetheless, the studies described here showcase the expected performance of a L1 hardware tracking system in a high-pileup environment and are documented in detail in Reference [14]. They constituted crucial inputs to the decision making process within the ATLAS Collaboration. Additionally, they led to the development of a flexible software framework used to emulate the `L1Track` system. This emulation procedure was not implemented by the author but it is used in the studies of the `L1Track` performance for signatures with multiple muons. Therefore, it is described in section 6.2.1. The treatment of fake tracks within the fast emulation is described in section 6.2.2. The expected impact of `L1Track` on multi-muon signatures was studied using the fast emulation and is presented in section 6.2.3.

6.2.1 Fast emulation design

The full bit-wise simulation of the `L1Track` system (`L1TrackSim`) is very time consuming and CPU intensive. It was designed to cover only four η regions ($[0.1, 0.3]$, $[0.7, 0.9]$, $[1.2, 1.4]$ and $[2.0, 2.2]$) and one ϕ slice ($[0.1, 0.3]$) and requires a very long training phase to extract the constants needed

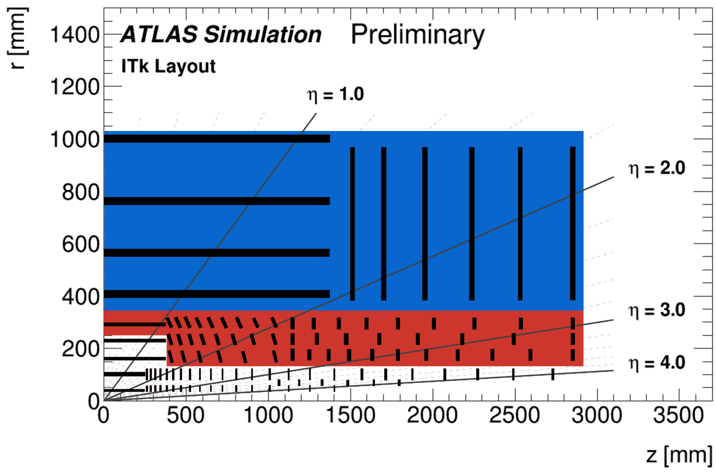

Figure 6.8: Schematic layout of the ITk used in these studies. Only the positions of the active sensors are shown. The modules highlighted in the blue area are used in the `Strip-Only` scenario, while the sum of blue and red areas represents the `TDR` scenario [14].

to simulate the behavior of the hardware system. These constants are highly dependent on the geometry of the detector and on the layers of the ITk used to perform track reconstruction.

This study focuses on the physics impact of different readout scenarios, which directly depend on the ITk geometry, that was, at the time, still evolving. For the reasons listed above, the use of full simulation was deemed too time-consuming and not flexible enough to perform such a study, leading to the development of a fast simulation, referred to as emulation.

The `L1Track` fast emulation is based on offline tracking algorithms and it only approximates the true behavior of the `L1Track` system. After the standard offline track reconstruction, that uses hits in all 13 layers of the inner detector, the track fitting step is repeated using only hits in 7 or 8 layers. If there are less than 7 hits, the track is not reconstructed and if there are more than 8 hits a selection criteria is applied to decide which hits to use to perform track reconstruction. The inner most pixel layers are always excluded since their high occupancy makes their readout too demanding for a low-latency system. From the remaining pixel modules, only those in the outer layers are used: one layer in the barrel (fifth layer) and three in the end-caps (third, fourth and fifth layers). The strip layers are always included. A more conservative scenario is to consider only the hits in the strip layers. The former is referred to as `TDR` scenario and the latter as `Strip-Only` scenario. These scenarios are illustrated in Figure 6.8 that also shows the schematic layout of the ITk used in these studies, in black. The blue rectangle represents the layers used for the readout in the `Strip-Only` scenario. In the `TDR` scenario, the sum of the layers highlighted in both red and blue is used.

Ideally, one would like to use the scenario in which the most inner layers of the ITk detector can be used, i.e., the `TDR` scenario, since the tracks reconstructed in this case are expected to have a resolution closer to offline tracks. However, the layers closer to the interaction point have the highest number of hits per chip (occupancy) and therefore drive the readout rate. It is possible that in Run 4 the occupancy in the inner layers will be larger than predicted by simulation. This could lead to a data readout rate above the system capabilities. This is the reason why a more conservative scenario, the `Strip-Only`, is considered.

The resolution of the track parameters obtained with the fast emulation procedure described above is evaluated from the distribution of the difference between the true value of the track parameter and the reconstructed one, using samples of single muons with fixed transverse momenta. No pileup simulation is overlaid, such that all reconstructed tracks originate from true muons. To reduce the effect of statistical fluctuations, the resolution is measured using an iterative procedure. The root mean square (RMS) of the distribution is calculated and hits laying outside a window of three times the RMS value are removed. The RMS is then recalculated and the procedure repeated until the RMS remains unchanged. Figure 6.9 shows the resolution of track parameters d_0, z_0, ϕ and p_{T} obtained from a double Gaussian fit.

Two components are visible in these plots: a narrow component and a broader one. The narrow peak corresponds to the contribution of real tracks, i.e., `L1Track` tracks that are matched to an offline track, and duplicate tracks that have parameters very close to those of an offline track, but are not matched to one. The broader component corresponds to tracks whose reconstruction is heavily impacted by random hits. The duplicate and random tracks are jointly referred to as fake tracks. The discussion of how they are treated within the fast emulation framework is postponed to section 6.2.2.

For the narrow component, the resolutions of the track parameters are extracted as a function of pseudo-rapidity and transverse momentum in bins of 0.1 in η and for six p_{T} bins (1, 2, 5, 10, 20 and 100 GeV), each corresponding to a single-muon sample. To obtain continuous and smooth smearing functions, an interpolation-extrapolation strategy is used. An inverse-law function is fitted to the resolution shape as a function of p_{T}, for each pseudo-rapidity bin ($f(p_{\mathrm{T}}) = a + b/p_{\mathrm{T}}$). The resolution curve as a function of η is then interpolated with sets of polynomial and Gaussian functions in twelve p_{T} bins ranging from 1 GeV to 1 TeV.

To account for differences between the offline track reconstruction algorithm and the linearized one implemented in hardware, scaling parameters are applied to emulate the track reconstruction efficiency and resolution. The expected `L1Track` reconstruction efficiency relative to offline has been extracted from the bit-wise simulation to be above 95% for tracks with $p_T > 4$ GeV and $|\eta| < 2.5$. A conservative scaling, ϵ, is thus included in the fast emulation as a constant efficiency reduction with respect to offline-reconstructed tracks: $N_{\text{emulated}} = \epsilon \times N_{\text{offline}}$. The resolution functions shown in Figure 6.9 are used to smear the parameters of offline tracks, IP_{offline}, using Gaussian distributions: $\mathcal{N}(IP_{\text{offline}}, \sigma_{\text{smear}})$, where

$$\sigma_{\text{smear}} = \sigma_{\text{offline}} \times \sqrt{\left(S \times \frac{\sigma_{\text{emulated}}}{\sigma_{\text{offline}}}\right)^2 - 1}, \tag{6.2}$$

with σ_{emulated} being the parameterized resolution and σ_{offline} the resolution of offline-reconstructed tracks. The scaling factor S ranges between 1 and 2 and it is used to account for residual differences between the resolutions obtained with the emulation procedure and the full simulation of the `L1Track` system. The ratios between the resolutions of the `TDR` and `Strip-Only` scenarios and the offline scenario are shown on the bottom pads of Figure 6.9 for the different track parameters.

6.2.2 Accounting for fake tracks

The fast emulation procedure described up to now leads to a parameterized representation of the tracks produced by a L1 tracking system working with a reduced number of layers, but it does not take into account other effects associated with the intrinsic nature of the hardware system, in particular the large contribution from fake tracks reconstructed online.

In hardware, fake tracks are reconstructed from random combinations of hits that do not originate from the same particle. The `L1Track` system is characterized by a large multiplicity of fake tracks because it uses hits from a limited number of ITk layers. Fake tracks can be reconstructed with hits belonging mostly to a legitimate track, thus having parameters close to those of an offline track and referred to as duplicates, or be reconstructed by associating uncorrelated hits, and are referred to as random fake tracks. These two categories of fake tracks are clearly seen in Figure 6.10 that shows the distributions of the d_0 and z_0 parameters for `L1TrackSim` tracks matched in ΔR to their closest offline tracks in a sample of dijet events with pileup 200. By the nature of the fast emulation procedure, fake tracks are not automatically taken into account. In the `L1Track` emulation, they are generated as copies of offline tracks by sampling a Poisson distribution with mean value equal to the expected number of fake tracks per offline track. To obtain duplicate fake tracks, the smearing functions described in 6.2 are used. For the random fake tracks, smearing functions describing a broad component are extracted from `L1TrackSim` using the distribution shown in Figure 6.10.

The fraction of fake tracks, f, is defined as the ratio between the number of online- and offline-reconstructed tracks per event, as shown on the left of equation 6.3. Among these, a fraction k is reconstructed within $\Delta R < 0.1$ of an offline-reconstructed track, as defined in equation 6.3, on the right.

$$f = \frac{N_{\text{online}}}{N_{\text{offline}}} \qquad\qquad k = \frac{N_{\text{online},\Delta R<0.1}}{N_{\text{offline}}}. \tag{6.3}$$

The values of f and k are extracted from `L1TrackSim` for the `TDR` and `Strip-Only` scenarios in bins of pseudo-rapidity using a dijet sample with pileup 200 and cross-checked with single muon samples. The values of f are of the order of $3-2$ for the `TDR` scenario and, for the `Strip-Only` scenario, they range between ~ 1.5 in the central pseudo-rapidity region to close to 3 for $|\eta| > 2$. The fraction of fake tracks is larger in the `TDR` scenario due to the larger occupancy of the outer pixel layers (not used in the `Strip-Only` scenario) compared to the inner strip layers. The fraction of duplicate fake tracks, k, ranges between 1.2 and 1.5 for the `TDR` scenario. For the `Strip-Only` scenario, it is slightly smaller in the central pseudo-rapidity region (~ 1.1) but becomes larger for $|\eta| > 2$ (~ 1.7).

Taking into account the `L1Track` reconstruction efficiency with respect to offline, $\epsilon = \frac{N_{\text{emulated}}}{N_{\text{offline}}}$, the total fraction of fake tracks per offline track can be defined as:

$$\frac{N_{\text{fakes}}}{N_{\text{offline}}} = \frac{N_{\text{online}} - N_{\text{emulated}}}{N_{\text{offline}}} = f - \epsilon. \tag{6.4}$$

Similarly, the amount of duplicate fake tracks, reconstructed close-by an offline track, is defined as:

$$\frac{N_{\text{fakes duplicate}}}{N_{\text{offline}}} = \frac{N_{\text{online},\Delta R<0.1} - N_{\text{emulated}}}{N_{\text{offline}}} = k - \epsilon. \tag{6.5}$$

The remainder $(f-k)$ fraction represents the random fake tracks.

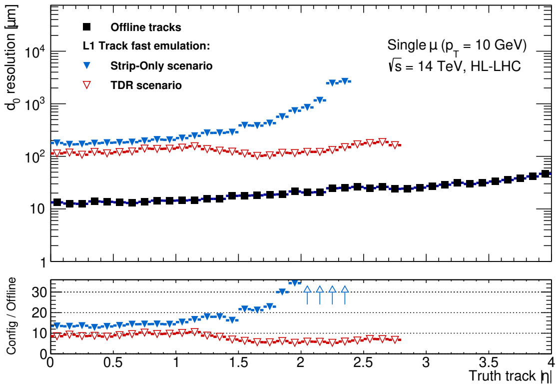

(a) d_0 resolution

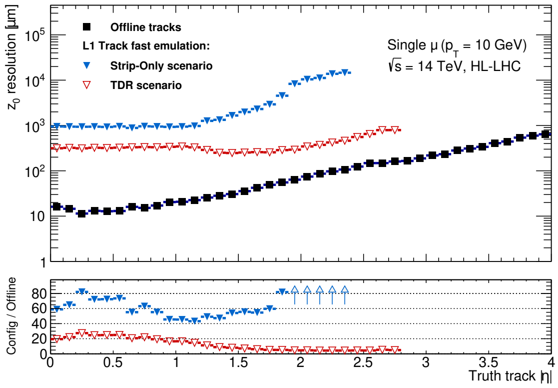

(b) z_0 resolution

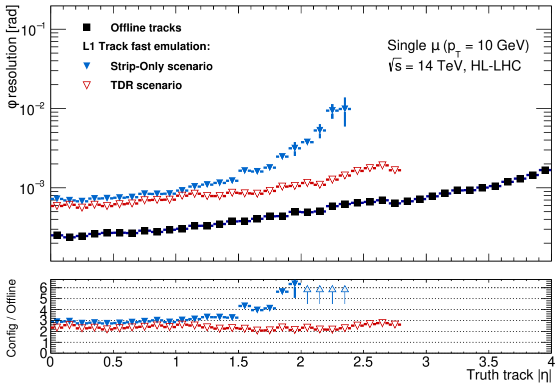

(c) ϕ resolution

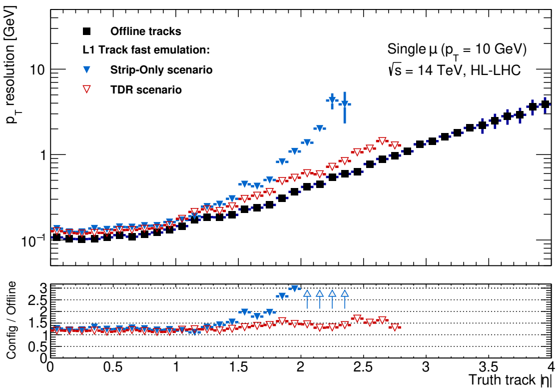

(d) p_{T} resolution

Figure 6.9: Effect of the fast emulation of the `TDR` (red empty markers) and `Strip-Only` (blue filled markers) scenarios on the d_0 (a), z_0 (b), ϕ (c) and p_{T}(d) resolutions with respect to the absolute η of tracks for single muons with p_{T}= 10 GeV. The offline tracking performance and the relative ratio are also shown.

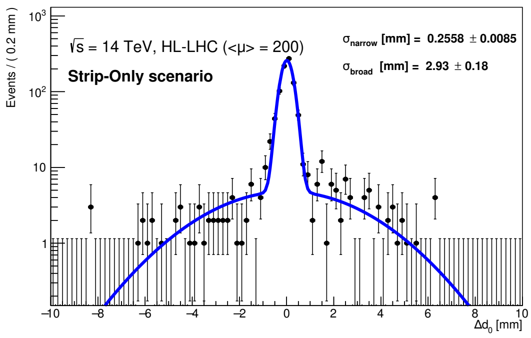

(a)

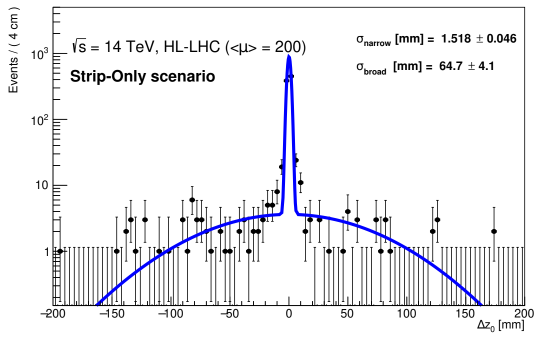

(b)

Figure 6.10: Residuals from the difference between tracks from `L1TrackSim` matched with the closest offline track and the corresponding offline track for (a) d_0 and (b) z_0 parameters, in dijet events embedded in pileup of 200 for the `Strip-Only` scenario. A double Gaussian fit is superimposed and the widths of the two curves are shown in the legend.

6.2.3 Impact of L1Track on dimuon signatures

In multi-lepton trigger signatures, one way of increasing acceptance while simultaneously keeping the trigger rate at a manageable level, is to require that the leptons are consistent with a common production vertex. This mitigates the contribution from pileup events where the leptons are produced from different interactions. In this study, $Z \to \mu\mu$ is considered as the reference signal process.

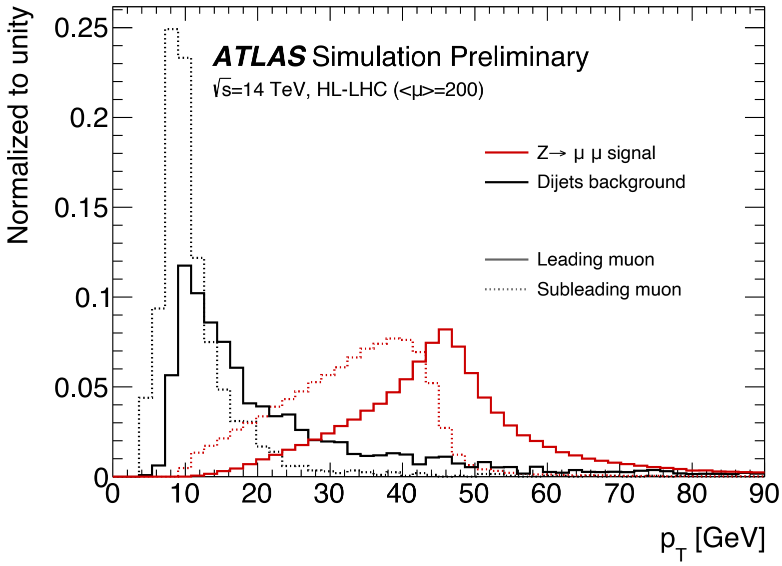

Figure 6.11: Transverse-momentum distributions of the two most-energetic muons (leading and sub-leading) from both signal $Z \to \mu\mu$ (red) and background di-jet (black) events, after applying the emulated L0 selection (two muons with $p_{\mathrm{T}} > 10$ GeV).

The trigger selection under study requires events with at least two L0 muons with $p_{\mathrm{T}} > 10$ GeV. At L0, with the future Run 4 upgrade, muons are expected to be identified in the muon spectrometer as described in the TDAQ TDR [123]. The expected resolution is determined by the high precision MDT chambers, and the resulting reconstructed muons are thus called standalone muons. To emulate the p_{T} spectrum of the L0 muons, the efficiency of the single muon trigger at 10 GeV threshold is extracted from the TDAQ TDR studies as a turn-on curve versus the muon p_{T}. The probability of the event passing the two-L0-muon trigger is then calculated as the product of the two muon probabilities. The p_{T} distributions of the two most energetic muons (leading and sub-leading) passing the L0 requirement on the signal and background events are shown in Figure 6.11. As expected, the p_{T} distribution of the most energetic muon peaks at around 45 GeV, approximately half of the Z boson mass. The resulting L0 efficiency is around 43% for the $Z \to \mu\mu$ signal process and is reduced to 1% for background di-jets events.

The Level-1 trigger selection requires that each of the two L0 muons is matched with at least one track and that the two tracks have a common decay vertex. For that, the closest track in a cone of $\Delta R < 0.3$ around each of the two L0 muons in the event is selected. Using the information from the chosen track pair, the distance along the z-axis between the two L0 muons (Δz_0) is calculated and used as a discriminant variable to better separate signal and background.

Figure 6.12a shows the distribution of the p_{T} of the closest track associated to the most energetic

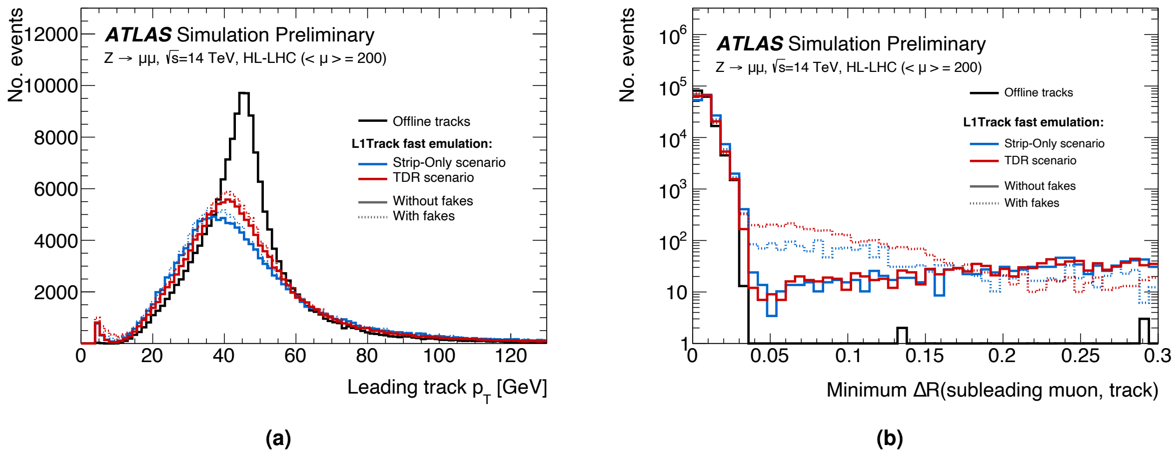

Figure 6.12: Distributions from $Z \to \mu\mu$ signal events: (a) p_{T} of the L1 tracks matched to the leading muon and (b) ΔR between the sub-leading muon and the closest L1 track.

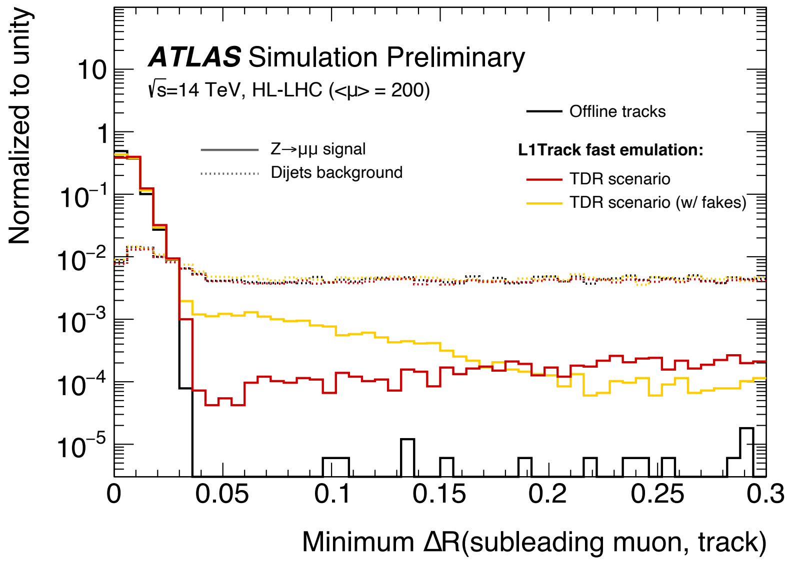

Figure 6.13: Distribution of the ΔR between the sub-leading muon and the closest track for $Z \to \mu\mu$ signal events (filled lines) and for di-jet background events (dotted lines) for emulated L1 tracks using the TDR scenario, with and without fake tracks included (orange and red, respectively). Offline tracks are reported for reference in black.

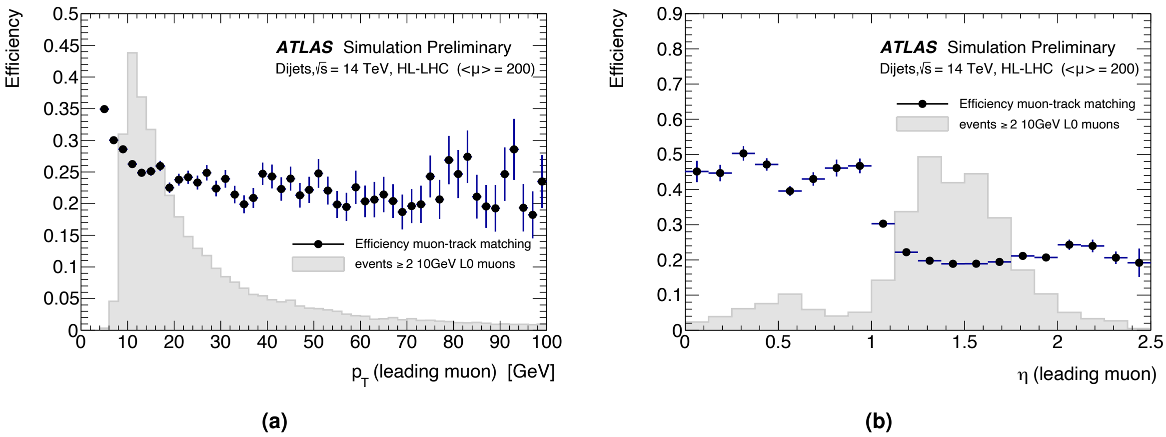

Figure 6.14: Distributions of events passing the emulated dimuon L0 selection (two standalone muons with $p_{\mathrm{T}}>$ 10 GeV with L0 weighted efficiency) and the corresponding muon-track efficiency, in di-jet background events, as a function of (a) p_{T} and (b) η of the leading muon.

L0 muon in the $Z \to \mu\mu$ signal events. The offline reconstructed tracks are shown as reference, while the emulated L1 tracks are shown in both scenarios and with and without the additional fake tracks. In a small fraction of the events, represented by the small peak at very low p_{T}, the matched track is not the legitimate muon but comes from the pileup events, and this is enhanced by the coarse resolution of the emulated tracks.

The distribution of the minimum ΔR distance between the sub-leading muon and the closest track in $Z \to \mu\mu$ events is shown in Figure 6.12b. The blue and red plots show a tail to larger values of ΔR that is not present for offline tracks (black plot). This reflects the larger uncertainty in the track coordinates after emulation, and motivates the choice of a large cone size for selecting the signal. Based on these plots, a cone size of $\Delta R = 0.3$ is chosen as track-muon matching requirement, which is approximately the size of the RoI for a L0 muon. It ensures a signal efficiency close to 100% for offline-reconstructed tracks, becoming 95% for a muon pair with L1 tracks, which is close to the working point considered in the TDAQ TDR.

Table 6.3: Signal efficiency and background rejection for finding at least one track within a $\Delta R < 0.3$ cone around each of the two leading standalone L0 muons, for events with ≥ 2 muons with $p_{\mathrm{T}} > 10$ GeV. The uncertainties are the sum in quadrature of statistical and systematic components, the latter calculated by comparing the two emulation strategies (fast and L1TRACKSIM -tuned emulations).

Two muons with $p_{\mathrm{T}} > 10$ GeV, track-matched in $\Delta R < 0.3$					
Tracking scenario	offline	TDR	TDR w/ fakes	STRIP-ONLY	STRIP-ONLY w/ fakes
$Z \to \mu\mu$ efficiency [%]	$99.8^{+0.2}_{-0.3}$	89.7 ± 0.4	95.8 ± 0.4	89.8 ± 0.4	94.0 ± 0.4
Background rejection	15 ± 2	17 ± 3	13 ± 1	17 ± 3	14 ± 1

The efficiency and rejection after applying the track-muon matching requirement on both muons, for all the L1TRACK scenarios, are summarized in Table 6.3. The minimum ΔR between the subleading L0 muon and the matched L1 track is shown in Figure 6.13 for signal and background, using filled and dotted lines, respectively. Offline-reconstructed tracks are shown for reference, in black. The L1 tracks in the `TDR` scenario are shown with and without fakes, in orange and red, respectively.

For the `TDR` and `Strip-Only` scenarios, some events lie in the tails of the distributions which leads to a smaller matching efficiency, ranging between $90\% - 96\%$, similar for both scenarios. When fake tracks are included (dotted lines), the peak of the distributions shifts to lower ΔR values, and the number of events in the peak increases slightly, as the number of available tracks for the matching cone increases. Consequently, the track-muon matching efficiency is larger when fake tracks are included in the emulation.

Background rejection after track-muon matching is not affected by the reduced resolution of the L1 tracks. Within the uncertainties, it has the same value for the `TDR` and `Strip-Only` scenarios. However, the background rejection does decrease when including fake tracks with respect to the same scenario but without fakes considered, as can be observed in Table 6.3.

The matching between L0 muons and L1 tracks is very effective in rejecting background. Figure 6.14 shows the p_{T} and η distributions of the leading muon in background di-jets events passing the

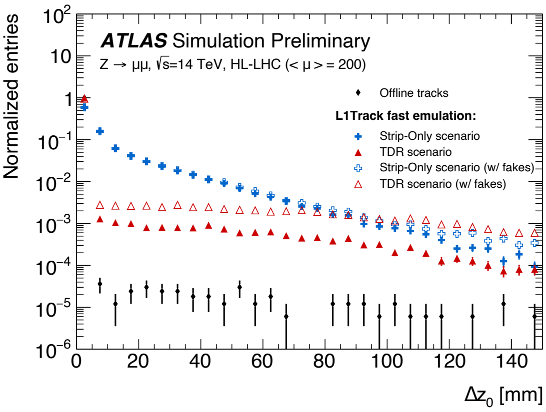

(a) Signal distributions

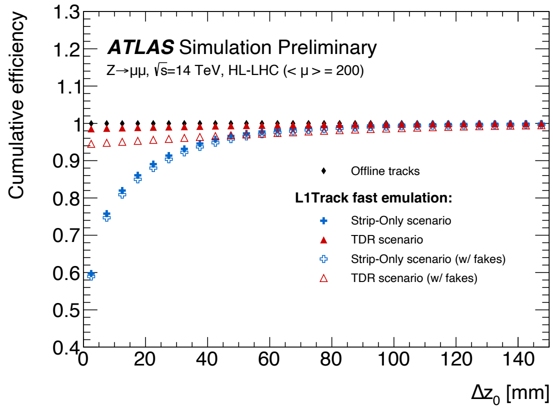

(b) Signal cumulative efficiency

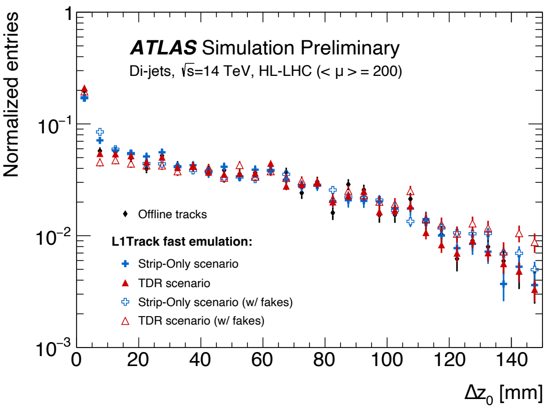

(c) Background distributions

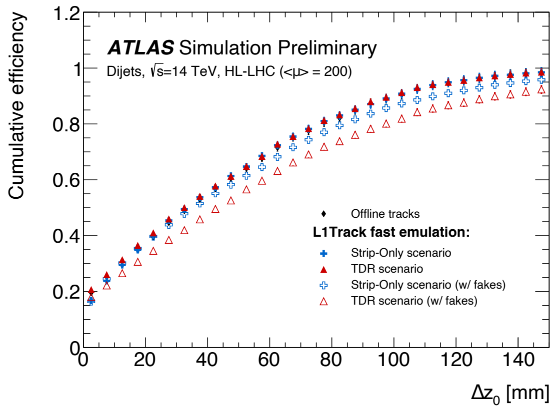

(d) Background cumulative efficiency

Figure 6.15: Distributions of the distance along the z-axis between the tracks matched to muons, Δz_0, (6.15a,6.15c) and corresponding efficiency of the window algorithm (6.15b,6.15d). Events from $Z \to \mu\mu$ signal (top row) and background (bottom row) are shown, with and without the contribution from fake tracks included, in the two L1TRACK scenarios, and compared to the corresponding offline-tracking distributions.

two-L0-muon selection. The efficiency of requiring an additional matching with offline tracks is superimposed. From the figure on the right, it is clear that the majority of L0 muons appear in the region between the barrel and the endcap, corresponding to $1 < |\eta| < 2$. The rejection in this region is also larger than in the barrel ($0 < |\eta| < 1$). The values for the background rejection shown in Table 6.3 are calculated inclusively in the full η range between zero and 2.5 and therefore include a large contribution from the large rejection in the region with $|\eta| > 1$. It is thus possible that the background rejection due to the matching between a L0 muon and a L1 track is overestimated in this study. This could be the case if the L0 muons considered in this study would not actually be accepted by the real L0 system. For Run 3, with the inclusion of the NSW and the new RPC BIS78, as well as the trigger coincidence between the big wheel TGCs and the tile calorimeter, a lot of the background from low-p_{T} muons in the region with $|\eta| > 1.0$ is expected to be reduced. Assuming that these systems can also be used during Run 4 by the L0 trigger, they could lead to a reduction of the amount of muons accepted with $|\eta| > 1.0$. This would in turn reduce the background rejection power of the L0 muon-L1 track matching, simply because early rejection would already be achieved.

The distance along the z axis between the two matched tracks (Δz_0) is the main parameter to investigate. The distributions of Δz_0 of offline and emulated tracks in the different `L1Track` scenarios are shown in Figures 6.15a and 6.15c for signal and background, respectively. For pairs of muons produced in the same vertex, like for the signal sample, Δz_0 is expected to be small, while a broader distribution comes from randomly associated pairs of muons. The degraded z_0 resolution in the `L1Track` scenarios smears the Δz_0 distributions from signal events, in particular in the `Strip-Only` scenario. Larger tails appear when the contribution from fake tracks is included, in particular for the `TDR` scenario. For background distributions, the difference among `L1Track` scenarios is less marked due to the abundance of random track pairs not originating from the same vertex. Figures 6.15b and 6.15d show the event efficiency when requiring the two tracks within the corresponding Δz_0 window, for signal and background, respectively. The efficiency is calculated with respect to events already passing the L0 muon-L1 track matching.

The background rejection versus signal efficiency as a function of the Δz_0 cut is shown in Figure 6.16a, comparing the performance with (dashed lines) and without (filled lines) fake tracks in the two scenarios. The same curve obtained with offline-reconstructed tracks is shown for reference. The bottom ratio plot shows that the degradation in performance derived by the inclusion of fake tracks is minimal over a large range of the $Z \to \mu\mu$ efficiency. One effect of reduced rejection at high efficiency is visible in the `TDR` scenario when the fake tracks are added: this is due to the large tails in the Δz_0 distributions for the signal (see Figure 6.15a), that require larger z_0 windows to achieve the same efficiency.

The systematic effect due to the emulation is shown in Figure 6.16b with a comparison between the two `L1Track` emulation strategies studied in this thesis, namely the fast emulation and the `L1TrackSim`-tuned. The bottom ratio plot shows the effect on both scenarios with fakes included. For the `Strip-Only` scenario, the effect of using the fast emulation as opposed to `L1TrackSim` is as large as 70% in the high $Z \to \mu\mu$ efficiency regime. For the `TDR` scenario it is always below 30%.

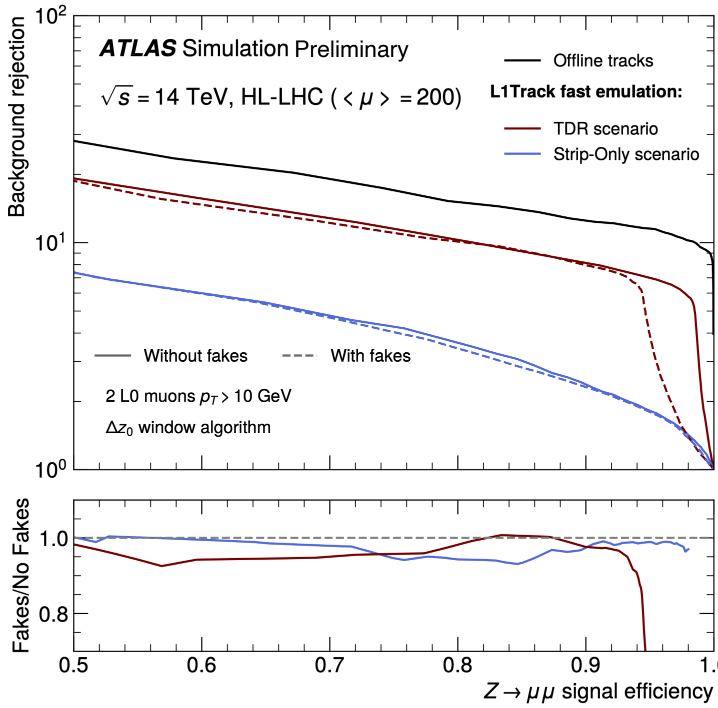

(a)

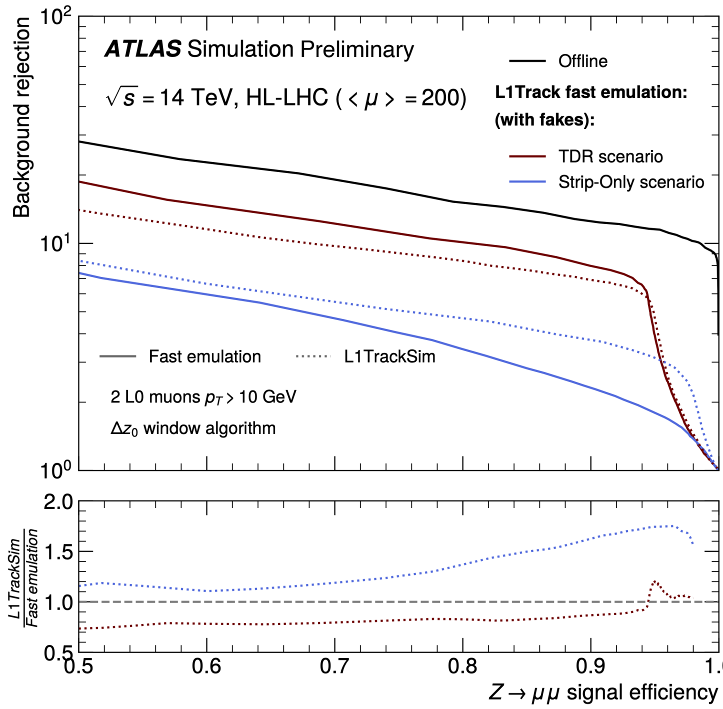

(b)

Figure 6.16: Background rejection versus $Z \to \mu\mu$ signal efficiency as a function of the Δz_0 cut for the TDR (red) and STRIP-ONLY (blue) scenarios, comparing L1TRACK emulations with and without fake tracks (6.16a) and fast and L1TRACKSIM -based emulations, both with fake tracks contribution included (6.16b).

In both figures 6.16a and 6.16b, signal efficiency and background rejection are calculated with respect to events with ≥ 2 muons with $p_{\mathrm{T}} > 10$ GeV and two matched tracks, in order to isolate the effect of the sole Δz_0 requirement. To obtain the total efficiency/rejection of the algorithm, the values can be multiplied by the muon-track matching probabilities shown in Table 6.3. For the `TDR` scenario with fake tracks included (red dashed line in Figure 6.16a), the background rejection coming only from the Δz_0 requirement for a signal efficiency of 95% is 4. The total rejection obtained by the algorithm, including the L0 muon-L1 track matching and the Δz_0 requirement, is thus 52. For the `Strip-Only` scenario, the rejection from the Δz_0 requirement is smaller in comparison to the `TDR` scenario. Its value is slightly below 2. For this scenario, the total rejection is ~ 28.

This study showcases the expected performance of a `L1Track` system for a signature with two muons. The algorithm that was studied involves two main components: the ΔR matching between the L0 muons and the L1 tracks; and the requirement that the L1 tracks originate from the same Δz_0 window. The ΔR matching part of the algorithm is fairly resilient to fake tracks and provides the largest rejection. The Δz_0 requirement shows large dependence on the ITk readout scenario considered. The `TDR` scenario is greatly affected by fakes in the high signal efficiency regime.

7

First full Run 2 analyses of Higgs boson produced in association with top quarks

Contents

This chapter summarizes the first two measurements of Higgs boson production in association with top quarks ($t\bar{t}H$ and tH) in the $H \to b\bar{b}$ decay channel, using 139 fb^{-1} of proton-proton collision data at $\sqrt{s} = 13$ TeV, collected with the ATLAS detector during the full Run 2 of the LHC. The $t\bar{t}H$ signal strength is measured as a function of the reconstructed Higgs boson p_{T}, in the context of the Simplified Template Cross-Section framework (STXS) [155]. A dedicated measurement of the charge-parity (CP) properties of the Yukawa coupling of the Higgs boson to the top quark is also performed [156].

The two analyses share the same data and MC samples (described in Section 7.1), object and event reconstruction (detailed in Section 7.2) and pre-selection (covered in Section 7.3) as well as a similar treatment of the systematic uncertainties and statistical methods, described in Sections 7.4 and 7.5, respectively. Therefore their main components are described together, with differences highlighted when necessary. The two sets of results are presented separately in Sections 7.6 and 7.7 for the STXS and CP measurements, respectively.

Measuring the cross-section of Higgs boson production with a pair of top quarks constitutes an important test of the SM. The cross-section of $t\bar{t}H$ production in the $H \to b\bar{b}$ decay channel has been measured by the ATLAS Collaboration using a partial Run 2 dataset corresponding to 36.1 fb^{-1}, in events with at least one lepton [157]. A combined signal strength of $0.84^{+0.64}_{-0.61}$ was measured, with an observed (expected) significance of 1.4 (1.6) standard deviations.

The CMS Collaboration searched for the same process using a partial Run 2 dataset corresponding to 35.9 fb^{-1} collected during 2016, in events with at least one lepton [158] or no leptons [159]. A signal strength of $0.72^{+0.24}_{-0.38}$ was measured in the leptonic channel, with an observed (expected) significance of 1.6 (2.2) standard deviations. In the hadronic channel, a signal strength of 0.9 ± 1.5 was measured. More recently, a search using 45.1 fb^{-1} of data collected during 2017 was published by the CMS Collaboration [160]. A signal strength of $1.49^{+0.44}_{-0.40}$ was measured using leptonic and fully hadronic events, corresponding to an observed (expected) significance of 3.7 (2.6) standard deviations. A statistical combination of these two results leads to a measured signal strength of $1.15^{+0.32}_{-0.29}$.

7.1 Data samples and MC simulation of physics processes

The expected yields and shapes of discriminant variables are estimated based on a Monte Carlo (MC) simulation of the underlying physics processes for both signal and backgrounds. The simulated events are produced using either the full ATLAS detector simulation based on GEANT4 [72] or a faster simulation, AtlFastII, where the calorimeter response is replaced by a detailed parameterization of the shower shapes [161]. The effects of multiple interactions in the same or neighbouring bunch crossings (pileup) are simulated by generating additional MC using PYTHIA8.186 (with the A3 tune [162]) and overlaying them onto the simulated hard-scatter events. Simulated events are reweighted to match the pileup distribution observed in the full Run 2 dataset, with a mean value of 34. All simulated events are processed by the same reconstruction and analysis algorithms as data.

The parton shower, hadronisation and multi-parton interactions are simulated using SHERPA [163] (which also generates the matrix element), PYTHIA8 [59] or HERWIG7 [61], depending on the samples. In PYTHIA8 and HERWIG7, the decays of b- and c-hadrons are simulated using the EVTGEN1.6.0 program [164]. The b-quark mass is set to $m_b = 4.80$ GeV (4.50 GeV) and the A14 [165] (H7UE [61]) tune and the NNPDF2.3LO (MMHT2014 LO [166]) PDF set are used for PYTHIA8 (HERWIG7). The Higgs boson mass is set to $m_H = 125$ GeV and the top quark mass to $m_t = 172.5$ GeV.

The precision of the matrix element calculation is next-to-leading order (NLO) in QCD for most samples. This is the case for the $t\bar{t}H$ signal sample that additionally includes NLO electroweak corrections to the cross-section. The inclusive $t\bar{t}$ samples is normalised to next-to-next-to-leading order (NNLO) in QCD.

7.1.1 $t\bar{t}H$ and tH modelling

The nominal $t\bar{t}H$ and tH predictions differ between the STXS and CP analyses. In the STXS analysis, it is sufficient to generate samples according to the SM predictions, since the goal is to measure the $t\bar{t}H$ production cross section in different kinematic regimes without taking into account potential BSM effects. Furthermore, the tH process is considered a (sub-dominant) background to the measurement. In the CP analysis, the goal is to measure or constrain the parameters related to the CP properties of the Yukawa coupling of the Higgs boson to the top quark. Therefore, samples produced in alternative CP scenarios are needed such that the different predictions can be compared to data.

In the STXS analysis, the production of $t\bar{t}H$ events and subsequent decays are modelled in the five-flavor scheme using the POWHEGBOX generator [57] at NLO in QCD with the NNPDF3.0NLO PDF set [167]. The h_{damp} parameter is set to $0.75\times(m_t+m_{\bar{t}}+m_H) = 352.5$ GeV. It controls the p_{T} of the first additional emissions beyond the Born configuration [168]. The functional form of the renormalisation and factorization scales are both set to $\sqrt[3]{m_T(t) \cdot m_T(\bar{t}) \cdot m_T(H)}$, where $m_T = \sqrt{m^2 + p_T^2}$ is the transverse mass. The parton shower and hadronisation are handled by PYTHIA8, with all Higgs decay modes considered. The samples are normalised to the fixed-order cross-section calculation of 507^{+35}_{-50} fb, which includes NLO QCD and EW corrections [49]. An alternative $t\bar{t}H$ sample is generated using MADGRAPH5_AMC@NLO 2.6.0 [56] and showered with PYTHIA8 and compared with the nominal prediction in order to assess the uncertainty coming from changing the NLO matching scheme. This alternative sample from the STXS analysis is used as nominal sample in the CP analysis.

In the CP measurement, the $t\bar{t}H$ and tH processes need to be simulated for different values of the coupling modifier and the CP-mixing angle. The non-SM coupling scenarios are generated using the NLO Higgs characterization model that is only implemented in MADGRAPH5_AMC@NLO using FeynRules [169]. This justifies the need to utilize a SM $t\bar{t}H$ signal sample that is also generated with MADGRAPH5_AMC@NLO. All CP-mixed or CP-odd signal samples are generated using MADGRAPH5_AMC@NLO 2.6.2 at NLO precision in QCD in the five-flavor scheme using the NNPDF3.0NLO PDF set, interfaced with PYTHIA8.230 with the A14 tune. The SM $t\bar{t}H$ sample is generated with MADGRAPH5_AMC@NLO 2.6.0, as mentioned in the previous paragraph. For the associated production of a single top quark and a Higgs boson, two sub processes are considered:

$tHjb$ and tWH. The samples for the SM scenario are common between the CP and STXS analyses. The functional form of the renormalisation and factorization scales is set to $0.5 \times \sum_i m_T(i)$, where the sum runs over all particles generated in the matrix element calculation. For $tHjb$ (tWH), events are generated in the four-flavor (five-flavor) scheme using the `NNPDF3.0NLOnf4` (`NNPDF3.0NLO`) PDF set, and the diagram removal procedure is employed to handle the interference with $t\bar{t}H$ in the tWH sample. In the dilepton channel, the $tHjb$ process is found to have a negligible contribution, even in non-SM scenarios where the cross-section is enhanced. Therefore, this process is removed from the total MC prediction template in the CP analysis. The yields of $tHjb$ in the dilepton analysis regions compared to those of $t\bar{t}H$ and tWH are shown in Appendix A.3.

Table 7.1 summarizes the generator settings used to produce the nominal and alternative $t\bar{t}H$ and tH samples in the STXS and CP analyses.

The signal yields are parameterized based on $t\bar{t}H$ and tH events generated with different values of $k_t^{'}$ and α, in each bin of the analysis, such that shape differences for different coupling structures are also taken into account, providing a smooth prediction of the signal yield across the entire range of $k_t^{'}$ and α. For $t\bar{t}H$, the yields for non-SM scenarios can be parameterized as a weighted sum of the yields of pure CP-even ($\alpha = 0$) and CP-odd ($\alpha = \pi/2$) samples:

$$N_{t\bar{t}H}(k_t^{'}, \alpha) = k_t^{'} \cos^2(\alpha) N_{\text{CP-even}} + k_t^{'} \sin^2(\alpha) N_{\text{CP-odd}}, \tag{7.1}$$

where $N_{\text{CP-even}}$ and $N_{\text{CP-odd}}$ are the yields predicted by the SM and CP-odd $t\bar{t}H$ simulations, respectively. The interference between CP-even and CP-odd $t\bar{t}H$ events was found to be negligible. This procedure was validated at truth-level using a sample produced for the maximal mixing scenario ($\alpha = \pi/4$). Comparisons between distributions of kinematic and angular variables obtained using Equation 7.1 or directly from MC samples generated in the maximal mixing scenario are shown in Appendix A for the single-lepton and dilepton channels. The two predictions agree within the statistical uncertainties with deviations well below 1%.

For tH, a parameterization is constructed taking into account contributions from diagrams with CP-even and CP-odd $t-H$ couplings (depicted in Figure 3.5a) and SM $W-H$ coupling at LO (depicted in Figure 3.5b). The event yields per bin can thus be parameterized as:

$$\frac{N_{tH}(k_t^{'}, \alpha)}{N_{tH}(k_t^{'} = 1, \alpha = 0)} = Ak_t^{'} \cos^2(\alpha) + Bk_t^{'} \sin^2(\alpha) + Ck_t^{'} \cos(\alpha) + Dk_t^{'} \sin(\alpha) + Ek_t^{'2} \cos(\alpha)\sin(\alpha) + F, \tag{7.2}$$

where the A and B terms correspond to the contribution from CP-even and CP-odd $t-H$ coupling, respectively. The C (D) term corresponds to the interference between CP-even (CP-odd) $t-H$ and $W-H$ couplings. The term E corresponds to the interference between CP-even and CP-odd $t-H$ couplings, which can not be neglected in the tH case. The term F corresponds to the pure $W-H$ contribution. The $W-H$ coupling is assumed to follow the SM prediction for every value of $k_t^{'}$ and α.

The values of the coefficients A-F are obtained by fitting the parameterization function defined in Equation 7.2 to the yields predicted by a set of simulated samples, spanning 11 points in the $(k_t^{'}, \alpha)$ parameter space. To extract the coefficients A-F, in addition to the SM sample, 10 samples were generated with different values of $k_t^{'}$ and α: 6 samples with $k_t^{'} = 1$ and α varied between $15°$ and $90°$

in steps of $15°$, 3 samples with $\alpha = 0$ and $k_t^{'} = -1, 0.5, 2$ and one sample with $\alpha = 45°$ and $k_t^{'} = 2$. The best fit values of the coefficients A-F are shown in Figures 7.1 and 7.2 for the single-lepton and dilepton channels, respectively. The comparison between the tWH and $tHjb$ yields obtained from the parameterization and directly from the MC samples is shown in appendix A.2. Each plot corresponds to one analysis bin, and the bins in each plot represent the points in the $(k_t^{'}, \alpha)$ parameter space used to derive the parameterization. The uncertainty originating from the limited MC statistics is propagated to the fitted coefficients and, in turn, to the parameterized yields. It is shown as a red band in the plots.

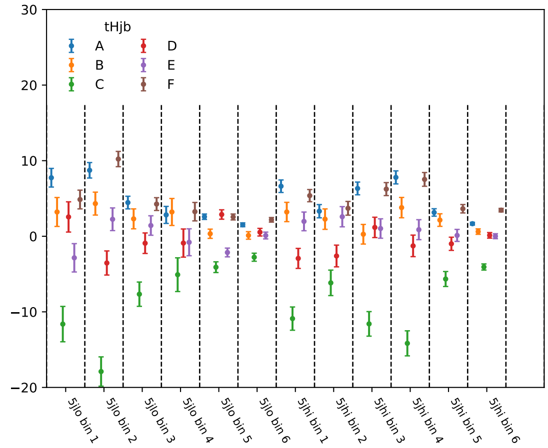

(a) tHjb, control regions

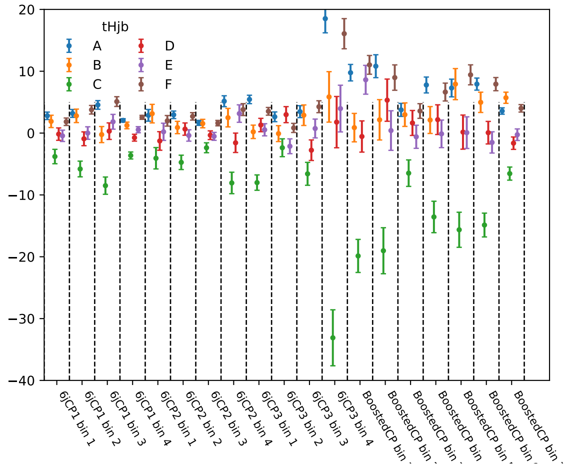

(b) tHjb, signal regions

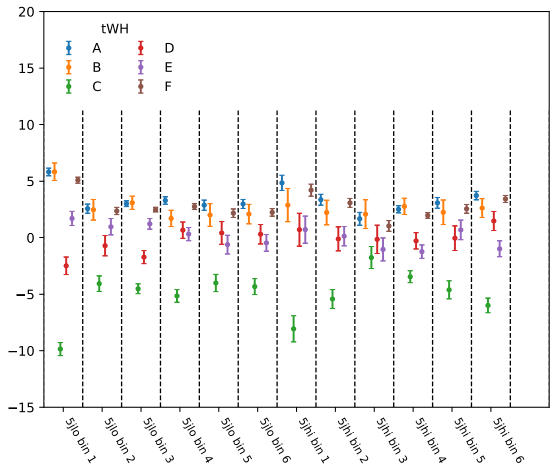

(c) tWH, control regions

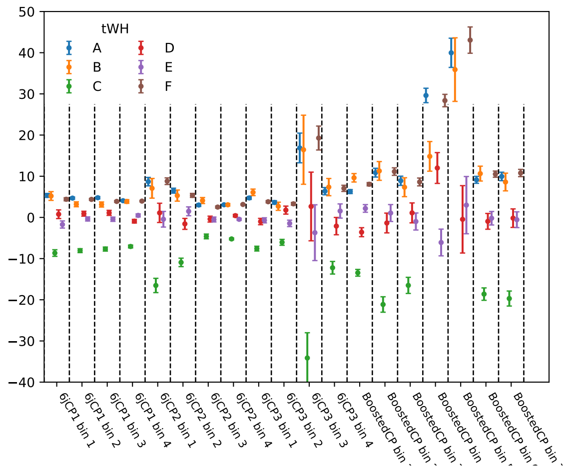

(d) tWH, signal regions

Figure 7.1: Best-fit values and uncertainties for the coefficients A through F in the single-lepton channel.

7.1.2 $t\bar{t}$+jets background

Simulated $t\bar{t}$+jets events are categorized based on the number and flavor of the partons matched to particle-level jets that do not originate from the decay of the $t\bar{t}$ system. For this purpose, jets are reconstructed from truth-level particles with a mean lifetime larger than 3×10^{-11} seconds, using the anti-k_t algorithm with radius parameter $R = 0.4$. The number of b- and c-hadrons within $\Delta R < 0.4$ of the jet axis are considered for the categorization, excluding particles produced by the top quark decays. Truth jets with $p_{\mathrm{T}} > 15$ GeV and $|\eta| < 2.5$ and b/c-hadrons with $p_{\mathrm{T}} > 5$ GeV are considered.

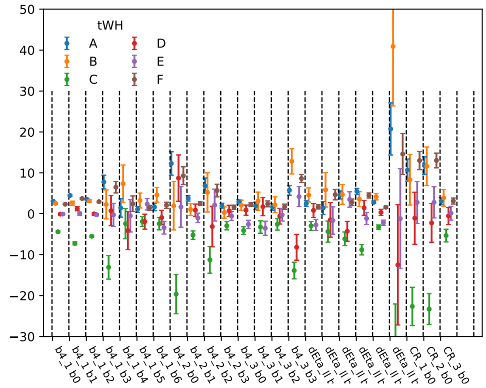

(a) tWH, dilepton regions

Figure 7.2: Best-fit values and uncertainties for the coefficients A through F in the dilepton channel.

Process	ME generator	ME PDF	PS	Normalisation
Higgs boson				
$t\bar{t}H$	MadGraph5_aMC@NLO v2.6.0	NNPDF3.0NLO	Pythia8.230	NLO+NLO (EW)
	PowhegBox v2	NNPDF3.0NLO	Pythia8.230	NLO+NLO (EW)
	PowhegBox v2	NNPDF3.0NLO	Herwig7.04	NLO+NLO (EW)
$tHjb$	MadGraph5_aMC@NLO v2.6.2	NNPDF3.0NLOnf4	Pythia8.230	–
tWH	MadGraph5_aMC@NLO v2.6.2 [DR]	NNPDF3.0NLO	Pythia8.235	

Table 7.1: Summary of MC generators used to produced the signal samples. The sample highlighted in blue is used as nominal prediction for the $t\bar{t}H$ process in the CP analysis. For the STXS measurement the nominal sample is highlighted in violet.

Process	ME generator	ME PDF	PS	Normalisation
$t\bar{t}$+jets				
$t\bar{t}$	POWHEGBOX v2	NNPDF3.0NLO	PYTHIA8.230	NNLO+NNLL
	POWHEGBOX v2	NNPDF3.0NLO	HERWIG7.04	NNLO+NNLL
	MADGRAPH5_aMC@NLO v2.6.0	NNPDF3.0NLO	PYTHIA8.230	NNLO+NNLL
$t\bar{t}+b\bar{b}$	POWHEGBOXRES	NNPDF3.0NLOnf4	PYTHIA8.230	–
	SHERPA v2.2.1	NNPDF3.0NNLOnf4	SHERPA	–

Table 7.2: Summary of the Monte Carlo generators used to produce the $t\bar{t}$+jets samples. The first line for each category corresponds to the nominal sample; the remaining ones are alternative samples used to estimate systematic uncertainties.

Jets matched to a single b- or c-hadron are labeled b- or c-jets, respectively. If a jet is matched to two or more b- or c-hadrons, it is labeled a B- or C-jet, respectively. Events with at least one b- or B-jet are categorized as $t\bar{t}+\geq 1b$. Similarly, events which are not categorized as $t\bar{t}+\geq 1b$, and with at least one c- or C-jet are labeled $t\bar{t}+\geq 1c$. The remaining events are labeled $t\bar{t}$+light. The $t\bar{t}+\geq 1b$ category can be further subdivided into $t\bar{t}+1b/B$ and $t\bar{t}+\geq 2b$, corresponding to events with exactly one or at least two b- or B-jets. A similar subdivision can be done for $t\bar{t}+\geq 1c$.

To accurately model the dominant $t\bar{t}+\geq 1b$ background a dedicated $t\bar{t}+b\bar{b}$ sample is produced, with the two additional b-quarks generated at the matrix element (ME) level at NLO QCD accuracy in the four-flavor scheme, with the mass of the b-quarks set to 4.95 GeV. The ME calculation is performed using POWHEGBOXRES and OPENLOOPS [170, 171] with the NNPDF3.0NLOnf4 PDF set. Parton shower and hadronisation are performed by PYTHIA8.230 with the A14 tune. The factorization scale is set to $0.5 \times \sum_{i=t,\bar{t},b,\bar{b},j} m_T(i)$, where j stands for extra partons, the renormalisation scale is set to $\sqrt[4]{m_T(t) \cdot m_T(\bar{t}) \cdot m_T(b) \cdot m_T(\bar{b})}$ and the h_{damp} parameter is set to $0.5 \times \sum_{i=t,\bar{t},b,\bar{b}} m_T(i)$.

The $t\bar{t}+\geq 1c$ and $t\bar{t}$+light backgrounds are modelled using an inclusive $t\bar{t}$+jets sample generated in the five-flavor scheme at NLO in QCD with POWHEGBOX V2 for the matrix element calculation and interfaced to PYTHIA8 for the parton shower and hadronisation. The h_{damp} parameter is set to $1.5 \times m_t$ and the renormalisation and factorization scales are set to $m_T(t)$. The $t\bar{t}+\geq 1b$ events from this sample are used to estimate systematic uncertainties originating from the modelling. This sample is normalised to the predicted $t\bar{t}$ cross section of 832^{+46}_{-51} pb, calculated for a top quark mass of 172.5 GeV at NNLO in perturbative QCD including next-to-next-to-leading logarithm soft gluon terms with top++2.0 [172–178].

Table 7.2 summarizes the generator settings used to simulate the nominal and alternative $t\bar{t}$ and $t\bar{t}+b\bar{b}$ processes.

7.1.3 Other backgrounds

Other background processes include W/Z-boson production with additional jets (V+jets), $t\bar{t}V$, tZq, tWZ, single-top quark, four-top quark and diboson events. These are all subdominant and modelled from simulation, as detailed below. A small fraction of events contain mis-identified leptons or leptons originating from the decays of heavy-flavor hadrons. These events are collectively referred to as fakes.

In the single-lepton channel, fakes mostly originate from multijet processes. Due to the identification and isolation criteria applied both at the trigger level and offline as well as the requirements of a large jet and b-jet multiplicities in the analysis regions, the majority of fakes is removed. Their contribution was found to be negligible in this analysis. The studies, documented in Reference [155] in Appendix G, involved calculating the relative difference between the data and MC yields for different lepton isolation requirements. This difference is expected to be reduced when using tighter isolation working points, if the mismodelling is due to the presence of fake leptons. If instead the mismodelling originates from the MC prediction of $t\bar{t}+\geq 1b$ then this difference is expected to be approximately similar for different isolation working points. This was found to be the case in regions with a high multiplicity of b-jets.

In the dilepton channel, the contribution from fake leptons is modelled from simulated events ($t\bar{t}, t\bar{t}Z, t\bar{t}W$, diboson, Z+jets, W+jets, s-channel and t-channel single top production) where at least one of the reconstructed leptons does not have a matching truth-level lepton in the event record.

The V+jets processes are simulated using SHERPA2.2.1 [163]. NLO accurate matrix element calculations are performed using Comix [179] and OPENLOOPS libraries for processes with up to two partons, and LO accurate for processes with up to four partons and matched with SHERPA parton shower simulation using the MEPS@NLO prescription [180] with a dedicated set of tune parameters based on NNPDF3.0NLO PDF set. A data-driven correction was derived in the dilepton channel for Z+jets events with at least two heavy-flavor jets using the distribution of the invariant mass of the dilepton system ($m_{\ell\ell}$) in regions with at least two jets and inside the Z-boson mass window ($|m_{\ell\ell} - 91| < 8$ GeV), to ensure orthogonality with the analysis regions. Three regions with zero, one or at least two b-tagged jets at 70% working point are defined to be enriched in Z-boson production with additional light jets, exactly one or at least two heavy-flavor jets. Scale factors between data and MC are calculated by equating the sum of the predicted Z+jets yields multiplied by the corresponding k-factors with the yield in data after the expected contribution from the other samples is removed. A 25% flat increase of the Z-boson plus heavy flavor jets yields is found to improve the modelling of this process, consistent with Reference [181].

The $t\bar{t}V$ events are generated using MADGRAPH5_AMC@NLO2.3.3 at NLO in QCD, with the renormalisation and factorization scales set to $0.5 \times \sum_i m_T(i)$, where the sum runs over all particles generated from the matrix element calculation.

Single-top t-channel, s-channel and tW processes are modelled using POWHEGBOXv2 at NLO in QCD. For t-channel production, events are generated in the four-flavor scheme with the NNPDF3.0NLONF4 PDF set and with the renormalisation and factorization scales set to $m_T(b)$ [182]. For s-channel and tW production, events are generated in the five-flavor scheme with the NNPDF3.0NLO PDF set and with renormalisation and factorization scales set to the top quark mass. For tW production, the diagram removal scheme is used to handle the interference with $t\bar{t}$ production. An additional sample in which the diagram subtraction scheme is employed instead, is used to assess the uncertainty associated with the modelling of the interference.

The tZq (tWZ) events are generated with MADGRAPH5_aMC@NLO 2.3.3 at LO (NLO) in QCD with the CTEQ6L1(NNPDF3.0NLO) PDF set and the renormalisation and factorization scales set to $4 \times m_T(b)$ ($m(t)$). The diagram removal scheme is used to handle the interference between tWZ and $t\bar{t}Z$.

Events with four top quarks ($t\bar{t}t\bar{t}$) are generated with MADGRAPH5_aMC@NLO2.3.3 at NLO in QCD with the NNPDF3.1NLO PDF set and the renormalisation and factorization scales set to $0.25 \times \sum_i m_T(i)$.

Diboson events are simulated with SHERPA using the NNPDF3.0NLO PDF set and a dedicated set of tune parameters. The multiple matrix element calculations are matched and merged with the SHERPA parton shower based on the Catani-Seymour dipole factorization using the MEPS@NLO prescription. For semileptonic or fully leptonic diboson samples, as well as loop-induced diboson samples, the virtual QCD corrections to the NLO matrix element are provided by the OPENLOOPS library. The NNPDF3.0NNLO PDF set is used, alongside a dedicated set of tunned parton shower parameters developed by the SHERPA authors.

7.2 Object and event reconstruction

The object and event reconstruction strategies are mostly common between the CP and STXS analyses. Proton-proton collision events at $\sqrt{s} = 13$ TeV recorded by the ATLAS detector between 2015 and 2018 during periods of LHC stable-beam collision mode and with all relevant subsystems operational are considered, amounting to a total of 139 fb^{-1}, corresponding to the full Run 2 data set.

Electrons are reconstructed from ID tracks matched to energy deposits in the electromagnetic calorimeter and are required to have $p_{\mathrm{T}} > 10$ GeV and $|\eta| < 2.47$ and to satisfy the *Medium* likelihood identification criterion. Candidates in the calorimeter barrel-endcap transition region are excluded. Muons are reconstructed by matching ID tracks to full detector tracks or to track segments in the muon spectrometer, are required to have $p_{\mathrm{T}} > 10$ GeV and $|\eta| < 2.5$, and to satisfy the *Loose* identification criterion. For electrons (muons), the longitudinal impact parameter is required to be $|z_0 \sin(\theta)| < 0.5$ mm and the transverse impact parameter significance must satisfy $d_0/\sigma(d_0) < 5(3)$, in order to ensure that their origin is compatible with the primary vertex of the event.

Small-R jets are reconstructed from noise-suppressed topo-clusters calibrated at the electromagnetic scale, using the anti-k_t algorithm with a radius parameter of 0.4. The average energy contribution from pileup is subtracted according to the jet area and jets are calibrated as described in Section 5.6. The effect of pileup is further reduced by using track information to ensure that the jets are consistent with the primary vertex of the event. Jets are required to have $p_{\mathrm{T}} > 25$ GeV and $|\eta| < 2.5$. Jets must pass quality criteria designed to reject jets originating from non-collisional background sources or detector noise. Any events containing at least one jet that does not pass these criteria is rejected. To reduce the effect of pileup, jets with $p_{\mathrm{T}} < 120$ GeV and $|\eta| < 2.5$ are required to be consistent with the primary vertex using the Jet Vertex Tagger (JVT) algorithm in the *Medium* working point.

For the boosted regime, the constituents of small-R jets are reclustered using the anti-k_t algorithm

Process	ME generator	ME PDF	PS	Normalisation
Other backgrounds				
tW	POWHEGBOX v2 [DR]	NNPDF3.0NLO	PYTHIA8.230	NLO+NNLL
	POWHEGBOX v2 [DS]	NNPDF3.0NLO	PYTHIA8.230	NLO+NNLL
	POWHEGBOX v2 [DR]	NNPDF3.0NLO	HERWIG7.04	NLO+NNLL
	MADGRAPH5_AMC@NLO v2.6.2 [DR]	CT10NLO	PYTHIA8.230	NLO+NNLL
t-chan	POWHEGBOX v2	NNPDF3.0NLOnf4	PYTHIA8.230	NLO
	POWHEGBOX v2	NNPDF3.0NLOnf4	HERWIG7.04	NLO
	MADGRAPH5_AMC@NLO v2.6.2	NNPDF3.0NLOnf4	PYTHIA8.230	NLO
s-chan	POWHEGBOX v2	NNPDF3.0NLO	PYTHIA8.230	NLO
	POWHEGBOX v2	NNPDF3.0NLO	HERWIG7.04	NLO
	MADGRAPH5_AMC@NLO v2.6.2	NNPDF3.0NLO	PYTHIA8.230	NLO
W+jets	SHERPAv2.2.1 (NLO [2j], LO [4j])	NNPDF3.0NNLO	SHERPA	NNLO
Z+jets	SHERPAv2.2.1 (NLO [2j], LO [4j])	NNPDF3.0NNLO	SHERPA	NNLO
VV (had.)	SHERPA v2.2.1	NNPDF3.0NNLO	SHERPA	–
VV (lep.)	SHERPA v2.2.2	NNPDF3.0NNLO	SHERPA	–
VV (lep.) + jj	SHERPA v2.2.2 (LO [EW])	NNPDF3.0NNLO	SHERPA	–
$t\bar{t}W$	MADGRAPH5_AMC@NLO v2.3.3	NNPDF3.0NLO	PYTHIA8.210	NLO+NLO (EW)
	SHERPA v2.0.0 (LO [2j])	NNPDF3.0NNLO	SHERPA	NLO+NLO (EW)
$t\bar{t}\ell\ell$	MADGRAPH5_AMC@NLO v2.3.3	NNPDF3.0NLO	PYTHIA8.210	NLO+NLO (EW)
	SHERPA v2.0.0 (LO [1j])	NNPDF3.0NNLO	SHERPA	NLO+NLO (EW)
$t\bar{t}Z(qq,\nu\nu)$	MADGRAPH5_AMC@NLO v2.3.3	NNPDF3.0NLO	PYTHIA8.210	NLO+NLO (EW)
	SHERPA v2.0.0 (LO [2j])	NNPDF3.0NNLO	SHERPA	NLO+NLO (EW)
$t\bar{t}t\bar{t}$	MADGRAPH5_AMC@NLO v2.3.3	NNPDF3.1NLO	PYTHIA8.230	NLO+NLO (EW)
tZq	MADGRAPH5_AMC@NLO v2.3.3 (LO)	CTEQ6L1	PYTHIA8.212	–
tWZ	MADGRAPH5_AMC@NLO v2.3.3 [DR]	NNPDF3.0NLO	PYTHIA8.230	–

Table 7.3: Summary of Monte Carlo generators used to simulate smaller background samples. The first line for each category corresponds to the nominal sample; the remaining ones are alternative samples used to estimate systematic uncertainties.

with a radius parameter of 1.0, resulting in a collection of fully-calibrated large-R jets, referred to as reclustered (RC) jets. These jets are required to have an invariant mass larger than 50 GeV, $p_{\mathrm{T}} > 200$ GeV and contain at least two small-R jets. By reclustering small-R jets as fully-calibrated constituents of RC jets, the uncertainties can be directly propagated to the large-R jets without the need for further calibrations or uncertainties. The collection of RC jets is used to identify the Higgs boson and top quark candidates in events where these particles have a high transverse momentum such that their decay products are very collimated.

Small-R jets containing b-hadrons are identified (b-tagged) with the MV2c10 multivariate algorithm described in Section 5.7. Four working points are used in the analyses, with efficiencies ranging from 85% to 60% for b-jets with $p_{\mathrm{T}} > 20$ GeV. Jets are assigned a pseudo-continuous b-tagging score based on the tightest working point they satisfy. Correction factors are applied to simulated events to account for differences in b-tagging efficiencies and mistag rates between simulation and data, as described in Section 5.7.

Hadronically-decaying τ-leptons (τ_{had}) are distinguished from jets through a multivariate discriminant based on calorimetric shower shapes and tracking information. They are required to have $p_{\mathrm{T}} > 25$ GeV and $|\eta| < 2.5$, and to satisfy the *Medium* τ-identification working point.

An overlap removal procedure is applied to avoid double-counting of objects. The closest jet within $\Delta R_y = \sqrt{(\Delta y)^2 + (\Delta\phi)^2} = 0.2$ of a selected electron is removed. If the closest jet passing this selection is within $\Delta R_y = 0.4$ of an electron, the electron is removed. Muons are usually removed if they are within $\Delta R_y < 0.4$ of a jet, to reduce the contribution from heavy-flavor decays inside jets. However, if the jet has less than three associated tracks, then the muon is kept and the jet removed. A τ_{had} candidate is removed if it is within $\Delta R_y < 0.2$ of an electron or muon. No overlap removal is performed between jets and τ_{had} candidates.

The missing transverse momentum (vector quantity with magnitude $E_{\mathrm{T}}^{\mathrm{miss}}$) is defined as the negative vector sum of the p_{T} of all electrons, muons, τ_{had} and jets, with an extra 'soft term' built from additional tracks associated with the primary vertex but not included in the reconstruction of any of the selected objects, to make it more robust against pileup contamination. The missing transverse momentum is not used to select events but it is used as input for the training of some of the multivariate discriminants used in the analyses.

7.2.1 Reconstruction of high-level objects

Particles that are not in the final state cannot be directly reconstructed from the signals measured in the detector. However, these intermediate particles, referred to as high-level objects, carry important information about the topology of the events. For example, the transverse momentum of the Higgs boson is used to define the STXS bins and the four-momenta of the top quarks is crucial to define CP-sensitive angular variables.

In the $t\bar{t}H$ analyses described here, in the resolved regime, the final state objects are combined to reconstruct the high-level objects. The most likely combination is identified using a BDT. In the boosted regime, the Higgs boson can be identified with a RC jet containing its decay products. The probability of a jet to originate from a Higgs boson is calculated by a deep neural network. These algorithms are described in detail below.

Reconstruction BDT

High-level objects are reconstructed from combinations of (b-)jets, leptons and missing transverse energy. In particular, the four-momenta of the W-bosons, Higgs boson and top quarks are reconstructed based on BDTs that are used to identify the most likely assignment of jets to partons. The BDTs take as input high-level variables calculated from reconstructed quantities. For each event, given the large number of (b-)jets present in the final state, multiple possibilities exist to reconstruct each object and for each combination the reconstructed variables will have different values. The correct combination is chosen based on a truth matching procedure that assigns jets to partons based on their ΔR distance. This information is used as target when training the BDTs.

In the single-lepton channel, in order to reconstruct the leptonically-decaying W-boson (referred to as leptonic W) the z-component of the neutrino four-vector is necessary. Its transverse component ($p_{T\nu}$) can be identified with the missing transverse energy (E_T^{miss}) but its longitudinal component ($p_{z\nu}$) can not be directly measured. It can be inferred by assuming that the lepton and E_T^{miss} originate solely from the W-boson decay and imposing a kinematic constraint on the W-boson mass: $m_W^2 = (p_l + p_\nu)^2$, where $p_l = (E_l, p_{xl}, p_{yl}, p_{zl})$ and $p_\nu = (E_\nu, p_{x\nu}, p_{y\nu}, p_{z\nu})$ are the four-momenta of the lepton and neutrino, respectively. This leads to a quadratic equation with two possible solutions:

$$p_{z\nu}^{\pm} = \frac{1}{2}\frac{p_{zl}\beta \pm \sqrt{\Delta}}{E_l^2 - p_{zl}^2}, \tag{7.3}$$

where $\beta = m_W^2 - m_l^2 + 2p_{xl}p_{x\nu} + 2p_{yl}p_{y\nu}$ and $\Delta = E_l^2(\beta^2 + (2p_{zl}p_{T\nu})^2 - (2E_l p_{T\nu})^2)$. If the equation does not have a real solution, which happens for around 20% of the events in a $t\bar{t}H$ sample, the quadratic discriminant is set to zero ($\Delta = 0$). If there are two solutions, both are considered.

The hadronically-decaying W-boson (referred to as hadronic W) is reconstructed from all possible combinations of two non-b-tagged jets. If the event has less than two non-b-tagged jets, combinations of one non-b-tagged jet and one b-tagged jet are used to reconstruct the hadronic W. The hadronic W is not reconstructed in regions with exactly five jets since the missing jet usually originates from the sub-leading quark from the W-boson decay. Variables can still be constructed using information from a single non-b-tagged jet as a *proxy* for the hadronic W-boson.

In the dilepton channel, due to the degeneracy introduced by the existence of two neutrinos, the reconstruction of the four-momenta of the W-bosons, and therefore of the top quarks, is more complicated. A technique called neutrino weighting is employed [183, 184]. Only the sum of the neutrinos' transverse momentum is measured as E_T^{miss} which leads to an under-constrained system of equations that cannot be solved analytically. This can be circumvented by imposing kinematic constraints based on the mass of the W-boson and top quark and on the pseudorapidities of the neutrinos:

$$
\begin{aligned}
(p_l^{1,2} + p_\nu^{1,2})^2 &= m_W^2 = (80.2\ \text{GeV})^2, \\
(p_l^{1,2} + p_\nu^{1,2} + p_b^{1,2})^2 &= m_t^2 = (172.5\ \text{GeV})^2, \\
\eta(\nu), \eta(\bar{\nu}) &= \eta_1, \eta_2,
\end{aligned}
\tag{7.4}
$$

where $p_l^{1,2}$, $p_\nu^{1,2}$ and $p_b^{1,2}$ are the four-momenta of the leptons, neutrinos and b-jets, respectively. The two superscripts correspond to the two top quarks and corresponding decay chains. The possible values of the neutrinos' pseudorapidities are η_1, η_2. Since these are unknown, they are scanned between -5 and 5 in steps of 0.2. For each pair of values for $\eta(\nu)$ and $\eta(\bar{\nu})$, Equation 7.4 can be solved, yielding two possible solutions for the neutrinos' four-vectors. The measured value of E_T^{miss} is compared to the value of E_T^{miss} obtained from Equation 7.4 through a weight defined as:

$$
w = \exp\left(\frac{-\Delta E_x^2}{2\sigma_x^2}\right) \cdot \exp\left(\frac{-\Delta E_y^2}{2\sigma_y^2}\right), \tag{7.5}
$$

where $\Delta E_{x,y}$ is the difference between the missing transverse momentum computed from Equation 7.4 and the observed E_T^{miss} in the x- and y-directions, with resolution $\sigma_{x,y}$. The larger the value of the weight, the closer these quantities are. The pair of values of $\eta(\nu)$, $\eta(\bar{\nu})$ that gives the largest weight is chosen as the correct one and used to reconstruct the $t\bar{t}$ system. However, for some events, Equation 7.4 might not have a real solution, in which case the events are treated separately and assigned to a dedicated category in the CP analysis.

In the single-lepton channel, the top quarks are reconstructed by pairing a W-boson and a b-jet. The remaining jets are used to reconstruct the Higgs boson. In the five-jet region, the hadronic top is reconstructed from a b-jet and a non-b-tagged jet and referred to as "incomplete hadronic top".

Reconstruction BDTs are employed in the dilepton and single-lepton resolved channels to distinguish between correct and incorrect jet-parton assignements using invariant masses and angular variables as well as other kinematic variables. The variables used to train the reconstruction BDTs in the dilepton and single-lepton channels are listed in appendix B in Tables B.1 and B.2, respectively. For each event, the jet-parton assignment corresponding to the highest BDT score is chosen as the correct one and used to calculate kinematic and topological quantities related to the top quarks and Higgs boson that are then used as inputs to a classification BDT, trained to separate signal from background (discussed in section 7.3). Two versions of the reconstruction BDT are trained in each channel: one using only kinematic information related to the decay products of the $t\bar{t}$ pair and another including information from the Higgs boson decay products. The latter leads to the best possible reconstruction performance but it biases the background distributions of the observables related to the Higgs boson towards the signal expectation, thus reducing the separation power between signal and background. Variables obtained from both versions are used as inputs to the classification BDTs.

The BDTs were trained for the previous iteration of the analysis using the TMVA framework [185]. The training was not redone given the good performance already achieved. The training is performed using simulated $t\bar{t}H$ events and iterating over all possible jet combinations. In the single-lepton (dilepton) channel the training is perfomed in an inclusive region with at least six (four) jets and at least four

b-jets at 85% WP.

The Higgs boson is correctly reconstructed in 48% (49%) of the selected $t\bar{t}H$ events in the single-lepton (dilepton) channel in a region with at least six (four) jets and at least four (three) b-jets at the 60% working point [186]. When not including information about the Higgs boson kinematics, the value is 32%.

Boosted region neural network

In the boosted region, a multi-class deep neural network (DNN) is trained to quantify the probability of a given RC jet originating from a Higgs boson, top quark or QCD process. To define the Higgs boson and top quark classes, RC jets are matched to hadronically-decaying Higgs bosons and top quarks at generator level. For the Higgs boson, two b-quarks are required to be within $\Delta R < 0.4$ of the RC jet constituents. For the top quark, one b-quark and at least one decay product of the W-boson are required to be within $\Delta R < 0.4$ of the RC jet. All the remaining jets are labeled as QCD jets.

The DNN is trained on a jet-by-jet basis on a $t\bar{t}H$ POWHEG+PYTHIA8 sample using events with at least one isolated lepton with $p_{\mathrm{T}} > 27$ GeV, at least four small-R jets, at least two of which are b-tagged at 85% WP, and two RC jets with $p_{\mathrm{T}} > 200$ GeV, mass above 50 GeV and at least two constituents. Table B.3 in appendix B summarizes the 17 input variables, related to the RC jet and its constituents, that are used for training the DNN. They are selected from a wider set of variables based on the network's performance, as measured by the diagonality of the confusion matrix (that shows, for each jet, the truth class in one axis and the predicted class in the other). Discrimination of Higgs jets was prioritized.

The DNN was built and trained using the KERAS software package [187] with the TENSORFLOW backend [188]. The architecture consists of 3 layers of 100 nodes each. The hidden layers use the Rectified Linear Unit (ReLU) activation function, defined as $f(x) = \max(0, x)$, where x represents the values of the inputs. The final layer has 3 nodes with softmax output, such that the probabilities of each node add up to unity. The output value of each node corresponds to the probability of a given jet belonging to one of the three categories: Higgs, top or QCD. The jet can then be assigned to the category that has the highest output score.

The Higgs boson jet is correctly identified 76% of the times and the top jets 67% of the times.

7.3 Event selection and analysis strategy

Events are recorded using single-lepton triggers with low p_{T} threshold and a lepton isolation requirement, or with a higher p_{T} threshold, looser identification and without an isolation requirement. The lowest p_{T} threshold for single-muon triggers is 20 (26) GeV in 2015 (2016-2018) and 24 (26) GeV for single-electron triggers. A logical 'OR' of the triggers listed in Table 7.4 is used. A brief explanation of the naming conventions follows below.

Single-electron triggers are seeded by `L1EM20VH` that requires at least one electromagnetic deposit with $p_{\mathrm{T}} > 20$ GeV, hadronic core isolation applied (`H`) and with a p_{T} threshold that varies with η to account for energy loss (`V`). At HLT, the electron p_{T} thresholds are 24, 60 and 120 GeV in 2015 and 26, 60 and 140 GeV in 2016-2018. In 2015, for the lower p_{T} thresholds, the *medium* identification working point based on a likelihood discriminant is used. For electrons with $p_{\mathrm{T}} \geq 120$ GeV the *loose* working point is used. In 2016-2018, the *tight* working point is used for the lower p_{T} threshold of 26 GeV. The `nod0` key word indicates that a specific tune of the likelihood algorithm is used that does not include information about the electron track d_0 parameter. For the lower p_{T} threshold, a track-based loose isolation requirement is also applied (`ivarloose`) in a variable cone around the electron candidate with a maximum size of $\Delta R = 0.2$.

Single-muon triggers are seeded by `L1MU15` that requires at least one muon with $p_{\mathrm{T}} > 15$ GeV. At HLT, the p_{T} thresholds are 20 and 50 GeV in 2015. In 2016-2018, the lower p_{T} threshold was increased to 26 GeV. For the lower p_{T} triggers, *loose* isolation in a cone of $\Delta R = 0.2$ and *medium* isolation in a variable cone with a maximum size of $\Delta R = 0.3$ are applied in 2015 and 2016-2018, respectively.

Years	Single-electron triggers	Single-muon triggers
2015	HLT_e24_lhmedium_L1EM20VH HLT_e60_lhmedium HLT_e120_lhloose	HLT_mu20_iloose_L1MU15 HLT_mu50
2016–2018	HLT_e26_lhtight_nod0_ivarloose HLT_e60_lhmedium_nod0 HLT_e140_lhloose_nod0	HLT_mu26_ivarmedium HLT_mu50

Table 7.4: Single-electron and single-muon trigger menus used in the dilepton and single-lepton channels, depending on the year of data-taking.

Two channels are considered based on the number of leptons in the event. In the single-lepton channel events must have exactly one lepton while in the dilepton channel exactly two leptons with opposite electrical charge are required (ee, $\mu\mu$ or $e\mu$). At least one of the leptons must have $p_{\mathrm{T}} > 27$ GeV and be matched to a corresponding trigger level object. In the ee and $\mu\mu$ channels, the dilepton invariant mass must be above 15 GeV and outside the Z-boson mass window (defined as $83 < m_{\ell\ell} < 99$ GeV, where $m_{\ell\ell}$ is the invariant mass of the dilepton system). To ensure orthogonality with other $t\bar{t}H$ analyses, events are vetoed if they contain at least one (two) τ_{had} candidates in the dilepton (single-lepton) channel. Leptons are required to satisfy additional identification and isolation criteria to further suppress background contributions: electrons (muons) must pass the *Tight* (*Medium*) identification criterion and the *Gradient* (*FixedCutTightTrackOnly*) isolation criterion [189–191]. Events in the single-lepton channel are further subdivided into resolved and boosted. Boosted events have a topology consistent with the decay of a Higgs boson with a large transverse momentum, such that its decay products can be reconstructed as a single large-R jet with a two-prong substructure.

Events are categorized into orthogonal regions based on the number of small- and large-R jets and b-tagged jets. The control regions (CRs) and inclusive signal regions (SRs) are summarized in Table 7.5. In the single-lepton channel, events are first assigned to the boosted category if they contain at least four b-tagged jets at the 85% working point, one boosted Higgs candidate (identified by the DNN described in Section 7.2) and at least two b-tagged jets at the 77% working point not belonging to the Higgs boson candidate. The boosted Higgs boson candidate must have $p_{\mathrm{T}} > 300$ GeV, an invariant mass in $[100 - 140]$ GeV, a DNN score above 0.6 and exactly two constituent jets b-tagged at the 85% working point. If more than one candidate is found, the one with the mass closest to that of the Higgs boson is chosen. The remaining events are assigned to the resolved category. Two control regions are defined by selecting events with exactly five jets and at least four b-tagged jets at the 70% or 60% working point: $\mathrm{CR}^{5j}_{\geq 4b@70}$ and $\mathrm{CR}^{5j}_{\geq 4b@60}$, respectively. The $\mathrm{CR}^{5j}_{\geq 4b@70}$ region is additionally required to have less than four b-jets tagged at 60% working point to ensure orthogonality with $\mathrm{CR}^{5j}_{\geq 4b@60}$. Events with at least six jets and at least four b-tagged jets at the 70% working point are assigned to an inclusive region, referred to as $\mathrm{SR}^{\geq 6j}_{\geq 4b@70}$.

In the dilepton channel, one control region is defined containing events with exactly three jets and exactly three b-jets at the 60% working point, $\mathrm{CR}^{3j}_{3b@60}$, and two control regions are defined by selecting events with at least four jets and exactly three b-tagged jets at the 70% and 60% working points, $\mathrm{CR}^{\geq 4j}_{3b@70}$ and $\mathrm{CR}^{\geq 4j}_{3b@60}$, respectively. Similarly to the single-lepton channel, in the $\mathrm{CR}^{\geq 4j}_{3b@70}$ events with exactly three b-jets at 60% working point are vetoed. Events with at least four jets and at least four b-jets at the 70% working point are assigned to an inclusive region, referred to as $\mathrm{SR}^{\geq 4j}_{\geq 4b@70}$.

Table 7.5: Definition of the CRs and inclusive SRs according to the number of jets (N_{jets}) and b-tagged jets ($N_{b-\text{jets}}$) using different b-tagging selection criteria, and the number of boosted Higgs boson candidates ($N_{\text{boosted cand.}}$). For the boosted region, the b-tagged jets flagged with † are not constituents of the boosted Higgs boson candidate. Events must pass $N_{b\text{-tag}}$ requirements for each b-tagging selection criteria.

Region		Dilepton				Single-lepton			
		$\mathrm{SR}^{\geq 4j}_{\geq 4b@70}$	$\mathrm{CR}^{\geq 4j}_{3b@60}$	$\mathrm{CR}^{\geq 4j}_{3b@70}$	$\mathrm{CR}^{3j}_{3b@60}$	$\mathrm{SR}^{\geq 6j}_{\geq 4b@70}$	$\mathrm{CR}^{5j}_{\geq 4b@60}$	$\mathrm{CR}^{5j}_{\geq 4b@70}$	Boosted
N_{jets}		≥ 4			$= 3$	≥ 6	$= 5$		≥ 4
$N_{b\text{-tag}}$	@85%	–				≥ 4			
	@77%	–				–			$\geq 2^{\dagger}$
	@70%	≥ 4	$= 3$			≥ 4			–
	@60%	–	$= 3$	< 3	$= 3$	–	≥ 4	< 4	–
$N_{\text{boosted cand.}}$		–				0			≥ 1

The inclusive signal regions and boosted region defined in Table 7.5 are further subdivided in different ways in the STXS and CP analyses, while the control regions are treated in the same way in both analyses. In the single-lepton resolved control regions, $\Delta R_{bb}^{\text{avg}}$ is used as discriminant variable while in the dilepton channel the event yield is used in all control regions. This variable is computed as the average ΔR distance between all pairs of b-jets constructed from the four b-jets with the highest b-tagging score. The comparison between data and MC prediction for the discriminant variables can be found in Figure 7.3 for the single-lepton and dilepton control regions, in the top and bottom rows, respectively.

STXS analysis

The signal regions in the single-lepton ($\text{SR}^{\geq 6j}_{\geq 4b@70}$) and dilepton channels ($\text{SR}^{\geq 4j}_{\geq 4b@70}$) and the boosted region are split based on the reconstructed Higgs p_{T} (p_{T}^{H}) using the bin boundaries defined within the LHC Higgs cross-section working group: $0 < p_{\text{T}}^{H} < 120$ GeV, $120 < p_{\text{T}}^{H} < 200$ GeV, $200 < p_{\text{T}}^{H} < 300$ GeV, $300 < p_{\text{T}}^{H} < 450$ GeV and $p_{\text{T}}^{H} > 450$ GeV. In the dilepton channel, due to the lower number of events, the last two bins are merged: $p_{\text{T}}^{H} > 300$ GeV. This leads to a total of 11 SRs: 5 in the single-lepton resolved channel, 4 in the dilepton channel and 2 in the boosted channel where the subdivision in bins of p_{T}^{H} starts only at 300 GeV, due to the requirement previously applied to the Higgs candidate p_{T}.

In most signal regions a multivariate discriminant is used for the statistical analysis. The exception is the highest p_{T}^{H} bin in the single-lepton resolved channel where the event yield is used due to the very low number of events. The comparison of the classification BDT output (or event yield) between data and MC is shown in Figures 7.4, 7.5 and 7.6 for the single-lepton resolved, dilepton and boosted signal regions, respectively.

BDTs are trained independently in the dilepton, single-lepton resolved and boosted signal regions to distinguish between signal and backgrounds, using the variables listed in Tables B.4, B.5 and B.6, respectively. These are commonly referred to as classification BDTs. General kinematic variables and variables obtained from the output of the reconstruction BDT or DNN are used as input for the training. In the single-lepton resolved channel, a likelihood discriminant (LHD) built to distinguish $t\bar{t}H$ from the $t\bar{t}+\geq 1b$ background is also used as input. The trainings are performed in the inclusive SRs defined in Table 7.5: $\text{SR}^{\geq 4j}_{\geq 4b@70}$, $\text{SR}^{\geq 6j}_{\geq 4b@70}$ and boosted. In the boosted region, in addition to the previously described selection, the truth Higgs boson p_{T} is required to be above 300 GeV. The nominal $t\bar{t}H$ POWHEG+PYTHIA8 sample is used as signal for the training. In the dilepton channel, only the $t\bar{t}+\geq 1b$ process estimated from the nominal $t\bar{t}b\bar{b}$ POWHEG+PYTHIA8 four-flavor scheme sample is used as background, while in the single-lepton resolved channel, $t\bar{t}+\geq 1c$ and $t\bar{t}+$light contributions from the $t\bar{t}$ POWHEG+PYTHIA8 five-flavor scheme sample are also included. In the single-lepton boosted region, all backgrounds are considered, since non-$t\bar{t}$ backgrounds have a higher contribution in this channel than in the resolved channels.

In the boosted region, the output of the classification BDT is required to be above -0.05 in order to remove the region dominated by the $t\bar{t}+$light background, that is known to be poorly modelled.

The BDTs are trained with the TMVA framework using events with either even or odd event number, while the final BDT output value is calculated on the other set. This removes potential biases

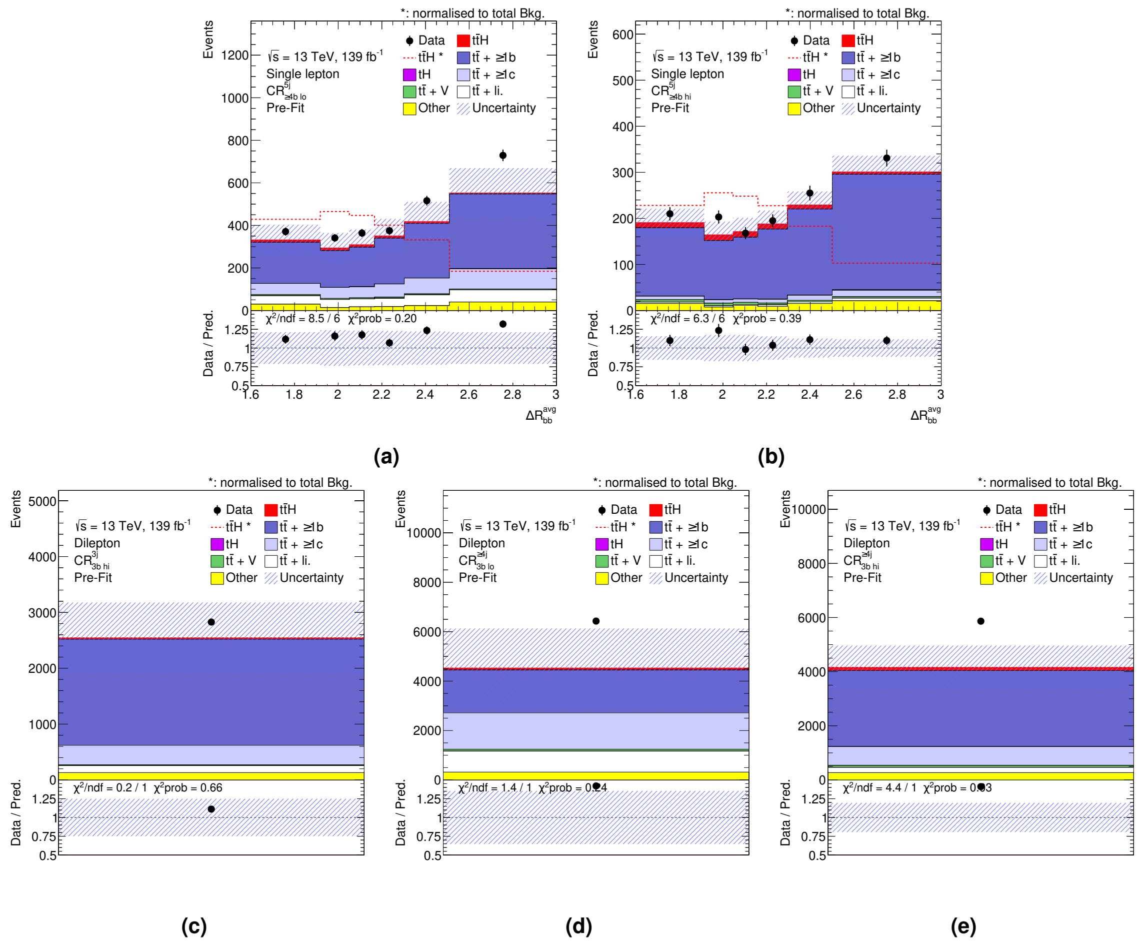

Figure 7.3: Dilepton and single-lepton CRs, common to STXS and CP.

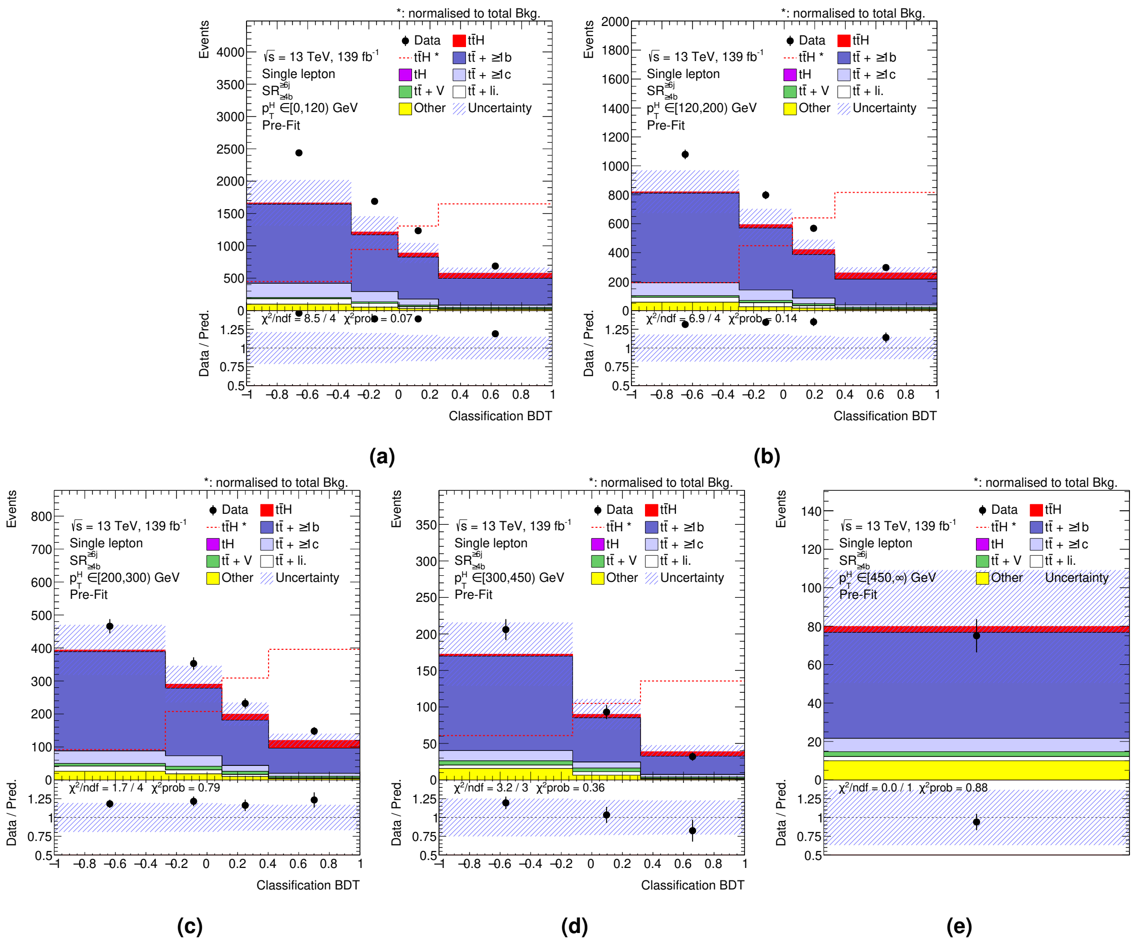

Figure 7.4: Single-lepton resolved STXS SRs.

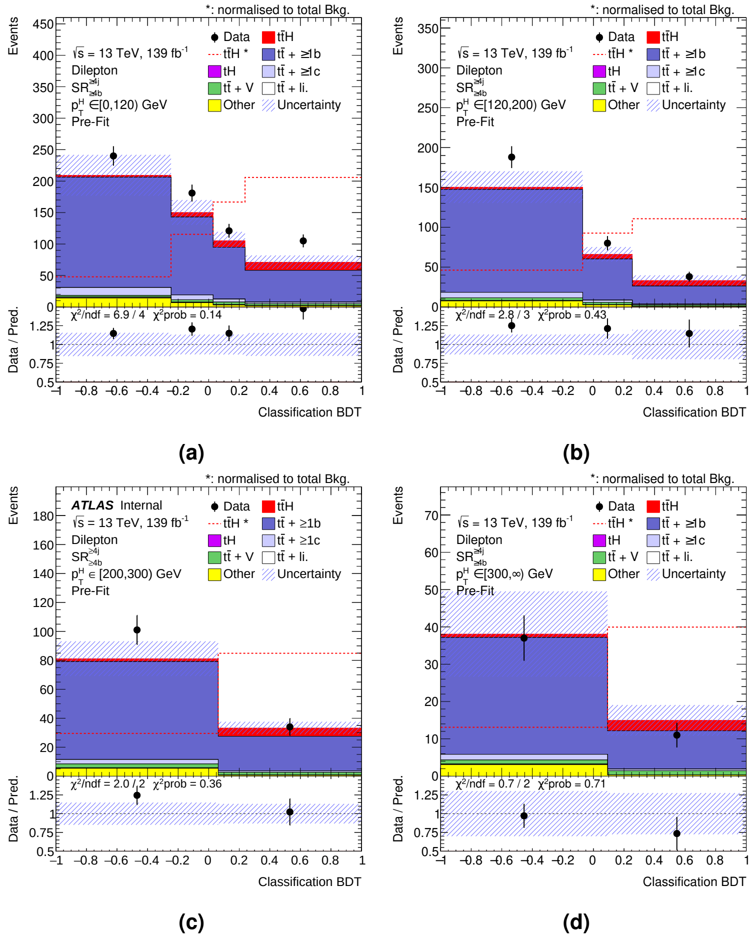

Figure 7.5: Dilepton STXS SRs.

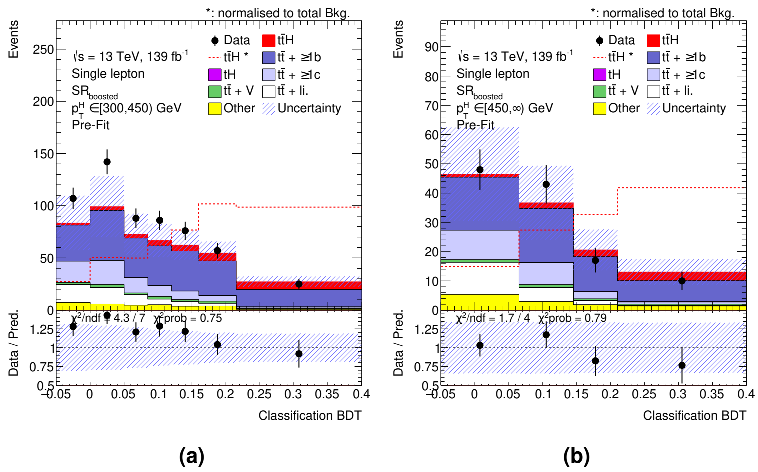

Figure 7.6: Single-lepton boosted STXS SRs.

from overtraining. No significant differences are observed between the trainings performed in even or odd event numbers. In the single-lepton resolved channel, the highest ranked variables are the LHD, $\Delta R_{bb}^{\text{avg}}$ and $m_{bb}^{\text{min }\Delta R}$. In the boosted channel, the DNN Higgs probability for the Higgs candidate, the sum of pseudo-continuous b-tagging scores of the jets associated to the Higgs and top, and the mass of the hadronic top have the highest importance.

CP analysis

The CP analysis makes use of the classification BDTs trained for the STXS analysis to split the inclusive signal regions in the dilepton and single-lepton resolved channel into regions increasingly more pure in $t\bar{t}H$. In these regions, variables sensitive to the CP properties of the $t\bar{t}H$ vertex are used as final discriminants for the statistical anaylsis.

In the SR$^{\geq 4j}_{\geq 4b@70}$ region, events for which the reconstruction of the $t\bar{t}$ pair is not possible, since the neutrino weighting method might not yield a real solution, are assigned to a dedicated control region: CR$^{\geq 4j,\geq 4b}_{\text{no-reco}}$. In this region, the pseudorapidity difference between the leptons, $\Delta\eta(\ell\ell)$, is used as discriminating variable. It works as a proxy for the pseudorapidity difference between the top quarks, which is known to be larger in CP-odd $t\bar{t}H$ production. The comparison between data and MC in this region is shown in Figure 7.8a. The remaining events are categorized into three regions based on the output of the classification BDT: CR$^{\geq 4j,\geq 4b}$ with BDT $\in [-1, -0.086[$, SR$^{\geq 4j,\geq 4b}_{1}$ with BDT $\in [-0.086, 0.186[$ SR$^{\geq 4j,\geq 4b}_{2}$ with BDT $\in [0.186, 1]$. In these regions, the $b_4(t\bar{t})$ variable is used in the statistical analysis. It is defined as:

$$b_4(t\bar{t}) = \frac{p^z_t p^z_{\bar{t}}}{|\vec{p}_t||\vec{p}_{\bar{t}}|}, \tag{7.6}$$

where p^z_i and $\vec{p_i}$ with $i = t, \bar{t}$ are the longitudinal momentum and momentum three-vector of particle i, respectively. It exploits the fact that in CP-odd $t\bar{t}H$ production the top quarks travel more often in opposite direction and closer to the beam pipe, when compared to CP-even $t\bar{t}H$ production.

Events in the SR$^{\geq 6j}_{\geq 4b@70}$ region are split into three regions based on the output of the classification BDT: CR$^{\geq 6j,\geq 4b}_{1}$ with BDT $\in [-1, -0.128[$, CR$^{\geq 6j,\geq 4b}_{2}$ with BDT $\in [-0.128, 0.249[$ and SR$^{\geq 6j,\geq 4b}$ with BDT $\in [0.249, 1]$. In these regions, the $b_2^{t\bar{t}H}(t\bar{t})$ variable is used. It is calculated as follows, using quantities defined in the rest frame of the $t\bar{t}H$ system:

$$b_2 = \frac{(\vec{p}_t \times \hat{n}) \cdot (\vec{p}_{\bar{t}} \times \hat{n})}{|\vec{p}_t||\vec{p}_{\bar{t}}|}, \tag{7.7}$$

where $\vec{p_i}$ with $i = t, \bar{t}$ is the momentum three-vector of particle i and $\hat{n}$ is the unit vector that defines the z-axis. In $t\bar{t}H$ CP-odd production the azimuthal separation of top quarks is smaller and their fraction of longitudinal momentum is larger when compared to $t\bar{t}H$ CP-even production. Both of these effects are exploited by this variable.

The distributions of the b_4 and b_2 variables in data and MC are shown in Figures 7.8b, 7.8c and 7.8d for the dilepton channel and in Figures 7.7a, 7.7b and 7.7c for the single-lepton resolved channel.

The boosted region is taken inclusively and the output of the classification BDT is used as discriminating variable. As in the STXS analysis, the output of the classification BDT in the boosted region is required to be above -0.05 to remove the contribution from the $t\bar{t}$+light background. The comparison between data and MC is shown in Figure 7.7d.

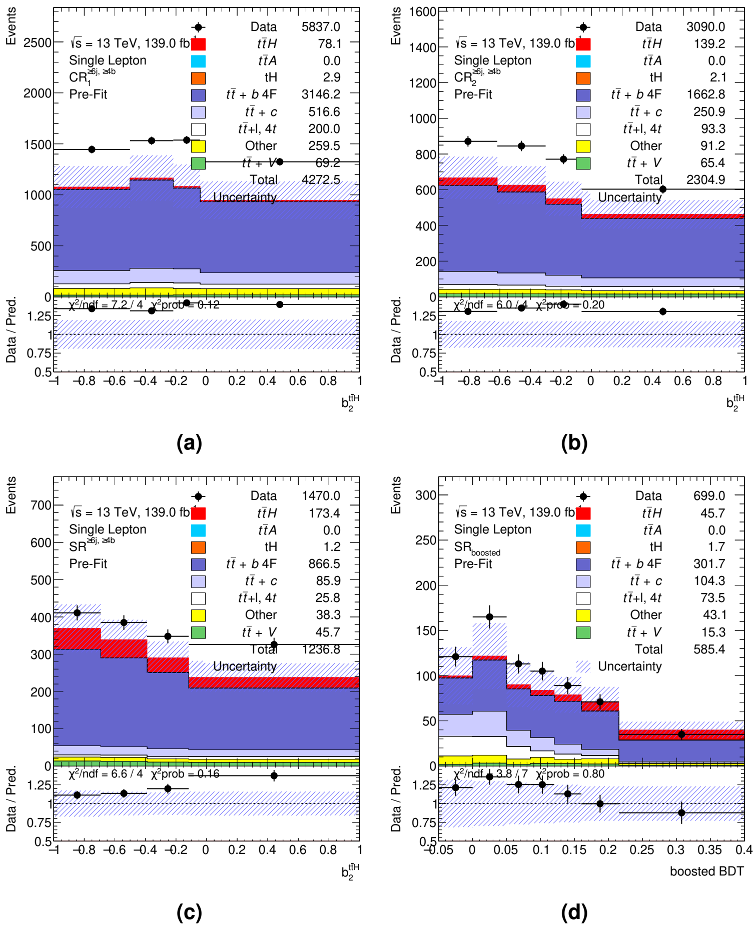

Figure 7.7: Single-lepton resolved and boosted dedicated CP-sensitive regions.

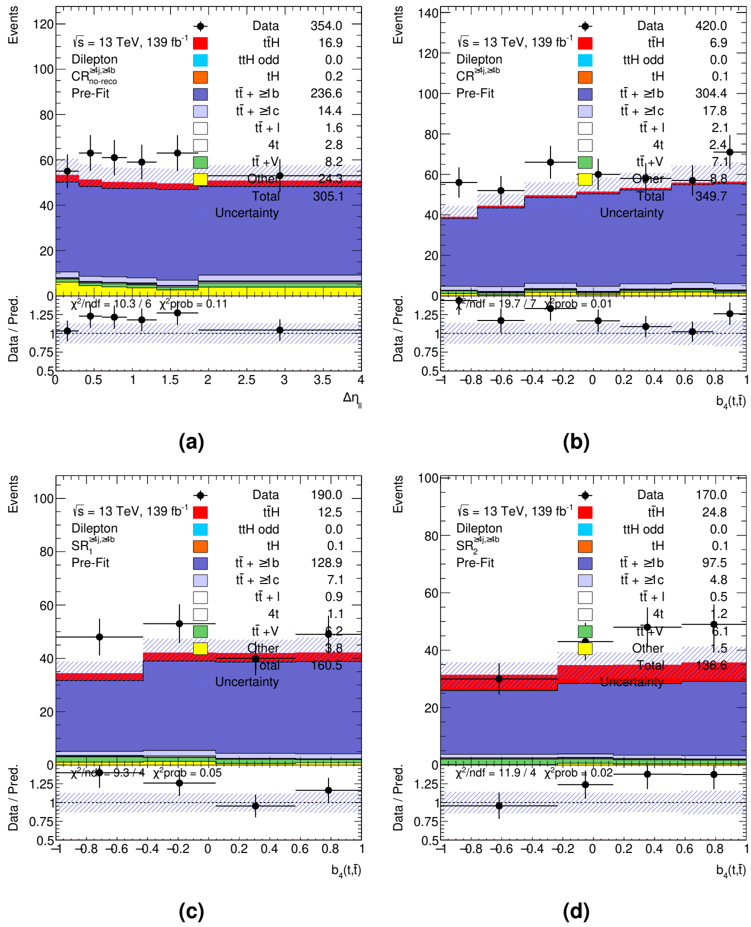

Figure 7.8: Dilepton dedicated CP-sensitive regions.

7.4 Systematic uncertainties

Systematic uncertainties are assessed for three main sources: theoretical uncertainties on the modelling of the signal process, background modelling uncertainties and experimental uncertainties associated to the reconstruction, identification and calibration of leptons, jets, b-jets and missing transverse momentum. Uncertainties accounting for the limited number of events are also considered for all simulated samples.

The number of nuisance parameters associated with each uncertainty source are listed in Table 7.6 for the STXS and CP analyses. The treatment of experimental uncertainties is common to both analyses. The signal and background modelling uncertainties differ between the analyses. For signal these differences arise from different $t\bar{t}H$ nominal samples and from the different treatment of the tH process. For background, an additional source of uncertainty is considered in the CP analysis. For the remaining common modelling uncertainties the number of nuisance parameters is decided based on the analysis regions and specific analysis needs. Further details follow below.

7.4.1 $t\bar{t}H$ and tH modelling

In this section the uncertainties associated with the modelling of the $t\bar{t}H$ and tH processes are described, even though tH is not considered as a signal in the STXS measurement, as previously mentioned.

For the $t\bar{t}H$ SM sample, the combined effect of PDF and α_S variations amounts to a $\pm3.6\%$ normalisation uncertainty [192]. The effect of including 30 independent nuisance parameters, corresponding to the comparisons between the 30 eigenvectors of the `PDF4LHC15_nlo_nf4_30` variation set and its nominal weights was found to have no impact in the STXS fit. Therefore, these nuisance parameters are not included in the fit in neither the STXS nor the CP analyses. Uncertainties due to missing higher order QCD corrections in the total cross-section calculation are estimated by varying the μ_{R} and μ_{F} scales in the matrix element up and down by a factor of 0.5 or 2.0. The largest effect on the cross-section is found to be $^{+5.8\%}_{-9.2\%}$. In the STXS analysis, this uncertainty is symmetrized amounting to $^{+9.2\%}_{-9.2\%}$. Additionally, due to the categorization in bins of the reconstructed Higgs p_{T}, this uncertainty needs to be estimated in each bin and the effects of bin migrations need to be taken into account. These are evaluated using the Stewart-Tackman procedure and the summary of the migration uncertainties, as well as the uncertainties on the bin-by-bin cross-sections are shown in Table 7.7. An uncertainty is also assigned to the Higgs boson decay modes, amounting to $^{+1.2\%}_{-1.3\%}$ for the $H \to b\bar{b}$ decay channel, $^{+1.6\%}_{-1.5\%}$ for $H \to WW^*$ which is the second most probable decay mode and $\pm5\%$ for all other decay modes, that are subdominant in the analysis phase space.

Uncertainties associated with the amount of radiation in the initial and final states, ISR and FSR, are estimated by varying internal settings of the generator and parton shower simulations, and are applied as event weights, following the same prescription as for $t\bar{t}H$.

To assess the uncertainties in the $t\bar{t}H$ process due to the NLO matching procedure and the parton shower and hadronization simulation, the nominal $t\bar{t}H$ POWHEG+PYTHIA8 sample is compared to

		No. of components	
Systematic uncertainty	Type	STXS	CP
Experimental uncertainties			
Luminosity	N	1	
Pileup modelling	SN	1	
Physics Objects			
Electrons	SN	7	
Muons	SN	15	
Jet energy scale	SN	31	
Jet energy resolution	SN	9	
Jet vertex tagger	SN	1	
$E_{\mathrm{T}}^{\mathrm{miss}}$	SN	3	
b-tagging			
Efficiency	SN	45	
Mis-tag rate (c)	SN	20	
Mis-tag rate (light)	SN	20	
Signal modelling			
$t\bar{t}H$ cross-section	N	2	
H branching fractions	N	3	
$t\bar{t}H$ modelling	SN	4	
$t\bar{t}$ background modelling			
$t\bar{t}$ cross-section	N	1	
$t\bar{t}+\geq 1c$ normalisation	N	1	
$t\bar{t}+\geq 1b$ normalisation	N (free floating)	1	
$t\bar{t}$+light modelling	SN	4	
$t\bar{t}+\geq 1c$ modelling	SN	4	
$t\bar{t}+\geq 1b$ modelling	SN	17	11
Other backgrounds			
$t\bar{t}W$ cross-section	N	2	
$t\bar{t}Z$ cross-section	N	2	
$t\bar{t}W$ modelling	SN	1	
$t\bar{t}Z$ modelling	SN	1	
Single top cross-section	N	3	
Single top modelling	SN	7	
W+jets normalisation	N	3	
Z+jets normalisation	N	3	
Diboson normalisation	N	1	
$t\bar{t}t\bar{t}$ cross-section	N	1	
Small backgrounds cross-sections	N	3	

Table 7.6: List of systematic uncertainties included in the analysis. An "N" means that the uncertainty is taken as normalisation-only for all processes and channels affected, whereas "SN" means that the uncertainty is taken on both the shapes and the normalisation. Some of the systematic uncertainties are split into several components for a more accurate treatment: the number of such components is indicated in the column labeled as "No. of components". "Small backgrounds" refers to the tZq, tWZ, $tHjb$, and tWH processes.

p_T(H) [GeV]	Δ_{yield} (%)	Δ_{60} (%)	Δ_{120} (%)	Δ_{200} (%)	Δ_{300} (%)	Δ_{450} (%)	Total (%)
0-60	9.2	-9.2	0.0	0.0	0.0	0.0	13.0
60-120	9.2	2.0	-4.6	0.0	0.0	0.0	10.5
120-200	9.2	0.0	6.8	-1.3	0.0	0.0	11.5
200-300	9.2	0.0	6.8	7.1	-0.4	0.0	13.5
300-450	9.2	0.0	6.8	7.1	7.4	-0.1	15.4
450-∞	9.2	0.0	6.8	7.1	7.4	7.6	17.2

Table 7.7: Summary of the uncertainties on total cross-section and on event migrations between STXS bins due to missing higher order terms in the perturbative QCD calculations.

alternative MADGRAPH5_aMC@NLO+PYTHIA8 and POWHEGBOX+HERWIG7 samples, respectively.

For the tH process, two sources of modelling uncertainties are considered for each subprocess ($tHjb$ and tWH). The uncertainty associated with missing higher order QCD corrections is estimated by simultaneously varying the $\mu_{\rm R}$ and $\mu_{\rm F}$ parameters by a factor of 0.5 or 2.0. For the uncertainty associated with the choice of PDF, a single nuisance parameter affecting only the normalisation is considered for each subcomponent in the STXS analysis, with values $\pm3.7\%$ for $tHjb$ and $\pm6.3\%$ for tWH. In the CP analysis, given the importance of this process, the uncertainty is estimated bin-by-bin as the standard deviation of 100 `NNPDF3.0NLO` PDF variations, available as event weights.

In the CP analysis, for all signal processes, the uncertainties are estimated using nominal and alternative samples produced in the SM scenario and the relative variation is propagated to the samples generated in CP-mixed scenarios.

The FeynRules implementation of the UFO model used to generate the samples for the alternative CP scenarios has been validated by comparing the distributions of the discriminant variables used in the fit generated for the SM scenario with and without the UFO model. The minor differences observed are well within the statistical uncertainty of the samples and are therefore deemed not significant. Additionally, a pseudo data test was performed to ensure that the choice of matrix element generator does not affect the signal extraction. A pseudo dataset was constructed by replacing the nominal $t\bar{t}H$ sample with the POWHEGBOX sample in the total MC prediction, for different values of the CP-mixing angle: $\alpha = 0$, $\pi/4$ and $\pi/2$. Since there is currently no implementation of the UFO model in POWHEGBOX, a CP-odd POWHEGBOX $t\bar{t}H$ sample is constructed by reweighting the CP-even POWHEGBOX sample by the percentage difference between the CP-even and CP-odd MADGRAPH5_aMC@NLO samples, bin-by-bin. A POWHEGBOX CP-mixed sample is then constructed by the weighted sum of the CP-even and CP-odd samples. The fit was then performed using the nominal fit model. Only minor deviations from the injected values of $k_t^{'}$ and α are observed and are much smaller than the expected uncertainty in these parameters.

7.4.2 $t\bar{t}$+jets background modelling

An uncertainty of $\pm6\%$ is assigned to the inclusive $t\bar{t}$ cross-section calculated at NNLO+NNLL in QCD, including effects from varying the factorization and renormalisation scales, the PDFs, α_S and the top-quark mass [193], and applied only to the $t\bar{t}+$light component, since this is dominant in $t\bar{t}$ production in the full phase-space. A conservative uncertainty of 100% is assigned to the normalisation of $t\bar{t}+\geq 1c$, while the normalisation of $t\bar{t}+\geq 1b$ is a free-floating parameter.

Systematic uncertainties on the shape and acceptance of the background are estimated by comparing the nominal MC prediction with alternative predictions, obtained with different MC generators or with different settings. Alternative setups can predict very different fractions of $t\bar{t}+\geq 1b$ in the analysis phase space from those of the nominal MC sample. However, the normalisation of $t\bar{t}+\geq 1b$ is measured from data and assigned a free-floating parameter in the fit because it is well known from previous measurements that there is a disagreement between data and the MC prediction. In order for the value extracted from the fit to be directly identified with the cross-section change with respect to the predicted value in the analysis phase space, it is necessary to normalise the systematic uncertainties assigned to this component, such that they do not change the total number of events in the analysis phase space and impact only the overall shape. The number of events in each analysis region can still change. The reweighting factors applied to each systematic sample are documented in Appendix C.

Uncertainties on the amount of initial and final state radiation, ISR and FSR, are estimated by varying the settings of the nominal $t\bar{t}b\bar{b}$ four-flavor scheme ($t\bar{t}$ five-flavor scheme) samples in $t\bar{t}+\geq 1b$ ($t\bar{t}+\geq 1c$ and $t\bar{t}$+light), expressed as event weights. For ISR, the amount of radiation is decreased (increased) by simultaneously varying the μ_R and μ_F scales by a factor 0.5 (2.0) and the VAR3C setting of the A14 tune up (down), which corresponds to setting $\alpha_S^{\text{ISR}} = 0.1423$ (0.115), while the nominal value is 0.127. The latter setting corresponds to varying the renormalisation scale for QCD emission in the initial state, with a larger value of α_S^{ISR} corresponding to less radiation. For FSR, the amount of radiation in the final state is decreased (increased) by varying the renormalisation scale for QCD emission by a factor (0.5) 2.0, corresponding to $\alpha_S^{\text{FSR}} = 0.1423$ (0.1147), with the nominal value being 0.127.

For the uncertainties associated with parton shower and hadronization and with the NLO matching procedure, alternative MC samples directly comparable to the nominal POWHEG+PYTHIA8 $t\bar{t}b\bar{b}$ four-flavor scheme sample could not be produced with enough statistics and within the time frame of the analysis. Therefore, to estimate the impact of these uncertainties on $t\bar{t}+\geq 1b$, comparisons with alternative generators are performed using $t\bar{t}$ five-flavor scheme samples, following the same procedure used for $t\bar{t}+\geq 1c$ and $t\bar{t}$+light, and the relative uncertainty is propagated to the nominal $t\bar{t}+\geq 1b$ prediction. The nominal POWHEG+PYTHIA8 sample is compared with POWHEG+HERWIG7 and MADGRAPH5_AMC@NLO+PYTHIA8 samples to estimate the uncertainties associated with the parton shower and hadronization model and with the NLO matching technique.

Two additional uncertainties are included for the $t\bar{t}+\geq 1b$ background, which is the dominant component in the analysis phase space. An uncertainty is assigned to the relative amount of the $t\bar{t}+\geq 1b$ subcomponents: $\pm 1\sigma$ variations correspond to varying in a correlated way the amount of $t\bar{t}+1b/B$ by $\pm 22\%$ and of $t\bar{t}+\geq 2b$ by $\mp 13\%$. To obtain these values, the ratios between the yields of each subcomponent ($t\bar{t}+1b/B$ and $t\bar{t}+\geq 2b$) and the inclusive $t\bar{t}+\geq 1b$ event yield are calculated for the nominal $t\bar{t}b\bar{b}$ and $t\bar{t}$ samples and for the alternative samples described in the previous paragraph.

The largest difference in the ratios is found to be between the nominal $t\bar{t}b\bar{b}$ four-flavor scheme sample and the POWHEG+HERWIG7 $t\bar{t}$ five-flavor scheme sample. The POWHEG+HERWIG7 $t\bar{t}$ five-flavor scheme sample predicts 13% less $t\bar{t}+\geq 2b$ and 22% more $t\bar{t}+1b/B$ than the nominal $t\bar{t}b\bar{b}$ four-flavor scheme sample. In order to avoid counting multiple times the same effect, the parton shower and NLO matching systematics are defined such that they do not change the fractions of $t\bar{t}+1b/B$ and $t\bar{t}+\geq 2b$.

Another uncertainty is applied to $t\bar{t}+\geq 1b$ to correct the mismodelling of the reconstructed p_{T} of the pair of additional b-jets ($p_{\mathrm{T}}^{b\bar{b}}$) in the signal regions. Here, additional b-jets refer to jets not originating from the decay of top quarks. For the $t\bar{t}H$ signal, this variable can be identified as the reconstructed p_{T} of the Higgs boson candidate. To derive this uncertainty, weights are applied to the ${p_{\mathrm{T}}}^{b\bar{b}}$ distribution in the inclusive signal regions of the dilepton and single-lepton resolved channels, $\mathrm{SR}^{\geq 4j}_{\geq 4b@70}$ and $\mathrm{SR}^{\geq 6j}_{\geq 4b@70}$. The weights are derived per bin and independently for both channels but the uncertainty is applied in a correlated manner. To derive the weights, the MC yields of the non-$t\bar{t}+\geq 1b$ backgrounds are subtracted from data and divided by the MC prediction for $t\bar{t}+\geq 1b$ background in a given bin with an additional factor, $N_{t\bar{t}+\geq 1b}$, included in the denominator to ensure that the weights do not change the total MC prediction of $t\bar{t}+\geq 1b$ in each region:

$$W^i = \frac{\mathrm{Data}^i - \mathrm{MC}^i_{\text{non-}t\bar{t}+\geq 1b}}{\mathrm{MC}^i_{t\bar{t}+\geq 1b}\cdot N_{t\bar{t}+\geq 1b}}, \tag{7.8}$$

where Data^i, $\mathrm{MC}^i_{\text{non-}t\bar{t}+\geq 1b}$ and $\mathrm{MC}^i_{t\bar{t}+\geq 1b}$ are the data, non-$t\bar{t}+\geq 1b$ and $t\bar{t}+\geq 1b$ MC yields in bin i and $N_{t\bar{t}+\geq 1b} = \frac{\mathrm{Data}-\mathrm{MC}_{\text{non-}t\bar{t}+\geq 1b}}{\mathrm{MC}_{t\bar{t}+\geq 1b}}$. The values of the weights are given in Table 7.8.

Channel	p_{T}^{H} bin [GeV]				
	$[0,120)$	$[120,200)$	$[200,300)$	$[300,450)$	$[450,\infty)$
Dilepton	1.01	1.03	0.99	0.76	0.62
Single-lepton	1.05	0.98	0.89	0.79	0.63

Table 7.8: Weights applied in the dilepton and single-lepton channels for the $p_{\mathrm{T}}^{b\bar{b}}$ shape systematic uncertainty, in each of the 5 p_{T}^{H} bins.

The weights derived for the single-lepton resolved channel are also applied to the boosted channel. In the dilepton channel, separate weights are derived for p_{T}^{H} bins in ranges $300-450$ GeV and >450 GeV to properly correlate these uncertainties with the single-lepton channel. The $+1\sigma$ variation corresponds to applying these weights to the nominal $t\bar{t}b\bar{b}$ prediction, thus fully correcting the data/MC disagreement in the inclusive signal regions.

In the CP analysis, an additional uncertainty is included for $t\bar{t}+\geq 1b$ to asses the impact of the choice of flavor scheme. The nominal $t\bar{t}b\bar{b}$ four-flavor scheme prediction is compared with the POWHEG+PYTHIA8 $t\bar{t}$ five-flavor scheme sample. These two samples predict very different shapes for CP-sensitive observables that are not covered by any of the other background modelling uncertainties. For the calculation of this systematic uncertainty, weights are applied to the $t\bar{t}$ sample in bins of the number of jets (nJets) and of $\Delta R^{\mathrm{avg}}_{bb}$ in the inclusive analysis phase space to match the shapes of these distributions in the $t\bar{t}b\bar{b}$ 4FS sample. Reweighting the nJets distribution factors out differences in the number of jets originating from different treatments of QCD radiation in the four- and five-flavor schemes. The distribution of $\Delta R_{bb}^{\text{avg}}$ shows larger disagreement between data and MC in the $t\bar{t}$ five-flavor scheme sample than in the $t\bar{t}b\bar{b}$ four-flavor scheme sample, which justifies using it as the second variable in the two-dimensional weighting procedure.

Feynman diagrams including virtual Higgs bosons are not included in the $t\bar{t}b\bar{b}$ matrix element calculation. In the CP analysis, the values of α and k_t' are free-floating parameters in the fit. Possible deviations of these parameters with respect to the SM could also impact the background prediction and, were the effects large, these should be taken into account coherently for signal and background. To this end, virtual Higgs boson corrections to the $t\bar{t}b\bar{b}$ process were implemented at truth level using the MCFM program. The variations of shape and normalisation of the fit observables (b_2 and b_4) for the $t\bar{t}b\bar{b}$ background were checked as a function of α and k_t'. The dependence on α was found to be negligible while variations of k_t' showed mainly a normalisation effect of $O(1\%)$. Due to the small size of the effect and the difficulties to propagate it from parton-level to the detector-level simulated samples, no uncertainty is applied to account for the missing diagrams.

Uncertainty source	Description		Components
$t\bar{t}$ cross-section	Up or down by 6%		$t\bar{t}$+light
$t\bar{t}+\geq 1b$ normalisation	Free-floating		$t\bar{t}+\geq 1b$
$t\bar{t}+\geq 1c$ normalisation	Up or down by 100%		$t\bar{t}+\geq 1c$
ISR	Varying $\mu_{\mathrm{R}}^{\mathrm{ISR}}$ (PS), μ_{R}&μ_{F} (ME)	in PP8 $t\bar{t}b\bar{b}$ 4FS	$t\bar{t}+\geq 1b$
		in PP8 $t\bar{t}$ 5FS	$t\bar{t}+\geq 1c$, $t\bar{t}$+light
FSR	Varying $\mu_{\mathrm{R}}^{\mathrm{FSR}}$ (PS)	in PP8 $t\bar{t}b\bar{b}$ 4FS	$t\bar{t}+\geq 1b$
		in PP8 $t\bar{t}$ 5FS	$t\bar{t}+\geq 1c$, $t\bar{t}$+light
NLO matching	aMC@NLO+P8 $t\bar{t}$ 5FS	vs. PP8 $t\bar{t}$ 5FS	All
PS & hadronisation	PH7 $t\bar{t}$ 5FS	vs. PP8 $t\bar{t}$ 5FS	All
flavor scheme	PP8 $t\bar{t}$ 5FS	vs. PP8 $t\bar{t}b\bar{b}$ 4FS	$t\bar{t}+\geq 1b$
$t\bar{t}+\geq 1b$ fractions	Variation of the relative fractions of $t\bar{t}+\geq 2b$ and $t\bar{t}+1b/B$		$t\bar{t}+\geq 1b$
$p_{\mathrm{T}}^{b\bar{b}}$ shape	Correction from data of $p_{\mathrm{T}}^{b\bar{b}}$ shape in signal regions		$t\bar{t}+\geq 1b$

Table 7.9: Summary of the sources of systematic uncertainty for $t\bar{t}$+jets modelling. The last column of the table indicates the $t\bar{t}$+jets components to which a systematic uncertainty is assigned. All systematic uncertainty sources are treated as uncorrelated across the three components. The systematic uncertainties listed in the third section of the table are evaluated in such a way as to have no impact on the normalisation of the $t\bar{t}+\geq 2b$ and $t\bar{t}+1b/B$ contribution, and the systematic uncertainty in the last section is evaluated in such a way as to have no impact on the normalisation of the $t\bar{t}+\geq 2b$ sub-components, in the phase-space selected in this analysis.

For each uncertainty source previously described, one or multiple nuisance parameters (NPs) can be considered. If a single NP is assigned to a given uncertainty source it means that it impacts all analysis regions in a correlated way. This is the default procedure, unless stated otherwise. However, this procedure might not be the optimal choice if it is known that a given uncertainty might be correlated with some variables used in the event selection, such as the number of (b-)jets or leptons. Additionally, assigning independent nuisance parameters to each channel or region provides the fit with additional degrees of freedom which might help reduce tensions in the statistical fit and constraints and avoid biasing the signal extraction.

In the STXS analysis, two NPs are considered for the PS uncertainty, for dilepton and single-lepton channels, and 11 for the NLO matching uncertainty, one per STXS bin in the SRs (five for single-lepton and four for dilepton) and two for the single-lepton and dilepton CRs.

In the CP analysis, the PS, NLO matching and choice of flavor scheme uncertainties have three associated NPs each, for the dilepton, single-lepton resolved and boosted channels.

7.4.3 Modelling of smaller backgrounds

A $\pm 5\%$ uncertainty is assigned to the normalisation of all three single-top processes (s-channel, t-channel and tW), with an independent nuisance parameter for each [194, 195]. Uncertainties associated with the NLO matching procedure and the PS and hadronization simulation are estimated for each sub-process by comparing the nominal samples with alternative samples generated with MADGRAPH5_aMC@NLO+PYTHIA8 and POWHEGBOX+HERWIG7, respectively. For the tW process, an uncertainty is assigned to the interference with the $t\bar{t}$ process by comparing the nominal sample produced in POWHEG+PYTHIA8 with the diagram removal scheme with an alternative sample produced by the same generator but using the diagram subtraction scheme. The diagram removal (DR) removes the diagrams at amplitude level while diagram subtraction (DS) removes the diagrams at matrix element level.

Uncertainties to the cross-section of the $t\bar{t}Z$ $(t\bar{t}W)$ backgrounds are assessed as two independent components, one combining the PDF and α_S choices and another associated with the factorization and renormalisation scales, amounting to $\pm 4\%$ $(\pm 3.4\%)$ and $^{+9.6\%}_{-11.3\%}$ $(^{+12.9\%}_{-11.5\%})$, respectively [192]. Uncertainties associated with the NLO matching procedure and PS and hadronization are also assessed for both processes by comparing the nominal MADGRAPH5_aMC@NLO+PYTHIA8 samples with alternative SHERPA samples.

A $\pm 50\%$ normalisation uncertainty is assigned to the $t\bar{t}t\bar{t}$ background, which covers the effects of varying the renormalisation and factorization scales, the PDFs and α_S. For tZq, two uncertainties are assigned to the normalisation: $^{+7.7\%}_{-7.9\%}$ corresponding to the variations of the renormalisation and factorization scales, and $\pm 0.9\%$ associated with the choice of PDF [196]. For tWZ, a single $\pm 50\%$ normalisation uncertainty is included.

A $\pm 40\%$ normalisation uncertainty is assigned to W+jets, as well as independent $\pm 30\%$ uncertainties for events with two and more than three heavy-flavor jets, estimated based on variations of the renormalisation and factorization scales and of the matching parameters of the SHERPA samples. For Z+jets, a $\pm 35\%$ normalisation uncertainty is applied. For diboson processes, a $\pm 50\%$ normalisation uncertainty is included.

7.4.4 Instrumental

Luminosity and pileup modelling The uncertainty on the full Run 2 integrated luminosity is 1.7%, measured by the LUCID-2 detector. MC events are weighted such that the simulated pileup distribution matches the one observed in data. The nominal weight corresponds to $1/1.03$ and it is varied to $1/0.99$ and $1/1.07$ to cover the uncertainty in the ratio of the predicted and measured inelastic cross-section in the fiducial phase-space defined by $M_X > 13$ GeV, where M_X is the mass of the hadronic system [197].

Leptons Experimental uncertainties associated with leptons (electrons and muons) arise from the trigger, reconstruction, identification, isolation, and momentum scale and resolution.

The efficiencies associated with trigger, reconstruction, identification and isolation differ between simulation and data, which is accounted for by applying scale factors (SFs) to MC. These SFs are derived using tag-and-probe methods applied to $Z \to \ell^+\ell^-$ and $J/\Psi \to \ell^+\ell^-$ data and simulated samples [129, 190]. They are subject to systematic uncertainties associated, for example, with the choice of electron identification or isolation working points or the background subtraction technique. These uncertainties are propagated as corrections to the MC event weight. A total of 4 independent nuisance parameters are considered for electrons, and 10 for muons.

Additional sources of uncertainties arise from the correction applied to the lepton's momentum scale and energy resolution in simulation to match those observed in data, measured using the reconstructed dilepton mass from $Z \to \ell^+\ell^-$ and $J/\Psi \to \ell^+\ell^-$ decays. In the case of electrons, the ratio between the energy measured in the calorimeters (E) and the momentum from the tracks reconstructed in the inner detetor (p), E/p, is also measured, benefiting from the larger statistics of the $W \to \ell\nu$ process. To evaluate the impact of the momentum scale uncertainties, the event selection is redone with the lepton energy or momentum varied by $\pm1\sigma$. For the momentum resolution uncertainties, the event selection is redone by smearing the lepton energy or momentum. In total, 3 independent nuisance parameters are considered for electrons and 5 for muons.

Jets and flavor-tagging Uncertainties associated with jets arise from the pileup rejection efficiency of the Jet Vertex Tagging discriminant (JVT), the Jet Energy Scale (JES) and Resolution (JER) and from b-tagging.

The efficiency of selecting hard-scatter jets using the JVT discriminant is measured in data and simulation using tag-and-probe techniques in $Z \to \mu^+\mu^-$+jets events [198]. The differences in efficiencies observed between data and simulation are corrected by applying scale factors, whose effect and associated uncertainties are propagated to the overall MC event weight.

Uncertainties associated with the JES determination arise from the in-situ calibration procedure, pileup mismodelling in MC, differences in response between jets of different flavors, punch-through corrections and from non-closure of the calibration procedure [199]. The final calibration includes a set of 80 uncertainties. Differences in jet response between data and simulation are quantified by balancing the jet p_{T} against a well-known reference object, for example a Z-boson, a photon or multijet system. The majority of the uncertainties arise from the Z/γ+jet and multijet balance calibrations. They correspond to 67 independent sources that are then reduced through principal component analysis to a smaller set of 15. The remaining 13 uncertainties are derived from other sources, summarized in what follows. Pileup uncertainties are included to account for potential MC mismodelling of N_{PV}, μ, ρ and the residual p_{T} dependence. Uncertainties in the η-intercalibration method account for potential mismodelling, statistical uncertainties and non-closure of the method in some regions of the phase space. Additional uncertainties account for differences in the jet response and simulated jet composition of light- and b-quark and gluon-initiated jets (using the conservative default value of

$50\%/50\%$ for the fraction of quark/gluon-initiated jets in all MC samples). An uncertainty is applied to the punch-through correction by comparing the jet response in data and simulation as a function of the number of muon segments. A high-p_T jet uncertainty is derived from single-particle response studies and it is applied to jets with $p_\mathrm{T} > 2$ TeV, which are outside the reach of the in-situ calibration methods. One AFII modelling uncertainty accounts for non-closure in the absolute JES calibration of fast-simulation jets and it is applied only to AFII samples. A total of 30 independent sources are considered, corresponding to 31 NPs since one of them differs between full simulation and AFII.

JER is measured in data and simulation as a function of p_T and η using similar in-situ methods as employed for the JES calibration. The p_T of simulated jets is smeared in MC to match the resolution observed in data. The size of the smearing corresponds to the uncertainty associated with the JER and amounts to 8 independent sources. One of them differs between full simulation and AFII samples, such that a total of 9 NPs are included in the fit.

The b-tagging efficiency and c- and light-mis-tag rates are corrected in simulation to match those observed in data. Scale factors are derived independently for b-, c- and light-jets as a function of $p_\mathrm{T}$using dedicated calibration analyses. The number of uncertainties associated with each calibration are reduced through principal component analysis, leading to 45 and 20 uncorrelated eigen variations for the b-jet and c- and light-jets, respectively. The numbers of these eigen-variations correspond to the number of p_T bins (9 for b-jets and 4 for c- and light-jets) multiplied by the number of bins in the pseudo-continuous MV2c10 discriminant.

Missing transverse momentum All the uncertainties described above related to the energy scale and resolution of the reconstructed objects are propagated to the missing transverse momentum. Additional uncertainties in the scale and resolution of the soft term are considered to account for differences in the p_T balance between the hard and soft components between data and simulation, amounting to three independent sources of uncertainties.

7.5 Statistical treatment

The statistical analysis is based on a binned profile likelihood function constructed as product over all analysis bins of Poisson probability distributions. The likelihood function depends on the parameter(s) of interest (POI) and on the NPs that encode information about the sources of systematic uncertainties considered ($\boldsymbol{\theta} = \{\theta_a, \theta_b, ...\}$). The nuisance parameters are implemented in the likelihood function as Gaussian or log-normal distributions, referred to as priors, that adjust the yields of signal and background. The parameters of interest scale the signal yields with respect to the prediction. In the STXS analysis, the POI is the signal strength, μ, that scales the $t\bar{t}H$ yields relative to the SM expectation. This is the most common use case and will be used here to illustrate the general form of the likelihood function:

$$\mathcal{L}(\mu, \boldsymbol{\theta}) = \prod_{i}^{\text{bins}} \mathcal{P}\left(N_i | \, \lambda\right) \times \prod_{j}^{\text{NPs}} \mathcal{F}_j\left(\tilde{\theta}_j | \, \theta_j\right), \qquad \lambda = \mu \cdot S_i(\boldsymbol{\theta}) + \sum_{b}^{\text{bkgs}} k_b \cdot B_{bi}(\boldsymbol{\theta}). \tag{7.9}$$

The first term describes the analysis regions using a product of Poisson functions over all the bins of the distributions under consideration. Each function returns the probability of observing, in each bin, N events in data given the signal plus background expectation of λ events:

$$\mathcal{P}(N|\lambda) = \frac{\exp^{-\lambda} \lambda^N}{N!}. \tag{7.10}$$

In the first term of equation 7.9 (left), each Poisson function corresponds to one of the analysis bins, including signal and control regions. N_i corresponds to the observed data yield in bin i, while $S_i(\boldsymbol{\theta})$ and $B_{bi}(\boldsymbol{\theta})$ refer to the expected signal and background yields, which depend on the nuisance parameters. The signal strength, μ, scales the signal yield. Dedicated parameters that scale the yields of different background components can also be included. They are usually referred to as normalisation factors and are free-floating parameters in the fit, such that the normalisation of certain backgrounds in the analysis phase space (usually the dominant ones) can be extracted directly from data. In equation 7.9 (right), they are represented by k_b. In this thesis, the notation $k(t\bar{t}+ \geq 1b)$ is used to refer to the $t\bar{t}+ \geq 1b$ background normalisation factor.

The second term in equation 7.9 (left) describes the product of auxiliary functions, $\mathcal{F}_j$, used to constrain the values of nuisance parameters θ_j using an auxiliary measurement $\tilde{\theta_j}$. Two types of constraints are used: unit Gaussian for the systematic uncertainties described in section 7.4 and Poisson for the uncertainties associated with the finite size of the MC samples.

As indicated by the definition of λ in equation 7.9 (right), the yields of signal and backgrounds are also a function of the nuisance parameters. These yields can be defined as:

$$S(\boldsymbol{\theta}) = S_0 \times \prod_k^{NPs} \nu(\theta_k), \qquad B(\boldsymbol{\theta}) = B_0 \times \prod_k^{NPs} \nu(\theta_k), \tag{7.11}$$

where S_0 and B_0 are the nominal values of the expected signal and background yields and the functions $\nu(\theta_k)$ parameterize the dependency of the signal and background yields on the nuisance parameters θ_k. Most of the nuisance parameters described in section 7.4 affect both the shape and normalisation of the distributions. For uncertainties affecting only the shape or only the normalisation, the functions $\nu(\theta_k)$ are defined as:

$$\nu_i^{\text{shape}}(\theta) = 1 + \epsilon_i \times \theta, \qquad \nu^{\text{norm}}(\theta) = (1+\epsilon)^{\theta}, \tag{7.12}$$

where ϵ is the variation in the expected yield obtained from varying the associated quantity θ by $\pm 1\sigma$. For shape uncertainties, each bin i is treated independently.

The test statistic q is a function of the parameter(s) of interest. It is defined as a ratio of likelihood functions. The numerator is calculated using the conditional maximum likelihood estimators, for a given value of the POI(s). The denominator is calculated using the unconditional maximum likelihood estimators, i.e., the values of the POI(s) and nuisance parameters that maximize the likelihood function. The exact expressions are discussed in sections 7.5.1 and 7.5.2 for the STXS and CP analyses, respectively. The test statistic is used to measure the compatibility of the observed data with the null hypothesis or to estimate the values of the parameters of interest and corresponding uncertainties with a given confidence level.

The final results are obtained from a fit to data of the discriminant distributions in all analysis regions, under the signal-plus-background hypothesis. The normalisation of the $t\bar{t} + \geq 1b$ background is also measured from data, simultaneously with the POI(s). The normalisations of smaller backgrounds, that do not have dedicated free-floating parameters, are controlled by the nuisance parameters. Statistical uncertainties in each bin of the discriminant distributions are also included in the fits through dedicated parameters.

Before a fit to data is performed, the expected results can be obtained from a fit to the Asimov dataset. In the case of binned distributions, the Asimov dataset is defined by setting the content of each bin to the signal-plus-background MC prediction, without accounting for statistical fluctuations. In this way, the results of an Asimov fit provide the median outcome under the signal-plus-background hypothesis.

The uncertainty on the best fit value of the POI, $\hat{\mu}$, arises from the uncertainties on the nuisance parameters, Δ_θ. The impact of a single NP on $\hat{\mu}$, $\Delta_{\hat{\mu}}$, can be calculated as:

$$\Delta_{\hat{\mu}} = \hat{\mu}(\hat{\theta} \pm \Delta_\theta) - \hat{\mu}(\hat{\theta}). \tag{7.13}$$

In the fit, the values and uncertainties of the NPs are adjusted to data. The NPs are said to be constrained if the post-fit uncertainty is smaller than the pre-fit one and pulled if their post-fit value differs from the pre-fit one. The statistical model is designed to avoid large pulls and constraints on the NPs but some might still be present. Large pulls indicate that data favors values of the NPs very different from their initial estimate and thus of the underlying physics process that they correspond to. This can be a symptom of a lack of degrees of freedom in the fit or the presence of mismodelling of data in some of the analysis regions not account for by any of the NPs and it might require further investigations to understand their origin or mitigate them.

The TRExFitter framework [200, 201], based on the RooFit package, is used to perform the statistical analyses.

7.5.1 Measurement of inclusive and STXS $t\bar{t}H$ cross-sections

When measuring the $t\bar{t}H$ cross-section, the parameter of interest is the signal strength μ, defined as the ratio between the observed cross-section and the value predicted by the SM. In this case, the test statistics $q(\mu)$ is defined as:

$$q(\mu) = -2 \ln \frac{\mathcal{L}\left(\mu, \hat{\hat{\boldsymbol{\theta}}}(\mu)\right)}{\mathcal{L}(\hat{\mu}, \hat{\boldsymbol{\theta}})}, \tag{7.14}$$

where $\hat{\hat{\boldsymbol{\theta}}}(\mu)$ is the conditional maximum likelihood estimator of $\boldsymbol{\theta}$ for a given value of μ, and $\hat{\mu}$ and $\hat{\theta}$ are the unconditional maximum likelihood estimators, i.e., the values of these parameters that maximize the likelihood.

The null hypothesis corresponds to $\mu = 0$, such that the background prediction alone is enough to explain the observed data.

7.5.2 Measurement of the CP mixing angle and coupling modifier

When measuring the CP-properties, two parameters of interest are considered: the CP-mixing angle (α) and the overall coupling modifier (k'_t). The test statistics is defined as:

$$q(\alpha, k'_t) = -2\ln\frac{\mathcal{L}\left(\alpha, k'_{t,}, \hat{\hat{\boldsymbol{\theta}}}(\alpha, k'_t)\right)}{\mathcal{L}\left(\hat{\alpha}, \hat{k}'_t, \hat{\boldsymbol{\theta}}\right)}, \tag{7.15}$$

where $\hat{\hat{\boldsymbol{\theta}}}(\alpha, k'_t)$ is the conditional maximum likelihood estimator for each pair of values (α, k'_t) and $\hat{\alpha}$, $\hat{k}'_t$ and $\hat{\boldsymbol{\theta}}$ are the unconditional maximum likelihood estimators. This test statistic, being a function of the two POIs, leads to exclusion contours that can be represented in a two dimensional plane. However, for a single value of α, the value of the likelihood calculated for the value k'_t that minimises it can also be plotted leading to a one-dimensional function of α. It has the advantage of allowing for simpler visualization and comparisons between different scenarios (for example, between dilepton and single-lepton individual fits; between expected likelihood scans for different CP scenarios; or comparing expected and observed). Both types of plots are shown and discussed in section 7.7.

7.5.3 Pruning and smoothing of systematic uncertainties

Pruning and smoothing of systematic uncertainties are essential techniques to reduce computation time for the fits, as well as to avoid issues related with the convergence of the minimisation.

The shape and normalisation variations of systematic uncertainties are pruned separately, per region and per sample. For each region and for each sample, the bin-by-bin variations of the systematic templates are checked and the systematic is dropped from the fit if the effects are below a configurable threshold. The pruning thresholds are set to 0.5% for both shape and normalisation. In the STXS analysis, it was shown that reducing the pruning threshold to 0.1% has no impact on the fit results.

In order to cope with statistical fluctuations in the MC samples used to estimate the systematic uncertainties, smoothing algorithms are applied to the systematic templates before the fit. For the systematics associated with the signal and $t\bar{t}+\geq 1b$ background modelling, parabolic smoothing is applied, while for all other systematics the maximum variation algorithm is used [201]. Given the large impact of the $t\bar{t}+\geq 1b$ modelling systematics in the fit, an alternative smoothing algorithm was evaluated using a background-only fit. The impact in the fit results was shown to be non-negligible. However, the small change in the measured value of the $t\bar{t}+\geq 1b$ normalisation factor is well covered by the total uncertainty. The parabolic smoothing was chosen due to its ability to capture the shapes well in most regions.

7.6 Results from inclusive and STXS measurements

The final results of the $t\bar{t}H$ cross-section measurement in the $H \to b\bar{b}$ decay channel using the full Run 2 dataset corresponding to a total integrated luminosity of 139 fb^{-1} are presented in this section.

7.6.1 Post-fit yields and distributions

The predicted (pre-fit) and fitted (post-fit) yields for signal and backgrounds are shown for the dilepton signal and control regions in Tables 7.10 and 7.11, respectively. For the single-lepton channel, these yields are shown in Tables 7.12 and 7.13 for the resolved signal regions and control regions and boosted signal regions, respectively. Post-fit yields are obtained from the inclusive combined fit to data and take into account the pulls and constraints in the NPs. All uncertainties, statistical and systematic, are included. In the post-fit uncertainties, the correlations between NPs are also taken into account.

For the dilepton signal regions, the post-fit distributions of the BDT are shown in Figure 7.9. Figure 7.10 shows the single-lepton post-fit distributions of the BDT in the signal regions and of $\Delta R_{bb}^{\text{avg}}$ in the control regions. In the dilepton control regions, only the event yield is used as discriminant variable in the fit, such that the plots would not add information to what is already presented in Table 7.11 and therefore are shown only in Appendix C, for completion.

In these plots, the stacked histograms represent the predictions from a fit of signal and background to data with μ as a free parameter. Data is shown with black dots. The solid red histogram shows the signal for the best-fit value(s) of the parameter(s) of interest. The red dashed line shows the $t\bar{t}H$ prediction for the SM scenario ($\mu = 1$), scaled to the total data yield in each region to illustrate the shapes of the signal distributions. The hashed bands represent the total post-fit uncertainty. The lower panel shows the ratio between data and the post-fit prediction.

The global goodness of fit is 92%, validating the good post-fit modelling obtained. This value is calculated by comparing the minimum value of the likelihood obtained from the nominal fit and from a fit using a saturated model [202], in which every bin has a dedicated nuisance parameter, and therefore perfect post-fit modelling can be achieved. The difference between the two minimum log-likelihood values is assumed to follow a χ^2 distribution. The probability of obtaining a value for the difference larger than the one observed can be calculated and identified as the goodness of fit.

7.6.2 Signal strength

The measured value of the inclusive signal strength is:

$$\mu = 0.35 \pm 0.20 \text{ (stat.)}^{+0.30}_{-0.28} \text{ (syst.)} = 0.35^{+0.36}_{-0.34}. \tag{7.16}$$

The contributions from statistical and systematic uncertainties are shown separately. The statistical uncertainty is obtained by repeating the fit to data with all NPs fixed to their post-fit values, except $k(t\bar{t}+\geq 1b)$ and μ. The total systematic uncertainty is calculated by subtracting in quadrature the statistical variance from the total variance. The normalisation factor of the $t\bar{t}+\geq 1b$ background is measured to be $k(t\bar{t}+\geq 1b) = 1.28 \pm 0.08$.

	SR$^{\geq 4j}_{\geq 4b}$, $p_{\mathrm{T}}^{H} \in$ [0,120) GeV		SR$^{\geq 4j}_{\geq 4b}$, $p_{\mathrm{T}}^{H} \in$ [120,200) GeV		SR$^{\geq 4j}_{\geq 4b}$, $p_{\mathrm{T}}^{H} \in$ [200,300) GeV		SR$^{\geq 4j}_{\geq 4b}$, $p_{\mathrm{T}}^{H} \in$ [300,∞) GeV	
	Pre-fit	Post-fit	Pre-fit	Post-fit	Pre-fit	Post-fit	Pre-fit	Post-fit
$t\bar{t}H$	33.6 ± 4.1	12 ± 12	15.6 ± 1.8	5.5 ± 5.3	7.71 ± 0.89	2.7 ± 2.6	3.72 ± 0.44	1.3 ± 1.3
tH	0.249 ± 0.065	0.249 ± 0.064	0.148 ± 0.063	0.146 ± 0.061	0.043 ± 0.032	0.043 ± 0.031	0.031 ± 0.027	0.031 ± 0.025
$t\bar{t}+ \geq 1b$	432 ± 59	546 ± 24	203 ± 27	263 ± 12	92 ± 14	116.9 ± 8.8	42 ± 15	37.9 ± 6.0
$t\bar{t}+ \geq 1c$	27 ± 29	48.5 ± 9.1	11 ± 12	16.3 ± 5.0	4.0 ± 4.2	6.5 ± 1.4	1.9 ± 2.1	3.69 ± 0.96
$t\bar{t} + Z$	12.5 ± 2.0	12.6 ± 2.0	7.4 ± 1.6	7.6 ± 1.6	4.18 ± 0.72	4.15 ± 0.70	2.05 ± 0.45	2.06 ± 0.44
$t\bar{t} + W$	0.75 ± 0.31	0.75 ± 0.31	0.38 ± 0.12	0.40 ± 0.11	0.27 ± 0.12	0.27 ± 0.11	0.124 ± 0.068	0.127 ± 0.068
$t\bar{t}$ + light	3.6 ± 4.9	4.8 ± 6.2	0.97 ± 0.96	0.92 ± 0.74	0.46 ± 0.65	0.41 ± 0.47	0.22 ± 0.31	0.22 ± 0.25
$t\bar{t}t\bar{t}$	3.1 ± 1.5	3.0 ± 1.5	2.4 ± 1.2	2.3 ± 1.2	1.38 ± 0.70	1.36 ± 0.69	0.81 ± 0.41	0.79 ± 0.40
Fakes	3.7 ± 1.1	3.7 ± 1.1	1.33 ± 0.51	1.33 ± 0.51	0.40 ± 0.23	0.40 ± 0.23	0.57 ± 0.30	0.57 ± 0.30
Other sources	19.1 ± 6.9	19.3 ± 7.0	7.1 ± 4.4	7.7 ± 4.3	4.3 ± 4.0	4.5 ± 4.1	2.0 ± 1.5	2.0 ± 1.5
Total	536 ± 71	651 ± 21	249 ± 32	305 ± 11	114 ± 16	137.2 ± 8.1	53 ± 15	48.7 ± 5.7
Data	647		306		135		48	

Table 7.10: Pre-fit and post-fit event yields in the dilepton signal regions. Post-fit yields are after the inclusive fit in all channels. All uncertainties are included, taking into account correlations in the post-fit case.

	CR$^{3j}_{3b@60}$		CR$^{\geq 4j}_{3b@60}$		CR$^{\geq 4j}_{3b@70}$	
	Pre-fit	Post-fit	Pre-fit	Post-fit	Pre-fit	Post-fit
$t\bar{t}H$	25.2 ± 3.1	8.8 ± 8.6	117 ± 13	42 ± 41	76.4 ± 8.4	27 ± 27
tH	1.26 ± 0.15	1.23 ± 0.15	2.06 ± 0.39	2.02 ± 0.38	1.19 ± 0.53	1.12 ± 0.50
$t\bar{t}+ \geq 1b$	1900 ± 510	2010 ± 130	2810 ± 300	4070 ± 210	1730 ± 210	2550 ± 160
$t\bar{t}+ \geq 1c$	350 ± 360	550 ± 130	700 ± 710	1190 ± 240	1500 ± 1500	2550 ± 470
$t\bar{t} + Z$	11.1 ± 1.8	10.8 ± 1.7	57.1 ± 7.4	57.5 ± 7.3	51.7 ± 7.0	52.3 ± 6.7
$t\bar{t} + W$	1.88 ± 0.59	1.84 ± 0.55	10.8 ± 1.6	10.9 ± 1.6	21.5 ± 3.7	21.8 ± 3.4
$t\bar{t}$ + light	128 ± 74	119 ± 61	200 ± 120	210 ± 120	850 ± 350	900 ± 340
$t\bar{t}t\bar{t}$	0.047 ± 0.026	0.044 ± 0.024	12.3 ± 6.1	12.0 ± 6.1	8.9 ± 4.5	8.8 ± 4.4
Fakes	6.3 ± 1.8	6.4 ± 1.8	47 ± 12	47 ± 12	56 ± 14	56 ± 14
Other sources	125 ± 35	125 ± 34	211 ± 62	211 ± 62	251 ± 73	257 ± 73
Total	2540 ± 630	2835 ± 54	4160 ± 810	5855 ± 79	4500 ± 1600	6431 ± 83
Data	2827		5865		6429	

Table 7.11: Pre-fit and post-fit event yields in the dilepton control regions.

	SR$^{\geq 6j}_{\geq 4b}$, $p_{\mathrm{T}}^{H} \in$ [0,120) GeV		SR$^{\geq 6j}_{\geq 4b}$, $p_{\mathrm{T}}^{H} \in$ [120,200) GeV		SR$^{\geq 6j}_{\geq 4b}$, $p_{\mathrm{T}}^{H} \in$ [200,300) GeV		SR$^{\geq 6j}_{\geq 4b}$, $p_{\mathrm{T}}^{H} \in$ [300,450) GeV		SR$^{\geq 6j}_{\geq 4b}$, $p_{\mathrm{T}}^{H} \in$ [450,∞) GeV	
	Pre-fit	Post-fit	Pre-fit	Post-fit	Pre-fit	Post-fit	Pre-fit	Post-fit	Pre-fit	Post-fit
$t\bar{t}H$	213 ± 29	76 ± 73	113 ± 15	40 ± 39	59.9 ± 7.8	21 ± 21	13.9 ± 2.0	4.8 ± 4.7	3.09 ± 0.49	1.0 ± 1.0
tH	3.01 ± 0.47	3.03 ± 0.44	1.81 ± 0.44	1.83 ± 0.40	1.24 ± 0.26	1.28 ± 0.25	0.26 ± 0.17	0.25 ± 0.14	0.000 ± 0.041	0.000 ± 0.041
$t\bar{t}+ \geq 1b$	3160 ± 490	4530 ± 160	1530 ± 210	2050 ± 80	720 ± 130	865 ± 47	215 ± 61	240 ± 22	55 ± 27	44.7 ± 8.5
$t\bar{t}+ \geq 1c$	510 ± 540	930 ± 190	220 ± 230	401 ± 83	96 ± 100	176 ± 36	26 ± 27	45 ± 10	6.9 ± 7.5	12.8 ± 3.2
$t\bar{t} + W$	7.0 ± 1.2	7.1 ± 1.1	4.31 ± 0.90	4.37 ± 0.84	2.47 ± 0.52	2.49 ± 0.46	1.05 ± 0.32	1.06 ± 0.30	0.47 ± 0.15	0.47 ± 0.14
$t\bar{t} + Z$	77 ± 11	77 ± 10	44.6 ± 6.6	45.6 ± 6.3	30.1 ± 4.9	30.8 ± 4.8	11.5 ± 2.4	11.6 ± 2.3	2.05 ± 0.64	2.11 ± 0.64
$t\bar{t}$ + light	180 ± 120	220 ± 130	85 ± 58	97 ± 58	37 ± 23	43 ± 25	10.5 ± 7.7	11.6 ± 7.8	2.2 ± 2.1	2.7 ± 2.3
Single top tW	71 ± 40	76 ± 42	40 ± 26	42 ± 27	17.9 ± 7.6	18.3 ± 7.7	8.5 ± 7.9	9.5 ± 9.0	6.0 ± 5.3	6.0 ± 5.4
$t\bar{t}t\bar{t}$	15.9 ± 8.0	15.7 ± 7.9	12.6 ± 6.3	12.5 ± 6.3	7.7 ± 3.9	7.6 ± 3.8	2.7 ± 1.4	2.7 ± 1.3	0.98 ± 0.50	0.95 ± 0.49
Other top sources	46 ± 24	45 ± 24	23 ± 16	24 ± 16	13 ± 10	12.7 ± 9.6	4.3 ± 2.8	4.4 ± 2.6	1.08 ± 0.54	1.06 ± 0.54
V & VV + jets	60 ± 24	60 ± 23	29 ± 11	29 ± 11	19.7 ± 8.3	19.7 ± 7.9	7.8 ± 3.4	7.8 ± 3.2	1.90 ± 0.88	1.84 ± 0.82
Total	4350 ± 810	6045 ± 82	2100 ± 360	2745 ± 48	1000 ± 180	1198 ± 33	301 ± 72	339 ± 16	80 ± 29	73.7 ± 7.2
Data	6047		2742		1199		331		75	

Table 7.12: Pre-fit and post-fit event yields in the single-lepton resolved signal regions.

	$\mathrm{SR}_{\mathrm{boosted}}$, $p_{\mathrm{T}}^{H} \in$ [300,450) GeV		$\mathrm{SR}_{\mathrm{boosted}}$, $p_{\mathrm{T}}^{H} \in$ [450,∞) GeV		$\mathrm{CR}^{5j}_{\geq 4b@70}$		$\mathrm{CR}^{5j}_{\geq 4b@60}$	
	Pre-fit	Post-fit	Pre-fit	Post-fit	Pre-fit	Post-fit	Pre-fit	Post-fit
$t\bar{t}H$	35.1 ± 4.1	12 ± 12	8.5 ± 1.1	3.0 ± 2.9	61.7 ± 8.1	21 ± 21	62.1 ± 8.6	22 ± 21
tH	1.31 ± 0.31	1.31 ± 0.29	0.42 ± 0.10	0.42 ± 0.10	3.15 ± 0.41	3.15 ± 0.40	3.16 ± 0.42	3.18 ± 0.42
$t\bar{t}+\geq 1b$	246 ± 49	295 ± 23	55 ± 24	52.5 ± 9.3	1370 ± 160	1581 ± 89	1000 ± 150	1118 ± 51
$t\bar{t}+\geq 1c$	84 ± 90	156 ± 35	21 ± 23	38 ± 10	390 ± 410	650 ± 140	56 ± 59	93 ± 23
$t\bar{t}+W$	1.86 ± 0.39	1.88 ± 0.35	0.55 ± 0.18	0.56 ± 0.17	2.53 ± 0.53	2.58 ± 0.45	0.54 ± 0.13	0.53 ± 0.12
$t\bar{t}+Z$	10.7 ± 2.1	10.9 ± 2.1	2.21 ± 0.60	2.32 ± 0.59	26.4 ± 3.7	26.0 ± 3.5	23.5 ± 3.4	23.0 ± 3.2
$t\bar{t}$ + light	56 ± 26	61 ± 25	17 ± 10	16.2 ± 7.3	260 ± 120	270 ± 95	22 ± 16	20 ± 14
Single top tW	13.1 ± 8.0	13.7 ± 8.3	6.1 ± 5.8	5.3 ± 4.6	58 ± 32	59 ± 32	27 ± 20	28 ± 20
$t\bar{t}t\bar{t}$	1.76 ± 0.89	1.74 ± 0.88	0.42 ± 0.22	0.41 ± 0.21	0.33 ± 0.17	0.31 ± 0.16	0.24 ± 0.13	0.23 ± 0.12
Other top sources	4.3 ± 3.2	4.4 ± 3.1	0.80 ± 0.78	0.82 ± 0.77	41 ± 16	41 ± 16	27 ± 11	26 ± 10
V & VV + jets	12.4 ± 5.7	12.4 ± 5.4	4.3 ± 2.3	4.2 ± 2.0	42 ± 16	41 ± 15	24.2 ± 8.8	24.2 ± 8.5
Total	470 ± 120	571 ± 22	117 ± 38	123.8 ± 9.7	2260 ± 490	2694 ± 53	1250 ± 170	1359 ± 36
Data	581		118		2696		1362	

Table 7.13: Pre-fit and post-fit event yields in the single-lepton boosted signal regions and resolved control regions with exactly five jets.

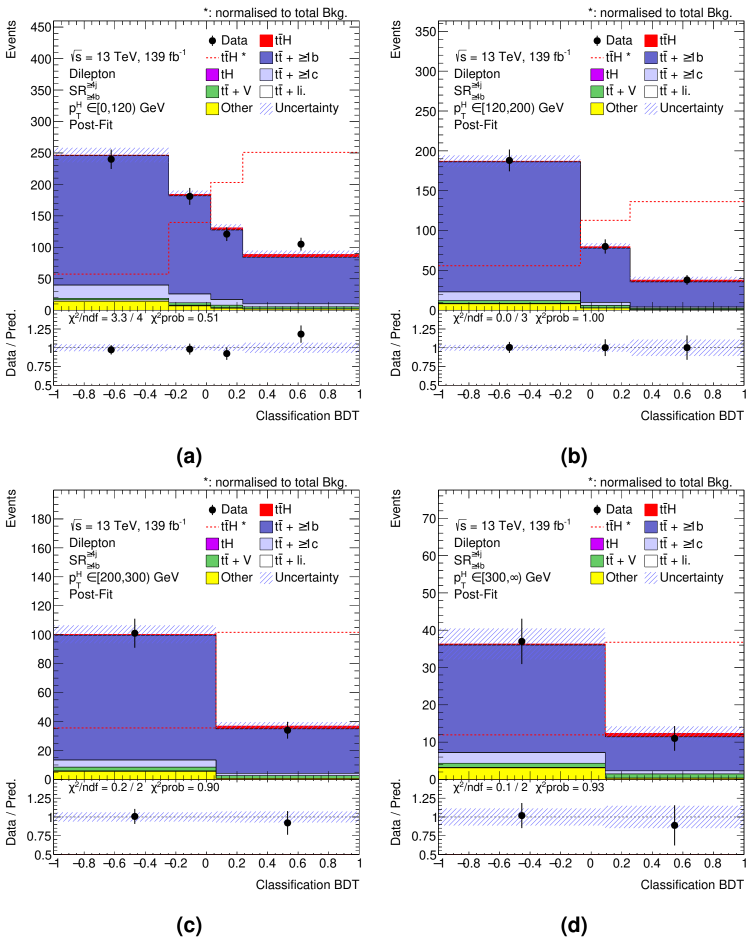

Figure 7.9: Distributions of the fitted variables in the dilepton STXS signal regions.

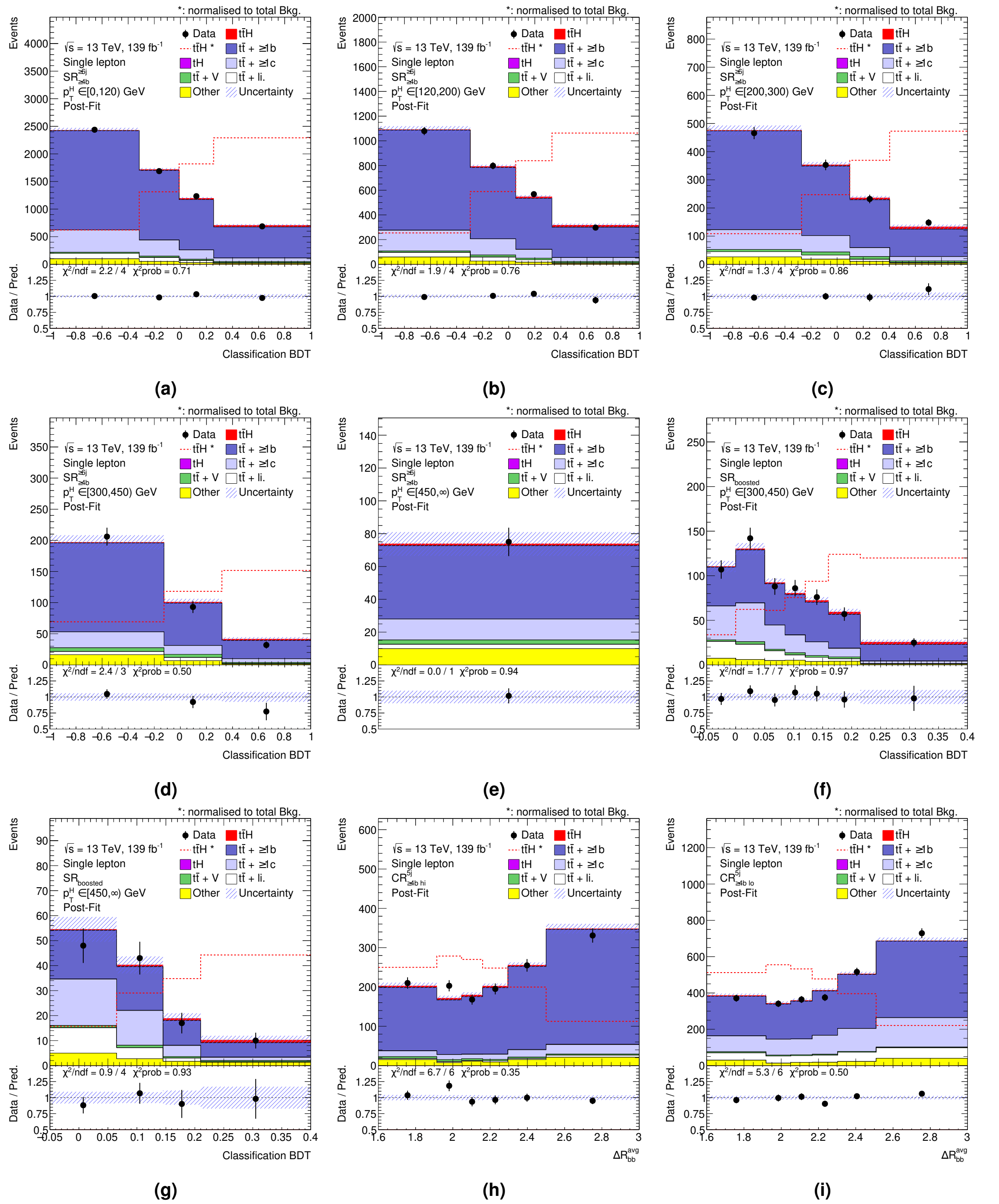

Figure 7.10: Distributions of the fitted variables in the STXS single-lepton resolved (7.10a,7.10b,7.10c,7.10d,7.10e) and boosted (7.10f,7.10g) signal regions and in the five-jets control regions (7.10h,7.10i).

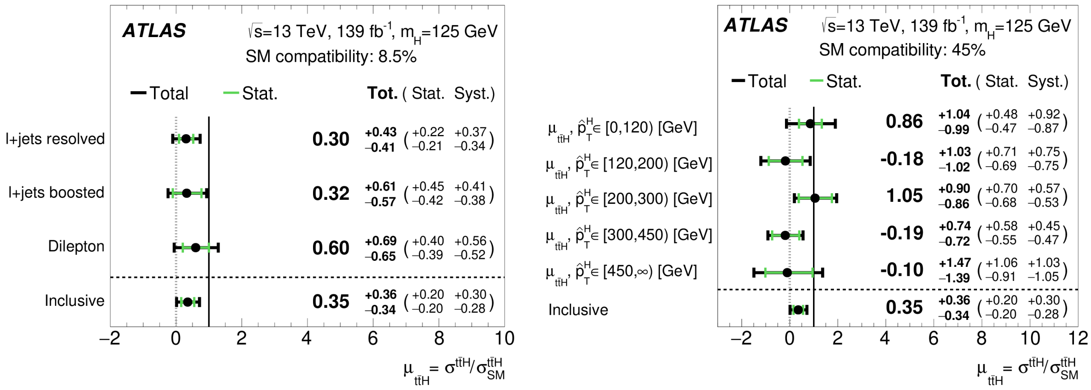

(a) **(b)**

Figure 7.11: Values of the inclusive $t\bar{t}H$ signal strength measured in the combined fit and in the individual channels (7.11a) and of the STXS signal strengths measured in each of the Higgs reconstructed p_{T} bins in the combined fit (7.11b)

Figure 7.11a shows the values of the signal strength measured in the single lepton resolved, boosted and dilepton channels. These values are obtained by repeating the fit to data with three independent signal strengths, one per channel. The inclusive signal strength, previously reported, is also shown. In this fit, the measured value of the $t\bar{t}+\geq 1b$ normalisation factor is $k(t\bar{t}+\geq 1b) = 1.27 \pm 0.08$, compatible with the value obtained in the single μ fit.

The fit to data is also repeated with five independent signal strengths, corresponding to the five truth p_{T}^{H} bins. The measured values of these signal strengths are shown in Figure 7.11b. In this fit, the value of $k(t\bar{t}+\geq 1b)$ is in perfect agreement with the one obtained from the single μ fit. The measurement is dominated by statistical uncertainty in the last three STXS bins. In the first two bins, it is dominated by systematic uncertainties, similarly to the inclusive measurement.

7.6.3 Cross-section exclusion limits

Upper limits on the $t\bar{t}H$ cross-section are also derived within the STXS framework. In this case, the likelihood model is slightly different: the effects of signal scale and PDF uncertainties on the predicted cross-section are not included. Scale effects are still included in the statistical model through the ISR uncertainty but they do not impact the overall $t\bar{t}H$ cross-section. The inclusive cross-section of 507 fb is used to calculate the limits, scaled by the fraction of signal events measured in each STXS bin to calculate the fiducial cross-section in each bin. The measured 95% confidence level (CL) cross-section upper limits are shown in Figure 7.12 for each STXS bin. The expected limits are also shown, assuming the background-only hypothesis (dashed black lines) and the SM hypothesis ($\mu = 1$, dashed red lines). The hashed uncertainty bands correspond to the theoretical uncertainty in the fiducial cross-sections predicted in each bin.

7.6.4 Impact of systematic uncertainties

These measurements are largely dominated by systematic uncertainties. In the TRExFitter framework, the pre-fit impact of each systematic uncertainty on the parameters of interest can be

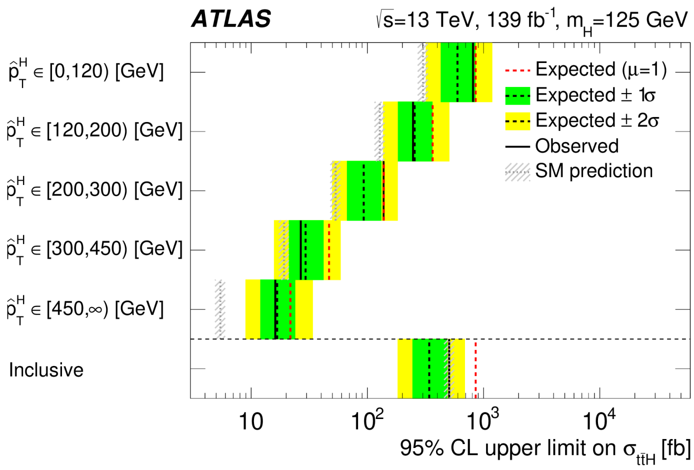

Figure 7.12: Expected and observed 95% CL cross-section upper limits in the individual STXS truth p_{T}^{H} bins, as well as the inclusive limit.

estimated by running the fit with the value of each nuisance fixed to its pre-fit value plus or minus the pre-fit uncertainty ($\theta = \hat{\theta} \pm \Delta\theta$), which is determined by the templates defined for the systematic uncertainties. The variation of the best-fit value of the POI with respect to the nominal fit ($\Delta\mu$, for example) is taken as the metric to rank the systematic uncertainties. To estimate the post-fit impact, a similar procedure is used, with the values of the NPs fixed to their best-fit values plus or minus their post-fit uncertainties obtained from the nominal fit ($\theta = \hat{\theta} \pm \Delta\hat{\theta}$).

The impact of the systematic uncertainties on the inclusive μ before and after the fit to data as well as the pulls and constraints on the NPs are shown in Figure 7.13 for the 20 uncertainties with the highest impact. The empty (filled) blue bars show the pre-fit (post-fit) impact of each NP on μ, following equation 7.13. The black points and error bars represent the best-fit value of each NP or normalisation factor and the associated constraint on the uncertainty. Table 7.14 shows the impact on μ for groups of systematic uncertainties instead of for each NP individually.

The dominant uncertainties are associated with the modelling of the $t\bar{t}+\geq 1b$ background, followed by signal modelling, tW modelling and b-tagging efficiency and mis-tag rates, the latter being the leading instrumental uncertainties. Within the $t\bar{t}+\geq 1b$ modelling uncertainties, the NLO matching uncertainties have the largest impact in the first two STXS bins.

The largest observed pull, as shown in Figure 7.13, corresponds to the $t\bar{t}+\geq 1b$ ISR uncertainty and has a value of about 1.2σ, mostly driven by the renormalisation scale (μ_{R}), indicating that data favors a softer renormalisation scale in the ME calculation. This pull was shown to not affect the shape of the BDT distribution in each region, while correcting the mismodelling in the number of jets distribution, which affects the categorization of events. This was observed by applying only this pull to produce the post-fit distribution of the number of jets. The pre-fit data/MC slope is corrected.

A large pull (close to 1σ) is also observed on the reconstructed $p_{\mathrm{T}}^{b\bar{b}}$ shape uncertainty. Given the definition of this uncertainty and the pre-fit disagreement between data and MC, a pull of this size is expected, since a $+1\sigma$ corrects the shape of the reconstructed $p_{\mathrm{T}}^{b\bar{b}}$ distribution in the inclusive signal

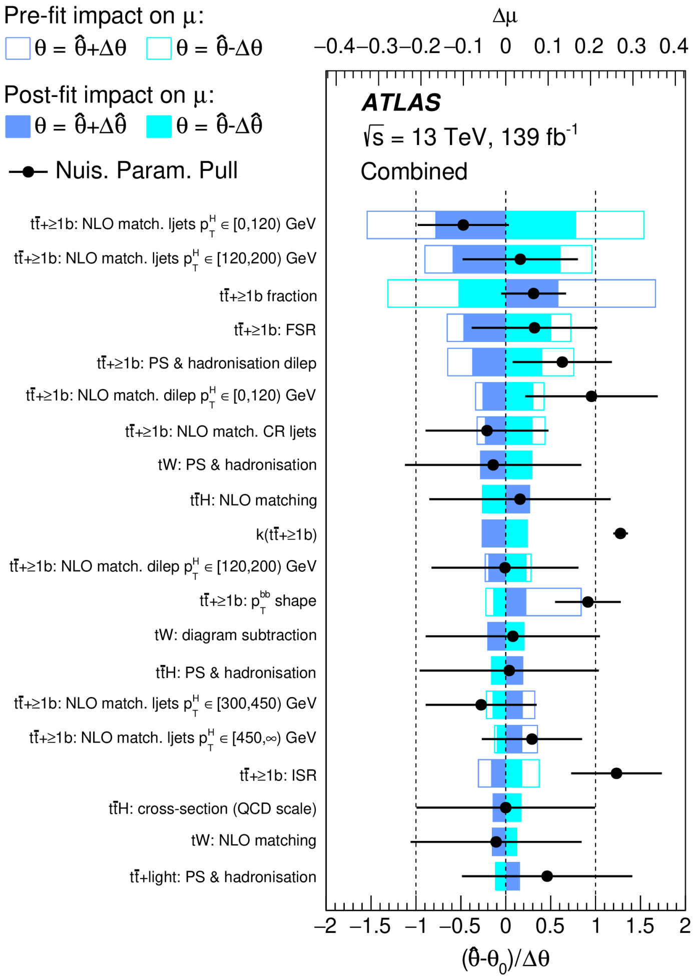

Figure 7.13: Pre- and post-fit impact of the systematic uncertainties on the inclusive signal strength in the combined fit.

regions, such that it agrees between data and the background model. The very good post-fit agreement between data and MC for this variable is shown in Figure 7.14 for the dilepton, single-lepton and boosted inclusive signal regions. Legitimate concerns can be raised about the definition of this uncertainty, since it is derived from data in the same regions that enter the final fit. To address these concerns, a fit to data was performed removing this uncertainty and using instead 11 independent $t\bar{t}+\geq 1b$ normalisation factors, decorrelated per channel and as a function of the reconstructed p_{T}^{H}. The value of μ obtained from this fit is compatible with the one obtained from the nominal fit model, within uncertainties.

The pulls and constraints obtained when performing the fit with five independent signal strengths, corresponding to the STXS bins, are very similar to those of the inclusive fit. In the first two STXS bins, the measurement of μ is dominated by systematic uncertainties on the modelling of the $t\bar{t}+\geq 1b$ background, in particular the choice of NLO matching procedure, while in the last three bins the statistical uncertainties dominate. The ranking plots for each of the five signal strengths can be found in Appendix C in Figure C.2.

Uncertainty source	$\Delta\mu$	
Process modelling		
$t\bar{t}H$ modelling	$+0.13$	-0.05
$t\bar{t}+\geq 1b$ modelling		
$t\bar{t}+\geq 1b$ NLO matching	$+0.21$	-0.20
$t\bar{t}+\geq 1b$ fractions	$+0.12$	-0.12
$t\bar{t}+\geq 1b$ FSR	$+0.10$	-0.11
$t\bar{t}+\geq 1b$ PS & hadronisation	$+0.09$	-0.08
$t\bar{t}+\geq 1b$ $p_{\mathrm{T}}^{b\bar{b}}$ shape	$+0.04$	-0.04
$t\bar{t}+\geq 1b$ ISR	$+0.04$	-0.04
$t\bar{t}+\geq 1c$ modelling	$+0.03$	-0.04
$t\bar{t}$+light modelling	$+0.03$	-0.03
tW modelling	$+0.08$	-0.07
Background-model statistical uncertainty	$+0.04$	-0.05
b-tagging efficiency and mis-tag rates		
b-tagging efficiency	$+0.03$	-0.02
c-mis-tag rates	$+0.03$	-0.03
l-mis-tag rates	$+0.02$	-0.02
Jet energy scale and resolution		
b-jet energy scale	$+0.00$	-0.01
Jet energy scale (flavor)	$+0.01$	-0.01
Jet energy scale (pileup)	$+0.00$	-0.01
Jet energy scale (remaining)	$+0.01$	-0.01
Jet energy resolution	$+0.02$	-0.02
Luminosity	$+0.01$	-0.00
Other sources	$+0.03$	-0.03
Total systematic uncertainty	$+0.30$	-0.28
$t\bar{t}+\geq 1b$ normalisation	$+0.04$	-0.07
Total statistical uncertainty	$+0.20$	-0.20
Total uncertainty	$+0.36$	-0.34

Table 7.14: Breakdown of the contributions to the uncertainties in μ evaluated after the fit. The $\Delta\mu$ values are obtained by repeating the fit after having fixed a certain set of nuisance parameters corresponding to a group of systematic uncertainties, and then evaluating $(\Delta\mu)^2$ by subtracting the resulting squared uncertainty of μ from its squared uncertainty found in the full fit. The same procedure is followed when quoting the effect of the $t\bar{t}+\geq 1b$ normalisation. The total uncertainty is different from the sum in quadrature of the different components due to correlations between nuisance parameters existing in the fit.

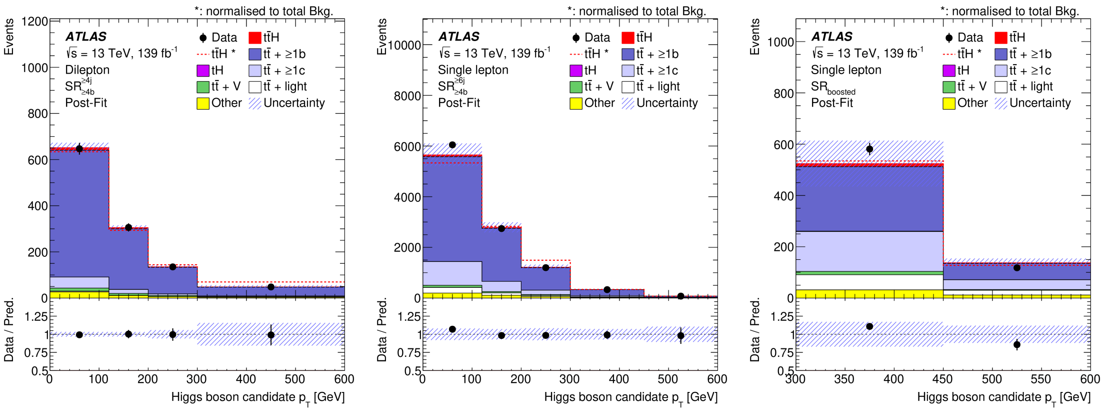

(a) **(b)** **(c)**

Figure 7.14: Post-fit distributions of the reconstructed Higgs boson candidate p_{T} for the dilepton $\mathrm{SR}^{\geq 4j}_{\geq 4b}$ region (7.14a), the single-lepton $\mathrm{SR}^{\geq 6j}_{\geq 4b}$ region (7.14b) and the boosted region (7.14c).

	$\text{CR}^{3j}_{3b@60}$		$\text{CR}^{\geq 4j}_{3b@70}$		$\text{CR}^{\geq 4j}_{3b@60}$	
	Pre-fit	Post-fit	Pre-fit	Post-fit	Pre-fit	Post-fit
$t\bar{t}H$	26 ± 4	18 ± 14	80 ± 8	50 ± 40	120 ± 12	80 ± 60
tH	1.1 ± 0.1	0.9 ± 0.5	0.9 ± 0.1	1.0 ± 1.9	1.7 ± 0.2	1.5 ± 1.3
$t\bar{t} + \geq 1b$	1900 ± 500	1990 ± 80	1700 ± 220	2520 ± 110	2800 ± 310	4040 ± 130
$t\bar{t} + \geq 1c$	400 ± 400	550 ± 50	1500 ± 1500	2510 ± 150	700 ± 700	1160 ± 90
$t\bar{t}$ + light	130 ± 80	143 ± 27	850 ± 350	960 ± 130	200 ± 120	230 ± 40
Other	140 ± 40	140 ± 11	390 ± 80	390 ± 19	340 ± 80	340 ± 40
Total	2500 ± 700	2840 ± 50	4500 ± 1600	6430 ± 80	4200 ± 800	5850 ± 80
Data	2827		6429		5865	

Table 7.15: Pre-fit and post-fit event yields in the dilepton control regions with exactly three b-jets at 60% or 70%. For $t\bar{t}H$ and tH the pre-fit yields are shown assuming the SM prediction ($\alpha = 0°$, $k'_t = 1$), while the post-fit yields are extracted from the fit to data and correspond to the best fit values: $\alpha = 11°^{+56°}_{-77°}$, $k'_t = 0.84^{+0.30}_{-0.46}$.

7.7 Results from CP measurement

The measurement of the CP properties of the top-Higgs Yukawa coupling, namely the CP-mixing angle and coupling modifier, in the $t\bar{t}H(H \to b\bar{b})$ channel using the full Run 2 dataset, consisting of 139 fb^{-1} of data, is presented in this section.

7.7.1 Post-fit yields and distributions

The predicted and fitted signal and background yields are shown in Tables 7.15, 7.16 and 7.17 for the dilepton (first two tables) and single-lepton regions. The post-fit yields are obtained from the combined fit to data with the CP-mixing angle and coupling modifier as parameters of interest and take into account the pulls in the NPs. Both statistical and systematic uncertainties are included. In the post-fit uncertainties, in addition to the constraints, the correlations between NPs are also taken into account.

Figure 7.15 shows the single-lepton post-fit distributions of $\Delta R^{\text{avg}}_{bb}$ in the five-jet control regions, $b_2^{t\bar{t}H}(t\bar{t})$ in the six-jet regions and of the classification BDT in the boosted region. Figure 7.16 shows the post-fit distributions of $\Delta\eta(\ell\ell)$ in the $\text{CR}^{\geq 4j, \geq 4b}_{\text{no-reco}}$ region and of $b_4(t\bar{t})$ for the remaining $\geq 4j, \geq 4b$ regions. The plots for the dilepton control regions with exactly three b-jets are not shown since in these regions no shape information is used in the fit, and therefore the yields can be read from Table 7.15.

The post-fit plots follow similar conventions to the ones shown in the previous section for the STXS analysis. The predicted yields displayed in these plots originate from a signal and background fit to data with k'_t and α as free parameters. The red dashed and blue dotted lines show the $t\bar{t}H + tH$ signal prediction for the pure CP-even and CP-odd scenarios, respectively, scaled to the total data yield in each region.

7.7.2 CP mixing angle and coupling modifier measurements

The best-fit values and exclusion contours in α and k'_t are shown in Figure 7.17 in the $(k'_t \cos\alpha, k'_t \sin\alpha)$ plane. The measured value of the CP-mixing angle is $\alpha = 11°^{+56°}_{-77°}$ and of the overall coupling modifier is $k'_t = 0.84^{+0.30}_{-0.46}$, in agreement with the SM expectation ($\alpha = 0°, k'_t = 1$), within the uncertainties. The measured value of the $t\bar{t} + \geq 1b$ background normalisation factor is $k_{t\bar{t}+\geq 1b} = 1.30^{+0.09}_{-0.08}$, consistent

	$\mathrm{CR}^{\geq 4j,\geq 4b}_{\text{no-reco}}$		$\mathrm{CR}^{\geq 4j,\geq 4b}$		$\mathrm{SR}_1^{\geq 4j,\geq 4b}$		$\mathrm{SR}_2^{\geq 4j,\geq 4b}$	
	Pre-fit	Post-fit	Pre-fit	Post-fit	Pre-fit	Post-fit	Pre-fit	Post-fit
$t\bar{t}H$	16.9 ± 2.1	11 ± 9	6.9 ± 1.1	4.7 ± 3.4	12.5 ± 1.5	8 ± 6	25.0 ± 2.9	17 ± 12
tH	0.19 ± 0.08	0.17 ± 0.16	0.087 ± 0.035	0.068 ± 0.016	0.100 ± 0.032	0.08 ± 0.14	0.09 ± 0.06	0.07 ± 0.09
$t\bar{t}+\geq 1b$	240 ± 32	288 ± 15	300 ± 40	371 ± 16	130 ± 17	160 ± 8	98 ± 17	122 ± 11
$t\bar{t}+\geq 1c$	14 ± 16	23 ± 4	18 ± 19	31.1 ± 2.5	7 ± 8	13.4 ± 1.6	5 ± 5	8.2 ± 1.0
$t\bar{t}$ + light	1.6 ± 1.7	1.7 ± 0.4	2.1 ± 2.3	2.3 ± 0.8	0.9 ± 1.2	1.4 ± 0.8	0.5 ± 0.6	0.57 ± 0.25
Other	35 ± 11	33 ± 8	18 ± 4	18.6 ± 2.5	11.1 ± 2.6	10.9 ± 1.3	8.9 ± 1.5	8.7 ± 1.0
Total	300 ± 40	358 ± 12	350 ± 50	428 ± 15	160 ± 20	194 ± 5	140 ± 19	156 ± 6
Data	354		420		190		170	

Table 7.16: Pre-fit and post-fit event yields in the dilepton regions with at least four jets. For $t\bar{t}H$ and tH the pre-fit yields are shown assuming the SM prediction ($\alpha = 0°$, $k_t' = 1$), while the post-fit yields are extracted from the fit to data and correspond to the best fit values: $\alpha = 11^{\circ+56^\circ}_{-77^\circ}$, $k_t' = 0.84^{+0.30}_{-0.46}$.

	$\mathrm{CR}^{5j}_{\geq 4j@70}$		$\mathrm{CR}^{5j}_{\geq 4j@60}$		$\mathrm{CR}_1^{\geq 6j,\geq 4b}$		$\mathrm{CR}_2^{\geq 6j,\geq 4b}$		$\mathrm{SR}^{\geq 6j,\geq 4b}$		$\mathrm{SR}_{\text{boosted}}$	
	Pre-fit	Post-fit	Pre-fit	Post-fit	Pre-fit	Post-fit	Pre-fit	Post-fit	Pre-fit	Post-fit	Pre-fit	Post-fit
$t\bar{t}H$	60 ± 9	40 ± 30	60 ± 10	41 ± 31	78 ± 11	50 ± 40	140 ± 18	90 ± 70	170 ± 26	110 ± 80	46 ± 6	30 ± 22
tH	3.5 ± 0.5	3 ± 4	3.8 ± 0.6	3.9 ± 1.9	3.3 ± 0.6	3.1 ± 1.9	2.3 ± 0.6	1.9 ± 0.8	1.3 ± 0.5	1.3 ± 1.7	1.9 ± 0.4	3 ± 5
$t\bar{t}+\geq 1b$	1370 ± 230	1530 ± 80	1000 ± 190	1090 ± 60	3200 ± 500	4300 ± 120	1700 ± 220	2220 ± 120	870 ± 140	1110 ± 110	300 ± 80	335 ± 30
$t\bar{t}+\geq 1c$	400 ± 400	650 ± 50	60 ± 60	96 ± 11	500 ± 600	950 ± 80	250 ± 270	450 ± 40	90 ± 90	153 ± 15	100 ± 110	196 ± 22
$t\bar{t}$ + light	260 ± 120	280 ± 40	22 ± 16	28 ± 8	200 ± 130	230 ± 60	90 ± 60	117 ± 26	26 ± 22	32 ± 11	73 ± 34	76 ± 15
Other	170 ± 40	173 ± 30	100 ± 30	99 ± 20	330 ± 70	320 ± 50	160 ± 30	159 ± 21	84 ± 14	83 ± 11	58 ± 15	60 ± 11
Total	2300 ± 500	2690 ± 50	1300 ± 210	1350 ± 40	4300 ± 800	5870 ± 80	2300 ± 400	3040 ± 70	1200 ± 190	1500 ± 50	590 ± 150	701 ± 31
Data	2696		1363		5837		3090		1470		699	

Table 7.17: Pre-fit and post-fit event yields in the single-lepton regions. For $t\bar{t}H$ and tH the pre-fit yields are shown assuming the SM prediction ($\alpha = 0°$, $k_t' = 1$), while the post-fit yields are extracted from the fit to data and correspond to the best fit values: $\alpha = 11^{\circ+56^\circ}_{-77^\circ}$, $k_t' = 0.84^{+0.30}_{-0.46}$.

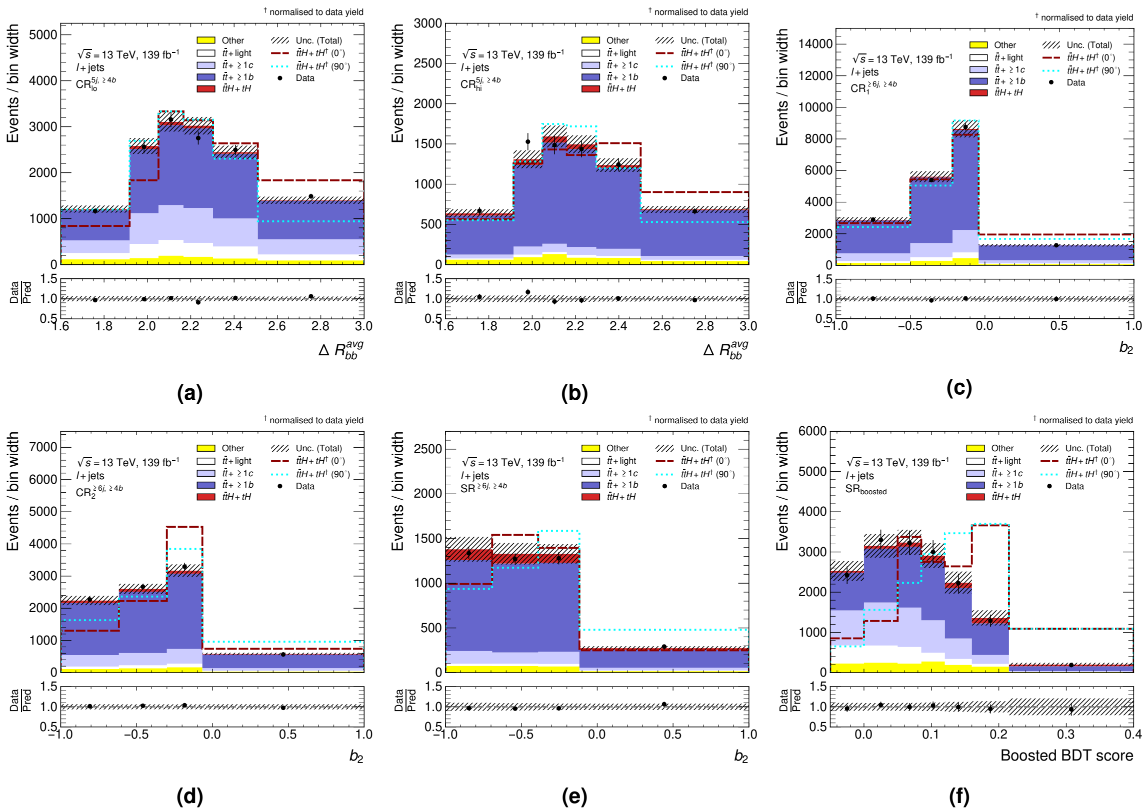

Figure 7.15: Distributions of the fitted variables in the single-lepton control regions (7.15a, 7.15b), resolved (7.15c,7.15d,7.15e) and boosted CP-sensitive signal regions (7.15f).

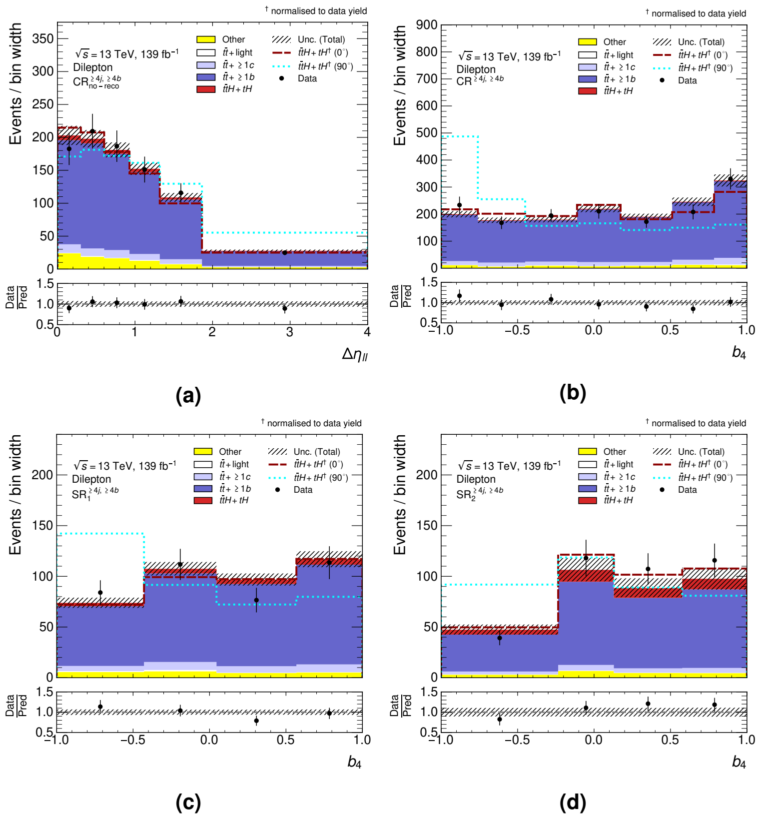

Figure 7.16: Distributions of the fitted variables in the dilepton control region without top quark pair reconstruction (7.16a) and in the CP-sensitive signal regions (7.16b,7.16c,7.16d).

with the STXS measurement.

The expected (dashed) and observed (filled) best-fit values of α and corresponding one-dimensional likelihood scans are shown in Figure 7.18. The expected curve is obtained from a fit to the Asimov dataset. The observed sensitivity to α is lower than the expected one, driven by the single-lepton channel, due to a downward fluctuation in the number of events in the signal-enriched bins with respect to the expectation.

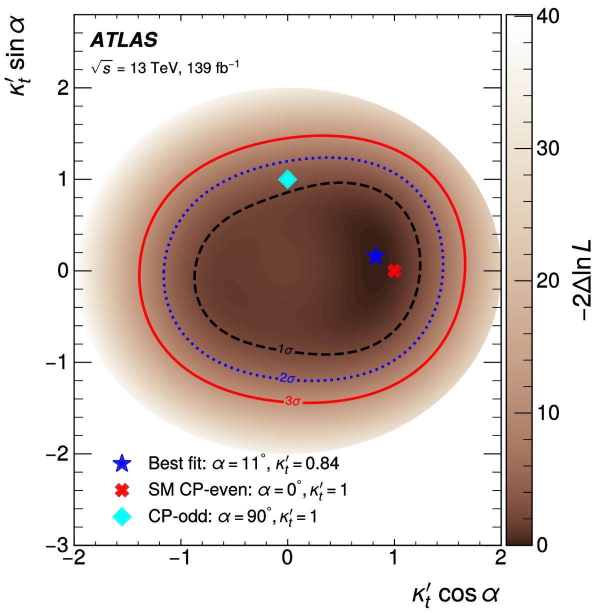

Figure 7.17: The observed exclusion contours in the $(k_t' \cos\alpha, k_t' \sin\alpha)$ plane. Regions contained in the dashed, dotted and solid lines are compatible with the best-fit results at 1, 2 and 3 σ standard deviations. The cross (diamond) represents the CP-even (CP-odd) signal hypothesis with $k_t' = 1$ and the best-fit result is represented with a star.

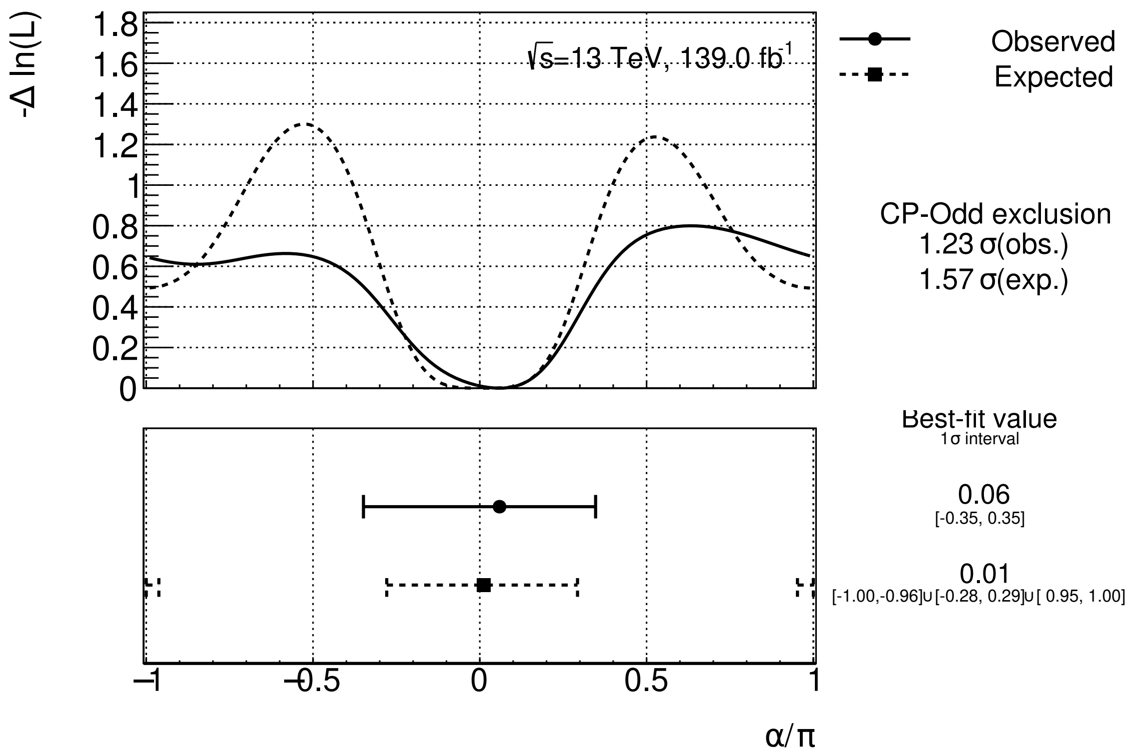

Figure 7.18: The expected (dashed line) and observed (filled line) likelihood scans on α. The expected curve is obtained assuming the SM scenario ($k_t' = 1, \alpha = 0$). The best fit values and uncertainties on α are shown in the bottom pad. The CP-odd exclusion significance is shown on the right.

7.7.3 Impact of systematic uncertainties

The method used in TRExFitter to estimate the pre- and post-fit impact of the systematic uncertainties (described in section 7.6.4) works well when the parameter of interest is a signal strength because in that case the minimum value of the POI might shift up and down while the likelihood retains its approximate parabolic shape around the minimum. However, in the CP analysis, the number of events, and therefore the likelihood, does not depend on the square of the CP-mixing angle but on some more complex expression that involves trigonometric functions. By fixing the value of a given NP to its up or down variation (either pre or post-fit) the initial shape of the full MC prediction is changed. To compensate for this change, the fit can easily displace the POI under study. For a given NP, the up and down variations might lead to changes in the fit model that favor a more CP-even or a more CP-odd value of α. The former would lead to a best-fit value of $\alpha = 0$ as in the nominal fit while the latter would lead to a best-fit value of α between zero and $\pm\pi/2$. This means that using the method described in the previous paragraph, the up and down impact of the same NP can become extremely asymmetric, with an impact close to zero for one of the variations. This issue is even more relevant for two-point systematics because only one of the variations comes from the comparison between the nominal and alternative samples while the other is simply its symmetrization, meaning that if the original variation favors a more CP-odd signal, the symmetrized one will necessarily favor a more CP-even one. This motivates the need to utilize an alternative method to rank the systematic uncertainties in the CP analysis.

One can redo the fit removing one NP at a time to estimate their impact based on the change in the total uncertainty of the POI, measured directly from the likelihood curve. This is the method adopted for the CP analysis. The impact is calculated as the quadrature difference between the uncertainty on the POI in the nominal fit and in the fit with each NP removed. The likelihood curves obtained from fits with the top ten most impact-full NPs removed are shown in Figure 7.19, for the combined fit to data. From these curves the impact of each NP is calculated and displayed in Figure 7.20. The observed values of pulls and constraints are also shown.

A very similar procedure can be followed by removing groups of systematics uncertainties from the fit, instead of individual NPs. The observed contributions of the systematic uncertainties to α and k_t' obtained using this method are shown in Table 7.18. The measurement is dominated by the uncertainties associated with the modelling of the $t\bar{t}+\geq 1b$ background. They contribute $^{+37^\circ}_{-51^\circ}$ to the overall α uncertainty, driven by the choice of the flavor scheme, the NLO matching procedure and the PS and hadronization. The experimental uncertainties are driven by the b-tagging efficiency ($^{+8.7^\circ}_{-15^\circ}$), followed by the c-mistag rates and jet energy scale. Through correlation, k_t' contributes $^{+17^\circ}_{-33^\circ}$ to the overall α uncertainty. The uncertainty in k_t' is largely dominated by the NLO matching procedure ($^{+0.15}_{-0.30}$).

Table 7.18: Observed contributions of uncertainties to α (in degrees) and k_t'. The values are derived by fixing the nuisance parameters associated to the group of uncertainties to their best fit value and subtracting derived uncertainty in quadrature from the full uncertainty on the POI. The total statistical uncertainty is obtained by fixing all nuisance parameters.

Uncertainty source	$\Delta\alpha[°]$		$\Delta k_t'$	
Process modelling				
Signal modelling	+8.8	-14	+10	-10
$t\bar{t}+\geq 1b$ modelling				
$t\bar{t}+\geq 1b$ 4V5 FS	+23	-37	+0.08	-0.08
$t\bar{t}+\geq 1b$ NLO matching	+22	-33	+0.15	-0.30
$t\bar{t}+\geq 1b$ fractions	+14	-21	+0.09	-0.21
$t\bar{t}+\geq 1b$ FSR	+5.2	-9.9	+0.01	-0.02
$t\bar{t}+\geq 1b$ PS & hadronisation	+16	-24	+0.09	-0.20
$t\bar{t}+\geq 1b$ $p_{\mathrm{T}}^{b\bar{b}}$ shape	+5.4	-4.6	+0.07	-0.11
$t\bar{t}+\geq 1b$ ISR	+14	-24	+0.07	-0.17
$t\bar{t}+\geq 1c$ modelling	+6.6	-11	+0.04	-0.10
$t\bar{t}$+light modelling	+2.5	-4.7	+0.00	-0.01
b-tagging efficiency and mis-tag rates				
b-tagging efficiency	+8.7	-15	+0.06	-0.12
c-mis-tag rates	+6.7	-11	+0.03	-0.07
l-mis-tag rates	+2.3	-2.7	+0.01	-0.03
Jet energy scale and resolution				
b-jet energy scale	+1.6	-3.8	+0.02	-0.02
Jet energy scale (flavor)	+7.8	-11	+0.01	-0.05
Jet energy scale (pileup)	+5.2	-7.9	+0.02	-0.05
Jet energy scale (remaining)	+8.1	-13	+0.04	-0.08
Jet energy resolution	+5.7	-9.3	+0.03	-0.09
Luminosity	$\leq \pm 1$		$\leq \pm 0.01$	
Other sources	+4.9	-8	+0.03	-0.07
Total systematic uncertainty	+41	-54	+0.29	-0.45
$t\bar{t}+\geq 1b$ normalisation	+8.2	-13	+0.05	-0.15
κ_t'	+17	-33	—	
α	—		+0.08	-0.07
Total statistical uncertainty	+32	-49	+0.09	-0.10
Total uncertainty	+52	-73	+0.30	-0.46

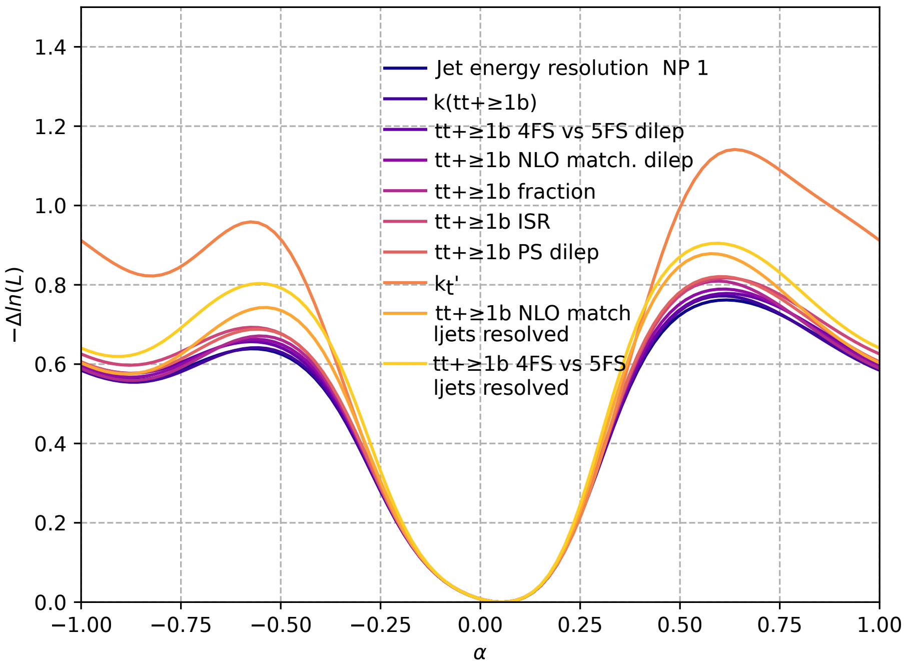

Figure 7.19: Observed likelihood scans on α obtained from combined fits to data with the ten nuisance parameters with the largest impact removed one at a time. The labels of the curves indicate which NP was removed. The nominal likelihood curve is not shown.

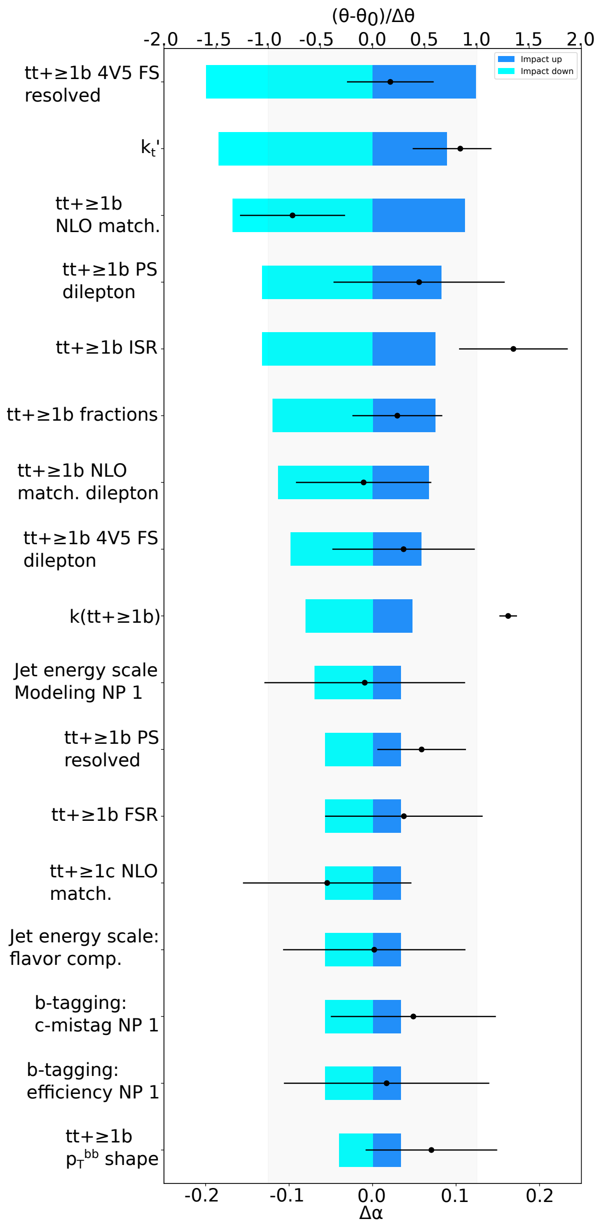

Figure 7.20: Ranking of the 17 nuisance parameters with an impact on α different from zero. The blue rectangles correspond to the post-fit up (dark blue) and down (light blue) impact on α, calculated by subtracting in quadrature the uncertainty on α between the nominal fit and a fit with each nuisance parameter removed. The black points and lines show the pulls and post-fit uncertainties on the nuisance parameters with respect to their nominal values, read in the upper scale.

8

Cross-section measurements of top quark pair production in association with charm quarks

Contents

When studying the Higgs boson in association with top quarks, the production of top quark pairs with additional heavy-flavor jets constitutes a major background. Its modelling is challenging due to the inherently different energy scales associated with the $t\bar{t}$ and $b\bar{b}$ or $c\bar{c}$ pairs and it limits the precision of $t\bar{t}H(H \to b\bar{b})$ cross-section and charge-parity measurements, as discussed in the previous chapter.

A lot of effort has been dedicated to a better understanding of the $t\bar{t}b\bar{b}$ process. Inclusive and differential production cross-sections have been calculated at NLO in QCD, developed hand-in-hand with multiple cross-section measurements performed by ATLAS and CMS Collaborations. At $\sqrt{s} = 13$ TeV, the ATLAS Collaboration has measured the $t\bar{t}b\bar{b}$ differential and inclusive cross-sections in the dileptonic and semileptonic final states [203]. The CMS Collaboration perfomed inclusive cross-section measurements in the same final states [204] and additionally in the fully hadronic final state [205].

For $t\bar{t}c\bar{c}$ the landscape is strikingly different. The only measurement of this process thus far has been performed by the CMS Collaboration, based on a partial Run 2 dataset corresponding to 41.5 fb^{-1} [206]. It targets the dileptonic final state with an electron and a muon ($e\mu$) and measures the $t\bar{t}b\bar{b}$, $t\bar{t}c\bar{c}$ and $t\bar{t}$+light cross-sections as well as the ratios of $t\bar{t}b\bar{b}$ and $t\bar{t}c\bar{c}$ to inclusive $t\bar{t}$ production with additional jets. The ratio of $t\bar{t}c\bar{c}$ to the inclusive $t\bar{t}$+jets cross section is found to be $(3.01 \pm 0.34(\text{stat}) \pm 0.31(\text{syst}))\%$ in the fiducial phase space. The measured value is in agreement with the predictions from both POWHEG and MADGRAPH5_aMC@NLO within 2σ.

This chapter describes the first ATLAS measurements of the $t\bar{t}+\geq 2c$ and $t\bar{t}+1c$ cross-sections in the dileptonic final state. The full Run 2 dataset is used, corresponding to 140 fb^{-1}. The difference with respect to the integrated luminosity of 139 fb^{-1} used in the $t\bar{t}H$ analyses arises from an updated list of the runs suitable for physics analyses (*Good Run List*). A combination with the semileptonic channel is foreseen and a paper is under preparation. At the moment, only ATLAS internal documentation exists [15].

Events with one or more c-jets are identified based on the heavy-flavor classification procedure described in section 7.1.2. It matches jets to truth level partons using the ghost-matching procedure to determine the true jet flavor. In this classification, $t\bar{t}+\geq 2c$ indicates events with at least two c-jets produced together with the top quark pair and $t\bar{t}+1c$ includes events with a single c-jet as well as events in which a single jet is matched to two c-partons.

A dedicated heavy-flavor tagging algorithm (b/c-tagger) is employed to increase the purity in $t\bar{t}+\geq 2c$ and $t\bar{t}+1c$ in the signal regions, while simultaneously discriminating against the dominant $t\bar{t}+\geq 1b$ and $t\bar{t}$+light backgrounds. Its development is not part of this work. Based on the output probabilities to tag b- and c-jets of the standard DL1r tagger, custom working points are defined in a two-dimensional plane. The b/c-tagger is discussed in more detail in section 8.3.

The data and MC samples used in this analysis are described in section 8.1 and differences in object reconstruction are highlighted in section 8.2. The analysis strategy and event selection are detailed in section 8.4. The systematic uncertainties follow closely the prescriptions already used in the $t\bar{t}H$ analyses. They are summarized with their differences highlighted in section 8.5. The results are presented in section 8.6.

8.1 Data samples and MC simulation of physics processes

The expected yields and distributions of the signal and background processes are estimated from MC simulation. The detector response is simulated using the GEANT4 software for all signal and background nominal samples with the exception of tH for which the fast ATLAS detector simulation, AFII, is used. The fast simulation is also employed to produce some of the alternative samples used to evaluate systematic uncertainties. The effects of multiple interactions in the same and neighbouring bunch crossings are modelled by overlaying the hard-scatter event with additional proton-proton interactions generated with PYTHIA8.186 with the A3 tune. The MC events are weighted to reproduce the pileup distribution observed in data.

For all MC samples in which the parton shower, hadronization and multi-parton interactions are simulated with PYTHIA8 or HERWIG7, the decays of b- and c-hadrons are simulated using EVTGEN1.6.0.

For all samples using MADGRAPH5_aMC@NLO to calculate the matrix element, as well as in the single-top t-channel POWHEG sample, the decays of top quarks, Z- and W-bosons are simulated at LO using MADSPIN [207, 208], thus preserving the spin correlations.

The top quark mass is set to $m_t = 172.5$ GeV, and the mass of the b-quarks from the top decay is set to $m_b = 4.95$ GeV when using POWHEGBOX or MADSPIN, and to $m_b = 4.75$ GeV when using SHERPA. The decay of the Higgs boson is handled by the parton shower generator including all decay modes, with the branching ratios recommended by the LHC Higgs Cross-Section Working Group. The Higgs boson mass is set to $m_H = 125.0$ GeV and the mass of the b-quark from the Higgs decay is set to $m_b = 4.80$ (4.50) GeV when using PYTHIA8 (HERWIG7).

For t- and s-channel single-top, tZq and V+jets production, only final states with at least one charged lepton are considered. For tWZ, only final states with $Z \to ee, \mu\mu, \tau\tau$ are included. For the remaining samples, all decay modes of the W- and Z-bosons are considered.

8.1.1 $t\bar{t}+\geq 1c$ signal and $t\bar{t}$+jets background

The $t\bar{t}+\geq 2c$ and $t\bar{t}+1c$ signals and the $t\bar{t}$+light background are modelled using the same inclusive $t\bar{t}$ sample, produced using POWHEGBOX at NLO in QCD. The h_{damp} parameter is set to $1.5m_{\text{top}}$. The functional form of the renormalisation and factorisation scales is set to $\sqrt{m_{\text{top}}^2 + p_T^2}$. Parton shower and hadronisation are handled by PYTHIA8.230 with the A14 set of tune parameters and the `NNPDF2.3LO` set of PDFs. The sample is normalised to the cross-section predicted at NNLO in QCD with NNLL resummation of soft-gluon terms, corresponding to $\sigma(t\bar{t})_{\text{NNLO+NNLL}} = 832 \pm 51$ pb, for $m_{\text{top}} = 172.5$ GeV [172–178]. The uncertainties on the cross-section are calculated by varying the PDF set and α_S, the renormalisation and factorization scales and the top quark mass, and are added in quadrature.

Alternative samples are produced in POWHEG+PYTHIA8 with the h_{damp} and p_T^{hard} parameters set to $3.0m_{\text{top}}$ and 1 GeV, respectively. The p_T^{hard} parameter regulates the definition of the vetoed region of the parton shower and thus allows to estimate the uncertainty associated with the matrix element and parton showering matching procedure. Its default value is zero.

An additional sample is produced with an alternative parton shower simulation, interfacing the nominal POWHEGBOX sample with HERWIG7.1.3.

8.1.2 $t\bar{t}b\bar{b}$ background

The contribution of the $t\bar{t}+\geq 1b$ background is estimated from a dedicated $t\bar{t}b\bar{b}$ sample generated in the four-flavor scheme at NLO in QCD using POWHEGBOXRES and OPENLOOPS with the `NNPDF3.0NLO` PDF set. The parton shower and hadronization are handled by PYTHIA8.244 with the A14 set of tune parameters and the `NNPDF2.3LO` PDF set. The b-quark mass is set to $m_b = 4.95$ GeV. The factorization scale is set to $0.5 \times \sum_{i=t,\bar{t},b,\bar{b},j} m_{T,i}$, the renormalisation scale is set to $\sqrt[4]{m_T(t)\cdot m_T(\bar{t})\cdot m_T(b)\cdot m_T(\bar{b})}$, and the h_{damp} parameter is set to $0.5\times\sum_{i=t,\bar{t},b,\bar{b}} m_{T,i}$. The internal POWHEG parameter that regulates the splitting into the finite and singular part of the real emission at NLO [168], h_{bzd}, is set to five.

An alternative sample is produced in POWHEG+PYTHIA8 using the dipole recoil scheme, as opposed to the global recoil scheme used for the nominal sample. In PYTHIA8, the recoil settings ensure that the emission of QCD radiation in the parton shower conserves the momentum of the system. Two options exist: either one single parton gets the full momentum recoil of a given emission or the recoil is distributed over the whole final state [168]. The former is referred to as dipole recoil and the latter as global recoil.

Another alternative sample is produced by interfacing the events generated with POWHEGBOXRES with HERWIG7.1.6.

8.1.3 Smaller backgrounds

Other background processes include single-top (t-channel, s-channel and tW), $t\bar{t}H$, $t\bar{t}V$, tZq, tWZ, W/Z+jets, tH and diboson production. Their contributions are subdominant and are estimated from MC simulation.

Single-top processes are generated at NLO in QCD using POWHEGBOX, interfaced to PYTHIA8.230. For t-channel production, events are generated in the four-flavor scheme with the `NNPDF3.0NLO` PDF set. The renormalisation and factorization scales are set to $\sqrt{m_b^2 + p_{T,b}^2}$. The s-channel and tW events are generated in the five-flavor scheme using the same PDF set. The renormalisation and factorization scales are set to the top quark mass. For tW, the diagram removal scheme [209] is employed to remove the overlap with $t\bar{t}$ processes.

Two alternative single-top samples are produced by interfacing the events generated with POWHEGBOX with HERWIG7.04; and by using MADGRAPH5_aMC@NLO2.6.0 as event generator, in the five-flavor scheme. To assess the uncertainty due to the modelling of the interference with $t\bar{t}$ production, an alternative tW sample is produced using the diagram subtraction overlap removal scheme [209, 210].

The production of $t\bar{t}H$ is modelled in the five-flavor scheme at NLO in QCD using POWHEGBOX, interfaced to PYTHIA8.230. The renormalisation and factorization scales are set to $\sqrt[3]{m_T(t)\cdot m_T(\bar{t})\cdot m_T(H)}$.

The sample is normalised to the cross-section predicted at NLO in QCD with NLO electroweak corrections: 507^{+35}_{-50} fb, where the uncertainties are estimated by varying α_S, renormalisation and factorization scales.

The production of $t\bar{t}V$, tZq and tWZ is modelled at NLO using MADGRAPH5_aMC@NLO2.3.3 with the NNPDF3.0NLO PDF set. The parton shower and hadronization are handled by PYTHIA8. For $t\bar{t}V$ and tWZ, the decays of b- and c-hadrons are handled by EVTGEN1.2.0. An alternative $t\bar{t}V$ sample is produced with SHERPA2.2.0 at LO.

The associated production of a vector boson with jets (W/Z+jets) is simulated using SHERPA2.2.1 with the NNPDF3.0NNLO PDF set. Matrix element calculations are performed with COMIX and OPENLOOPS, at NLO for up to two partons, and LO for up to four. They are matched to parton showers in SHERPA using the MEPS@NLO prescription, using a dedicated set of tune parameters. The samples are normalised to NNLO cross-section predictions.

The associated production of a Higgs boson with a single-top quark is modelled as two independent subprocesses, $tHjb$ and tWH, generated using MADGRAPH5_aMC@NLO v2.6.2 at NLO in QCD. The functional form of the renormalisation and factorization scales is set to $0.5 \times \sum_i \sqrt{m_i^2 + p_{\mathrm{T},i}^2}$. For $tHjb$ (tWH), the events are generated in the four (five) flavor scheme using the NNPDF3.0NLONF4 (NNPDF3.0NLO) PDF set, and showered with PYTHIA8.230 (PYTHIA8.235).

Diboson events (VV) are simulated with SHERPA2.2.1 or 2.2.2, depending on the process. Fully leptonic and semileptonic final states are included and are generated at NLO in QCD for up to one additional parton and at LO for up to three additional partons. The loop-induced process $gg \to VV$ is generated at LO for up to one additional parton. The matrix element calculations are matched and merged with the SHERPA parton shower algorithm based on the Catani-Seymour dipole factorization [179, 211] using the MEPS@NLO prescription. Virtual QCD corrections are provided by the OPENLOOPS library. The NNPDF3.0NNLO PDF set is used, as well as a dedicated set of tuned parton shower parameters.

8.1.4 Non-prompt lepton background

Hadrons, leptons produced inside jets, and electrons produced in photon conversions may satisfy the selection criteria of leptons produced in the hard-scattering (prompt leptons). They constitute a small, yet non-negligible background in the dilepton channel, usually referred to as *Fakes*. The contribution of this background is estimated from MC simulation, using a truth-level flag that identifies events with at least one fake lepton. The samples included are $t\bar{t}$ in the semileptonic final state, W+jets, diboson, $t\bar{t}V$, single top (t-channel, s-channel and tW), tWZ, tZq and tH. Events that are flagged as containing a fake lepton are removed from the respective sample and their contribution added to the *Fakes* category, that is treated independently.

8.2 Object reconstruction

The reconstruction of physics objects follows closely the procedures described for the $t\bar{t}H$ analyses (section 7.2) and therefore these are not detailed again. The differences are highlighted here.

Electrons and muons are required to satisfy the same identification criteria as in the $t\bar{t}H$ analyses: *Tight* and *Medium*, respectively. The muon isolation criterion is also the same, *FixedCutTightTrack-Only*. Electrons are required to be isolated both in the inner detector and calorimeter, using the *TightVarRad* isolation working point, described in section 5.3.

Small-R jets are reconstructed using the anti-k_t jet clustering algorithm with a radius parameter of 0.4 using as input particle-flow objects. Jets with $p_{\mathrm{T}} < 60$ GeV and $|\eta| < 2.4$ are required to be consistent with the primary vertex using the *Tight* working point of the JVT algorithm.

The overlap between leptons and jets is removed following the same procedure as described for the $t\bar{t}H$ analyses in section 7.2.

8.3 Identification of heavy-flavor jets

The standard DL1r flavor-tagging algorithm assigns to each jet the probability of being a b-jet (p_b), c-jet (p_c) or light-flavored jet (p_l). In this analysis, these probabilities are combined to construct discriminants to separate b- and c-jets from the other two classes:

$$\mathcal{D}_b = \log \frac{p_b}{f_c \cdot p_c + (1 - f_c) \cdot p_l}, \qquad \mathcal{D}_c = \log \frac{p_c}{f_b \cdot p_b + (1 - f_b) \cdot p_l}, \tag{8.1}$$

where f is a configurable parameter that controls which background contributes more to the decision of assigning a category to the jet. In the b/c-tagger developed for this analysis, f_c is set to 0.018, the same value that is used in the standard ATLAS b-tagging discriminant. The f_b parameter is set to 0.4, optimized using $t\bar{t}$ MC to maximize the separation between b- and c-jets. The discriminants $\mathcal{D}_b$ and $\mathcal{D}_c$ are combined in a single algorithm that jointly discriminates b- and c-jets from light-jets. This algorithm is referred to as the b/c-tagger.

Working points are defined in a non-regular binning through horizontal and vertical cuts in the plane formed by D_c in the x-axis and D_b in the y-axis. For consistency with the current flavor tagging working points used in ATLAS, five bins are defined, indicated with dashed lines in Figure 8.1. The coloured contours represent the normalised density of each jet class: light-jets in blue, c-jets in orange and b-jets in green. The calibrated working points are defined by the horizontal and vertical grey dashed lines. The two bins in the left upper corner of the plot are defined to have b-jet efficiencies of 70% and 60%, consistent with the standard b-tagging working points used in the ATLAS Collaboration. To the right of the vertical cut are bins enriched in c-jets. The upper and lower bins in this region correspond to c-tagging efficiencies of 11% and 22%, respectively, henceforth referred to as tight and loose. Finally, the left lower bin is dominated by light-jets. The efficiencies and rejection factors of the b/c-tagger working points are summarized in Table 8.1.

The calibration of the b/c-tagger follows the same pseudo-continuous calibration procedure as used for DL1r, described in section 5.7.3. Before performing the calibration, MC-to-MC scale factors are derived to remove the differences between different parton shower simulations in the distributions of the variables used for flavor tagging. Firstly, light-flavor jet calibration is performed. The resulting scale factors and uncertainties are used in the b-jet calibration. Lastly, the c-jet calibration uses the results from the previous two.

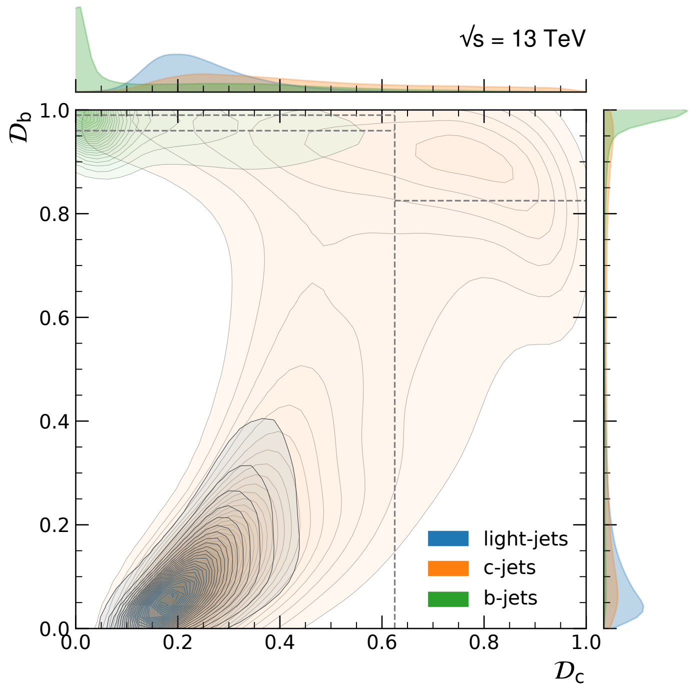

Figure 8.1: The two-dimensional b/c-tagger used in this analysis [15]. The x- and y-axis show the D_c and D_b discriminants, respectively. The grey dashed lines define the five calibrated working points. The contours represent the relative density of light-, c- and b-jets, in blue, orange and green, respectively, in a $t\bar{t}$ MC sample.

Table 8.1: The b- and c-jet efficiencies with their corresponding rejection factors for the working points derived from the five bins of the b/c-tagger. Both the $b@70\%$ and $c@22\%$ working points contain their respective tighter working points.

	b efficiency	c rejection	light rejection	$\mathcal{D}_b$	$\mathcal{D}_c$
$b@60\%$	60.3%	37.1	2320	≥ 0.990	< 0.625
$b@70\%$	70.0%	12.2	573	≥ 0.963	< 0.625
	c efficiency	b rejection	light rejection	$\mathcal{D}_b$	$\mathcal{D}_c$
$c@11\%$	11.3%	28.7	1051	≥ 0.825	≥ 0.625
$c@22\%$	22.4%	18.9	104	–	≥ 0.625

Table 8.2: Fiducial phase space selection.

Selection	Dilepton
Leptons	$= 2$ (opposite charge) $\|\eta\| < 2.5$ $p_{\mathrm{T}} > 27$ GeV
Jets	$N_{\text{jets}} \geq 3$ $\|\eta\| < 2.5$ $p_{\mathrm{T}} > 25$ GeV ≥ 2 with ghost matched b-hadron
Overlap removal	$\Delta R(e, \mathrm{jet}) < 0.4 \rightarrow$ remove e $\Delta R(\mu, \mathrm{jet}) < 0.4 \rightarrow$ remove μ

8.4 Analysis strategy and event selection

The goal of this analysis is to measure the $t\bar{t}+\geq 2c$ and $t\bar{t}+1c$ production cross-sections and their ratios to the inclusive $t\bar{t}$+jets production cross-section. Two kinds of measurements are performed: one using the $t\bar{t}+\geq 2c$, $t\bar{t}+1c$, $t\bar{t}+\geq 1b$ and $t\bar{t}$+light yield and shape predictions in the full phase space included in the event generation (henceforth referred to as *generator phase space*), and one using the predictions in a fiducial phase space defined at truth-level to mimic the detector-level event selection.

The fiducial phase space is defined to be very close to the reconstructed phase space and therefore it is expected to suffer less from theoretical uncertainties that affect the extrapolation from the fiducial to the full phase space. The full phase space is better suited for comparisons with theoretical predictions.

In the dilepton channel, the fiducial phase space definition is detailed in Table 8.2. Events are required to have exactly two leptons (ee, $\mu\mu$ or $e\mu$) within $|\eta| < 2.5$ with $p_T > 27$ GeV for the leading lepton and $p_T > 10$ GeV for the subleading one; at least three jets with $p_T > 25$ GeV and $|\eta| < 2.5$, two of which must be ghost-matched to b-hadrons. The invariant mass of the lepton pair is required to be larger than 15 GeV to exclude backgrounds from Drell-Yan production and within $83 < M_{ll} < 99$ GeV to exclude the Z-boson mass peak. Electrons and muons are removed if they overlap with a jet within $\Delta R < 0.4$. No requirement is imposed on the presence of c-jets, allowing for a simultaneous measurement of the $t\bar{t}+\geq 2c$, $t\bar{t}+1c$, $t\bar{t}+\geq 1b$ and $t\bar{t}$+light cross-sections.

Different generators and parameter settings within the same generator might lead to different predictions of the total yields of the $t\bar{t}$+jets sub-components. To avoid double-counting effects when performing the fits to data, the fractions of $t\bar{t}+\geq 2c$, $t\bar{t}+1c$, $t\bar{t}+\geq 1b$ and $t\bar{t}$+light in the alternative samples are scaled to match the fraction predicted by the nominal samples. These scaling factors are derived at particle level in the generator phase space for the full phase space fit or in the fiducial phase space for the fiducial fit. They are listed in the appendix, in Table D.1.

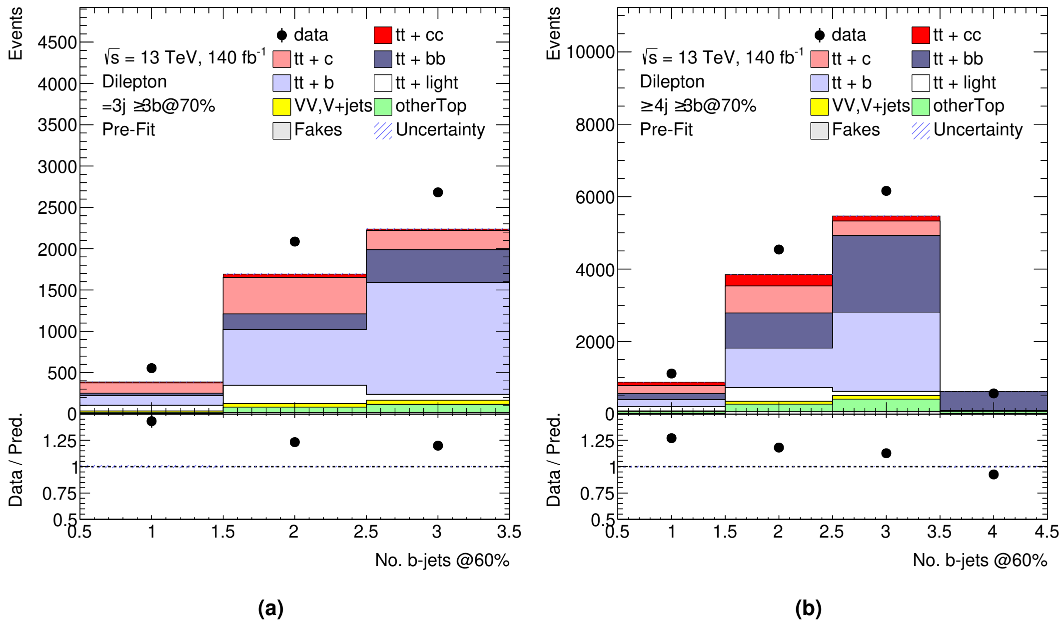

Figure 8.2: Comparison between data and MC prediction of the number of b-jets $@60\%$ WP in regions with exactly three (8.2a) or at least four jets (8.2b) and at least three b-jets $@70\%$ WP. The error band includes only the statistical contribution.

8.4.1 Preselection

Events are collected using a logical OR of different single lepton triggers shown in Table 7.4. These are the same triggers as used for the $t\bar{t}H$ analyses.

A common pre-selection is applied before dividing events into signal and control regions, aiming at selecting dileptonic $t\bar{t}$ events with additional jets. Each event is required to have exactly two leptons (electrons or muons: ee, $\mu\mu$ or $e\mu$) with opposite charge. At least one must have $p_T > 27$ GeV and be matched to a lepton with the same flavor reconstructed by the trigger algorithm within $\Delta R < 0.15$. In the ee and $\mu\mu$ channels, the dilepton invariant mass must be above 15 GeV and outside the Z-boson mass window of $83 - 99$ GeV. Events are required to have zero reconstructed hadronic tau τ_{had} candidates, to ensure orthogonality with possible future analyses targeting the same process with different decay modes.

Events are required to have at least three jets, at least two of which must be b-tagged using the 70% WP of the DL1r b-tagging algorithm. To ensure that all regions entering the fit rely only on the b/c-tagger WPs, events are required to have at least two b-jets tagged with the tight working point of the b/c-tagger (which is tighter than the 70% WP of the standard DL1r algorithm). In the rest of the text, unless stated otherwise, the WPs refer to the b/c-tagger WPs.

Figure 8.2 shows the multiplicity of b-jets tagged with the 60% WP in events with exactly three and at least four jets, with at least three b-jets $@70\%$ WP. It highlights the different relative amounts of $t\bar{t}+\geq 1b$ and $t\bar{t}$+light that can be achieved when requiring at least three b-jets at 60% WP or exactly two b-jets at 60% WP. This feature is used to define control regions, as described in the following section.

8.4.2 Signal and control regions

Events are split based on the number of jets, b-jets at 60% and 70% WPs, and c-jets tagged using the loose working point of the b/c-tagger. In the dileptonic channel, a good $t\bar{t}+\geq 2c$ and $t\bar{t}+1c$ purity can be achieved without using the tight c-tagging working point, which would lead to a significant reduction in the available statistics.

Signal and control regions are defined per jet multiplicity (exactly three or at least four jets), resulting in a total of nine fit regions, whose selection criteria are summarized in Table 8.3. Regions with at least three jets b-tagged at 70% WP and exactly two or at least three b-jets at 60% are used as $t\bar{t}+\geq 1b$ control regions, with different relative amounts of $t\bar{t}+\geq 2c$, $t\bar{t}+1c$ and $t\bar{t}$+light. Regions with exactly two b-jets at 70% and a veto on c-jets are dominated by $t\bar{t}$+light and used to control the normalisation of this background. Signal regions with exactly two b-jets at 70% and exactly one and at least two c-jets at 22% (only in the four jet inclusive regions) are defined to have a high-purity in $t\bar{t}+1c$ and $t\bar{t}+\geq 2c$, respectively. Very few events exist with exactly three jets and at least two c-jets. Therefore, in this case, only a region with at least one c-jet is considered.

In the signal regions with at least four jets, the number of jets is used as discriminating variable. In the signal region with exactly three jets and at least one c-jet, the discriminant variable is the invariant mass of the leading c-jet and the closest c- or non-c-jet. The choice of discriminant variables ensures consistency with the fit model used in the single-lepton channel, while simultaneously providing good sensitivity and ensuring an optimal modelling of data, with minimal dependence on the leading systematic uncertainties.

The expected signal and background composition of each region is shown in Figure 8.3. The $t\bar{t}+1c$ and $t\bar{t}+\geq 2c$ signals are shown in light and dark red, respectively. The $t\bar{t}+\geq 1b$ background is shown in shades of blue, separately for $t\bar{t}+1b$ and $t\bar{t}+\geq 2b$. The contribution from $t\bar{t}$+light is shown in white. The smaller backgrounds are also shown: diboson and V+jets in yellow, other top processes in green and *Fakes* in grey. The $SR^{2\ell\geq 4j}_{\text{tight}}$ signal region has the highest $t\bar{t}+\geq 2c$ signal to background ratio of 78.1%.

The summary of the composition of each region as well as the pre-fit yield comparison between MC and data is shown in Figure 8.4. Figure 8.5 shows pre-fit data/MC comparisons of the distributions used in each of the analysis regions. The *Other top* category includes smaller backgrounds such as $t\bar{t}H$, $t\bar{t}V$ and single-top production. The contribution from fake leptons (*Fakes* category) is estimated from MC samples, following the procedure described in section 8.1.

Table 8.3: Summary of the analysis regions, defined based on the number of jets, the number of b-jets tagged using the 70% and 60% working points and the number of c-jets tagged with the loose working point of the b/c-tagger.

Regions	No. jets	b@70%	b@60%	c@22%
$CR_1^{2\ell 3j}$	3	2	—	0
$CR_2^{2\ell 3j}$		3	3	—
$CR_3^{2\ell 3j}$		3	< 3	—
$SR_{\text{loose}}^{2\ell 3j}$		2	—	1
$CR_1^{2\ell \geq 4j}$	≥ 4	2	—	0
$CR_2^{2\ell \geq 4j}$		≥ 3	≥ 3	—
$CR_3^{2\ell \geq 4j}$		≥ 3	< 3	—
$SR_{\text{loose}}^{2\ell \geq 4j}$		2	—	1
$SR_{\text{tight}}^{2\ell \geq 4j}$		2	—	≥ 2

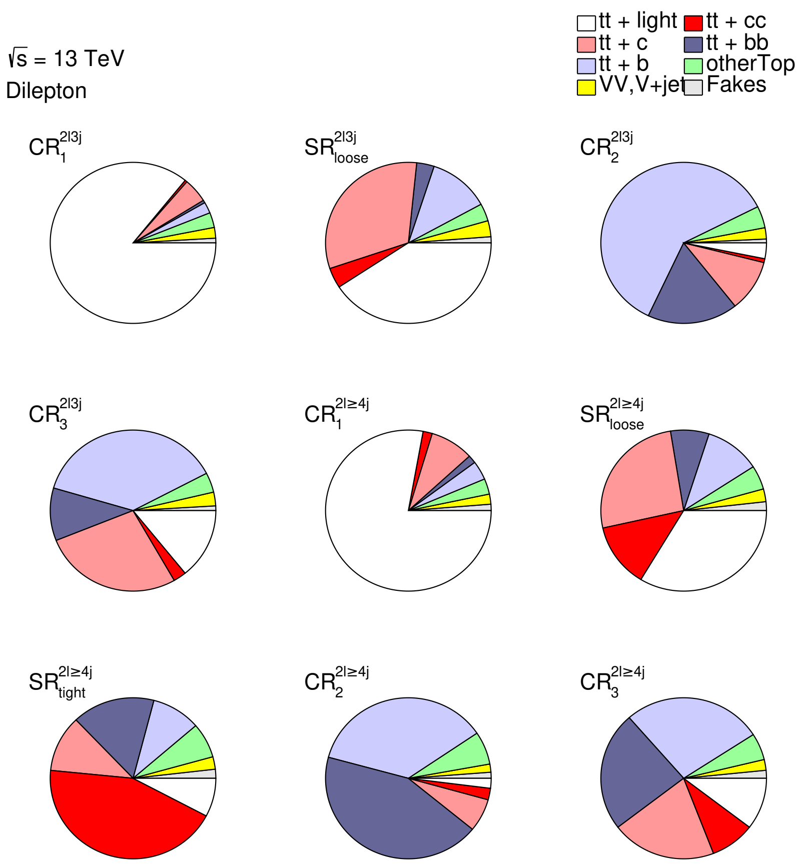

Figure 8.3: Expected composition of the analysis regions. The fractional contribution of each background and signal to total MC estimate is shown in each region.

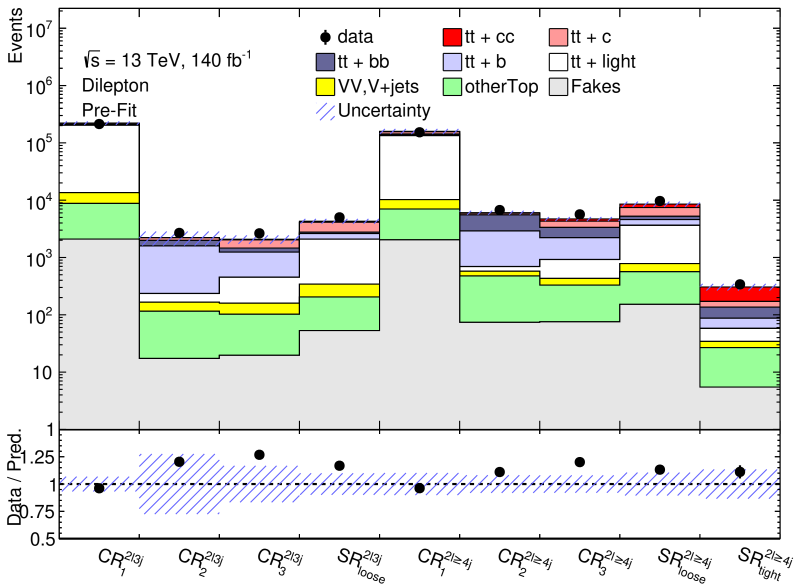

Figure 8.4: Summary plot showing pre-fit comparison between total MC prediction and data yields in the analysis regions.

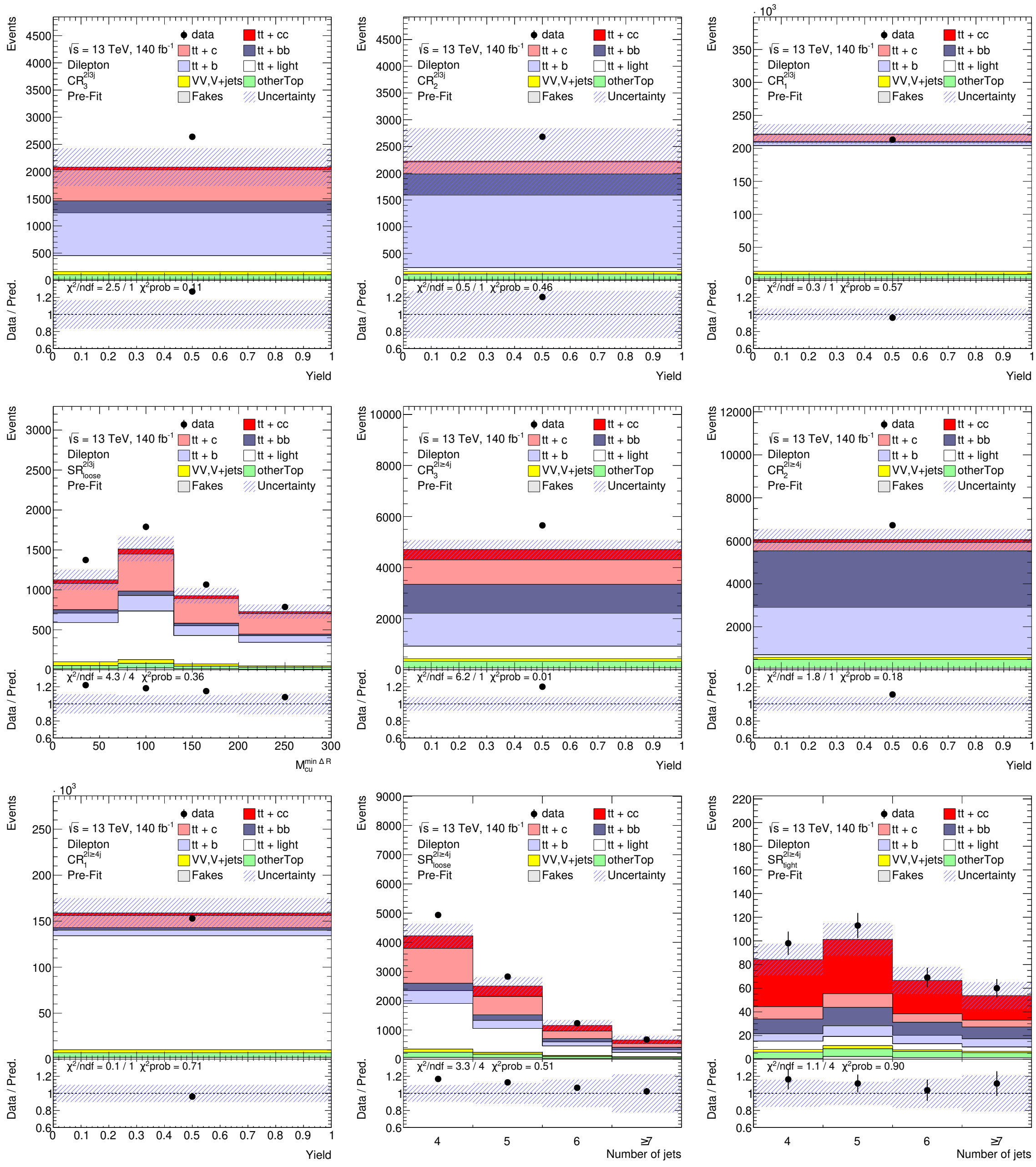

Figure 8.5: Pre-fit data/MC comparisons of the discriminant variables in the regions used in the fit.

8.5 Systematic uncertainties

Systematic uncertainties are assessed from two main sources: theoretical uncertainties related with the MC modelling of signal and background processes and instrumental uncertainties associated with the reconstruction, identification and calibration of all physics objects used in the analysis, including detector effects.

The number of nuisance parameters associated with each uncertainty source are listed in Table 8.4.

8.5.1 Modelling of $t\bar{t}$

Systematic uncertainties on the shape and acceptance of $t\bar{t}+\geq 2c$, $t\bar{t}+1c$ and $t\bar{t}$+light are estimated from comparing the nominal sample with samples simulated with different generators or different settings of the nominal generator. Unless stated otherwise, the uncertainties associated with $t\bar{t}+\geq 2c$ and $t\bar{t}+1c$ are taken as fully correlated.

Three independent uncertainties are assigned to the initial state radiation, ISR: the internal PYTHIA8 up and down VAR3C variations of the A14 tune; and the variation of the renormalisation and factorization scales by a factor 2 and 0.5 with respect to the nominal value. To estimate the uncertainty associated with final state radiation, FSR, the FSR renormalisation scale is varied up and down by a factor 2 and 0.5.

The uncertainties associated with the choice of PDF are assessed using the PDF4LHC15 error set, consisting of 30 independent nuisance parameters, most of which are pruned from the fit.

To estimate the uncertainty associated with the modelling of the parton shower and hadronization, the alternative POWHEG+PYTHIA8 samples are used. The alternative sample are produced using a fast detector simulation and therefore it is compared to the nominal sample passed through the fast detector simulation. The relative per bin uncertainty is propagated to the nominal sample (full detector simulation). This procedure, followed whenever an alternative sample is produced with the fast detector simulation, removes effects related to differences between full and fast detector simulation, which are non-negligible in this phase space.

Different decorrelation schemes are employed for the parton shower uncertainties. For $t\bar{t}$+light a total of two nuisance parameters are used: one assigned to regions with exactly three jets and one to regions with at least four jets. The POWHEG+PYTHIA8 alternative sample predicts fewer events than the nominal sample in the regions with exactly three jets, while in the regions with at least four jets it always predicts more events. This leads to a strong constraint in this nuisance parameter if no decorrelation is performed. Independent parton shower nuisance parameters are assigned to $t\bar{t}+1c$ and $t\bar{t}+\geq 2c$ and similarly for $t\bar{t}+1b$ and $t\bar{t}+\geq 2b$, to relax the constraints observed in the Asimov fit.

The uncertainty associated with the matching between the matrix element calculation and the parton shower is estimated using the alternative sample with $p^{T}_{\text{hard}} = 1$ GeV. Independent nuisance parameters are assigned to $t\bar{t}+1c$ and $t\bar{t}+\geq 2c$. The uncertainty associated with the choice of h_{damp} parameter is evaluated using the alternative sample with $h_{\text{damp}} = 3 \times m_{\text{top}}$.

Systematic	Type	No. of components
Luminosity	N	1
pileup	SN	1
Electrons (trigger, reco, ID, isolation)	SN	4
Electrons (resolution, scale)	SN	2
Muons (trigger, reco, ID, isolation)	SN	10 (5 stat., 5 syst.)
Muons (resolution, scale)	SN	4
Jet vertex tagging (JVT)	SN	1
Jet energy scale (JES)	SN	35
Jet energy resolution (JER)	SN	13
flavor tagging	SN	85
$t\bar{t}$ parton shower and hadronisation	SN	4
$t\bar{t}\ p^T_{\text{hard}}$	SN	3
$t\bar{t}\ h_{\text{damp}}$	SN	2
$t\bar{t}$ FSR	SN	2
$t\bar{t}$ Var3c	SN	2
$t\bar{t}\ \mu_R$	SN	2
$t\bar{t}\ \mu_F$	SN	2
$t\bar{t}$ PDF	SN	60
$t\bar{t}+\geq 1b$ parton shower and hadronisation	SN	2
$t\bar{t}+\geq 1b$ dipole recoil	SN	1
$t\bar{t}+\geq 1b$ FSR	SN	1
$t\bar{t}+\geq 1b$ Var3c	SN	1
$t\bar{t}+\geq 1b\ \mu_R$	SN	1
$t\bar{t}+\geq 1b\ \mu_F$	SN	1
$t\bar{t}+\geq 1b$ PDF	SN	30
Wt diagram removal vs subtraction	SN	1
Wt matrix element generator	SN	1
Wt norm uncertainty	N	3
$t\bar{t}V$ hadronisation and matrix element	SN	2
$t\bar{t}V$ cross-section uncertainties	N	2
Other top	N	1
$t\bar{t}H$	N	1
W+jets	N	3
Z+jets	N	1
Diboson	N	1
Fakes norm uncertainty	N	1

Table 8.4: Complete list of systematic uncertainties considered before pruning is applied. S in the Type column indicates that this uncertainty has a shape effect, while N indicates a normalisation effect. The "No. of components" column describes how many independent nuisance parameters are used for this uncertainty in the fit before potential pruning.

8.5.2 $t\bar{t}b\bar{b}$ modelling

The contributions of the $t\bar{t}+\geq 2b$ and $t\bar{t}+1b$ backgrounds are simulated using the same $t\bar{t}b\bar{b}$ sample. Unless otherwise stated, the uncertainties are treated as fully correlated between these two background components. The ISR, FSR and PDF uncertainties are defined as for the inclusive $t\bar{t}$ sample.

The uncertainty associated with the parton shower and hadronization is evaluated using the alternative POWHEG+HERWIG7 sample, produced with the fast detector simulation. The alternative sample with $h_{\text{bzd}} = 2$ is used to estimate the uncertainty associated with this parameter.

The alternative sample produced with the dipole recoil scheme is used to assign an uncertainty to the choice of this parameter. The alternative sample is only available with $h_{\text{bzd}} = 2$ and therefore it is compared with a global recoil scheme sample with the same h_{bzd} value.

Similarly to the procedure followed for inclusive $t\bar{t}$ production, the uncertainty associated with the matching between the matrix element calculation and the parton shower is estimated using the alternative sample with $p^T_{\text{hard}} = 1$. Independent nuisance parameters are assigned to $t\bar{t}+1b$ and $t\bar{t}+\geq 2b$.

8.5.3 Modelling of smaller backgrounds

The removal of LO $t\bar{t}$ diagrams from the NLO corrections to tW can be performed in two ways: diagram removal (DR) removes the diagrams at amplitude level while diagram subtraction (DS) removes the diagrams at matrix element level. The nominal tW sample is generated using the DR method. An alternative sample produced with the DS scheme is used to evaluate the uncertainty associated with this procedure. The uncertainty on the parton shower and hadronization model and on the matrix element generator are evaluated by comparing the nominal sample with the alternative samples produced with POWHEGBOX+HERWIG7 and MADGRAPH5_AMC@NLO, respectively. An additional 5% normalisation uncertainty is assigned to tW.

In the dilepton channel, all single-top t- and s-channel events passing the analysis selection have at least one fake lepton, identified at truth level. Therefore these samples are used only to estimate the *Fakes* contribution. As such, no uncertainties are assigned to these samples. Instead, a 25% normalisation uncertainty is assigned to the contribution from events with fake leptons, following the prescription used in the $t\bar{t}H(H \to b\bar{b})$ analyses.

For $t\bar{t}V$ processes, the uncertainty associated with the choice of generator and parton shower and hadronization model is estimated by comparing the nominal sample with the alternative SHERPA sample. Independent nuisance parameters are assigned to $t\bar{t}W$ and $t\bar{t}Z$. Cross section uncertainties of $^{+10.4\%}_{-12.0\%}$ and $^{+13.3\%}_{-12.0\%}$ are assigned to $t\bar{t}Z$ and $t\bar{t}W$, respectively.

A conservative 50% normalisation uncertainty is assigned to all other top processes (tZq, tWZ, tH and $t\bar{t}H$), with one nuisance parameter assigned to $t\bar{t}H$ and another to the remaining samples.

Cross-section uncertainties of $\pm 40\%$, $\pm 35\%$ and $\pm 50\%$ are assigned to W+jets, Z+jets and diboson processes, respectively. The Z+jets contribution is scaled up by 25% to improve the modelling of this process, following the procedure implemented in the $t\bar{t}H$ analyses [155]. An additional 40% normalisation uncertainty is assigned to W+jets events with exactly two or at least three heavy-flavor jets, as independent nuisance parameters.

8.5.4 Instrumental uncertainties

The uncertainties associated with the luminosity and with the differences between the pileup distributions in data and MC are evaluated following the same prescription as described in section 7.4.4 for the $t\bar{t}H$ analyses. The same is true for the uncertainties associated with the trigger, reconstruction, identification and energy calibration of electrons and muons, even though different identification and isolation working points are used.

The uncertainties associated with the JVT discriminant are included in the form of scale factors derived in $Z(\rightarrow \mu\mu)$+jets events to account for the JVT efficiency difference in data and MC. An additional uncertainty is included to account for non-negligible differences in the hard-scattering efficiency for fixed JVT cuts between the SHERPA and the POWHEG+PYTHIA8 $Z(\rightarrow \mu\mu)$+jets samples, attributed to different fragmentation models used in SHERPA and PYTHIA8 [212].

To evaluate the uncertainties associated with the jet energy scale, the procedure described in section 7.4.4 is followed. The jet energy resolution is measured in dijet events in a fit that yields a total of 117 nuisance parameters [11]. The dijet balance method is used. It consists of calculating the asymmetry between the transverse momentum of the two leading jets. Any deviations from an exact symmetry are due to experimental resolution effects, the presence of additional radiation and biases introduced by the event selection. An eigenvector decomposition is used, leading to 12 nuisance parameters. An additional nuisance parameter associated with the comparison between data and MC is included, yielding a total of 13 independent nuisance parameters for this uncertainty source [213].

The b/c-tagger is calibrated following the standard procedure used in the ATLAS Collaboration to calibrate the standard DL1r b-tagging algorithm. The uncertainties of this procedure result in 45 NPs for b-jets and 20 NPs for c- and light-jets each.

Table 8.5: Measured values of the $t\bar{t}+\geq 2c$ and $t\bar{t}+1c$ signal strengths and ratios to inclusive $t\bar{t}$+jets production in the fiducial and full generator phase spaces.

Parameter of interest	Fiducial phase space	Full phase space
$\mu(t\bar{t}+\geq 2c)$	1.26 ± 0.30	1.30 ± 0.33
$\mu(t\bar{t}+1c)$	1.60 ± 0.20	1.47 ± 0.31
$\sigma(t\bar{t}+\geq 2c)/\sigma(t\bar{t}+\text{jets})$	1.28 ± 0.29	1.31 ± 0.32
$\sigma(t\bar{t}+1c)/\sigma(t\bar{t}+\text{jets})$	1.62 ± 0.19	1.48 ± 0.28

8.6 Cross-section measurement results

The first ATLAS measurements of the $t\bar{t}+\geq 2c$ and $t\bar{t}+1c$ signal strengths and ratios to inclusive $t\bar{t}$+jets production in the dileptonic channel are discussed in this section. The full Run 2 dataset is used, corresponding to a total integrated luminosity of 140 fb^{-1}.

Two types of measurements are performed: in the fiducial and generator phase spaces. A summary of the results is presented in Table 8.5. Section 8.6.1 shows the post-fit yields and distributions obtained from the fit to data in the fiducial phase space. The results from the measurements in the fiducial and full phase spaces are discussed in sections 8.6.2 and 8.6.3, respectively.

8.6.1 Post-fit yields and distributions

The measured signal and background yields in the fiducial phase space are shown in Tables 8.6 and 8.7 for the analysis regions with exactly three and at least four jets, respectively. The expected $t\bar{t}+\geq 2c$ and $t\bar{t}+1c$ signal yields are also shown, in the first two lines. The post-fit yields are obtained from the dilepton fit to data in the fiducial phase space. The uncertainties include the statistical and systematic components. The pulls, constraints and correlations between nuisance parameters are taken into account when computing the yields and uncertainties.

Figure 8.6a shows the post-fit distribution of the invariant mass between the leading c-jet and the closest c- or light-jet in the $SR^{2\ell 3j}_{\text{loose}}$. Figures 8.6b and 8.6c show the distributions of the number of jets in the $SR^{2\ell\geq 4j}_{\text{loose}}$ and $SR^{2\ell\geq 4j}_{\text{tight}}$. A good post-fit agreement is observed between data and prediction, characterized by a goodness of fit above 99% (very close to the one obtained in the full phase space fit). The uncertainties are largely constrained by the fit. In the remaining regions, no shape information is used in the fit and therefore the post-fit plots do not add information to Tables 8.6 and 8.7.

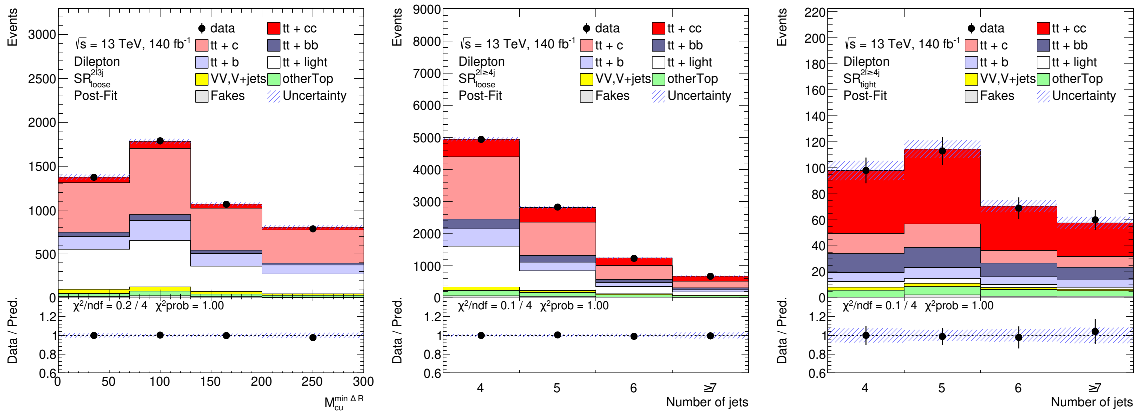

(a) (b) (c)

Figure 8.6: Post-fit data/MC comparisons in the analysis regions obtained from the fit to data in the fiducial phase space. Only the regions in which more than one bin is fitted are shown.

	$CR_1^{2\ell 3j}$	$CR_2^{2\ell 3j}$	$CR_3^{2\ell 3j}$	$SR_{\text{loose}}^{2\ell 3j}$
$t\bar{t}+\geq 2c$ pre-fit	942 $\pm$ 103	16 $\pm$ 3	53 $\pm$ 10	176 $\pm$ 42
$t\bar{t}+1c$ pre-fit	10 588 $\pm$ 945	225 $\pm$ 25	568 $\pm$ 50	1357 $\pm$ 151
$t\bar{t}+\geq 2c$	1242 $\pm$ 348	22 $\pm$ 5	71 $\pm$ 17	226 $\pm$ 57
$t\bar{t}+1c$	16 839 $\pm$ 2436	357 $\pm$ 45	925 $\pm$ 100	2172 $\pm$ 237
$t\bar{t}+\geq 2b$	1447 $\pm$ 267	456 $\pm$ 50	265 $\pm$ 42	177 $\pm$ 29
$t\bar{t}+1b$	6107 $\pm$ 759	1625 $\pm$ 88	951 $\pm$ 62	617 $\pm$ 50
$t\bar{t}$+light	173 950 $\pm$ 3081	62 $\pm$ 18	257 $\pm$ 52	1503 $\pm$ 196
VV,V+jets	4803 $\pm$ 1635	51 $\pm$ 18	59 $\pm$ 21	138 $\pm$ 48
Other top	6683 $\pm$ 1246	95 $\pm$ 29	81 $\pm$ 20	147 $\pm$ 42
Fakes	2106 $\pm$ 525	17 $\pm$ 4	20 $\pm$ 5	52 $\pm$ 13
Total	213 178 $\pm$ 469	2685 $\pm$ 50	2629 $\pm$ 42	5032 $\pm$ 66
Data	213 185	2682	2640	5015

Table 8.6: Post-fit yields in the signal and control regions with exactly three jets, obtained from the fit to data in the fiducial phase space.

	$CR_1^{2\ell\geq 4j}$	$CR_2^{2\ell\geq 4j}$	$CR_3^{2\ell\geq 4j}$	$SR_{\text{loose}}^{2\ell\geq 4j}$	$SR_{\text{tight}}^{2\ell\geq 4j}$
$t\bar{t}+\geq 2c$ pre-fit	2817 ± 299	137 ± 22	407 ± 42	1107 ± 91	135 ± 20
$t\bar{t}+1c$ pre-fit	$13\,355 \pm 1163$	386 ± 35	957 ± 97	2208 ± 273	35 ± 9
$t\bar{t}+\geq 2c$	3727 ± 970	178 ± 42	529 ± 104	1407 ± 273	166 ± 26
$t\bar{t}+1c$	$21\,662 \pm 2964$	631 ± 69	1608 ± 172	3613 ± 406	51 ± 9
$t\bar{t}+\geq 2b$	2625 ± 370	2869 ± 163	1226 ± 79	678 ± 61	50 ± 6
$t\bar{t}+1b$	6244 ± 888	2399 ± 164	1418 ± 105	986 ± 85	26 ± 7
$t\bar{t}$+light	$108\,365 \pm 3397$	92 ± 31	416 ± 89	2219 ± 328	13 ± 5
VV,V+jets	3249 ± 1094	100 ± 34	103 ± 35	216 ± 73	7 ± 3
Other top	5020 ± 1122	396 ± 111	252 ± 61	405 ± 76	21 ± 5
Fakes	2043 ± 509	74 ± 19	76 ± 19	151 ± 39	5 ± 1
Total	$152\,935 \pm 417$	6740 ± 81	5628 ± 68	9674 ± 93	340 ± 18
Data	152 931	6725	5655	9668	340

Table 8.7: Post-fit yields in the signal and control regions with at least four jets, obtained from the fit to data in the fiducial phase space.

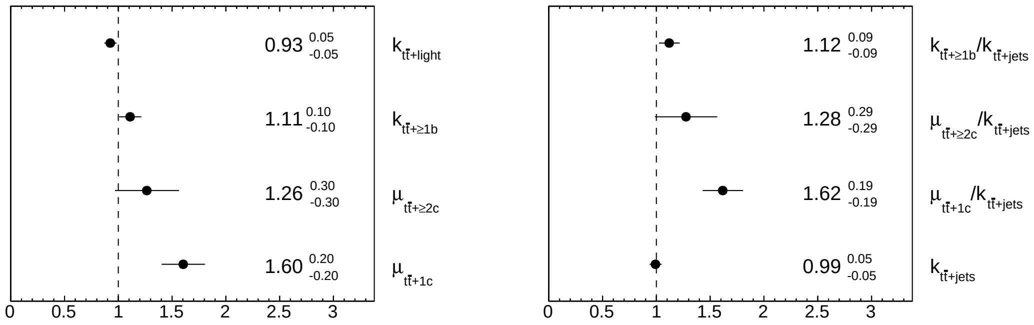

(a) **(b)**

Figure 8.7: Measured values of the $t\bar{t}+\geq 2c$ and $t\bar{t}+1c$ parameters of interest and of $t\bar{t}$+light or $t\bar{t}$+jets and $t\bar{t}+\geq 1b$ normalisation factors in a fit to data in the fiducial phase space, extracting the signal strengths (8.7a) or the ratios (8.7b).

8.6.2 Fiducial phase space results

The measured values of the $t\bar{t}+\geq 2c$ and $t\bar{t}+1c$ signal strengths in the fiducial phase space are shown in Figure 8.7a. The $t\bar{t}+\geq 2c$ signal strength is compatible with the expected value of 1 within the uncertainties. The measured value of the $t\bar{t}+1c$ signal strength differs from the prediction by more than 2σ. A precision slightly above 20% is achieved for $t\bar{t}+\geq 2c$, and of around 12% for $t\bar{t}+1c$. The measured values of the $t\bar{t}$+light and $t\bar{t}+\geq 1b$ background normalisation factors, $k(t\bar{t}+\text{light})$ and $k(t\bar{t}+\geq 1b)$, are also shown. They are measured to be very close to the expected values, with a precision of 5% and 9%, respectively. The best fit value of $k(t\bar{t}+\text{light})$ is slightly below 1.

Figure 8.7b shows the measured values of the ratios of $t\bar{t}+\geq 2c$ and $t\bar{t}+1c$ to inclusive $t\bar{t}$+jets production. The parameters of interest are re-expressed to allow for the extraction of the ratios but the fit converges to the same minimum. Additionally, instead of measuring the signal strength of $t\bar{t}$+light production, the inclusive $t\bar{t}$+jets normalisation factor is extracted, as well as the ratio of $(t\bar{t}+\geq 1b)$/($t\bar{t}$+jets) production.

When extracting the ratios of $t\bar{t}+\geq 2c$ and $t\bar{t}+1c$ to inclusive $t\bar{t}$+jets production, the uncertainties on the parameters of interest are slightly reduced. The best fit values are compatible with the ones obtained when fitting the signal strengths. Given that the systematic uncertainties associated with the modelling of the background processes are decorrelated between $t\bar{t}$+light, $t\bar{t}+\geq 1c$ and $t\bar{t}+\geq 1b$, the decrease in the uncertainty is mainly due to cancellations of the instrumental systematic uncertainties. The sensitivity could be enhanced by correlating the modelling nuisance parameters between $t\bar{t}$+light and $t\bar{t}+\geq 1c$ since these backgrounds are modelled using the same inclusive $t\bar{t}$ inclusive five-flavor scheme sample. This possibility is under study.

Impact of systematic uncertainties

The pre- and post-fit impact of the nuisance parameters on the $t\bar{t}+\geq 2c$ and $t\bar{t}+1c$ signal strengths are shown by empty and filled blue bars in Figures 8.8a and 8.8b, respectively. The pulls and constraints on the nuisance parameters are overlayed in the same plots using black markers and lines. The flavor-tagging systematic uncertainties have the largest impact, in particular the first eigenvalues associated with the light- and c-jet mistag-rate calibrations. Both uncertainties are among the top-four highest ranked nuisance parameters for the $t\bar{t}+1c$ and $t\bar{t}+\geq 2c$ signal strength measurements. The $t\bar{t}+1c$ h_{damp} uncertainty has a large impact in the measurement of the $t\bar{t}+\geq 2c$ signal strength (second highest ranked). Uncertainties associated with the modelling of $t\bar{t}$+light and $t\bar{t}+\geq 1b$ parton shower have a large impact on the measurement of the $t\bar{t}+1c$ signal strength. In particular, for $t\bar{t}$+light, the nuisance parameter associated with the two-point systematic based on POWHEG-BOX+HERWIG7 in the regions with three jets occupies the third position in the ranking. The $t\bar{t}+\geq 1b$ dipole recoil scheme parton shower nuisance parameter ranks fourth. These background modelling systematic uncertainties are the highest ranked, following the flavor-tagging uncertainties.

The ranking plots for the ratio fits are included in appendix D. They are fairly consistent with the ones obtained when measuring the signal strengths. The two systematic uncertainties with the largest impact on the measurement of the $t\bar{t}+\geq 2c/t\bar{t}+$jets cross-section ratio are the same as in the measurement of $\mu(t\bar{t}+\geq 2c)$. For the $t\bar{t}+1c$ ratio some differences arise. The first eigenvalue of the light mistag-rate calibration is still the highest ranked uncertainty but it is followed by the normalisation factor associated with the ratio $t\bar{t}+\geq 1b/t\bar{t}+$jets. This is due to a sizable anti-correlation between these two ratios that is not present in the fit of the signal strengths.

No pulls above 1σ are observed. The uncertainties associated with the modelling of $t\bar{t}$+light and $t\bar{t}+\geq 1c$ show the largest pulls. The $t\bar{t}+\geq 1c$ nuisance parameter associated with the final state radiation is pulled to approximately -0.5σ. The nuisance parameters associated with the $t\bar{t}$+light parton shower uncertainties in regions with exactly three or at least four jets are pulled to around 0.5σ and -0.5σ, respectively. The existence of sizable pulls in opposite directions supports the decision to decorrelate these nuisance parameters. The $t\bar{t}$+light nuisance parameter associated with the h_{damp} variation is pulled to $\sim -0.6\sigma$.

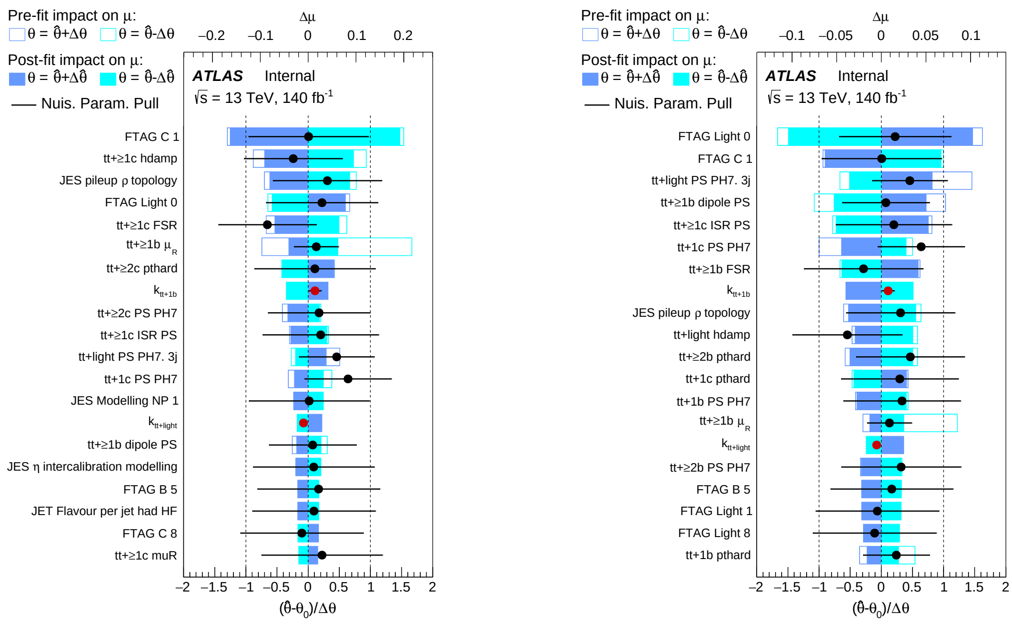

(a) **(b)**

Figure 8.8: Ranking plots showing the impact of each nuisance parameter on the $t\bar{t}+\geq 2c$ (8.8a) and $t\bar{t}+1c$ (8.8b) signal strengths in the fit to data in the fiducial phase space. Only the 20 nuisance parameters with the highest impact are shown. With respect to the plots shown for $t\bar{t}H(H\to b\bar{b})$ analysis, a newer version of the TRExFITTER software was used to produce these plots. With this version, the normalisation factors are shown as red markers and their default value is one.

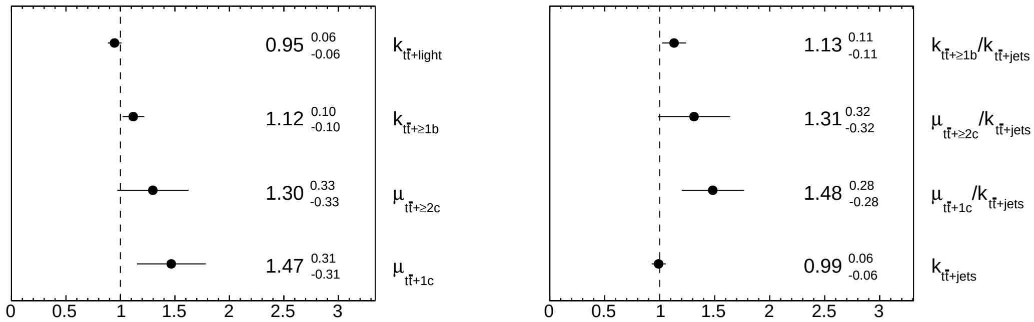

(a) (b)

Figure 8.9: Measured values of the $t\bar{t}$+light or $t\bar{t}$+jets and $t\bar{t}+\geq 1b$ normalisation factors in a fit to data in the generator phase space, extracting the signal strengths (8.9a) or the ratios (8.9b).

8.6.3 Full generator phase space results

The measured values of the parameters of interest and background normalisation factors in the full generator phase space are shown in Figure 8.9. The results for the signal strength and ratio fits are shown in Figures 8.9a and 8.9b, respectively.

The results obtained in the full generator phase space are consistent with the ones from the fiducial phase space fit, as can be observed from Table 8.5. The largest difference is in the $t\bar{t} + 1c$ signal strength and ratio that are measured to be approximately 8% smaller and with larger uncertainties in the generator phase space with respect to the fiducial phase space. Nonetheless, the values are compatible within 1σ.

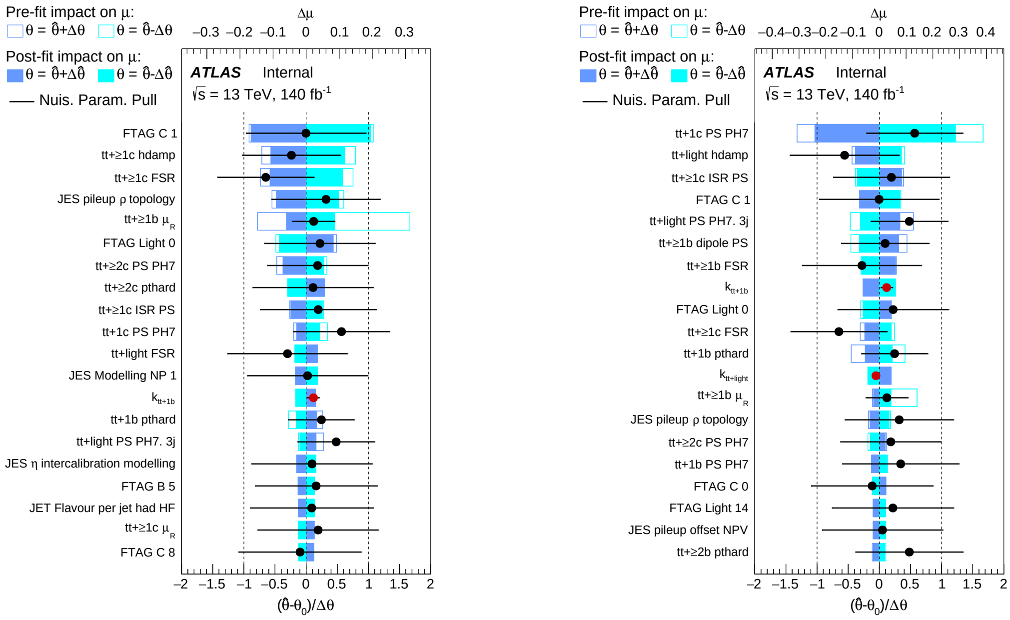

(a) **(b)**

Figure 8.10: Ranking plots showing the impact of each nuisance parameter on the $t\bar{t}+\geq 2c$ (8.10a) and $t\bar{t}+1c$ (8.10b) signal strengths in fit the to data in the generator phase space. Only the 20 nuisance parameters with the highest impact are shown.

Impact of systematic uncertainties

The impact of the systematic uncertainties in the full phase space extraction of the $t\bar{t}+\geq 2c$ and $t\bar{t}+1c$ signal strengths is shown in Figures 8.10a and 8.10b, respectively.

The measurement of $\mu(t\bar{t}+\geq 2c)$ is dominated by the uncertainty associated with the first eigenvalue of the c-jet mistag-rate calibration, similarly to the fiducial phase space fit, and followed by $t\bar{t}+1c$ modelling uncertainties. Unlike in the fiducial phase space fit, the measurement of $\mu(t\bar{t}+1c)$ is dominated by the uncertainties associated with the modelling of $t\bar{t}+1c$ and $t\bar{t}$+light. The highest ranked uncertainty is the $t\bar{t}+1c$ parton shower uncertainty, estimated based on the POWHEG-BOX+HERWIG7 sample; it is followed by the $t\bar{t}$+light h_{damp} uncertainty.

9

Conclusions and Future Work

In the years that followed the end of Run 2, the priority for the LHC experiments was to fully exploit the dataset accumulated thus far, while simultaneously preparing the beginning of Run 3. The work developed for this thesis has contributed to both of these goals.

With this unprecedentedly large dataset, the experiments could move away from simple signal strength measurements and target more fine-grained measurements of individual Higgs boson production modes in various kinematic regimes; and develop analyses sensitive to the quantum structure of the Higgs boson couplings.

As part of this effort, the inclusive $t\bar{t}H(H \to b\bar{b})$ signal strength was measured to be $\mu = 0.35 \pm 0.20$(stat.)$^{+0.30}_{-0.28}$(syst.), compatible with the SM expectation within $\sim 2\sigma$. The downward fluctuation with respect to the expected value of one is driven by the high Higgs p_{T} STXS bins ($[300, 450)$ GeV and $[450, \infty)$ GeV) and by the $[120, 200)$ GeV bin, where the measured signal strengths are close to zero. Using the same dataset and relying on newly-introduced CP-sensitive angular variables, the CP-mixing angle was measured to be $\alpha = 11^{\circ}{}^{+56^{\circ}}_{-77^{\circ}}$ and the overall coupling modifier $k_t' = 0.84^{+0.30}_{-0.46}$, consistent with the SM expectation ($\alpha = 0^{\circ}$, $k_t' = 1$), within 1σ. This analysis constitutes the first measurement of the charge-parity properties of the top Yukawa coupling in the $H \to b\bar{b}$ decay channel.

These measurements are largely dominated by the systematic uncertainties associated with the modelling of the dominant background: $t\bar{t}$ production with additional heavy flavor jets. In the corner of the phase space that they target, defined by a large number of jets and b-jets, the irreducible background $t\bar{t}b\bar{b}$ is the most challenging one. Its normalisation is measured from data but the shape of the distributions are modelled using MC simulation.

Currently, the development of the legacy $t\bar{t}H(H \to b\bar{b})$ cross-section is underway. The analysis has evolved to require a looser pre-selection and to use a multiclass neural network to define control regions enriched in each of the $t\bar{t}$+jets components. In this scenario, the relative amount of $t\bar{t}$+light and $t\bar{t}+\geq 1c$ backgrounds increases, creating the need for a more precise understanding of these processes. This is particularly relevant for $t\bar{t}+\geq 1c$, since it has been less explored theoretically and experimentally and it is harder to disentangle from $t\bar{t}+\geq 1b$ due to the higher c-jet mistag rates. In view of this, an analysis targeting the measurement of the $t\bar{t}+1c$ and $t\bar{t}+\geq 2c$ signal strengths in the dileptonic channel was developed by the author. The combination with the single-lepton channel is underway. In the dileptonic channel, that provides the highest sensitivity, the $t\bar{t}+1c$ and $t\bar{t}+\geq 2c$ signal strengths were measured within the detector acceptance to be $\mu(t\bar{t}+1c) = 1.54 \pm 0.19$ and $\mu(t\bar{t}+\geq 2c) = 1.24 \pm 0.28$. The $t\bar{t}+1c$ signal strength deviates from the prediction by more than 2σ. The dominant systematic uncertainties are associated with the light- and c-jet mistag-rate calibration of the dedicated flavor-tagging algorithm. The uncertainties associated with the modelling of the $t\bar{t}$ plus heavy flavor processes also have a large impact on these measurements.

The preparation and development of the ATLAS trigger system for Run 3 and beyond are also crucial aspects of this work. In order to fully exploit the potential of the ATLAS Forward Proton detectors (AFP) it is essential to include them in data-taking with standard pileup conditions. In this environment and with a dedicated trigger strategy, the measurement of the central exclusive production of a jet pair is within reach. The HLT algorithm responsible for matching the jets measured in the central detector with the proton tracks reconstructed in both AFP stations was developed as part of this work and implemented within the common ATLAS experiment software. This work constitutes a proof-of-principle and serves as a first step towards the development of triggers dedicated to central exclusive production processes in high-pileup environments. The expected rate of triggers seeded by jets at L1, requiring at least two high-p_{T} jets and the matching between jets and AFP tracks was estimated using data collected during 2023.

As preparation for the High-Luminosity phase of the LHC, a proposed Level-1 hardware tracking trigger system was studied. The performance of the system for muon signatures was quantified using a software emulation. By requiring at least two muons with $p_T > 10$ GeV and matched to a track within $\Delta R = 0.3$ a background rejection of 13 (14) can be achieved for a signal efficiency of 96% (94%) for the upgrade scenario in which the outer layers of the pixel detector are included (excluded) in the readout. Additional, yet modest, rejection can be achieved by requiring that the muons are consistent with the same production vertex. These studies highlight the performance of a possible future hardware tracking trigger.

The legacy $t\bar{t}H(H \to b\bar{b})$ analysis employs a more sophisticated multivariate approach to reconstruct the Higgs boson transverse momentum. Another exciting development is the inclusion of a boosted region in the dilepton channel, which further enhances the sensitivity in the high-p_{T} regime. The author performed early studies for this analysis focusing mainly on the possibility of including the c-tagging discriminant in the training of the multivariate method to increase the separation between $t\bar{t}+\geq 1c$ and $t\bar{t}+\geq 1b$. The author continues to be involved in the development of the analysis and is one of the paper editors. The publication is planned for later this year.

The $t\bar{t}+\geq 1c$ cross-section measurement is also well advanced and planning for a publication in Autumn. The author's involvement in this analysis will remain crucial in the following months to guarantee that the results are ready for publication and to address the comments from the Collaboration throughout the internal review process. For the future, differential and unfolded cross-section measurements of the $t\bar{t}+1c$ and $t\bar{t}+\geq 2c$ processes will become increasingly more relevant and are planned by the ATLAS Collaboration. From the theory side, dedicated matrix element calculations of $t\bar{t}c\bar{c}$ are expected to be a very interesting development in the coming years.

Bibliography

[1] R. L. Workman *et al.*, "Review of Particle Physics," *PTEP*, vol. 2022, p. 083C01, 2022.

[2] A. M. Sirunyan *et al.*, "Measurement of the Higgs boson production rate in association with top quarks in final states with electrons, muons, and hadronically decaying tau leptons at $\sqrt{s} = 13$ TeV," *Eur. Phys. J. C*, vol. 81, no. 4, p. 378, 2021.

[3] J. Rojo, "PDF4LHC recommendations for Run II," *PoS*, vol. DIS2016, p. 018, 2016.

[4] M. Tanabashi *et al.*, "Review of Particle Physics," *Phys. Rev. D*, vol. 98, no. 3, p. 030001, 2018.

[5] F. Siegert, "Monte-Carlo event generation for the LHC," 2010. [Online]. Available: https://cds.cern.ch/record/1600005

[6] "A detailed map of Higgs boson interactions by the ATLAS experiment ten years after the discovery," *Nature*, vol. 607, no. 7917, pp. 52–59, 2022, [Erratum: Nature 612, E24 (2022)].

[7] F. Demartin, F. Maltoni, K. Mawatari, and M. Zaro, "Higgs production in association with a single top quark at the LHC," *Eur. Phys. J. C*, vol. 75, no. 6, p. 267, 2015.

[8] E. Mobs, "The CERN accelerator complex in 2019. Complexe des accélérateurs du CERN en 2019," 2019, general Photo. [Online]. Available: https://cds.cern.ch/record/2684277

[9] G. Aad *et al.*, "The ATLAS Experiment at the CERN Large Hadron Collider," *JINST*, vol. 3, p. S08003, 2008, also published by CERN Geneva in 2010. [Online]. Available: https://cds.cern.ch/record/1129811

[10] A. Ruiz-Martinez and A. Collaboration, "The Run-2 ATLAS Trigger System," CERN, Geneva, Tech. Rep., 2016. [Online]. Available: https://cds.cern.ch/record/2133909

[11] G. Aad *et al.*, "Jet energy scale and resolution measured in proton–proton collisions at $\sqrt{s} = 13$ TeV with the ATLAS detector," *Eur. Phys. J. C*, vol. 81, no. 8, p. 689, 2021.

[12] ——, "ATLAS b-jet identification performance and efficiency measurement with $t\bar{t}$ events in pp collisions at $\sqrt{s} = 13$ TeV," *Eur. Phys. J. C*, vol. 79, no. 11, p. 970, 2019.

[13] "Public jet trigger plots for collision data," https://twiki.cern.ch/twiki/bin/view/AtlasPublic/JetTriggerPublicResults, accessed: 2023-08-09.

[14] "Performance studies of tracking-based triggering using a fast emulation," CERN, Geneva, Tech. Rep., 2023, all figures including auxiliary figures are available at https://atlas.web.cern.ch/Atlas/GROUPS/PHYSICS/PUBNOTES/ATL-DAQ-PUB-2023-001. [Online]. Available: http://cds.cern.ch/record/2848431

[15] C. J. Ainsworth, L. Carvalho, L. Ehrke, T. Golling, M. Guth, M. B. Habbaba, J. Jovicevic, A. Khanov, R. J. Morais Silva Goncalo, A. Quadt, J. Raine, F. Rizatdinova, E. Shabalina, and K. Zoch, "Inclusive cross-section measurements of top-quark pair production in association with charm quarks with the ATLAS experiment," CERN, Geneva, Tech. Rep., 2021. [Online]. Available: https://cds.cern.ch/record/2789804

[16] C. Patrignani *et al.*, "Review of Particle Physics," *Chin. Phys.*, vol. C40, no. 10, p. 100001, 2016.

[17] G. Aad *et al.*, "Combined Measurement of the Higgs Boson Mass in pp Collisions at $\sqrt{s} = 7$ and 8 TeV with the ATLAS and CMS Experiments," *Phys. Rev. Lett.*, vol. 114, p. 191803, 2015.

[18] C.-N. Yang and R. L. Mills, "Conservation of Isotopic Spin and Isotopic Gauge Invariance," *Phys. Rev.*, vol. 96, pp. 191–195, 1954.

[19] J. Goldstone, "Field Theories with Superconductor Solutions," *Nuovo Cim.*, vol. 19, pp. 154–164, 1961.

[20] Y. Nambu and G. Jona-Lasinio, "Dynamical Model of Elementary Particles Based on an Analogy with Superconductivity. 1." *Phys. Rev.*, vol. 122, pp. 345–358, 1961, [,127(1961)].

[21] V. C. Rubin and W. K. Ford, Jr., "Rotation of the Andromeda Nebula from a Spectroscopic Survey of Emission Regions," *Astrophys. J.*, vol. 159, pp. 379–403, 1970.

[22] E. Corbelli and P. Salucci, "The Extended Rotation Curve and the Dark Matter Halo of M33," *Mon. Not. Roy. Astron. Soc.*, vol. 311, pp. 441–447, 2000.

[23] D. Clowe, M. Bradac, A. H. Gonzalez, M. Markevitch, S. W. Randall, C. Jones, and D. Zaritsky, "A direct empirical proof of the existence of dark matter," *Astrophys. J. Lett.*, vol. 648, pp. L109–L113, 2006.

[24] Y. Fukuda *et al.*, "Evidence for oscillation of atmospheric neutrinos," *Phys. Rev. Lett.*, vol. 81, pp. 1562–1567, 1998.

[25] Q. R. Ahmad *et al.*, "Measurement of the rate of $\nu_e + d \to p + p + e^-$ interactions produced by ^8B solar neutrinos at the Sudbury Neutrino Observatory," *Phys. Rev. Lett.*, vol. 87, p. 071301, 2001.

[26] ——, "Direct evidence for neutrino flavor transformation from neutral current interactions in the Sudbury Neutrino Observatory," *Phys. Rev. Lett.*, vol. 89, p. 011301, 2002.

[27] H.-Y. Chiu, "Symmetry between particle and anti-particle populations in the universe," *Phys. Rev. Lett.*, vol. 17, p. 712, 1966.

[28] J. L. Sievers *et al.*, “Cosmological parameters from Cosmic Background Imager observations and comparisons with BOOMERANG, DASI, and MAXIMA,” *Astrophys. J.*, vol. 591, pp. 599–622, 2003.

[29] J. C. Romão, “O modelo standard das interações eletrofracas,” http://porthos.ist.utl.pt/ftp/textos/fie.pdf, 2013, accessed 2018/01/11. Notes by Professor Jorge Romão.

[30] M. E. Peskin and D. V. Schroeder, *An Introduction to quantum field theory*. Reading, USA: Addison-Wesley, 1995.

[31] M. Thomson, *Modern particle physics*. New York: Cambridge University Press, 2013.

[32] E. Noether, “Invariante variationsprobleme,” *Nachrichten von der Gesellschaft der Wissenschaften zu Göttingen, Mathematisch-Physikalische Klasse*, vol. 1918, pp. 235–257, 1918. [Online]. Available: http://eudml.org/doc/59024

[33] P. A. M. Dirac, “The quantum theory of the electron,” *Proc. Roy. Soc. Lond. A*, vol. 117, pp. 610–624, 1928.

[34] N. Cabibbo, “Unitary Symmetry and Leptonic Decays,” *Phys. Rev. Lett.*, vol. 10, pp. 531–533, 1963.

[35] M. Kobayashi and T. Maskawa, “CP Violation in the Renormalizable Theory of Weak Interaction,” *Prog. Theor. Phys.*, vol. 49, pp. 652–657, 1973.

[36] J. H. Christenson, J. W. Cronin, V. L. Fitch, and R. Turlay, “Evidence for the 2π Decay of the K_2^0 Meson,” *Phys. Rev. Lett.*, vol. 13, pp. 138–140, 1964.

[37] V. Fanti *et al.*, “A New measurement of direct CP violation in two pion decays of the neutral kaon,” *Phys. Lett. B*, vol. 465, pp. 335–348, 1999.

[38] A. Alavi-Harati *et al.*, “Observation of direct CP violation in $K_{S,L} \to \pi\pi$ decays,” *Phys. Rev. Lett.*, vol. 83, pp. 22–27, 1999.

[39] B. Aubert *et al.*, “Observation of direct CP violation in $B^0 \to K^+\pi^-$ decays,” *Phys. Rev. Lett.*, vol. 93, p. 131801, 2004.

[40] Y. Chao *et al.*, “Evidence for direct CP violation in B0 —> K+ pi- decays,” *Phys. Rev. Lett.*, vol. 93, p. 191802, 2004.

[41] P. del Amo Sanchez *et al.*, “Measurement of CP observables in $B^{+-} - > D_{CP}K^{+-}$ decays and constraints on the CKM angle γ,” *Phys. Rev. D*, vol. 82, p. 072004, 2010.

[42] A. Poluektov *et al.*, “Evidence for direct CP violation in the decay B->D(*)K, D->KsPi+Pi- and measurement of the CKM phase phi3,” *Phys. Rev. D*, vol. 81, p. 112002, 2010.

[43] R. Aaij *et al.*, “Observation of CP violation in $B^\pm \to DK^\pm$ decays,” *Phys. Lett. B*, vol. 712, pp. 203–212, 2012, [Erratum: Phys.Lett.B 713, 351 (2012)].

[44] Aaij, Roel and others, "Observation of CP Violation in Charm Decays," *Phys. Rev. Lett.*, vol. 122, no. 21, p. 211803, 2019.

[45] N. Aghanim *et al.*, "Planck 2018 results. VI. Cosmological parameters," *Astron. Astrophys.*, vol. 641, p. A6, 2020, [Erratum: Astron.Astrophys. 652, C4 (2021)].

[46] V. Branchina, F. Contino, and P. M. Ferreira, "Electroweak vacuum lifetime in two Higgs doublet models," 2018.

[47] "A profile likelihood approach to measure the top quark mass in the lepton+jets channel at $\sqrt{s} = 13\ \mathrm{TeV}$," CERN, Geneva, Tech. Rep., 2022. [Online]. Available: https://cds.cern.ch/record/2806509

[48] I. I. Bigi, Y. L. Dokshitzer, V. Khoze, J. Kühn, and P. M. Zerwas, "Production and decay properties of ultra-heavy quarks," *Phys. Lett. B*, vol. 181, pp. 157–163, 1986. [Online]. Available: http://cds.cern.ch/record/171099

[49] D. de Florian *et al.*, "Handbook of LHC Higgs Cross Sections: 4. Deciphering the Nature of the Higgs Sector," 2016.

[50] F. Demartin, F. Maltoni, K. Mawatari, B. Page, and M. Zaro, "Higgs characterisation at NLO in QCD: CP properties of the top-quark Yukawa interaction," *Eur. Phys. J. C*, vol. 74, no. 9, p. 3065, 2014.

[51] G. P. Salam, "Elements of QCD for hadron colliders," in *High-energy physics. Proceedings, 17th European School, ESHEP 2009, Bautzen, Germany, June 14-27, 2009*, 2010. [Online]. Available: http://inspirehep.net/record/880643/files/arXiv:1011.5131.pdf

[52] M. Cacciari, G. P. Salam, and G. Soyez, "The Anti-k(t) jet clustering algorithm," *JHEP*, vol. 04, p. 063, 2008.

[53] S. D. Ellis and D. E. Soper, "Successive combination jet algorithm for hadron collisions," *Phys. Rev.*, vol. D48, pp. 3160–3166, 1993.

[54] M. Wobisch and T. Wengler, "Hadronization corrections to jet cross-sections in deep inelastic scattering," in *Monte Carlo generators for HERA physics. Proceedings, Workshop, Hamburg, Germany, 1998-1999*, 1998, pp. 270–279. [Online]. Available: https://inspirehep.net/record/484872/files/arXiv:hep-ph_9907280.pdf

[55] M. L. Mangano, M. Moretti, F. Piccinini, R. Pittau, and A. D. Polosa, "ALPGEN, a generator for hard multiparton processes in hadronic collisions," *JHEP*, vol. 07, p. 001, 2003.

[56] J. Alwall, R. Frederix, S. Frixione, V. Hirschi, F. Maltoni, O. Mattelaer, H. S. Shao, T. Stelzer, P. Torrielli, and M. Zaro, "The automated computation of tree-level and next-to-leading order differential cross sections, and their matching to parton shower simulations," *JHEP*, vol. 07, p. 079, 2014.

[57] C. Oleari, “The POWHEG-BOX,” *Nucl. Phys. Proc. Suppl.*, vol. 205-206, pp. 36–41, 2010.

[58] T. Gleisberg, S. Hoeche, F. Krauss, M. Schonherr, S. Schumann, F. Siegert, and J. Winter, “Event generation with SHERPA 1.1,” *JHEP*, vol. 02, p. 007, 2009.

[59] T. Sjostrand, S. Mrenna, and P. Z. Skands, “A Brief Introduction to PYTHIA 8.1,” *Comput. Phys. Commun.*, vol. 178, pp. 852–867, 2008.

[60] M. Bahr *et al.*, “Herwig++ Physics and Manual,” *Eur. Phys. J. C*, vol. 58, pp. 639–707, 2008.

[61] J. Bellm, S. Gieseke, D. Grellscheid, S. Plätzer, M. Rauch, C. Reuschle, P. Richardson, P. Schichtel, M. H. Seymour, A. Siódmok, A. Wilcock, N. Fischer, M. A. Harrendorf, G. Nail, A. Papaefstathiou, and D. Rauch, “Herwig 7.0 / Herwig++ 3.0 Release Note,” *Eur. Phys. J. C*, vol. 76, p. 196, 2016, 8 pages. Herwig is available from https://herwig.hepforge.org. [Online]. Available: http://cds.cern.ch/record/2110873

[62] S. Catani, F. Krauss, R. Kuhn, and B. R. Webber, “QCD matrix elements + parton showers,” *JHEP*, vol. 11, p. 063, 2001.

[63] J. Alwall *et al.*, “Comparative study of various algorithms for the merging of parton showers and matrix elements in hadronic collisions,” *Eur. Phys. J. C*, vol. 53, pp. 473–500, 2008.

[64] B. R. Webber, “Hadronization,” in *Summer School on Hadronic Aspects of Collider Physics*, 11 1994, pp. 49–77.

[65] Webber, B. R., “Fragmentation and hadronization,” *Int. J. Mod. Phys. A*, vol. 15S1, pp. 577–606, 2000.

[66] ——, “A QCD Model for Jet Fragmentation Including Soft Gluon Interference,” *Nucl. Phys. B*, vol. 238, pp. 492–528, 1984.

[67] G. Marchesini and B. R. Webber, “Monte Carlo Simulation of General Hard Processes with Coherent QCD Radiation,” *Nucl. Phys. B*, vol. 310, pp. 461–526, 1988.

[68] X. Artru and G. Mennessier, “String model and multiproduction,” *Nucl. Phys. B*, vol. 70, pp. 93–115, 1974.

[69] M. G. Bowler, “e+ e- Production of Heavy Quarks in the String Model,” *Z. Phys. C*, vol. 11, p. 169, 1981.

[70] B. Andersson, G. Gustafson, and B. Soderberg, “A General Model for Jet Fragmentation,” *Z. Phys. C*, vol. 20, p. 317, 1983.

[71] B. Andersson, G. Gustafson, G. Ingelman, and T. Sjostrand, “Parton Fragmentation and String Dynamics,” *Phys. Rept.*, vol. 97, pp. 31–145, 1983.

[72] S. Agostinelli *et al.*, “GEANT4: A Simulation toolkit,” *Nucl. Instrum. Meth.*, vol. A506, pp. 250–303, 2003.

[73] G. Aad *et al.*, "The ATLAS Simulation Infrastructure," *Eur. Phys. J. C*, vol. 70, pp. 823–874, 2010.

[74] M. Beckingham, M. Duehrssen, E. Schmidt, M. Shapiro, M. Venturi, J. Virzi, I. Vivarelli, M. Werner, S. Yamamoto, and T. Yamanaka, "The simulation principle and performance of the ATLAS fast calorimeter simulation FastCaloSim," 10 2010.

[75] G. Aad *et al.*, "Observation of a new particle in the search for the Standard Model Higgs boson with the ATLAS detector at the LHC," *Phys. Lett. B*, vol. 716, pp. 1–29, 2012.

[76] S. Chatrchyan *et al.*, "Observation of a New Boson at a Mass of 125 GeV with the CMS Experiment at the LHC," *Phys. Lett. B*, vol. 716, pp. 30–61, 2012.

[77] N. Berger *et al.*, "Simplified Template Cross Sections - Stage 1.1," 6 2019.

[78] M. Aaboud *et al.*, "Observation of Higgs boson production in association with a top quark pair at the LHC with the ATLAS detector," *Phys. Lett. B*, vol. 784, pp. 173–191, 2018.

[79] A. M. Sirunyan *et al.*, "Observation of $\mathrm{t\bar{t}}$H production," *Phys. Rev. Lett.*, vol. 120, no. 23, p. 231801, 2018.

[80] G. Aad *et al.*, "CP Properties of Higgs Boson Interactions with Top Quarks in the $t\bar{t}H$ and tH Processes Using $H \to \gamma\gamma$ with the ATLAS Detector," *Phys. Rev. Lett.*, vol. 125, no. 6, p. 061802, 2020.

[81] A. M. Sirunyan *et al.*, "Measurements of $\mathrm{t\bar{t}}H$ Production and the CP Structure of the Yukawa Interaction between the Higgs Boson and Top Quark in the Diphoton Decay Channel," *Phys. Rev. Lett.*, vol. 125, no. 6, p. 061801, 2020.

[82] G. Aad *et al.*, "Search for a CP-odd Higgs boson decaying to Zh in pp collisions at $\sqrt{s} = 8$ TeV with the ATLAS detector," *Phys. Lett. B*, vol. 744, pp. 163–183, 2015.

[83] Aad, Georges and others, "Test of CP invariance in vector-boson fusion production of the Higgs boson in the $H \to \tau\tau$ channel in proton-proton collisions at $\sqrt{s} = 13$ TeV with the ATLAS detector," *Phys. Lett. B*, vol. 805, p. 135426, 2020.

[84] M. Aaboud *et al.*, "Measurements of Higgs boson properties in the diphoton decay channel with 36 fb^{-1} of pp collision data at $\sqrt{s} = 13$ TeV with the ATLAS detector," *Phys. Rev. D*, vol. 98, p. 052005, 2018.

[85] Aaboud, Morad and others, "Measurement of the Higgs boson coupling properties in the $H \to ZZ^* \to 4\ell$ decay channel at $\sqrt{s}$ = 13 TeV with the ATLAS detector," *JHEP*, vol. 03, p. 095, 2018.

[86] V. Khachatryan *et al.*, "Combined search for anomalous pseudoscalar HVV couplings in VH(H $\to b\bar{b}$) production and H $\to$ VV decay," *Phys. Lett. B*, vol. 759, pp. 672–696, 2016.

[87] A. M. Sirunyan *et al.*, "Constraints on anomalous Higgs boson couplings using production and decay information in the four-lepton final state," *Phys. Lett. B*, vol. 775, pp. 1–24, 2017.

[88] Sirunyan, Albert M and others, “Measurements of the Higgs boson width and anomalous HVV couplings from on-shell and off-shell production in the four-lepton final state,” *Phys. Rev. D*, vol. 99, no. 11, p. 112003, 2019.

[89] O. S. Brüning, P. Collier, P. Lebrun, S. Myers, R. Ostojic, J. Poole, and P. Proudlock, *LHC Design Report*, ser. CERN Yellow Reports: Monographs. Geneva: CERN, 2004. [Online]. Available: https://cds.cern.ch/record/782076

[90] K. Aamodt *et al.*, “The ALICE experiment at the CERN LHC,” *JINST*, vol. 3, p. S08002, 2008.

[91] G. Aad *et al.*, “The ATLAS Experiment at the CERN Large Hadron Collider,” *JINST*, vol. 3, p. S08003, 2008.

[92] S. Chatrchyan *et al.*, “The CMS Experiment at the CERN LHC,” *JINST*, vol. 3, p. S08004, 2008.

[93] A. A. Alves, Jr. *et al.*, “The LHCb Detector at the LHC,” *JINST*, vol. 3, p. S08005, 2008.

[94] O. Adriani *et al.*, “The LHCf detector at the CERN Large Hadron Collider,” *JINST*, vol. 3, p. S08006, 2008.

[95] G. Anelli *et al.*, “The TOTEM experiment at the CERN Large Hadron Collider,” *JINST*, vol. 3, p. S08007, 2008.

[96] J. Pinfold, “The MoEDAL experiment at the LHC,” *EPJ Web Conf.*, vol. 145, p. 12002, 2017.

[97] S. Baird, “Accelerators for pedestrians; rev. version,” CERN, Geneva, Tech. Rep., 2007. [Online]. Available: http://cds.cern.ch/record/1017689

[98] L. Evans and P. Bryant, “Lhc machine,” *Journal of Instrumentation*, vol. 3, no. 08, p. S08001, aug 2008. [Online]. Available: https://dx.doi.org/10.1088/1748-0221/3/08/S08001

[99] M. Aaboud *et al.*, “Measurement of the Inelastic Proton-Proton Cross Section at $\sqrt{s} = 13$ TeV with the ATLAS Detector at the LHC,” *Phys. Rev. Lett.*, vol. 117, no. 18, p. 182002, 2016.

[100] R. Alemany-Fernandez, E. Bravin, L. Drosdal, A. Gorzawski, V. Kain, M. Lamont, A. Macpherson, G. Papotti, M. Pojer, L. Ponce, S. Redaelli, G. Roy, M. Solfaroli Camillocci, W. Venturini, and J. Wenninger, “Operation and Configuration of the LHC in Run 1,” Nov 2013. [Online]. Available: https://cds.cern.ch/record/1631030

[101] H. Damerau, A. Funken, R. Garoby, S. Gilardoni, B. Goddard, K. Hanke, A. Lombardi, D. Manglunki, M. Meddahi, B. Mikulec, G. Rumolo, E. Shaposhnikova, M. Vretenar, and J. Coupard, *LHC Injectors Upgrade, Technical Design Report*, Dec 2014. [Online]. Available: https://cds.cern.ch/record/1976692

[102] O. Aberle *et al.*, *High-Luminosity Large Hadron Collider (HL-LHC): Technical design report*, ser. CERN Yellow Reports: Monographs. Geneva: CERN, 2020. [Online]. Available: https://cds.cern.ch/record/2749422

[103] T. A. Collaboration, “The atlas experiment at the cern large hadron collider,” *Journal of Instrumentation*, vol. 3, no. 08, p. S08003, aug 2008. [Online]. Available: https://dx.doi.org/10.1088/1748-0221/3/08/S08003

[104] *ATLAS magnet system: Technical Design Report, 1*, ser. Technical design report. ATLAS. Geneva: CERN, 1997. [Online]. Available: https://cds.cern.ch/record/338080

[105] G. Aad *et al.*, “Studies of the performance of the ATLAS detector using cosmic-ray muons,” *Eur. Phys. J. C*, vol. 71, p. 1593, 2011.

[106] “Technical Design Report for the ATLAS Inner Tracker Pixel Detector,” CERN, Geneva, Tech. Rep., 2017. [Online]. Available: https://cds.cern.ch/record/2285585

[107] G. Aad *et al.*, “Atlas pixel detector electronics and sensors,” *Journal of Instrumentation*, vol. 3, no. 07, p. P07007, jul 2008. [Online]. Available: https://dx.doi.org/10.1088/1748-0221/3/07/P07007

[108] A. Abdesselam and T. Akimoto, “The Barrel Modules of the ATLAS SemiConductor Tracker,” CERN, Geneva, Tech. Rep., 2006. [Online]. Available: https://cds.cern.ch/record/974073

[109] G. Aad *et al.*, “Operation and performance of the ATLAS semiconductor tracker in LHC Run 2,” *JINST*, vol. 17, no. 01, p. P01013, 2022.

[110] T. A. T. collaboration *et al.*, “The atlas transition radiation tracker (trt) proportional drift tube: design and performance,” *Journal of Instrumentation*, vol. 3, no. 02, p. P02013, feb 2008. [Online]. Available: https://dx.doi.org/10.1088/1748-0221/3/02/P02013

[111] M. Aaboud *et al.*, “Performance of the atlas transition radiation tracker in run 1 of the lhc: tracker properties,” *Journal of Instrumentation*, vol. 12, no. 05, p. P05002, may 2017. [Online]. Available: https://dx.doi.org/10.1088/1748-0221/12/05/P05002

[112] “ATLAS liquid argon calorimeter: Technical design report,” 1996.

[113] *ATLAS tile calorimeter: Technical Design Report*, ser. Technical design report. ATLAS. Geneva: CERN, 1996. [Online]. Available: https://cds.cern.ch/record/331062

[114] *ATLAS muon spectrometer: Technical Design Report*, ser. Technical design report. ATLAS. Geneva: CERN, 1997. [Online]. Available: https://cds.cern.ch/record/331068

[115] G. Avoni *et al.*, “The new LUCID-2 detector for luminosity measurement and monitoring in ATLAS,” *JINST*, vol. 13, no. 07, p. P07017, 2018.

[116] S. A. Khalek *et al.*, “The alfa roman pot detectors of atlas,” *Journal of Instrumentation*, vol. 11, no. 11, p. P11013, nov 2016. [Online]. Available: https://dx.doi.org/10.1088/1748-0221/11/11/P11013

[117] P. Jenni, M. Nessi, and M. Nordberg, “Zero Degree Calorimeters for ATLAS,” CERN, Geneva, Tech. Rep., Jan 2007. [Online]. Available: https://cds.cern.ch/record/1009649

[118] L. Adamczyk, E. Banaś, A. Brandt, M. Bruschi, S. Grinstein, J. Lange, M. Rijssenbeek, P. Sicho, R. Staszewski, T. Sykora, M. Trzebiński, J. Chwastowski, and K. Korcyl, "Technical Design Report for the ATLAS Forward Proton Detector," Tech. Rep., 2015. [Online]. Available: https://cds.cern.ch/record/2017378

[119] *ATLAS level-1 trigger: Technical Design Report*, ser. Technical design report. ATLAS. Geneva: CERN, 1998. [Online]. Available: https://cds.cern.ch/record/381429

[120] P. Jenni, M. Nessi, M. Nordberg, and K. Smith, *ATLAS high-level trigger, data-acquisition and controls: Technical Design Report*, ser. Technical design report. ATLAS. Geneva: CERN, 2003. [Online]. Available: https://cds.cern.ch/record/616089

[121] R. Achenbach *et al.*, "The ATLAS level-1 calorimeter trigger," *JINST*, vol. 3, p. P03001, 2008.

[122] G. Aad *et al.*, "Technical Design Report for the Phase-I Upgrade of the ATLAS TDAQ System," 9 2013.

[123] "Technical Design Report for the Phase-II Upgrade of the ATLAS TDAQ System," CERN, Geneva, Tech. Rep., 2017. [Online]. Available: https://cds.cern.ch/record/2285584

[124] C. ATLAS, "Technical Design Report for the Phase-II Upgrade of the ATLAS Trigger and Data Acquisition System - Event Filter Tracking Amendment," CERN, Geneva, Tech. Rep., 2022. [Online]. Available: https://cds.cern.ch/record/2802799

[125] M. Aaboud *et al.*, "Performance of the ATLAS track reconstruction algorithms in dense environments in LHC run 2," *The European Physical Journal C*, vol. 77, no. 10, oct 2017. [Online]. Available: https://doi.org/10.1140%2Fepjc%2Fs10052-017-5225-7

[126] N. Berger, M. Kiehn, A. Kozlinskiy, and A. Schöning, "A New Three-Dimensional Track Fit with Multiple Scattering," *Nucl. Instrum. Meth. A*, vol. 844, p. 135, 2017.

[127] G. Borissov, D. W. Casper, K. Grimm, S. Pagan Griso, L. E. Pedersen, K. Prokofiev, M. S. Rudolph, and A. M. Wharton, "ATLAS strategy for primary vertex reconstruction during Run-2 of the LHC," CERN, Geneva, Tech. Rep. 7, 2015. [Online]. Available: https://cds.cern.ch/record/2015220

[128] G. Aad *et al.*, "Topological cell clustering in the ATLAS calorimeters and its performance in LHC Run 1," *Eur. Phys. J. C*, vol. 77, p. 490, 2017.

[129] M. Aaboud *et al.*, "Electron reconstruction and identification in the ATLAS experiment using the 2015 and 2016 LHC proton-proton collision data at $\sqrt{s}$ = 13 TeV," *Eur. Phys. J. C*, vol. 79, no. 8, p. 639, 2019.

[130] G. Aad *et al.*, "Electron and photon performance measurements with the ATLAS detector using the 2015–2017 LHC proton-proton collision data," *JINST*, vol. 14, no. 12, p. P12006, 2019.

[131] Aad, Georges and others, “Muon reconstruction and identification efficiency in ATLAS using the full Run 2 pp collision data set at $\sqrt{s} = 13$ TeV,” *Eur. Phys. J. C*, vol. 81, no. 7, p. 578, 2021.

[132] G. Aad *et al.*, “Performance of the ATLAS muon triggers in Run 2,” *JINST*, vol. 15, no. 09, p. P09015, 2020.

[133] “Measurement of the tau lepton reconstruction and identification performance in the ATLAS experiment using pp collisions at $\sqrt{s} = 13 \text{ TeV}$,” CERN, Geneva, Tech. Rep., 2017, all figures including auxiliary figures are available at https://atlas.web.cern.ch/Atlas/GROUPS/PHYSICS/CONFNOTES/ATLAS-CONF-2017-029. [Online]. Available: https://cds.cern.ch/record/2261772

[134] G. Aad *et al.*, “Performance of jet substructure techniques for large-R jets in proton-proton collisions at $\sqrt{s}$ = 7 TeV using the ATLAS detector,” *JHEP*, vol. 09, p. 076, 2013.

[135] M. Cacciari, G. P. Salam, and G. Soyez, “The Catchment Area of Jets,” *JHEP*, vol. 04, p. 005, 2008.

[136] M. Cacciari and G. P. Salam, “Pileup subtraction using jet areas,” *Phys. Lett. B*, vol. 659, pp. 119–126, 2008.

[137] “The ATLAS Tau Trigger in Run 2,” CERN, Geneva, Tech. Rep., 2017, all figures including auxiliary figures are available at https://atlas.web.cern.ch/Atlas/GROUPS/PHYSICS/CONFNOTES/ATLAS-CONF-2017-061. [Online]. Available: https://cds.cern.ch/record/2274201

[138] M. Cacciari, G. P. Salam, and G. Soyez, “FastJet User Manual,” *Eur. Phys. J.*, vol. C72, p. 1896, 2012.

[139] Aad, Georges and others, “Jet energy scale measurements and their systematic uncertainties in proton-proton collisions at $\sqrt{s} = 13$ TeV with the ATLAS detector,” *Physical Review D*, vol. 96, no. 7, oct 2017. [Online]. Available: https://doi.org/10.1103%2Fphysrevd.96.072002

[140] “Selection of jets produced in 13TeV proton-proton collisions with the ATLAS detector,” CERN, Geneva, Tech. Rep., 2015, all figures including auxiliary figures are available at https://atlas.web.cern.ch/Atlas/GROUPS/PHYSICS/CONFNOTES/ATLAS-CONF-2015-029. [Online]. Available: https://cds.cern.ch/record/2037702

[141] M. Aaboud *et al.*, “Jet reconstruction and performance using particle flow with the ATLAS Detector,” *Eur. Phys. J. C*, vol. 77, no. 7, p. 466, 2017.

[142] “Performance of missing transverse momentum reconstruction for the ATLAS detector in the first proton-proton collisions at at $\sqrt{s}$= 13 TeV,” CERN, Geneva, Tech. Rep., 2015, all figures including auxiliary figures are available at https://atlas.web.cern.ch/Atlas/GROUPS/PHYSICS/PUBNOTES/ATL-PHYS-PUB-2015-027. [Online]. Available: https://cds.cern.ch/record/2037904

[143] M. Aaboud *et al.*, "Performance of the ATLAS Trigger System in 2015," *Eur. Phys. J. C*, vol. 77, no. 5, p. 317, 2017.

[144] "Optimisation and performance studies of the ATLAS b-tagging algorithms for the 2017-18 LHC run," CERN, Geneva, Tech. Rep., 2017, all figures including auxiliary figures are available at https://atlas.web.cern.ch/Atlas/GROUPS/PHYSICS/PUBNOTES/ATL-PHYS-PUB-2017-013. [Online]. Available: https://cds.cern.ch/record/2273281

[145] "Identification of Jets Containing b-Hadrons with Recurrent Neural Networks at the ATLAS Experiment," CERN, Geneva, Tech. Rep., 2017, all figures including auxiliary figures are available at https://atlas.web.cern.ch/Atlas/GROUPS/PHYSICS/PUBNOTES/ATL-PHYS-PUB-2017-003. [Online]. Available: https://cds.cern.ch/record/2255226

[146] "Secondary vertex finding for jet flavour identification with the ATLAS detector," CERN, Geneva, Tech. Rep., 2017, all figures including auxiliary figures are available at https://atlas.web.cern.ch/Atlas/GROUPS/PHYSICS/PUBNOTES/ATL-PHYS-PUB-2017-011. [Online]. Available: https://cds.cern.ch/record/2270366

[147] "Topological b-hadron decay reconstruction and identification of b-jets with the JetFitter package in the ATLAS experiment at the LHC," CERN, Geneva, Tech. Rep., 2018, all figures including auxiliary figures are available at https://atlas.web.cern.ch/Atlas/GROUPS/PHYSICS/PUBNOTES/ATL-PHYS-PUB-2018-025. [Online]. Available: https://cds.cern.ch/record/2645405

[148] G. Aad *et al.*, "ATLAS b-jet identification performance and efficiency measurement with $t\bar{t}$ events in pp collisions at $\sqrt{s} = 13$ TeV," *Eur. Phys. J. C*, vol. 79, no. 11, p. 970, 2019.

[149] "Calibration of the b-tagging efficiency on charm jets using a sample of W+c events with $\sqrt{s}$ = 13 TeV ATLAS data," CERN, Geneva, Tech. Rep., 2018, all figures including auxiliary figures are available at https://atlas.web.cern.ch/Atlas/GROUPS/PHYSICS/CONFNOTES/ATLAS-CONF-2018-055. [Online]. Available: https://cds.cern.ch/record/2652195

[150] "Calibration of light-flavour b-jet mistagging rates using ATLAS proton-proton collision data at $\sqrt{s} = 13$ TeV," CERN, Geneva, Tech. Rep., 2018, all figures including auxiliary figures are available at https://atlas.web.cern.ch/Atlas/GROUPS/PHYSICS/CONFNOTES/ATLAS-CONF-2018-006. [Online]. Available: https://cds.cern.ch/record/2314418

[151] M. Trzebinski, "Study of QCD and Diffraction with the ATLAS detector at the LHC," 2013, presented 20 Sep 2013. [Online]. Available: https://cds.cern.ch/record/1616661

[152] M. Aaboud *et al.*, "Measurement of the inclusive jet cross-sections in proton-proton collisions at $\sqrt{s} = 8$ TeV with the ATLAS detector," *JHEP*, vol. 09, p. 020, 2017.

[153] "Trigger monitoring and rate predictions using Enhanced Bias data from the ATLAS Detector at the LHC," CERN, Geneva, Tech. Rep., 2016, all figures including auxiliary

figures are available at https://atlas.web.cern.ch/Atlas/GROUPS/PHYSICS/PUBNOTES/ATL-DAQ-PUB-2016-002. [Online]. Available: https://cds.cern.ch/record/2223498

[154] "Trigcosttutorial2021," https://twiki.cern.ch/twiki/bin/viewauth/Atlas/TriggerCostTutorial2021, accessed: 2023-06-13.

[155] G. Aad *et al.*, "Measurement of Higgs boson decay into b-quarks in associated production with a top-quark pair in pp collisions at $\sqrt{s} = 13$ TeV with the ATLAS detector," *JHEP*, vol. 06, p. 097, 2022.

[156] "Probing the CP nature of the top-Higgs Yukawa coupling in $t\bar{t}H$ and tH events with $H \to b\bar{b}$ using the ATLAS detector at the LHC," CERN, Geneva, Tech. Rep., 2022, all figures including auxiliary figures are available at https://atlas.web.cern.ch/Atlas/GROUPS/PHYSICS/CONFNOTES/ATLAS-CONF-2022-016. [Online]. Available: https://cds.cern.ch/record/2805772

[157] M. Aaboud *et al.*, "Search for the standard model Higgs boson produced in association with top quarks and decaying into a $b\bar{b}$ pair in pp collisions at $\sqrt{s}$ = 13 TeV with the ATLAS detector," *Phys. Rev. D*, vol. 97, no. 7, p. 072016, 2018.

[158] A. M. Sirunyan *et al.*, "Search for $\mathrm{t\bar{t}H}$ production in the $\mathrm{H} \to \mathrm{b\bar{b}}$ decay channel with leptonic $\mathrm{t\bar{t}}$ decays in proton-proton collisions at $\sqrt{s} = 13$ TeV," *JHEP*, vol. 03, p. 026, 2019.

[159] Sirunyan, Albert M and others, "Search for $\mathrm{t\bar{t}}$H production in the all-jet final state in proton-proton collisions at $\sqrt{s} =$ 13 TeV," *JHEP*, vol. 06, p. 101, 2018.

[160] "Measurement of $\mathrm{t\bar{t}H}$ production in the $\mathrm{H} \to \mathrm{b\bar{b}}$ decay channel in $41.5\,\mathrm{fb}^{-1}$ of proton-proton collision data at $\sqrt{s} = 13\,\mathrm{TeV}$," CERN, Geneva, Tech. Rep., 2019. [Online]. Available: https://cds.cern.ch/record/2675023

[161] G. Aad *et al.*, "The ATLAS Simulation Infrastructure," *Eur. Phys. J. C*, vol. 70, pp. 823–874, 2010.

[162] "The Pythia 8 A3 tune description of ATLAS minimum bias and inelastic measurements incorporating the Donnachie-Landshoff diffractive model," CERN, Geneva, Tech. Rep., 2016, all figures including auxiliary figures are available at https://atlas.web.cern.ch/Atlas/GROUPS/PHYSICS/PUBNOTES/ATL-PHYS-PUB-2016-017. [Online]. Available: https://cds.cern.ch/record/2206965

[163] E. Bothmann, G. S. Chahal, S. Höche, J. Krause, F. Krauss, S. Kuttimalai, S. Liebschner, D. Napoletano, M. Schönherr, H. Schulz, S. Schumann, and F. Siegert, "Event generation with sherpa 2.2," *SciPost Physics*, vol. 7, no. 3, sep 2019. [Online]. Available: https://doi.org/10.21468%2Fscipostphys.7.3.034

[164] D. J. Lange, "The ev§tgen particle decay simulation package," *Nuclear Instruments and Methods in Physics Research Section A: Accelerators, Spectrometers, Detectors*

and Associated Equipment, vol. 462, no. 1, pp. 152–155, 2001, bEAUTY2000, Proceedings of the 7th Int. Conf. on B-Physics at Hadron Machines. [Online]. Available: https://www.sciencedirect.com/science/article/pii/S0168900201000894

[165] "ATLAS Pythia 8 tunes to 7 TeV data," CERN, Geneva, Tech. Rep., 2014, all figures including auxiliary figures are available at https://atlas.web.cern.ch/Atlas/GROUPS/PHYSICS/PUBNOTES/ATL-PHYS-PUB-2014-021. [Online]. Available: https://cds.cern.ch/record/1966419

[166] L. A. Harland-Lang, A. D. Martin, P. Motylinski, and R. S. Thorne, "Parton distributions in the LHC era: MMHT 2014 PDFs," *The European Physical Journal C*, vol. 75, no. 5, may 2015. [Online]. Available: https://doi.org/10.1140%2Fepjc%2Fs10052-015-3397-6

[167] R. D. Ball, , V. Bertone, S. Carrazza, C. S. Deans, L. D. Debbio, S. Forte, A. Guffanti, N. P. Hartland, J. I. Latorre, J. Rojo, and M. Ubiali, "Parton distributions for the LHC run II," *Journal of High Energy Physics*, vol. 2015, no. 4, apr 2015. [Online]. Available: https://doi.org/10.1007%2Fjhep04%282015%29040

[168] "Studies of Monte Carlo predictions for the $t\bar{t}b\bar{b}$ process," CERN, Geneva, Tech. Rep., 2022, all figures including auxiliary figures are available at https://atlas.web.cern.ch/Atlas/GROUPS/PHYSICS/PUBNOTES/ATL-PHYS-PUB-2022-006. [Online]. Available: https://cds.cern.ch/record/2802806

[169] N. D. Christensen and C. Duhr, "FeynRules - Feynman rules made easy," *Comput. Phys. Commun.*, vol. 180, pp. 1614–1641, 2009.

[170] F. Buccioni, J.-N. Lang, J. M. Lindert, P. Maierhöfer, S. Pozzorini, H. Zhang, and M. F. Zoller, "OpenLoops 2," *Eur. Phys. J. C*, vol. 79, no. 10, p. 866, 2019.

[171] F. Cascioli, P. Maierhöfer, and S. Pozzorini, "Scattering Amplitudes with Open Loops," *Phys. Rev. Lett.*, vol. 108, p. 111601, 2012.

[172] M. Beneke, P. Falgari, S. Klein, and C. Schwinn, "Hadronic top-quark pair production with NNLL threshold resummation," *Nucl. Phys. B*, vol. 855, pp. 695–741, 2012.

[173] M. Cacciari, M. Czakon, M. Mangano, A. Mitov, and P. Nason, "Top-pair production at hadron colliders with next-to-next-to-leading logarithmic soft-gluon resummation," *Phys. Lett. B*, vol. 710, pp. 612–622, 2012.

[174] P. Bärnreuther, M. Czakon, and A. Mitov, "Percent Level Precision Physics at the Tevatron: First Genuine NNLO QCD Corrections to $q\bar{q} \to t\bar{t} + X$," *Phys. Rev. Lett.*, vol. 109, p. 132001, 2012.

[175] M. Czakon and A. Mitov, "NNLO corrections to top-pair production at hadron colliders: the all-fermionic scattering channels," *JHEP*, vol. 12, p. 054, 2012.

[176] ——, "NNLO corrections to top pair production at hadron colliders: the quark-gluon reaction," *JHEP*, vol. 01, p. 080, 2013.

[177] M. Czakon, P. Fiedler, and A. Mitov, "Total Top-Quark Pair-Production Cross Section at Hadron Colliders Through $O(\alpha_S^4)$," *Phys. Rev. Lett.*, vol. 110, p. 252004, 2013.

[178] M. Czakon and A. Mitov, "Top++: A Program for the Calculation of the Top-Pair Cross-Section at Hadron Colliders," *Comput. Phys. Commun.*, vol. 185, p. 2930, 2014.

[179] E. Re, "Single-top Wt-channel production matched with parton showers using the POWHEG method," *Eur. Phys. J. C*, vol. 71, p. 1547, 2011.

[180] S. Höche, F. Krauss, M. Schönherr, and F. Siegert, "QCD matrix elements + parton showers. The NLO case," *JHEP*, vol. 04, p. 027, 2013.

[181] Aad, G. and others, "Measurements of the production cross-section for a z boson in association with b-jets in proton-proton collisions at $\sqrt{s} = 13$ tev with the ATLAS detector," *Journal of High Energy Physics*, vol. 2020, no. 7, jul 2020. [Online]. Available: https://doi.org/10.1007%2Fjhep07%282020%29044

[182] R. Frederix, E. Re, and P. Torrielli, "Single-top t-channel hadroproduction in the four-flavour scheme with POWHEG and aMC@NLO," *Journal of High Energy Physics*, vol. 2012, no. 9, sep 2012. [Online]. Available: https://doi.org/10.1007%2Fjhep09%282012%29130

[183] Aad, G. and others, "Measurements of top-quark pair differential cross-sections in the $e\mu e\mu$ channel in pp collisions at $\sqrt{s} = 13$ tev using the ATLAS detector," *The European Physical Journal C*, vol. 77, no. 5, may 2017. [Online]. Available: https://doi.org/10.1140%2Fepjc%2Fs10052-017-4821-x

[184] Abbott, B. and others, "Measurement of the top quark mass using dilepton events," *Phys. Rev. Lett.*, vol. 80, pp. 2063–2068, Mar 1998. [Online]. Available: https://link.aps.org/doi/10.1103/PhysRevLett.80.2063

[185] M. Aaboud *et al.*, "Search for the standard model higgs boson produced in association with top quarks and decaying into a $b\bar{b}$ pair in pp collisions at $\sqrt{s} = 13$ TeV with the atlas detector," *Phys. Rev. D*, vol. 97, p. 072016, Apr 2018. [Online]. Available: https://link.aps.org/doi/10.1103/PhysRevD.97.072016

[186] ——, "Search for the standard model Higgs boson produced in association with top quarks and decaying into a $b\bar{b}$ pair in pp collisions at $\sqrt{s}$ = 13 TeV with the ATLAS detector," *Phys. Rev. D*, vol. 97, no. 7, p. 072016, 2018.

[187] F. Chollet *et al.*, "Keras," https://keras.io, 2015.

[188] M. Abadi, A. Agarwal, P. Barham, E. Brevdo, Z. Chen, C. Citro, G. S. Corrado, A. Davis, J. Dean, M. Devin, S. Ghemawat, I. Goodfellow, A. Harp, G. Irving, M. Isard, Y. Jia, R. Jozefowicz, L. Kaiser, M. Kudlur, J. Levenberg, D. Mané, R. Monga, S. Moore, D. Murray, C. Olah, M. Schuster, J. Shlens, B. Steiner, I. Sutskever, K. Talwar, P. Tucker, V. Vanhoucke,

V. Vasudevan, F. Viégas, O. Vinyals, P. Warden, M. Wattenberg, M. Wicke, Y. Yu, and X. Zheng, "TensorFlow: Large-scale machine learning on heterogeneous systems," 2015, software available from tensorflow.org. [Online]. Available: https://www.tensorflow.org/

[189] "Electron efficiency measurements with the ATLAS detector using the 2015 LHC proton-proton collision data," CERN, Geneva, Tech. Rep., 2016, all figures including auxiliary figures are available at https://atlas.web.cern.ch/Atlas/GROUPS/PHYSICS/CONFNOTES/ATLAS-CONF-2016-024. [Online]. Available: https://cds.cern.ch/record/2157687

[190] G. Aad *et al.*, "Muon reconstruction performance of the ATLAS detector in proton–proton collision data at $\sqrt{s}$ =13 TeV," *Eur. Phys. J. C*, vol. 76, no. 5, p. 292, 2016.

[191] "Lepton isolation recommendations," https://twiki.cern.ch/twiki/bin/viewauth/AtlasProtected/IsolationSelectionTool, accessed: 2023-07-07.

[192] D. de Florian *et al.*, "Handbook of LHC Higgs Cross Sections: 4. Deciphering the Nature of the Higgs Sector," vol. 2/2017, 10 2016.

[193] "Lhctopworkinggroup, atlas-cms recommended predictions for top-quark-pair cross-sections," https://twiki.cern.ch/twiki/bin/view/LHCPhysics/TtbarNNLO, accessed: 2023-07-07.

[194] P. Kant, O. M. Kind, T. Kintscher, T. Lohse, T. Martini, S. Mölbitz, P. Rieck, and P. Uwer, "HatHor for single top-quark production: Updated predictions and uncertainty estimates for single top-quark production in hadronic collisions," *Comput. Phys. Commun.*, vol. 191, pp. 74–89, 2015.

[195] "Lhctopwg, atlas-cms recommended predictions for single-top cross sections," https://twiki.cern.ch/twiki/bin/view/LHCPhysics/SingleTopRefXsec, accessed: 2023-07-10.

[196] J. Alwall, R. Frederix, S. Frixione, V. Hirschi, F. Maltoni, O. Mattelaer, H. S. Shao, T. Stelzer, P. Torrielli, and M. Zaro, "The automated computation of tree-level and next-to-leading order differential cross sections, and their matching to parton shower simulations," *JHEP*, vol. 07, p. 079, 2014.

[197] M. Aaboud *et al.*, "Measurement of the inelastic proton-proton cross section at $\sqrt{s} = 13\ \mathrm{TeV}$ with the atlas detector at the lhc," *Phys. Rev. Lett.*, vol. 117, p. 182002, Oct 2016. [Online]. Available: https://link.aps.org/doi/10.1103/PhysRevLett.117.182002

[198] G. Aad *et al.*, "Performance of pile-up mitigation techniques for jets in pp collisions at $\sqrt{s} = 8$ TeV using the ATLAS detector," *Eur. Phys. J. C*, vol. 76, no. 11, p. 581, 2016.

[199] M. Aaboud *et al.*, "Jet energy scale measurements and their systematic uncertainties in proton-proton collisions at $\sqrt{s} = 13$ TeV with the ATLAS detector," *Phys. Rev. D*, vol. 96, no. 7, p. 072002, 2017.

[200] "Trexfitter framework twiki page," https://twiki.cern.ch/twiki/bin/view/AtlasProtected/TtHFitter, accessed: 2023-07-10.

[201] "Trexfitter framework gitlab project," https://gitlab.cern.ch/TRExStats/TRExFitter/, accessed: 2023-07-10.

[202] J. Lindsey, *Parametric Statistical Inference*, ser. Oxford science publications. Clarendon Press, 1996. [Online]. Available: https://books.google.pt/books?id=YnsQ-NnMxJ8C

[203] M. Aaboud *et al.*, "Measurements of inclusive and differential fiducial cross-sections of $t\bar{t}$ production with additional heavy-flavour jets in proton-proton collisions at $\sqrt{s}$ = 13 TeV with the ATLAS detector," *JHEP*, vol. 04, p. 046, 2019.

[204] A. M. Sirunyan *et al.*, "Measurement of the cross section for $\mathrm{t\bar{t}}$ production with additional jets and b jets in pp collisions at $\sqrt{s} =$ 13 TeV," *JHEP*, vol. 07, p. 125, 2020.

[205] ——, "Measurement of the $\mathrm{t\bar{t}b\bar{b}}$ production cross section in the all-jet final state in pp collisions at $\sqrt{s} =$ 13 TeV," *Phys. Lett. B*, vol. 803, p. 135285, 2020.

[206] Sirunyan, Albert M and others, "First measurement of the cross section for top quark pair production with additional charm jets using dileptonic final states in pp collisions at s=13TeV," *Phys. Lett. B*, vol. 820, p. 136565, 2021.

[207] S. Frixione, E. Laenen, P. Motylinski, and B. R. Webber, "Angular correlations of lepton pairs from vector boson and top quark decays in Monte Carlo simulations," *JHEP*, vol. 04, p. 081, 2007.

[208] P. Artoisenet, R. Frederix, O. Mattelaer, and R. Rietkerk, "Automatic spin-entangled decays of heavy resonances in Monte Carlo simulations," *JHEP*, vol. 03, p. 015, 2013.

[209] S. Frixione, E. Laenen, P. Motylinski, C. White, and B. R. Webber, "Single-top hadroproduction in association with a W boson," *JHEP*, vol. 07, p. 029, 2008.

[210] E. Re, "Single-top Wt-channel production matched with parton showers using the POWHEG method," *Eur. Phys. J. C*, vol. 71, p. 1547, 2011.

[211] S. Schumann and F. Krauss, "A parton shower algorithm based on Catani–Seymour dipole factorisation," *JHEP*, vol. 03, p. 038, 2008.

[212] "Tagging and suppression of pileup jets with the ATLAS detector," CERN, Geneva, Tech. Rep., 2014, all figures including auxiliary figures are available at https://atlas.web.cern.ch/Atlas/GROUPS/PHYSICS/CONFNOTES/ATLAS-CONF-2014-018. [Online]. Available: https://cds.cern.ch/record/1700870

[213] "Small-R (R=0.4) jet energy scale and jet energy resolution uncertainties for full run 2 analyses (release 21) ." [Online]. Available: https://twiki.cern.ch/twiki/bin/viewauth/AtlasProtected/JetUncertaintiesRel21Summer2018SmallR

A

Signal yields for CP analysis

A.1 $t\bar{t}H$ parameterization

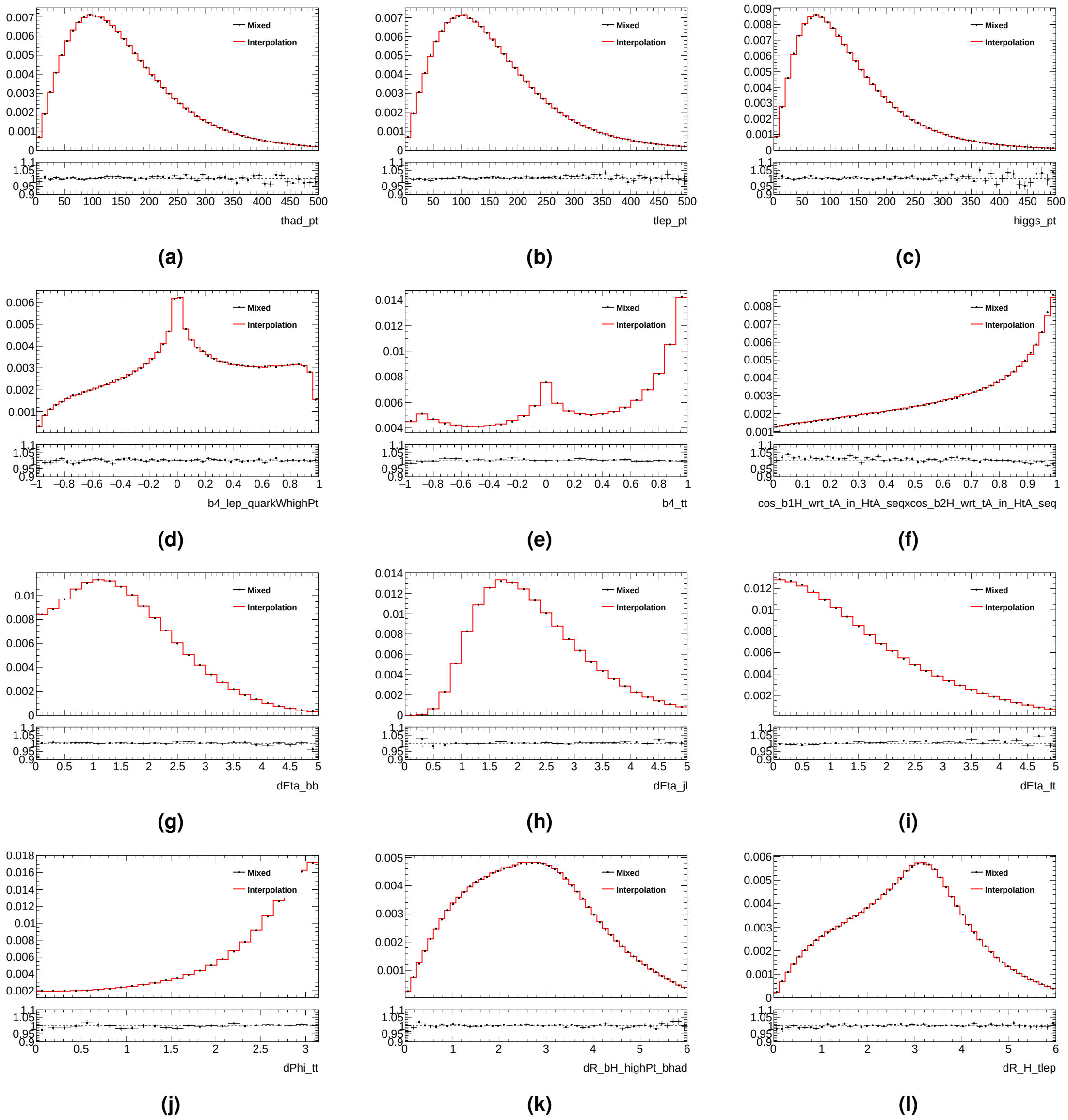

Figure A.1: Comparison between the interpolation of a pure CP-even and pure CP-odd sample with a mixing angle of 45° (red) and a dedicated MC samples generated with the same mixing angle for different kinematic and angular variables in the single-lepton channel.

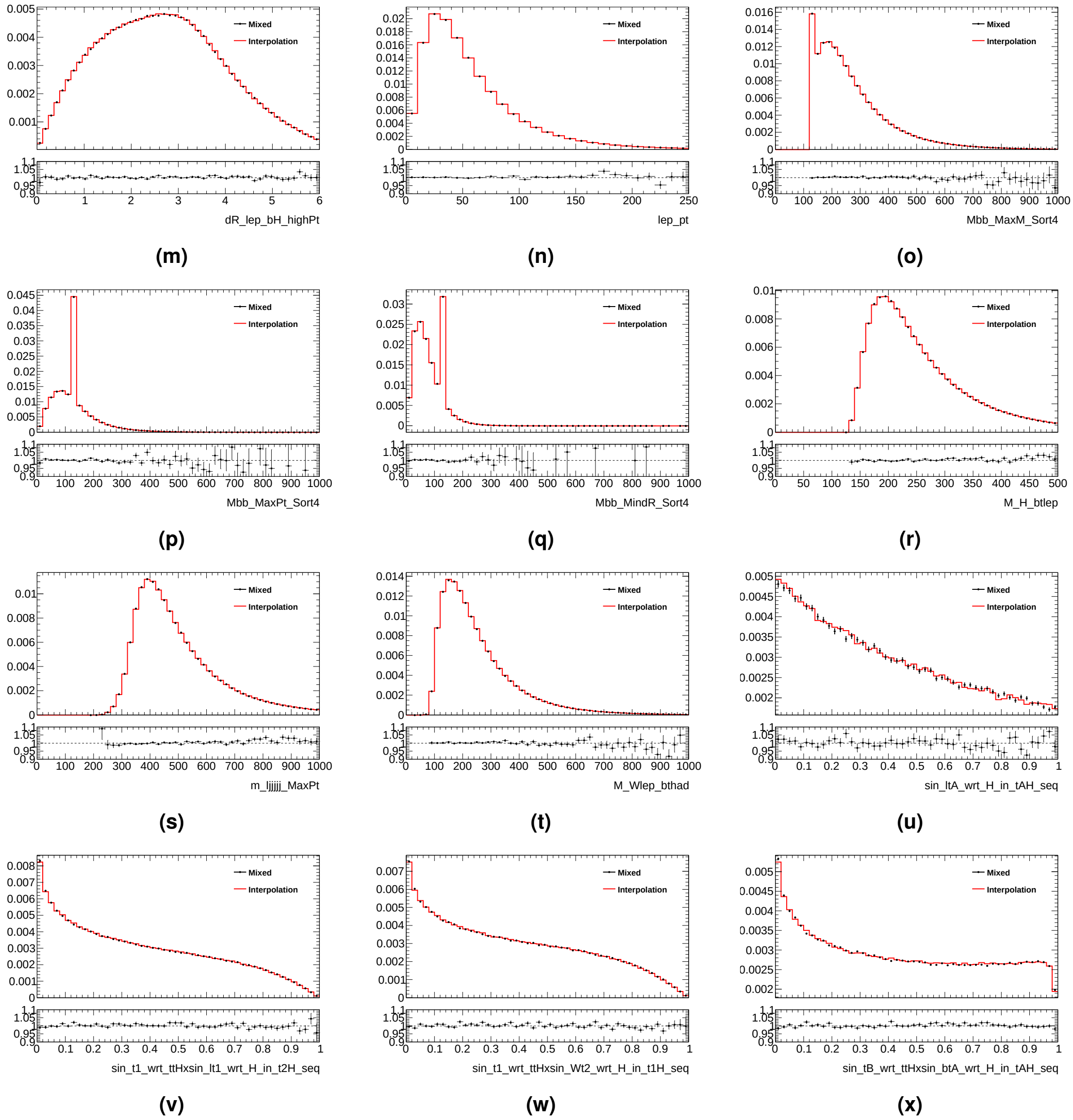

Figure A.1: Comparison between the interpolation of a pure CP-even and pure CP-odd sample with a mixing angle of $45°$ (red) and a dedicated MC samples generated with the same mixing angle for different kinematic and angular variables in the single-lepton channel.

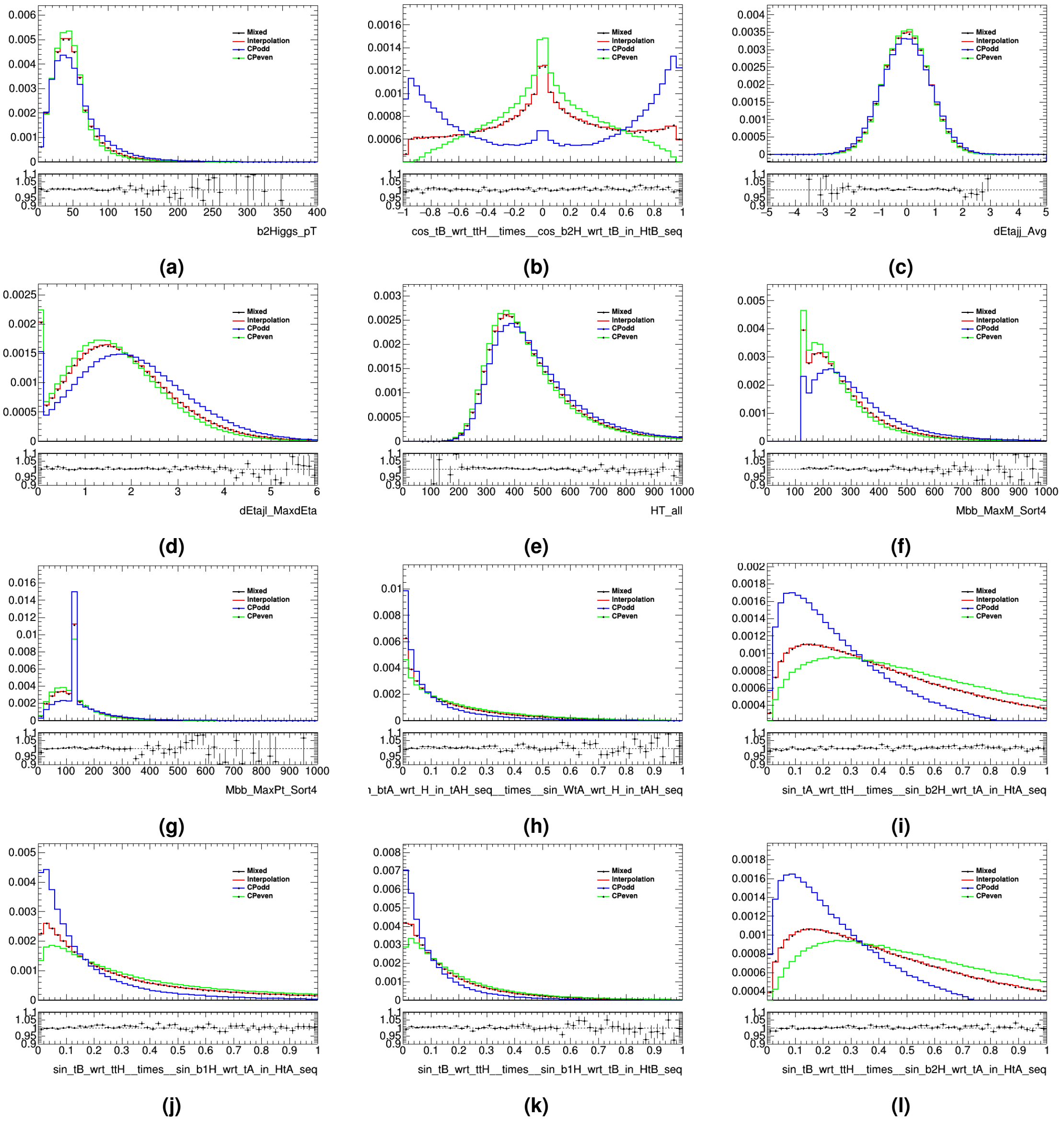

Figure A.2: Comparison between the interpolation of a pure CP-even and pure CP-odd sample with a mixing angle of 45° (red) and a dedicated MC samples generated with the same mixing angle for different kinematic and angular variables in the dilepton channel. The distributions for the pure CP-even and CP-odd samples are also shown in green and blue, respectively.

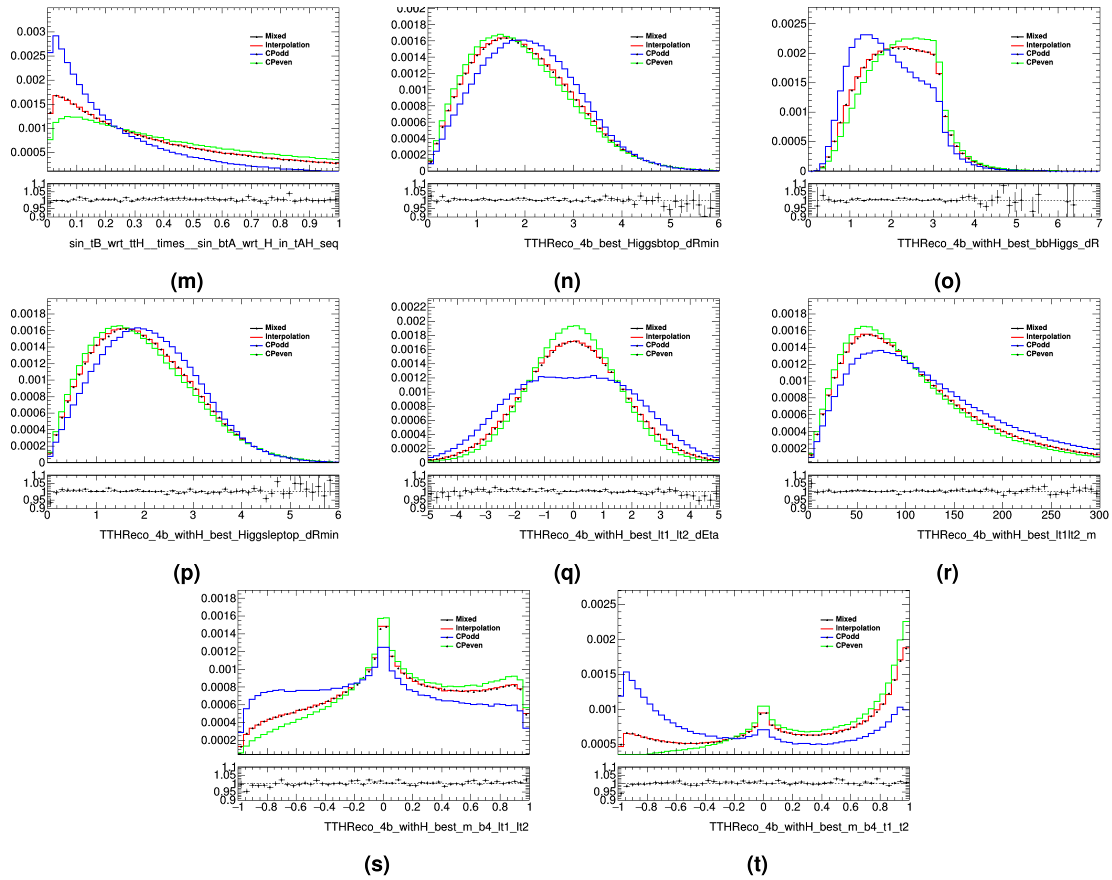

Figure A.2: Comparison between the interpolation of a pure CP-even and pure CP-odd sample with a mixing angle of 45° (red) and a dedicated MC samples generated with the same mixing angle for different kinematic and angular variables in the dilepton channel. The distributions for the pure CP-even and CP-odd samples are also shown in green and blue, respectively.

A.2 tH parameterization

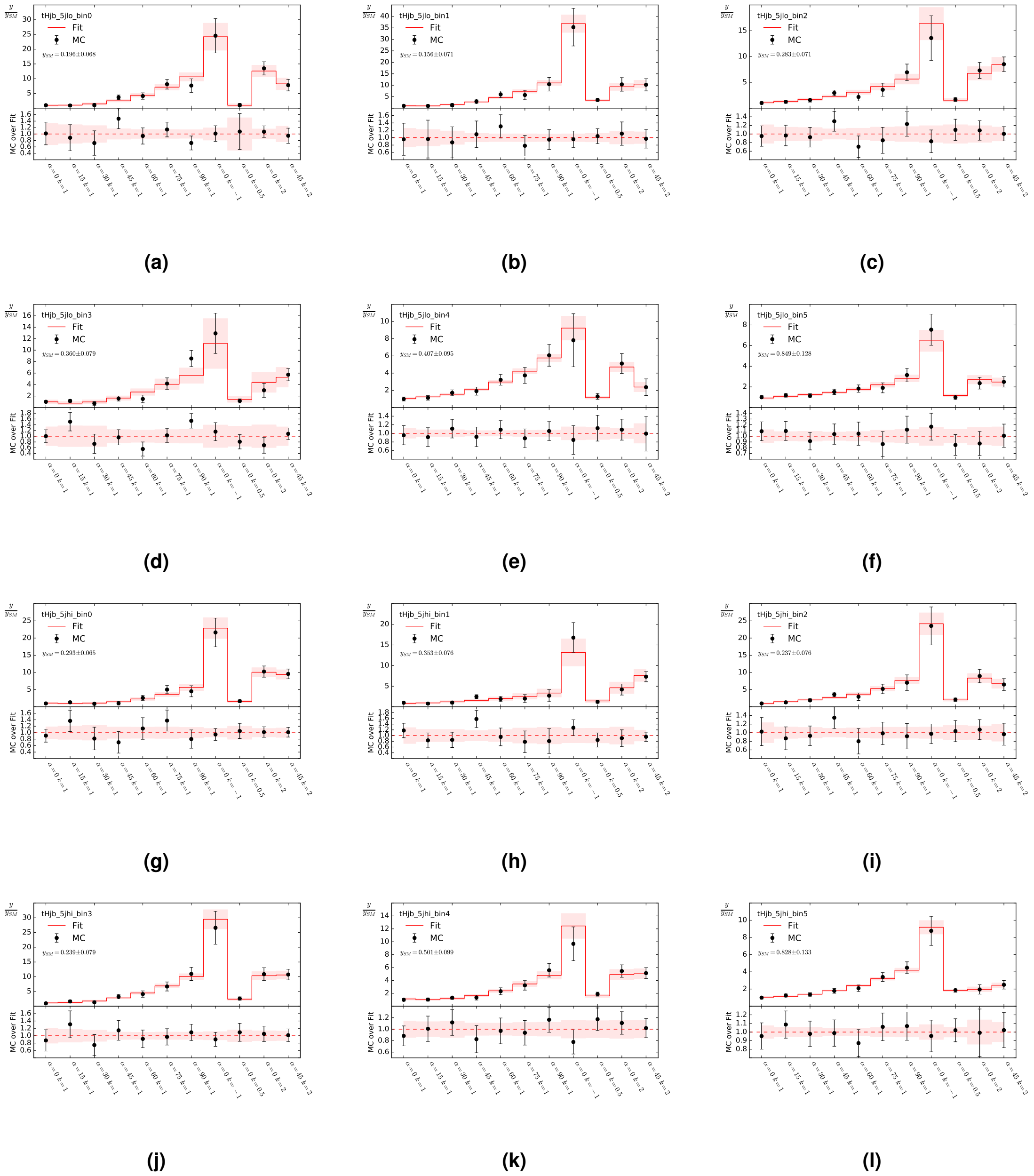

Figure A.3: Comparison of $tHjb$ yields in single-lepton 5j regions, obtained using the parameterization or directly from MC samples. The parameter space points shown are the ones used to fit the coefficients A-F.

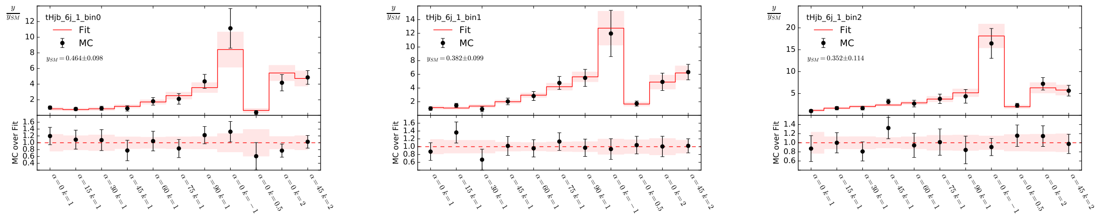

(a) (b) (c)

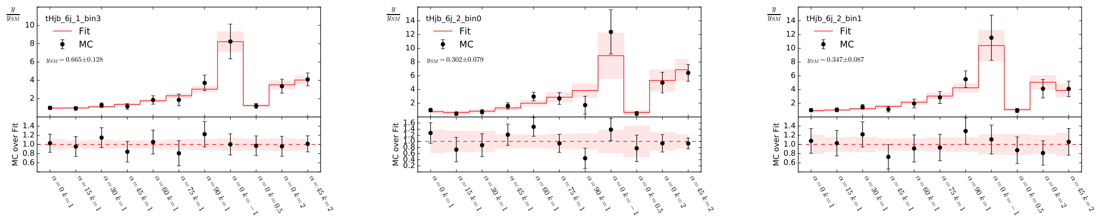

(d) (e) (f)

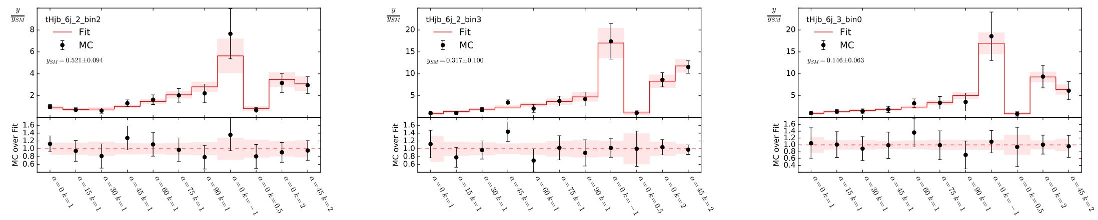

(g) (h) (i)

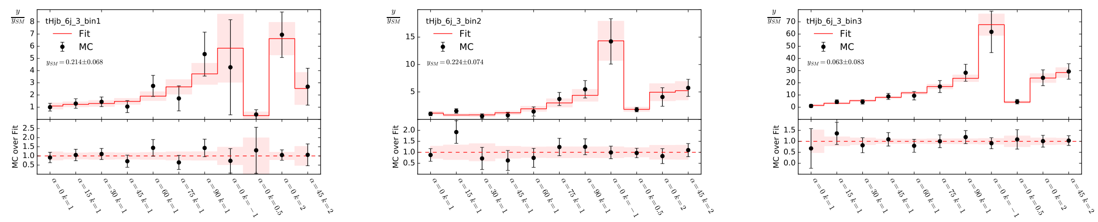

(j) (k) (l)

Figure A.4: Comparison of $tHjb$ yields in single-lepton 6j regions, obtained using the parameterization or directly from MC samples. The parameter space points shown are the ones used to fit the coefficients A-F.

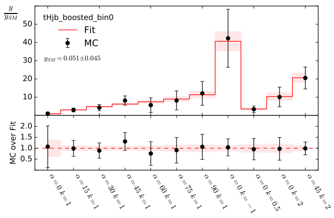

(a)

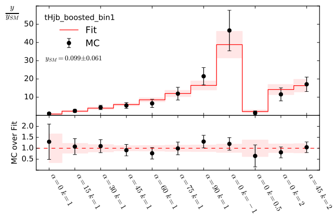

(b)

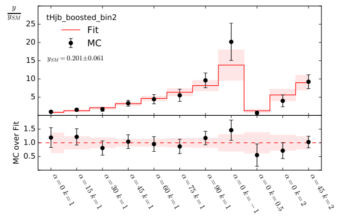

(c)

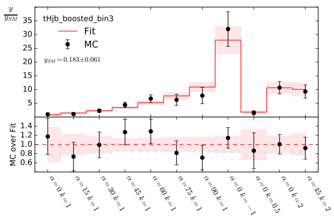

(d)

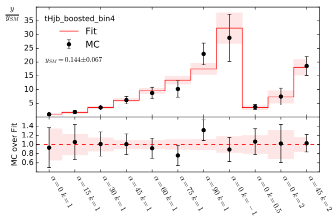

(e)

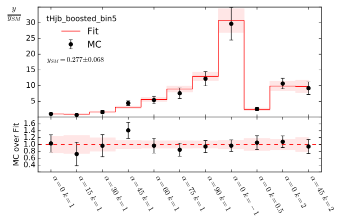

(f)

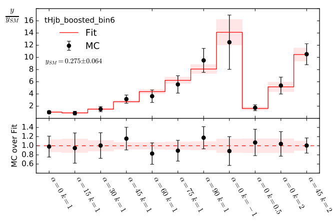

(g)

Figure A.5: Comparison of $tHjb$ yields in the single-lepton boosted region, obtained using the parameterization or directly from MC samples. The parameter space points shown are the ones used to fit the coefficients A-F.

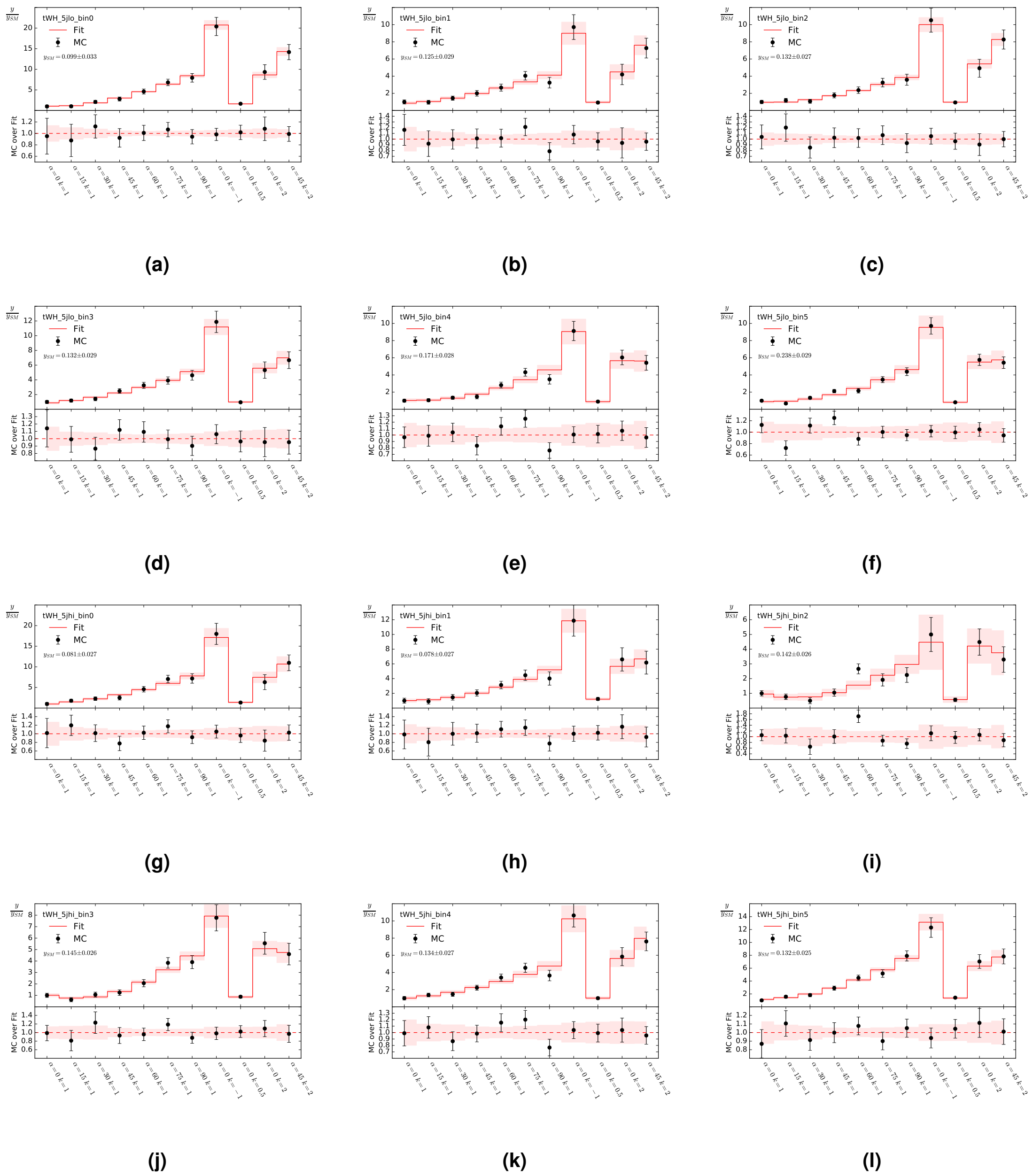

Figure A.6: Comparison of tWH yields in single-lepton 5j regions, obtained using the parameterization or directly from MC samples. The parameter space points shown are the ones used to fit the coefficients A-F.

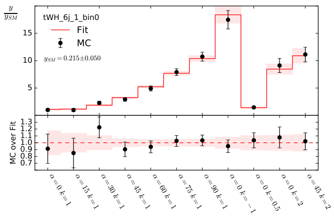

(a)

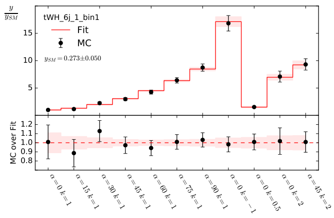

(b)

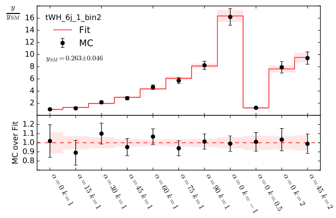

(c)

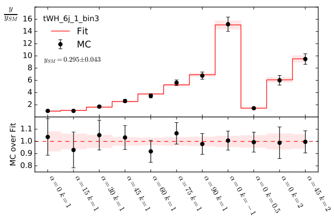

(d)

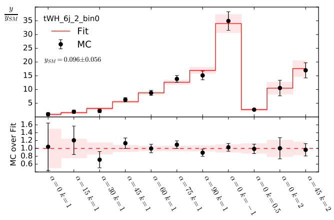

(e)

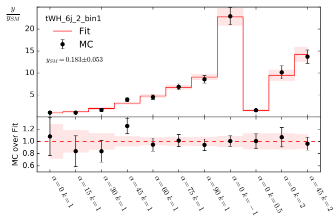

(f)

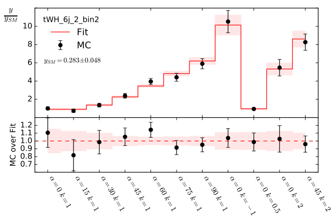

(g)

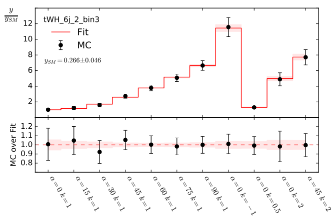

(h)

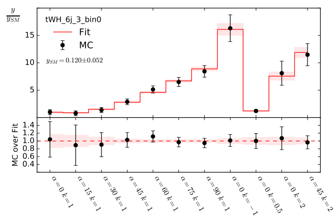

(i)

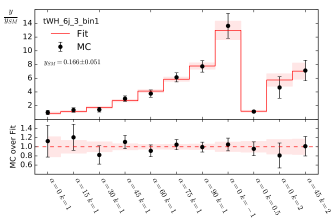

(j)

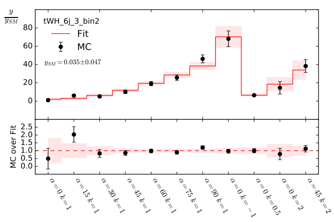

(k)

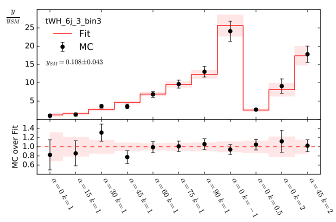

(l)

Figure A.7: Comparison of tWH yields in single-lepton 6j regions, obtained using the parameterization or directly from MC samples. The parameter space points shown are the ones used to fit the coefficients A-F.

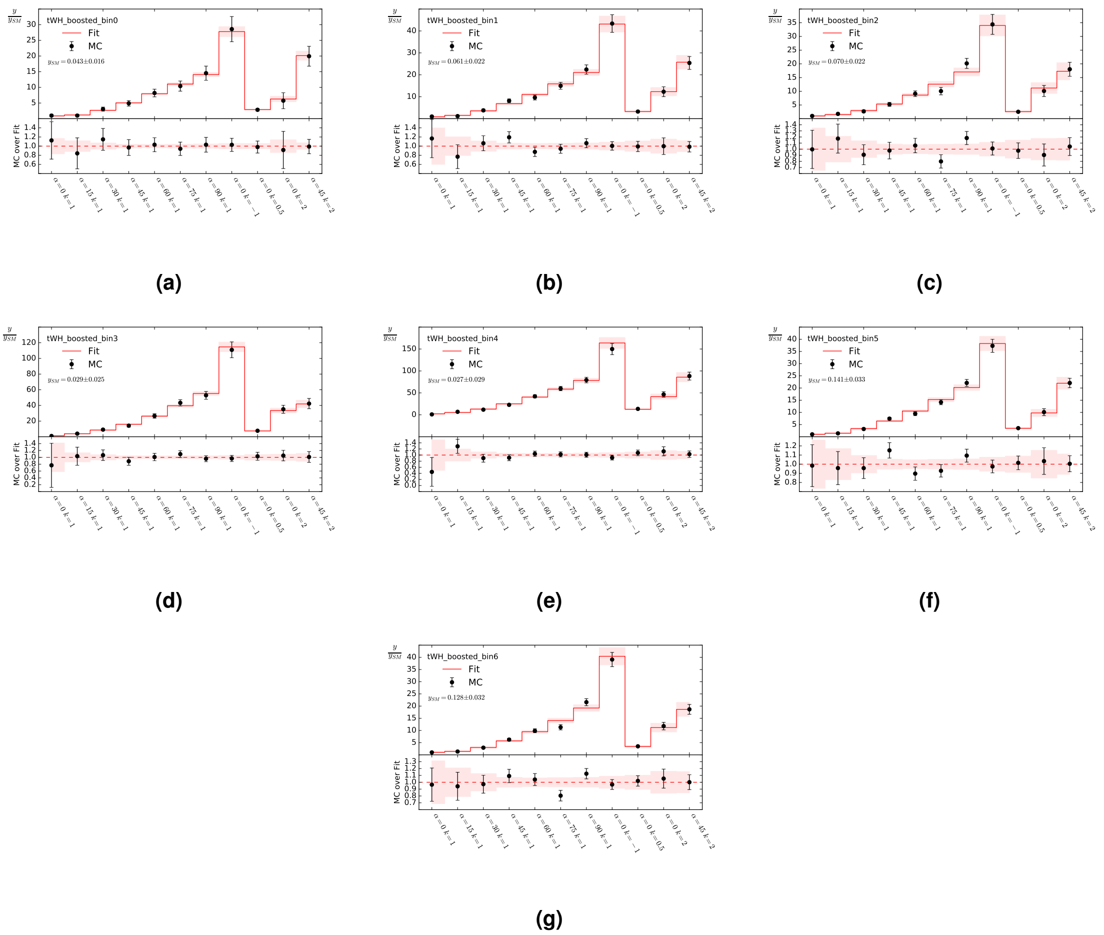

Figure A.8: Comparison of tWH yields in the single-lepton boosted region, obtained using the parameterization or directly from MC samples. The parameter space points shown are the ones used to fit the coefficients A-F.

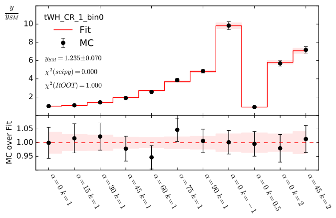

(a)

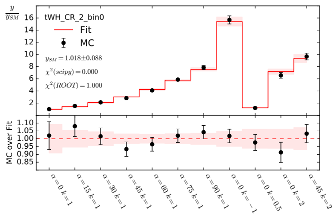

(b)

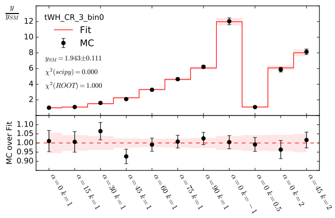

(c)

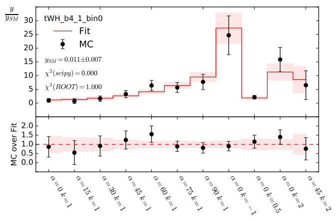

(d)

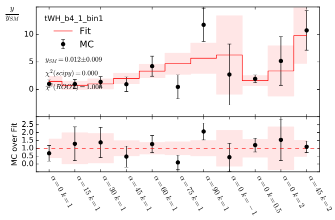

(e)

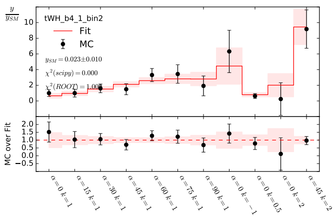

(f)

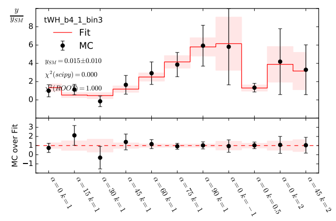

(g)

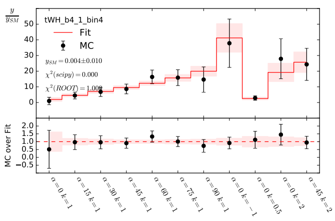

(h)

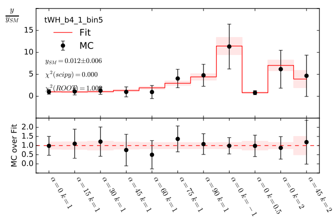

(i)

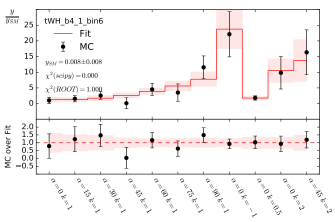

(j)

Figure A.9: Comparison of tWH yields in the dilepton control regions CR[hi]33, CR[lo]43, CR[hi]43 and CR[]44, obtained using the parameterization or directly from MC samples. The parameter space points shown are the ones used to fit the coefficients A-F.

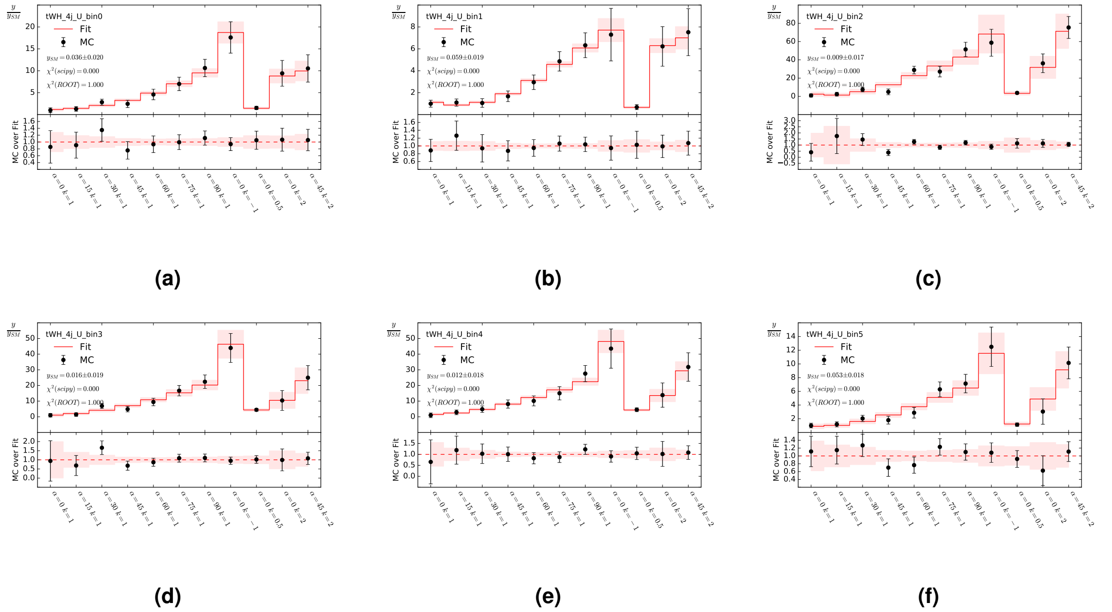

(a) (b) (c)

(d) (e) (f)

Figure A.10: Comparison of tWH yields in the dilepton control region CR[no-reco]44, obtained using the parameterization or directly from MC samples. The parameter space points shown are the ones used to fit the coefficients A-F.

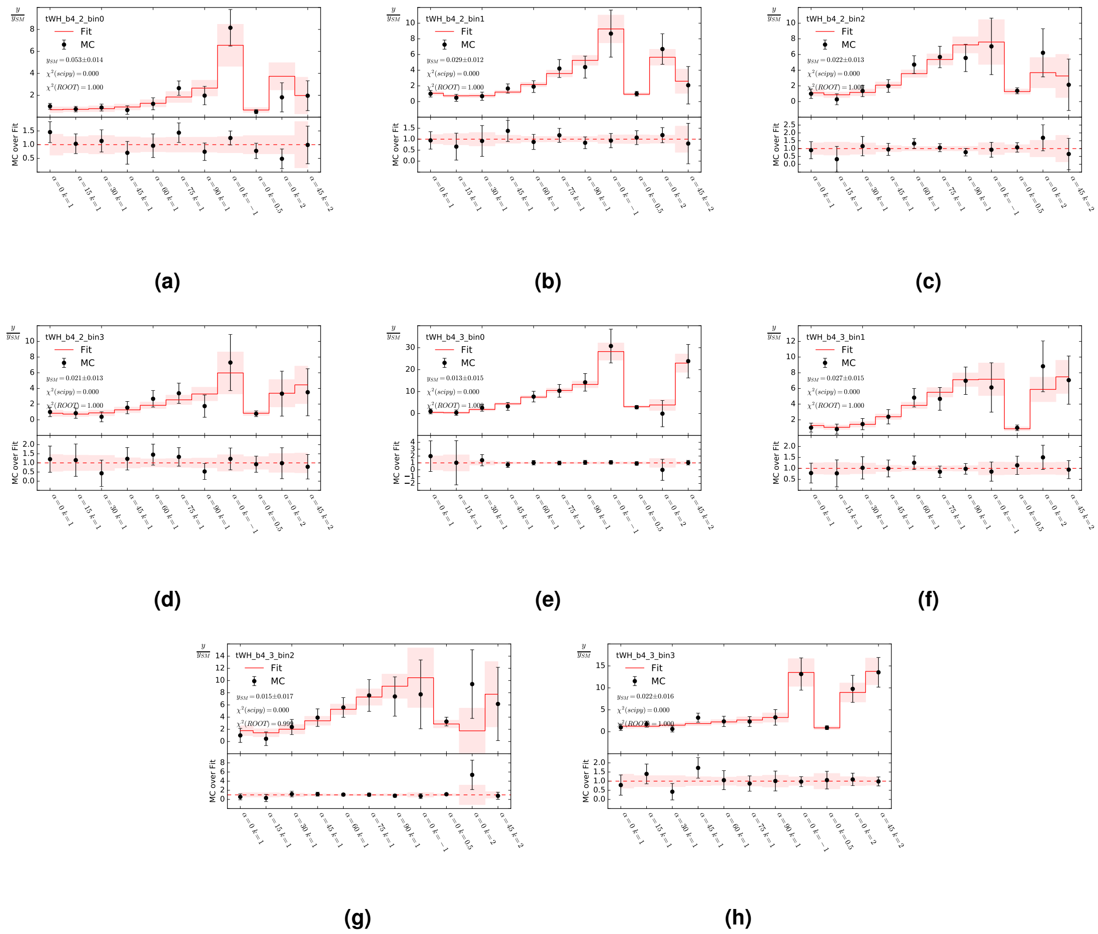

(a) (b) (c)

(d) (e) (f)

(g) (h)

Figure A.11: Comparison of tWH yields in dilepton signal regions, obtained using the parameterization or directly from MC samples. The parameter space points shown are the ones used to fit the coefficients A-F.

A.3 tH yields

	SR[hi]33					SR[lo]43					SR[hi]43					SR[bin 1]44					SR[bin 2]44					SR[bin 3]44					SR[bin 4]44				
	raw	weight.	%all	%ttH	%tWH	raw	weight.	%all	%ttH	%tWH	raw	weight.	%all	%ttH	%tWH	raw	weight.	%all	%ttH	%tWH	raw	weight.	%all	%ttH	%tWH	raw	weight.	%all	%ttH	%tWH	raw	weight.	%all	%ttH	%tWH
$\alpha = 0$																																			
ttH	55858	26.554	1.05%	—	—	199315	80.963	1.82%	—	—	310984	122.103	3.04%	—	—	7043	2.700	0.96%	—	—	23278	8.723	3.45%	—	—	48073	18.119	8.56%	—	—	83421	32.403	22.19%	—	—
tWH	1656	1.251	0.05%	4.71%	—	2906	1.029	0.02%	1.27%	—	4417	1.988	0.05%	1.63%	—	155	0.067	0.02%	2.47%	—	409	0.125	0.05%	1.44%	—	454	0.150	0.07%	0.83%	—	498	0.126	0.09%	0.39%	—
$tHjb$	14	0.015	0.00%	0.06%	1.20%	117	0.179	0.00%	0.22%	17.38%	61	0.124	0.00%	0.10%	6.25%	0	0.000	0.00%	0.00%	0.00%	2	0.000	0.00%	0.00%	0.12%	1	-0.007	-0.00%	-0.04%	-4.46%	0	0.000	0.00%	0.00%	0.00%
$\alpha = 45$																																			
ttH	37685	12.081	0.48%	—	—	150108	40.254	0.91%	—	—	230562	59.028	1.47%	—	—	6133	1.552	0.55%	—	—	18686	4.538	1.80%	—	—	35771	8.916	4.21%	—	—	59874	15.146	10.37%	—	—
tWH	1650	2.364	0.09%	19.57%	—	3062	2.972	0.07%	7.38%	—	4493	4.175	0.10%	7.07%	—	218	0.118	0.04%	7.58%	—	488	0.331	0.13%	7.30%	—	421	0.315	0.15%	3.53%	—	435	0.302	0.21%	1.99%	—
$tHjb$	25	0.160	0.01%	1.32%	6.76%	125	0.370	0.01%	0.92%	12.46%	79	0.215	0.01%	0.36%	5.16%	2	-0.007	-0.00%	-0.47%	-6.21%	1	0.008	0.00%	0.18%	2.50%	3	0.013	0.01%	0.15%	4.18%	1	0.009	0.01%	0.06%	2.85%
$\alpha = 90$																																			
ttH	44952	9.713	0.39%	—	—	204645	33.364	0.75%	—	—	313317	50.066	1.24%	—	—	10565	1.658	0.59%	—	—	29137	4.414	1.75%	—	—	50042	7.729	3.65%	—	—	78725	12.552	8.60%	—	—
tWH	1821	6.057	0.24%	62.36%	—	3170	8.168	0.18%	24.48%	—	4687	12.268	0.30%	24.50%	—	205	0.559	0.20%	33.72%	—	530	1.474	0.58%	33.39%	—	421	1.050	0.50%	13.59%	—	372	0.836	0.57%	6.66%	—
$tHjb$	17	0.005	0.00%	0.05%	0.08%	127	0.799	0.02%	2.39%	9.78%	74	0.498	0.01%	0.99%	4.06%	7	-0.096	-0.03%	-5.77%	-17.12%	3	-0.007	-0.00%	-0.15%	-0.44%	1	-0.033	-0.02%	-0.43%	-3.13%	1	0.045	0.03%	0.36%	5.43%
$\alpha = 60$																																			
tWH	1641	3.219	0.13%	—	—	3164	4.253	0.10%	—	—	4613	6.531	0.16%	—	—	194	0.216	0.08%	—	—	507	0.748	0.30%	—	—	466	0.586	0.28%	—	—	370	0.514	0.35%	—	—
$tHjb$	25	0.199	0.01%	—	6.18%	133	0.732	0.02%	—	17.22%	64	0.205	0.01%	—	3.14%	1	0.028	0.01%	—	13.14%	8	0.042	0.02%	—	5.66%	2	-0.013	-0.01%	—	-2.19%	1	-0.015	-0.01%	—	-2.93%
$\alpha = 75$																																			
tWH	1714	4.795	0.19%	—	—	3147	6.173	0.14%	—	—	4716	9.260	0.23%	—	—	222	0.538	0.19%	—	—	496	0.742	0.29%	—	—	456	0.956	0.45%	—	—	334	0.632	0.43%	—	—
$tHjb$	20	0.285	0.01%	—	5.95%	110	0.840	0.02%	—	13.61%	67	0.374	0.01%	—	4.04%	2	0.056	0.02%	—	10.32%	1	-0.029	-0.01%	—	-3.92%	2	0.006	0.00%	—	0.61%	2	0.001	0.00%	—	0.09%
$\alpha = 15$																																			
tWH	1551	1.364	0.05%	—	—	2926	1.599	0.04%	—	—	4389	2.166	0.05%	—	—	179	0.070	0.02%	—	—	401	0.105	0.04%	—	—	491	0.166	0.08%	—	—	498	0.178	0.12%	—	—
$tHjb$	14	0.018	0.00%	—	1.30%	86	0.257	0.01%	—	16.06%	61	-0.025	-0.00%	—	-1.14%	3	0.021	0.01%	—	29.81%	1	-0.009	-0.00%	—	-8.50%	4	0.014	0.01%	—	8.17%	2	0.005	0.00%	—	2.54%
$\alpha = 30$																																			
tWH	1634	1.764	0.07%	—	—	3090	2.223	0.05%	—	—	4519	3.165	0.08%	—	—	202	0.103	0.04%	—	—	448	0.348	0.14%	—	—	460	0.239	0.11%	—	—	457	0.202	0.14%	—	—
$tHjb$	17	0.104	0.00%	—	5.91%	111	0.214	0.00%	—	9.65%	65	0.188	0.00%	—	5.95%	3	-0.006	-0.00%	—	-6.26%	3	0.027	0.01%	—	7.69%	0	0.000	0.00%	—	0.00%	1	-0.008	-0.01%	—	-3.81%
$\alpha = 0, y_t = 0.5$																																			
tWH	1670	1.110	0.04%	—	—	2930	1.265	0.03%	—	—	4469	2.145	0.05%	—	—	219	0.100	0.04%	—	—	446	0.205	0.08%	—	—	438	0.211	0.10%	—	—	412	0.168	0.12%	—	—
$tHjb$	16	-0.004	-0.00%	—	-0.38%	89	0.081	0.00%	—	6.43%	41	0.122	0.00%	—	5.68%	2	0.004	0.00%	—	4.17%	3	0.003	0.00%	—	1.53%	1	-0.007	-0.00%	—	-3.42%	0	0.000	0.00%	—	0.00%
$\alpha = 0, y_t = 2$																																			
tWH	1628	7.107	0.28%	—	—	2947	6.983	0.16%	—	—	4494	11.533	0.29%	—	—	180	0.470	0.17%	—	—	454	1.109	0.44%	—	—	463	0.811	0.38%	—	—	482	0.898	0.62%	—	—
$tHjb$	12	0.010	0.00%	—	0.14%	156	1.328	0.03%	—	19.02%	92	0.600	0.01%	—	5.20%	2	0.003	0.00%	—	0.71%	0	0.000	0.00%	—	0.00%	5	0.153	0.07%	—	18.83%	4	0.081	0.06%	—	9.07%
$\alpha = 0, y_t = -1$																																			
ttH	55858	26.554	1.05%	—	—	199315	80.963	1.82%	—	—	310984	122.103	3.04%	—	—	7043	2.700	0.96%	—	—	23278	8.723	3.45%	—	—	48073	18.119	8.56%	—	—	83421	32.403	22.19%	—	—
tWH	1746	12.167	0.48%	45.82%	—	3153	16.369	0.37%	20.22%	—	4722	23.680	0.59%	19.39%	—	209	0.927	0.33%	34.34%	—	492	2.420	0.96%	27.74%	—	422	2.091	0.99%	11.54%	—	335	1.222	0.84%	3.77%	—
$tHjb$	17	-0.343	-0.01%	-1.29%	-2.82%	114	3.568	0.08%	4.41%	21.80%	65	1.409	0.04%	1.15%	5.95%	2	0.161	0.06%	5.97%	17.38%	3	0.072	0.03%	0.83%	2.99%	3	0.296	0.14%	1.63%	14.14%	1	-0.063	-0.04%	-0.19%	-5.12%
$\alpha = 45, y_t = 2$																																			
$tHjb$	26	0.313	0.01%	—	—	159	1.062	0.02%	—	—	87	0.184	0.00%	—	—	4	0.049	0.02%	—	—	3	-0.030	-0.01%	—	—	2	0.013	0.01%	—	—	1	0.000	0.00%	—	—
$\alpha = 90, y_t = 2$																																			
tWH	1556	8.920	0.35%	—	—	2781	10.050	0.23%	—	—	4089	16.233	0.40%	—	—	189	1.105	0.39%	—	—	446	1.459	0.58%	—	—	397	0.959	0.45%	—	—	400	1.348	0.92%	—	—

Table A.1: Yields obtained from the different $tHjb$ and tWH samples in the dilepton regions.

B

Input variables of MVA algorithms

B.1 Reconstruction BDT

Variables	BDT w/ Higgs info.	BDT w/o Higgs info.
Topological information from $t\bar{t}$		
Mass of top	✓	✓
Mass of anti-top	✓	✓
Mass difference between top and anti-top	✓	✓
ΔR(ℓ, b) from top	✓	✓
ΔR(ℓ, b) from anti-top	✓	✓
|ΔR(ℓ, b) from top - ΔR(ℓ, b) from anti-top|	–	✓
ΔR(b from top, b from anti-top)	✓	–
$\Delta\phi$(b from top, b from anti-top)	–	✓
p_T b from top	–	✓
p_T b from anti-top	–	✓
Min. $\Delta\eta$(ℓ, b from top or anti-top)	–	✓
Topological information from the Higgs-boson candidate		
Max. ΔR(Higgs, b from top or anti-top)	✓	–
Mass of Higgs	✓	–
ΔR(Higgs,$t\bar{t}$)	✓	–
ΔR(b_1 from Higgs, b_2 from Higgs)	✓	–

Table B.1: List of input variables for the reconstruction BDTs in the dilepton channel. The top and anti-top candidates are built from one lepton and one b-jet. The lepton charge defines the top or anti-top candidates. Topological information from the Higgs-boson candidate is only used for the BDT that includes Higgs-boson candidate information.

Variables	BDT w/ Higgs info.	BDT w/o Higgs info.
Topological information from $t\bar{t}$		
Mass of top$_{\mathrm{lep}}$	✓	✓
Mass of top$_{\mathrm{had}}$	✓	✓
Mass of W_{had}	✓	✓
Mass of W_{had} and b from top$_{\mathrm{lep}}$	✓	✓
Mass of W_{lep} and b from top$_{\mathrm{had}}$	✓	✓
ΔR(W_{had}, b from top$_{\mathrm{had}}$)	✓	✓
ΔR(W_{had}, b from top$_{\mathrm{lep}}$)	✓	✓
ΔR(ℓ, b from top$_{\mathrm{lep}}$)	✓	✓
ΔR(ℓ, b from top$_{\mathrm{had}}$)	✓	✓
ΔR(b from top$_{\mathrm{lep}}$, b from top$_{\mathrm{had}}$)	✓	✓
ΔR(q_1 from W_{had}, q_2 from W_{had})	✓	✓
ΔR(b from t_{had}, q_1 from W_{had})	✓	✓
ΔR(b from t_{had}, q_2 from W_{had})	✓	✓
Min. ΔR(b from top$_{\mathrm{had}}$, q_i from W_{had})	✓	✓
ΔR(lep, b from top$_{\mathrm{lep}}$) $-$ min. ΔR(b from top$_{\mathrm{had}}$, q_i from W_{had})	✓	✓
Topological information from the Higgs-boson candidate		
Mass of Higgs	✓	–
Mass of Higgs and q_1 from W_{had}	✓	–
ΔR(b_1 from Higgs, b_2 from Higgs)	✓	–
ΔR(b_1 from Higgs, lepton)	✓	–

Table B.2: List of input variables for the reconstruction BDTs in the single-lepton resolved channel. The subscript had (lep) indicates the hadronically (leptonically) decaying W-boson or the corresponding top quark candidates. The symbol b_i refers to b-tagged jets from the Higgs-boson candidate decay sorted by p_{T}. The symbol q_i refers to jets from the W-boson candidate decay sorted by p_{T}. Topological information from the Higgs-boson candidate is only used for the BDT that includes Higgs-boson candidate information.

B.2 Boosted DNN

Variable	Description
m^{RCjet}	mass of reclustered jet
$\sqrt{d_{12}}$	first splitting scale
$\sqrt{d_{23}}$	second splitting scale
Q_W	minimum invariant mass of constituent pairs
$n_{\mathrm{constituents}}$	number of constituents in the RC jet
$p_{\mathrm{T}}^{\mathrm{const}_1}$	$p_{\mathrm{T}}$of the constituent leading in p_{T}
$p_{\mathrm{T}}^{\mathrm{const}_2}$	$p_{\mathrm{T}}$of the constituent sub-leading in p_{T}
$\mathrm{mv2}^{\mathrm{const}_1}$	PC MV2c10 score of the constituent leading in p_{T}
$\mathrm{mv2}^{\mathrm{const}_2}$	PC MV2c10 score of the constituent sub-leading in p_{T}
$\Delta R(\mathrm{const1}, \mathrm{const2})$	angular separation between leading and sub-leading constituents in p_{T}
$m^{b-\mathrm{jets}}$	invariant mass of all b-tagged constituents
$m^{\mathrm{light-jets}}$	invariant mass of all untagged constituents
$\mathrm{mv2}_{\mathrm{min}}$	minimum constituent PC MV2c10 score
$\mathrm{mv2}_{\mathrm{max}}$	maximum constituent PC MV2c10 score
$\Delta R(\mathrm{consts})_{\mathrm{max}}$	maximum angular separation between two constituents
$\Delta R(\mathrm{consts})_{\mathrm{min}}$	minimum angular separation between two constituents
$\mathrm{mv2}^{\mathrm{rest}}$	PC MV2c10 score of all constituents except the leading and sub-leading in p_{T}

Table B.3: List of variables included in the DNN training. The substructure variables $\sqrt{d_{12}}$, $\sqrt{d_{23}}$ and Q_W are calculated using the constituents information of the RC jets.

B.3 Classification BDT

Variable	Definition	
General kinematic variables		
m_{bb}^{min}	Minimum invariant mass of a b-tagged jet pair	✓
$m_{bb}^{\text{min } \Delta R}$	Invariant mass of the b-tagged jet pair with minimum ΔR	✓
$m_{jj}^{\text{max } p_{\text{T}}}$	Invariant mass of the jet pair with maximum p_{T}	✓
$m_{bb}^{\text{max } p_{\text{T}}}$	Invariant mass of the b-tagged jet pair with maximum p_{T}	✓
$\Delta\eta_{bb}^{\text{avg}}$	Average $\Delta\eta$ for all b-tagged jet pairs	✓
$N_{bb}^{\text{Higgs } 30}$	Number of b-tagged jet pairs with invariant mass within 30 GeV of the Higgs-boson mass	✓
Variables from reconstruction BDT		
BDT outputs	Output of the reco. BDT w/ Higgs info. for the combination selected by the reco. BDTs w/ or w/o Higgs info.	✓**
m_{bb}^{Higgs}	Higgs candidate mass	✓
$\Delta R_{H,t\bar{t}}$	ΔR between Higgs candidate and $t\bar{t}$ candidate system	✓*
$\Delta R_{H,\ell}^{\text{min}}$	Minimum ΔR between Higgs candidate and lepton	✓
$\Delta R_{H,b}^{\text{min}}$	Minimum ΔR between Higgs candidate and b-jet from top	✓

Table B.4: Variables used in the classification BDTs in the dilepton signal regions. For variables depending on b-tagged jets, only jets b-tagged using the 70% working point are considered. For variables from the reconstruction BDT, those with a * are from the BDT using Higgs-boson information, those with no * are from the BDT without Higgs-boson information while for those with a ** both versions are used.

Variable	Definition	
General kinematic variables		
$\Delta R_{bb}^{\text{avg}}$	Average ΔR for all b-tagged jet pairs	✓
$\Delta R_{bb}^{\text{max } p_{\text{T}}}$	ΔR between the two b-tagged jets with the largest vector sum p_{T}	✓
$\Delta \eta_{jj}^{\text{max}}$	Maximum $\Delta \eta$ between any two jets	✓
$m_{bb}^{\text{min } \Delta R}$	Mass of the combination of two b-tagged jets with the smallest ΔR	✓
$N_{bb}^{\text{Higgs } 30}$	Number of b-tagged jet pairs with invariant mass within 30 GeV of the Higgs-boson mass	✓
Aplanarity	$1.5\lambda_2$, where λ_2 is the second eigenvalue of the momentum tensor built with all jets	✓
H_1	Second Fox–Wolfram moment computed using all jets and the lepton	✓
Variables from reconstruction BDT		
BDT output	Output of the reconstruction BDT	✓*
m_{bb}^{Higgs}	Higgs candidate mass	✓
$m_{H,b_{\text{lep top}}}$	Mass of Higgs candidate and b-jet from leptonic top candidate	✓
$\Delta R_{bb}^{\text{Higgs}}$	ΔR between b-jets from the Higgs candidate	✓
$\Delta R_{H,t\bar{t}}$	ΔR between Higgs candidate and $t\bar{t}$ candidate system	✓*
$\Delta R_{H,\text{lep top}}$	ΔR between Higgs candidate and leptonic top candidate	✓
Variables from likelihood calculations		
LHD	Likelihood discriminant	✓
Variables from b-tagging		
$w_{b\text{-tag}}^{\text{Higgs}}$	Sum of b-tagging discriminants of jets from best Higgs candidate from the reconstruction BDT	✓
B_{jet}^{3}	3$^{\text{rd}}$ largest jet b-tagging discriminant	✓
B_{jet}^{4}	4$^{\text{th}}$ largest jet b-tagging discriminant	✓
B_{jet}^{5}	5$^{\text{th}}$ largest jet b-tagging discriminant	✓

Table B.5: Input variables to the classification BDTs in the single-lepton signal regions. For variables depending on b-tagged jets, jets are sorted by their pseudo-continuous b-tag score, and by their p_{T} when they have the same pseudo-continuous b-tag score. For variables from the reconstruction BDT, those with a * are from the BDT using Higgs-boson information, those with no * are from the BDT without Higgs-boson information. Variables B_{jet}^{3} and B_{jet}^{4} carry no discriminating information in the $\text{SR}_{\geq 4b@70}^{\geq 6j}$ region.

Variable	Description
m_{Higgs}	Higgs candidate mass
$p_{\mathrm{T}}{}^{\mathrm{Higgs}}$	Higgs candidate transverse momentum
$\eta^{\mathrm{lep}}_{\mathrm{Higgs}}$	η of the Higgs candidate relative to the lepton
$\mathrm{P(H)}_{\mathrm{Higgs}}$	DNN Higgs probability for the Higgs candidate
m_{hadTop}	hadronic top candidate mass
$p_{\mathrm{T}}{}^{\mathrm{hadTop}}$	hadronic top candidate transverse momentum
$\eta^{\mathrm{lep}}_{\mathrm{hadTop}}$	η of the hadronic top candidate relative to the lepton
$\mathrm{PCB}^{\mathrm{jet_i}}_{\mathrm{hadTop}}$	PCB score of the i^{th} jet associated to the hadronic top
m_{lepTop}	leptonic top candidate mass
$p_{\mathrm{T}}{}^{\mathrm{lepTop}}$	leptonic top candidate transverse momentum
$\mathrm{PCB}^{\mathrm{jet}}_{\mathrm{lepTop}}$	PCB score of the jet associated to the leptonic top
n_{jets}	small-R jets multiplicity
$\Delta R(\mathrm{Higgs}, \mathrm{hadTop})$	ΔR between the Higgs and the hadronic top candidates
$\Delta R(\mathrm{Higgs}, \mathrm{lepTop})$	ΔR between the Higgs and the leptonic top candidates
$\Delta R(\mathrm{hadTop}, \mathrm{lepTop})$	ΔR between the hadronic top and the leptonic top candidates
$p_{\mathrm{T}}{}^{t\bar{t}H}$	transverse momentum of the $t\bar{t}H$system
$p_{\mathrm{T}}{}^{t\bar{t}}$	transverse momentum of the $t\bar{t}$ system
$\mathrm{PCB}^{\mathrm{sum}}$	PCB score sum of the jets associated to the Higgs, hadronic and leptonic top
$\mathrm{PCB}^{\mathrm{add\,jet}}$	PCB score of the additional jet in the event

Table B.6: Input variables to the classification BDTs in the boosted single-lepton signal region. For variables depending on b-tagged jets, jets are sorted by their pseudo-continuous b-tag (PCB) score, and by their p_{T} when they have the same b-tag score. Moreover, the i index goes from zero to two.

C

Additional material from STXS analysis

C.1 Post-fit plots dilepton channel

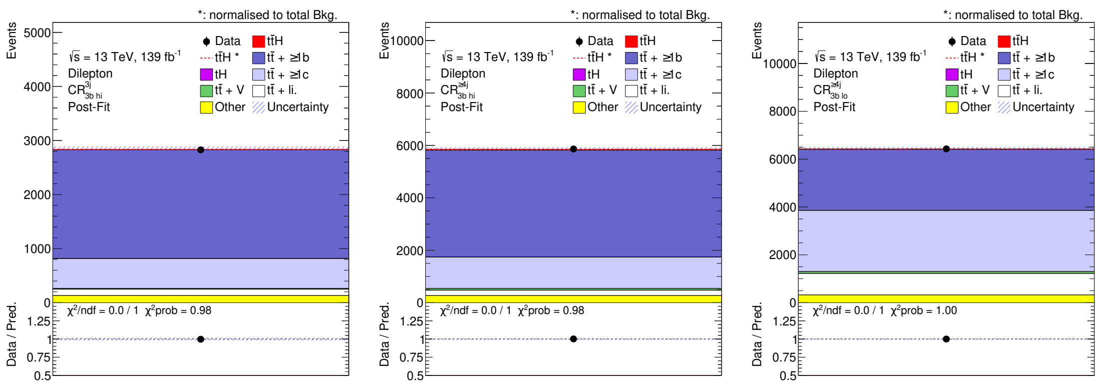

(a) (b) (c)

Figure C.1: Post-fit event yield in the dilepton regions with exactly three b-jets.

C.2 Renormalisation of systematic uncertainties

Uncertainty source	MC sample	Renormalisation factor
NLO matching	MADGRAPH5_aMC@NLO+PYTHIA8 $t\bar{t}$ (5FS)	1.0057
PS & hadronisation	POWHEGBOX+HERWIG7 $t\bar{t}$ (5FS)	1.3542
ISR up	POWHEGBOX+PYTHIA8 $t\bar{t}b\bar{b}$ (4FS)	0.9987
ISR down		0.9892
FSR up		0.9635
FSR down		1.0441

Table C.1: Renormalisation factors applied to each alternative MC sample used for the $t\bar{t}+\geq 1b$ modelling systematic uncertainties, so that the fraction of $t\bar{t}+\geq 1b$ events in the phase-space selected in the analysis is identical as for the nominal production.

C.3 Ranking STXS signal strengths

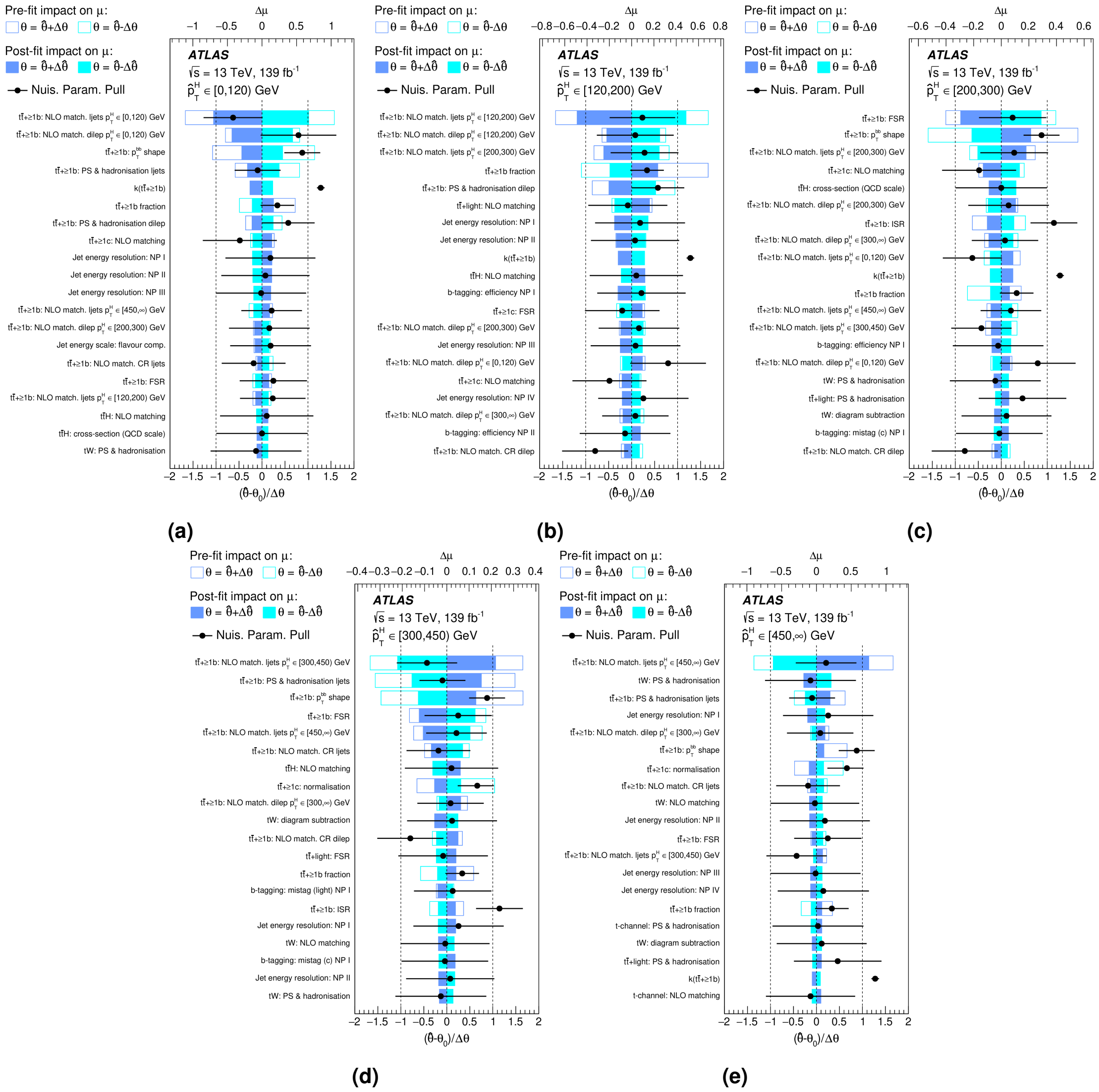

Figure C.2: Ranking plots for each of the STXS signal strengths.

D

Additional material from ttc analysis

D.1 Sample normalisation

Table D.1: Ratio of predicted events in the dilepton channel in the generator and fiducial phase space on particle level of the nominal POWHEGBOX+PYTHIA8 sample to the specified sample split into $t\bar{t}+1c$, $t\bar{t}+\geq 2c$, $t\bar{t}+\geq 1b$, and $t\bar{t}$+light. A '–' in the table refers to a variation that is not present for that $t\bar{t}$ component.

	Generator phase space				Fiducial phase space			
Sample	$t\bar{t}+1c$	$t\bar{t}+\geq 2c$	$t\bar{t}+\geq 1b$	$t\bar{t}$+light	$t\bar{t}+1c$	$t\bar{t}+\geq 2c$	$t\bar{t}+\geq 1b$	$t\bar{t}$+light
POWHEG+HERWIG7	1.2943	1.0789	1.0101	0.9876	1.0645	1.0474	0.9966	0.9826
$p_{\text{hard}}^{\text{hard}}$ variation	0.9845	0.9872	1.0244	1.0045	0.9737	0.9836	1.0376	0.9999
h_{damp} variation	0.9661	0.9396	–	1.0073	0.9470	0.9335	–	0.9805
h_{bzd} variation	–	–	1.0305	–	–	–	1.0316	–
Sherpa	–	–	1.0251	–	–	–	0.9778	–
Dipole recoil	–	–	1.0309	–	–	–	1.0454	–
ISR $\mu_{\text{R}} \times 2.0$	1.0008	1.0063	1.0107	1.0013	1.0023	1.0059	1.0261	1.0030
ISR $\mu_{\text{R}} \times 0.5$	0.9982	0.9914	0.9727	1.0046	0.9966	0.9917	0.9255	0.9954
ISR $\mu_{\text{F}} \times 2.0$	1.0005	1.0037	1.0106	1.0044	1.0013	1.0041	1.0151	1.0022
ISR $\mu_{\text{F}} \times 0.5$	0.9996	0.9958	0.9974	1.0050	0.9986	0.9955	0.9858	0.9975
ISR `Var3cUp`	0.9952	0.9791	1.0035	1.0077	0.9939	0.9768	0.9993	1.0002
ISR `Var3cDown`	1.0045	1.0200	1.0054	1.0027	1.0059	1.0229	1.0018	0.9998
$\mu_{\text{R}}^{\text{FSR}} \times 2.0$	1.0680	1.0648	1.0036	0.9885	1.0366	1.0264	0.9928	0.9631
$\mu_{\text{R}}^{\text{FSR}} \times 0.625$	0.9357	0.9407	1.0058	1.0218	0.9641	0.9795	1.0091	1.0380
$\mu_{\text{R}}^{\text{FSR}} \times 0.5$	0.9004	0.9075	1.0075	1.0321	0.9460	0.9735	1.0117	1.0620
`PDF4LHC15`	1.0017	1.0008	1.0030	1.0060	1.0024	1.0022	1.0010	1.0021
`PDF4LHC15` NP1	1.0018	1.0011	1.0031	1.0077	1.0013	1.0013	1.0013	1.0008
`PDF4LHC15` NP2	1.0014	1.0012	1.0033	1.0063	1.0020	1.0019	1.0007	1.0012
`PDF4LHC15` NP3	1.0017	1.0008	1.0031	1.0064	1.0020	1.0019	1.0005	1.0017
`PDF4LHC15` NP4	1.0012	1.0015	1.0030	1.0037	1.0036	1.0033	1.0006	1.0032
`PDF4LHC15` NP5	1.0012	1.0015	1.0030	1.0071	1.0003	1.0011	1.0005	1.0000
`PDF4LHC15` NP6	1.0015	1.0012	1.0037	1.0060	1.0011	1.0011	1.0018	1.0006
`PDF4LHC15` NP7	1.0018	1.0008	1.0033	1.0062	1.0025	1.0024	1.0010	1.0022
`PDF4LHC15` NP8	1.0017	1.0009	1.0030	1.0069	1.0011	1.0011	1.0009	1.0008
`PDF4LHC15` NP9	1.0017	1.0010	1.0033	1.0062	1.0024	1.0023	1.0015	1.0021
`PDF4LHC15` NP10	1.0018	1.0008	1.0033	1.0067	1.0017	1.0016	1.0020	1.0014
`PDF4LHC15` NP11	1.0015	1.0010	1.0035	1.0066	1.0020	1.0019	1.0020	1.0016
`PDF4LHC15` NP12	1.0017	1.0009	1.0032	1.0065	1.0016	1.0015	1.0011	1.0013
`PDF4LHC15` NP13	1.0018	1.0008	1.0034	1.0058	1.0025	1.0023	1.0031	1.0022
`PDF4LHC15` NP14	1.0016	1.0007	1.0031	1.0061	1.0025	1.0023	1.0013	1.0021
`PDF4LHC15` NP15	1.0016	1.0007	1.0032	1.0050	1.0026	1.0024	1.0007	1.0024
`PDF4LHC15` NP16	1.0016	1.0009	1.0033	1.0052	1.0029	1.0027	1.0012	1.0026
`PDF4LHC15` NP17	1.0016	1.0007	1.0036	1.0058	1.0019	1.0016	1.0012	1.0015
`PDF4LHC15` NP18	1.0018	1.0007	1.0028	1.0055	1.0030	1.0028	1.0000	1.0027
`PDF4LHC15` NP19	1.0015	1.0011	1.0030	1.0056	1.0016	1.0018	1.0004	1.0012
`PDF4LHC15` NP20	1.0017	1.0010	1.0030	1.0047	1.0030	1.0028	1.0005	1.0027
`PDF4LHC15` NP21	1.0017	1.0008	1.0030	1.0063	1.0022	1.0020	1.0007	1.0018
`PDF4LHC15` NP22	1.0020	1.0007	1.0032	1.0044	1.0061	1.0055	1.0015	1.0058
`PDF4LHC15` NP23	1.0017	1.0008	1.0028	1.0057	1.0024	1.0022	0.9999	1.0021
`PDF4LHC15` NP24	1.0017	1.0008	1.0031	1.0062	1.0025	1.0023	1.0007	1.0020
`PDF4LHC15` NP25	1.0018	1.0008	1.0030	1.0059	1.0025	1.0023	1.0010	1.0022
`PDF4LHC15` NP26	1.0017	1.0007	1.0030	1.0065	1.0018	1.0017	1.0006	1.0015
`PDF4LHC15` NP27	1.0017	1.0007	1.0029	1.0065	1.0020	1.0019	1.0006	1.0018
`PDF4LHC15` NP28	1.0015	1.0007	1.0029	1.0063	1.0006	1.0005	1.0002	1.0002
`PDF4LHC15` NP29	1.0017	1.0008	1.0031	1.0059	1.0025	1.0023	1.0013	1.0021
`PDF4LHC15` NP30	1.0017	1.0008	1.0031	1.0059	1.0024	1.0023	0.9990	1.0022

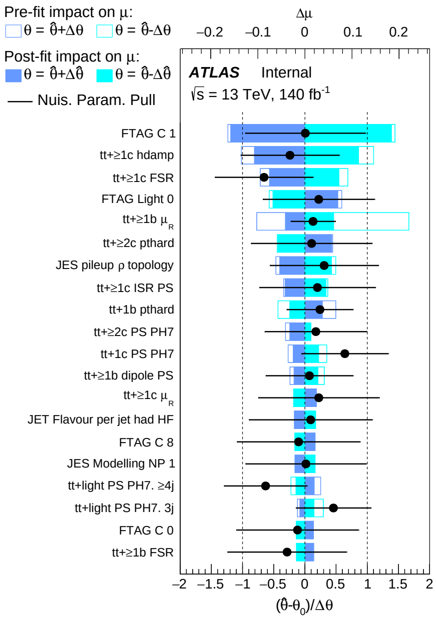

(a) Impact of systematic uncertainties on the ratio of $t\bar{t}+\geq 2c$ to inclusive $t\bar{t}$+jets production.

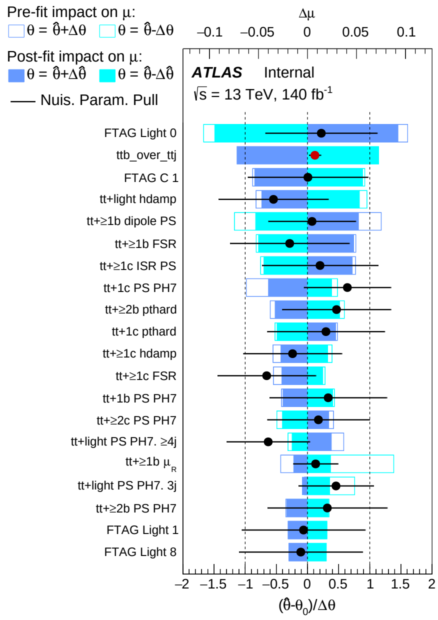

(b) Impact of systematic uncertainties on the ratio of $t\bar{t}+1c$ to inclusive $t\bar{t}$+jets production.

Figure D.1: Ranking plots showing the impact of each nuisance parameter on the ratios of $t\bar{t}+\geq 2c$ (left) and $t\bar{t}+1c$ (right) to inclusive $t\bar{t}$+jets production in fit to data in the fiducial phase space. Only the 20 nuisance parameters with the highest impact are shown.

D.2 Ratio rankings

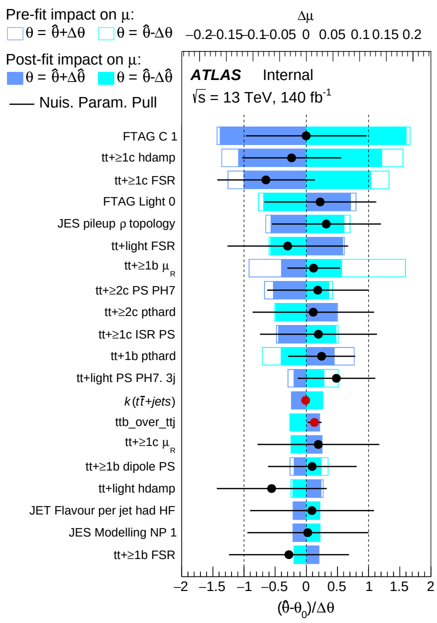

(a) Impact of systematic uncertainties on the ratio of $t\bar{t}+\geq 2b$ to inclusive $t\bar{t}$+jets production.

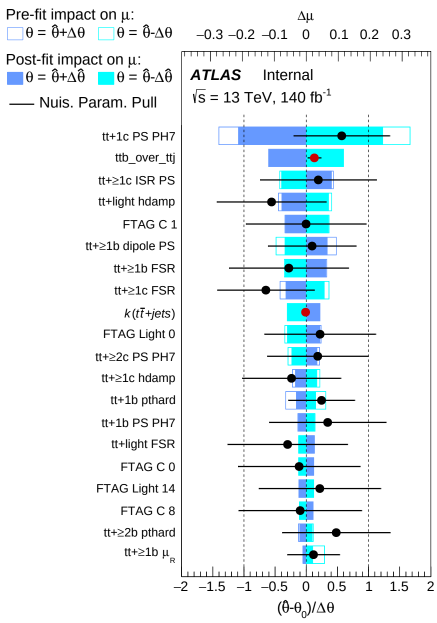

(b) Impact of systematic uncertainties on the ratio of $t\bar{t}+1c$ to inclusive $t\bar{t}$+jets production.

Figure D.2: Ranking plots showing the impact of each nuisance parameter on the ratios of $t\bar{t}+\geq 2b$ (left) and $t\bar{t}+1c$ (right) to inclusive $t\bar{t}$+jets production in fit to data in the generator phase space. Only the 20 nuisance parameters with the highest impact are shown.